THE UNIVERSITY OF HULL

Large Eddy Simulation of Acoustic Propagation in Turbulent Flow through Ducts and Mufflers

being a Thesis submitted for the Degree of

Doctor of Philosophy

to The University of Hull

by

Nishant Kumar Singh

February 2012

Contents

List of Figures

Abstract

This research involves study of acoustic propagation of pulse in a simple expansion muffler, which is very often used in HVAC or automotive exhausts. A hybrid pressure-based compressible solver is developed and validated for a low Mach number flow simulation of acoustic pulse. This new solver is developed using C++ based OpenFOAM toolkit and further tested for low Mach number flow test case. The analysis of simple expansion muffler for various structures, frequency ranges and numerical schemes is performed and results are summarized. RANS simulation of duct and muffler with mean flow is conducted and results are presented with inherent limitations associated with the method. Further, a mixed synthetic inflow boundary condition is also developed and validated for LES of channel flow. The mixed synthetic boundary is then used for LES of a simple expansion muffler to analyse the flow-acoustic and acoustic-pulse interactions inside the expansion muffler. The improvement in the prediction of tonal noise and vortex shedding inside the chamber is highlighted in comparison to the RANS method. Further, the effect of forced pulsation on flow-acoustic is observed in regard to the shift in Strouhal number inside the simple expansion muffler. Finally, a set of benchmark results for experimental analysis of the simple expansion muffler both, with and without flow is obtained to compare attenuation in forced pulsation for various mean-flow velocities. These experimental results are then used for validation of the proposed pressure-based compressible solver.

Declaration

No portion of the work referred to in the thesis has been submitted in support of an application for another degree or qualification of this or any other university or other institution of learning.

Acknowledgments

I would like to express my sincere gratitude to my Supervisor, Dr. Philip A. Rubini, Department of Engineering for his invaluable suggestions, careful supervision and constant availability during my research work.

I am thankful to Dr. Qin Qin for his advice and support in experimental planning and to all my colleagues- Brian, Carl, Haydar, Imran, Sujeet and Adnan- during this course for their friendship and collaboration. I would like to thank Mr. Steve Coopland for his help in obtaining software licences and hardware related issues on various occasions. I would also like to thank Avishek Ranjan, St John's College, University of Cambridge for his valuable feedback on the thesis.

Special thanks go to my parents and family for their continuous support throughout these years of research. I also would like to dedicate this work to my grandfather Shri. Jagdeo Singh, who has been an inspiration to me throughout my life.

Finally, I would like to acknowledge the Department of Engineering and Head of Department for sponsoring this research which allowed the work to be carried out successfully.

Nomenclature

ρ	Density
u_i	Velocity
P	Pressure
h	Enthalpy
R	Gas Constant
T	Temperature
τ_{ij}	Shear stress
S_i	Source term
k	Turbulent kinetic energy
ε	Turbulent dissipation
U^+	Velocity wall units
y^+	Distance wall units
Re_τ	Friction Reynolds number
U, V, W	Velocity component in x, y and z directions
u_η	Velocity scale
l_η	Length scale
τ_η	Time scale
ω	Angular frequency
c	Velocity of sound
k	Wavenumber
a_j	Co-efficient of central differencing or DRP scheme
φ	Flux across the face
d_e	Expansion chamber diameter
d_i	Inlet/tailpipe diameter
R_j	Two-point spatial or temporal correlation tensor
v_{rms}	RMS velocity
ψ_{ij}	Velocity spectrum
E_{ii}	Energy spectrum function
Γ	Gamma function

R_{ij}	Reynolds stress tensor
r_m	Series of random data
v_{ik}	Eigen vectors in digital filers
b_k	Filter co-efficients in digital filters
ϕ_k	Phase angle
$U'(x)$	Modified velocity spectrum
σ_r	Direction of the rth Fourier mode
$G(x)$	Filter kernel
Δ	Grid spacing
$\bar{S}$	Strain rate tensor
C_s	Smagorinsky constant
v_{sgs}	SGS viscosity
δ	Channel half-width
u_f	Forced pulse velocity

Conventions

$.^+$	Normalised wall units
$\langle . \rangle$	Ensemble averaging
$\bar{.}$	Filtered variable in LES and Reynolds average in RANS
$\hat{.}$	Density averaged Filtered (LES) or Rey. averaged (RANS) variable.

Acronyms

CFD	Computational Fluid Dynamics
DNS	Direct Numerical Simulation
LES	Large Eddy Simulation
DES	Detached-Eddy Simulation
RANS	Reynolds Averaged Navier-Stokes
PDF	Probability Density Function
RMS	Root Mean Square
PISO	Pressure-Implicit with Splitting of Operator
SIMPLE	Semi-Implicit Pressure Linked Equations

Chapter 1

Introduction

1.1 Motivation

Noise has been one of the most unproductive wastes in recent technological inventions. With increasing challenges and complexities in the design process of mechanical devices and stricter environment norms set by governments, the control and reduction of noise has become a bigger challenge today. The study of sound attenuation has been an active area of research for researchers over many decades. In order to understand the control and attenuation of noise in industry, sound propagation in acoustic devices has been extensively researched.

Acoustic filters and ducts are usually employed in various automotive or aerospace applications to attenuate noise, the classic example being that of an automotive silence, see figure 1. An acoustic high-pass filter, like the vented duct, blocks the low frequency waves and lets the high frequency waves pass. A band-stop filter, such as the Helmholtz resonator, blocks any sound within a band of frequency around the resonance frequency and lets all other frequencies pass. However, the most notably used low-pass filter is a simple expansion muffler, which lets the low frequency waves pass and blocks the high frequency waves. Because of the numerous applications in exhaust silencer and HVAC (Heating, Ventilating, and Air Conditioning) systems, simulation of expansion mufflers has been extensively researched.

A muffler works on the principle of destructive interference to reduce noise. The flow separation inside the expansion chamber leads to reflection of noise which interacts with the incoming noise

in a destructive way to attenuate noise inside the device. The widening at the inlet of the expansion chamber provides the flow separation which results in the change of impedance. Due to this impedance change, a portion of the incoming wave is reflected back to the source and creates back-pressure. The transmitted wave, however, first interacts with the waves inside the expansion chamber and then with the downstream edge of the expansion chamber to produce respectively, vortex shedding and the tonal noise inside muffler. These noises are of great significance to the industry and therefore more research is required in this area. Figure 1.1(a) shows wave propagation in a simple expansion muffler and Figure 1.1(b) shows a muffler installed in an automobile.

Computational Fluid Dynamics (CFD) has been developed as an important modelling and simulation tool for engineering applications in the past four decades. CFD has helped develop faster, efficient and cost effective design as an alternative to costly experimental work for industry. The modelling of turbulence is believed to be a difficult process to simulate in CFD and it often involves simplifications which cause inaccuracies in the simulation. The difficulty is owing to the very large range of length scales which could be hard to model and also because of the complex nature and sensitivity of the flow fields to the initial conditions. Turbulence is also found to be one of the major contributors to the sound attenuation in propagation media and therefore an accurate prediction of turbulence is crucial for modelling noise propagation.

In addition to the difficulties in turbulence modelling, CFD simulation of a simple expansion muffler comes with additional problems of back pressure and flow separation due to the sudden expansion in the muffler, which further enhances the turbulent fluctuations inside the computational domain. Moreover, in order to capture the acoustic scales and avoid aliasing in the simulation of an expansion muffler, the discretization should be accurate and turbulence should be

modelled accurately. A solver also needs to be robust in order to simulate low Mach number simulation of acoustic pulse propagation through an expansion muffler. The problem becomes more complicated when mean flow is also included in the simulation, which leads to the interaction of various length scales in the same computational domain.

(a)

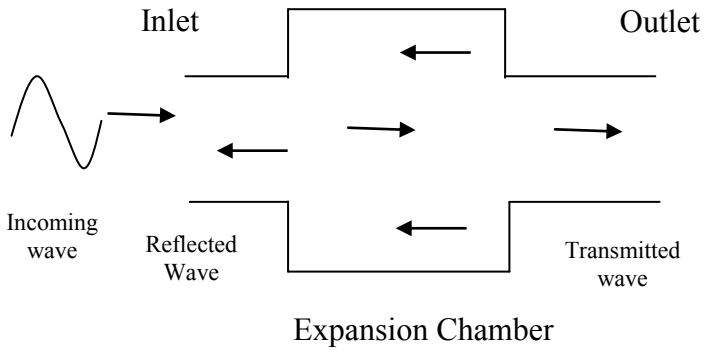

(b)

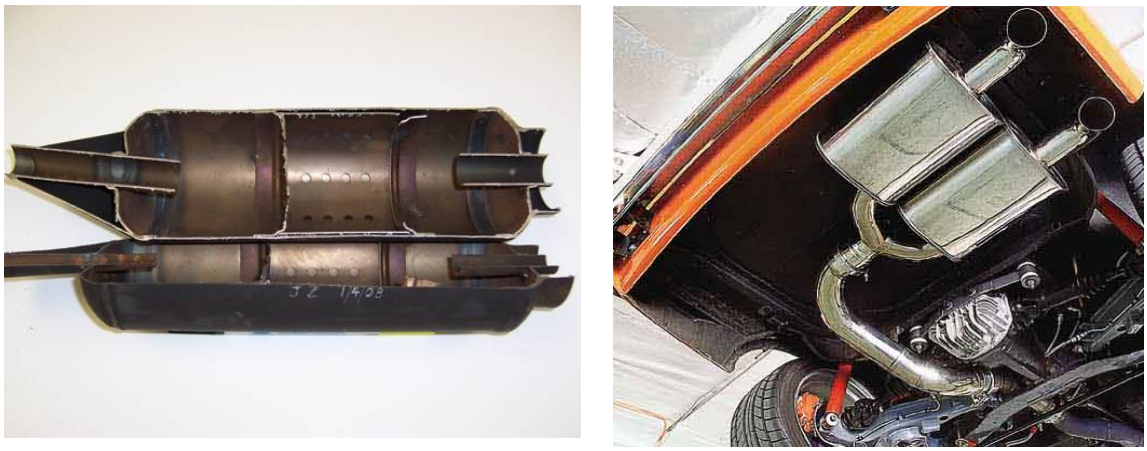

Figure 1.1: *(a) Wave propagation in a simple expansion muffler; (b) A typical expansion muffler (left) and installation of muffler as automobile exhaust (right). Courtesy: Datsunparts.com Inc.*

Direct Numerical Simulation (DNS) involves the solution of Navier-Stokes equation by resolving all the scales of motion without any turbulence model and therefore is very expensive in terms of computational resources and time. Currently computational resources available are not enough to simulate engineering problems and therefore direct computation is restricted to low Reynolds

number flow only. As a practical alternative, the Reynolds-averaged Navier-Stokes (RANS) simulation method is more common in engineering and industrial applications. On the other hand, RANS involves averaging of Navier-Stokes equations and is not found to be very accurate and effective in unsteady flow. However, a compromise between RANS and DNS lies in Large-Eddy Simulation (LES). LES spatially filters the equations of motion using appropriate filter and resolves eddies larger than the filter size and models only the effect of smaller eddies on larger ones. The benefit of LES is that it is more reliable and accurate than RANS and yet it does not have to solve the entire range of turbulence scales like DNS.

1.2 Objectives

A set of Navier-Stokes equations provides a full range of length scales in a physical problem and involves no simplifications. The computation of the set of Navier-Stokes equation can provide the true solution of the physical problem. In fluid dynamics problems, DNS computes the full range of length scales of Navier-Stokes equations and therefore requires extremely fine mesh for the computation. On the other hand, LES only computes the larger scales of the Navier-Stokes equations and the effects of smaller scales are modelled and therefore mesh requirements are only moderately high. In case of unsteady flow simulation, these LES simulations consume enormous computational time and resource. However, with recent advances in computational resources, these moderate mesh requirements can now be simulated. Acoustics, being a fluid dynamics problem, can also be correctly represented by the set of Navier-Stokes equations, which can be computed using DNS or LES to obtain solutions. Simulation of a simple expansion muffler involves either a long inlet/outlet or a non-reflection boundary at the ends to avoid any reflections into the computational domain. In the case of a long inlet/outlet, the DNS or LES of Navier-Stokes equations would require a large number of points and therefore such computation has so far been

avoided. The present investigation, therefore, focuses on LES simulation of pulse propagation in a simple expansion muffler and duct.

The main objectives of this research are:

- Develop and validate a Navier-Stokes solver for low Mach number computation of internal acoustic flow.
- Develop and validate a mixed synthetic inflow boundary for LES of internal acoustic flow.
- Investigate the pulse propagation and its interaction with flow-acoustic in a simple expansion muffler.

1.3 Thesis Outline

The research carried out in this thesis can be outlined as follows:

Chapter 2 introduces the proposed pressure based Karki-PISO compressible low Mach number solver and the C++ based OpenFOAM software. A mesh independence study is carried out for a typical pulse propagation problem through simple expansion muffler to acknowledge the spatial discretization in the simulation.

Chapter 3 provides background theory on turbulence along with several turbulence models and introduces a wall-bounded turbulence-generation mechanism.

In Chapter 4, different configurations and numerical schemes are investigated for the simple expansion muffler for pulse propagation in a no-flow condition. Later on, RANS simulations with considerable mean flow are carried out for circular pipe and simple expansion muffler to investigate the transmission loss spectrum.

In Chapter 5, experimental analysis of an expansion muffler is carried out for a range of random pulsating noises both with and without considerable mean flow. The analysis of transmission loss for various flow speeds is also conducted for several pulsating flow frequencies.

Chapter 6 introduces the mixed synthetic boundary condition for inflow turbulence and the evolution of the synthetic boundary along with other contemporary inflow boundary condition is introduced.

In Chapter 7, LES of channel flow is performed and comparison of various sub-grid models is conducted to demonstrate the ability of OpenFOAM to conduct LES of wall bounded flow. The mixed synthetic boundary condition for inflow generation is also used for LES of a long channel.

In Chapter 8, extending the experience gained in the use of LES for channel flow presented in the preceding chapter, the acoustic mean flow simulation of simple expansion muffler and a detailed analysis of various frequencies available in the muffler is presented. Further, a simple expansion muffler is analysed for various frequencies of forced pulsation at the inlet and the effect of forced pulsation on the flow-acoustic interaction are discussed.

Chapter 2

Low Mach number Compressible Solver

2.1 Introduction

Simulation of acoustic propagation and attenuation has been an essential component of the design and development of noise reduction systems. With increasingly stricter regulations on noise level in various engineering appliances, study of acoustic propagation and attenuation has gained considerable importance for industry and society. Generally, the compressible solvers preserve more acoustic information in comparison to the incompressible solvers but it comes at the expense of extra computation costs. However, due to advances in the memory and speed of high performance computers, the application of computational method to such problems is becoming viable. This chapter introduces a new pressure based compressible solver for simulation of low Mach compressible flow. This solver is then verified with simulation of a single sinusoidal pulse imposed on the inlet of a simple expansion muffler.

Despite these advances, however, there are several issues hindering the growth of the area of Computational acoustics. These issues include the disparity in the scales of flow fields and fields associated with acoustic waves. Although incompressible solvers provide savings in duration of computational effort, that saving comes at the cost of losing some acoustic information from the solution, which is often critical to the problem, especially in understanding the physics of acoustic pulse propagation in various acoustic devices. For compressible solvers, spatial pressure variations vanish as the Mach number tends towards zero, but they still affect the velocity to a high degree. Therefore, many unsteady flow problems, especially acoustic noise simulations or turbulent flow

simulations, require highly accurate simulation. Besides that, the governing equations for acoustic flow change their type and therefore equations for unsteady inviscid compressible flow form a hyperbolic system with finite wave speed, whereas their incompressible counterpart is hyperbolic-elliptic with infinite propagation rates. These are the reasons why most of the time-dependent Computational Acoustic studies in the past have avoided Computational Fluid Dynamics (CFD) methods for simulation of acoustic pulse and instead, some computational models were used. However, with the current advances in high performance computing and CFD techniques, it has become possible to simulate a time dependent computational acoustic problem at low Mach number.

Two different approaches named pressure-based methods and density-based methods have traditionally been adopted in developing numerical methods for solving low Mach number flows. There has been a lot of work in the density based methods in the past but the pressure-based methods are also gaining popularity among researchers. The pioneer work in this area was done by Chorin (Chorin 1967, Chorin 1968), which was further enhanced and modified by Patankar in their SIMPLE family of scheme. (Patankar 1980) Clearly, the SIMPLE scheme was one of the most robust and widely applicable finite-volume methods available at that time. Karki and Patankar (Karki, Patankar 1989) further extended the scheme to make a unified algorithm for both compressible and incompressible flow problems, which worked for all Mach number flow ranges. Shyy and Chen (Shyy, Chen et al. 1992a) also introduced a pressure-based multi-grid method using upwind schemes for density and convective terms. A non-orthogonal boundary-fitted mesh with collocated grid was used and a comparative study for the efficiency and robustness was carried out. The method was found to be more efficient than the single grid methods and found to achieve faster convergence and performance speed-ups.

On the other hand, an implicitly discretised time dependent non-iterative pressure-based Operator Splitting method named PISO (Pressure-Implicit with Splitting of Operators) was developed by Issa (Issa 1985). This Operator splitting method uses the splitting of operators into a series of steps in such a way that the pressure equations are decoupled from the velocity equation at each time step. The fields obtained at each time step are a close approximation of the exact differencing equation with an order of accuracy depending upon the power of number of operator splitting on time-step increment (δt). PISO was also tested for its stability and its applicability to the steady state problem (Issa, Gosman et al. 1986). PISO was further extended for implementation to combustion related problems by Isaa *et al*.(Issa, Ahmadi-Befrui et al. 1991). Some semi-implicit methods have also been implemented recently for the resolution of acoustic wave in low Mach number flows (Wall, Pierce et al. 2002).

There has been some extensive works done in the past in the area of density-based methods for low Mach number flow regions (Chorin 1967, Pulliam, Steger 1980, Merkle, Venkateswaran et al. 1992, Merkle, Choi 1988, Choi, Merkle 1993). Previously, Turkel (Turkel 1987) extended Chorin's method to compressible governing equations and devised a preconditioning scheme for Euler equations for all Mach number flows. Merkle and Choi (Merkle, Choi 1988) further improved Turkel's work by adopting the splitting of the static and dynamic pressure contributions to solve the problem of low Mach numbers as small as 10^{-6}. Choi and Merkle improved preconditioning procedure to achieve Mach number independent convergence and twice improved speed-up later on in their work (Choi, Merkle 1993).

Finite difference methods have been widely using the central schemes for solving nonlinear convection-diffusion equations governing spontaneous evolution of large gradient phenomena. The preference for the finite difference method for central schemes is because the

convection-diffusion equations are not tied to specific eigen-structures, like most finite volume methods. The most famous of these methods is the first-order central Lax-Friedrichs scheme (Lax 1954). This method was further improved by providing higher resolution and maintaining the simplicity of the Riemann-solver-free characteristic by central scheme of Nessyahu and Tadmor (NT) (Nessyahu, Tadmor 1990). Kurganov and Tadmor (Kurganov, Tadmor 2000) further modified the NT-scheme by using precise local propagation speed information without requiring any other specific information except the CFL (Courant–Friedrichs–Lewy) number. This central scheme provides approximate solutions in terms of cell averages integrated over Riemann fans of varying size. In order to improve the compressible flow solver in the low Mach region for finite-element methods, Schneider (Schneider, Karimian 1994) proposed a Finite Element Differential Scheme (FIELDS) for compressible flow using mass flux instead of velocity as the dependent variable in addition to pressure and temperature. This method seems to have overcome the pressure checkerboard problem (like SIMPLE schemes) but the robustness of the algorithm has remained questionable. Jenny and Muller (Jenny, Muller 1999) attempted a technique to accelerate convergence of compressible low Mach number flow solvers by artificially reducing the speed of the sound and subtracting a constant term from the pressure in the entire flow field to perform a steady-state simulation. A unique attempt has been made to formulate a finite-element Characteristic-Based-Splitting (CBS) method based on Taylor-Galerkin/pressure-correction for both compressible and incompressible flows. (Zienkiewicz, Codina 1995, Hawken, Tamaddon-Jahromi et al. 1990)

There have been many attempts to construct a unified solver to simulate low Mach number flow using finite difference and finite volume methods for both compressible and incompressible flow problems. The first such attempt was made by Harlow and Amsden (Harlow, Amsden 1968,

Harlow, Amsden 1971) in their Implicit Continuous-fluid Eulerian (ICE) to solve time-dependent viscous compressible and incompressible flow problems. This method essentially reduces to the Marker and Cell (MAC) method in the low Mach number flow region. The MAC method was proposed by Harlow and Welch (Harlow, Welch 1965) to overcome the formation of a checkerboard pressure field by introducing the staggered grid arrangement. Patankar and Spalding (Patankar, Spalding 1972), however, extended this method and incorporated it into their SIMPLE (Semi-Implicit Pressure Linked Equations) code. Currently, the collocated scheme is preferred over scattered grid because of the complicated computational effort required in extension of staggered arrangement to non-orthogonal grids. Rhie and Chow (Rhie, Chow 1983) constructed the first such procedure for the finite-volume based method, which uses non-orthogonal co-ordinates and a collocated variable arrangement. Rhie introduced a notable procedure named multi-grid method in his next work to accelerate the iteration procedure (Rhie 1989). Later, Shyy *et al.* (Shyy, Chen et al. 1992a, Shyy, Chen et al. 1992b) extended this to pressure based methods and compared their results and efficiency with those of the single grid methods. This method seems to have higher speed-ups while working with incompressible methods. Initial work in this area was also done by Brandt (Brandt 1977) and Braaten et al. (Braaten, Shyy 1987)

In the present work, a pressure-based hybrid algorithm derived from Issa's PISO solver (Issa 1985, Issa, Gosman et al. 1986) and Karki's low Mach number flow solver (Karki, Patankar 1989), is proposed to simulate low Mach aero-acoustic flow in a simple expansion muffler. An attempt is made in the present work to formulate a low Mach number compressible flow solver for acoustic propagation problems. A recent attempt of developing pressure based low Mach number flow solver is made by Wall *et al*. (Wall, Pierce et al. 2002), which is similar to incompressible pressure-correction method but involves more iterations at each time step. Moureau *et al.*

(Moureau, Berat et al. 2007) has also devised a similar strategy for application in combustion stability problem. The hybrid pressure-based compressible flow solver is specially designed to handle low Mach number flow regions, instead of the general pressure based subsonic flow compressible solver used by commercial CFD codes. Section 2.2 explains well-known pressure-based finite volume compressible solvers and central scheme based finite difference compressible solvers. In section 2.3, a new proposed hybrid Karki-PISO compressible solver is put forward. In the end, some test cases are performed for validation of the proposed solver.

2.2 Computational Solver for Low Mach number Flow

The most common computational methods used for simulation of acoustic pulse through a muffler are Analytical method and Boundary Element Method. Advanced CFD methods like Finite Volume Methods (FVM) have been more or less restricted in application to acoustic propagation problem because of constraints in terms of the vast computational requirement for acoustic problems. The other problem in solving acoustic problems is the time-dependent nature of these simulations, which again puts extra computational load in terms of computational requirement and computational robustness. However, with the remarkable improvement in the computational resources in last decade, it has become possible to apply these CFD methods to acoustic problems. These CFD studies have the capacity to provide a better insight into the physics of these problems (DeSpirito, Binseel 2008, Middelberg, Barber et al. 2004, Mohiuddin, Rahman et al. 2007). Unlike BEM methods which solve a Helmholtz equation to obtain results, CFD methods usually solve Navier-Stokes equation or Euler equations to simulate flow.

2.2.1 Governing Equations:

The equations which need to be solved in laminar CFD solver are continuity equation, momentum equation, energy equation and equation of state:

$$\frac{\partial \rho}{\partial t} + \frac{\partial \rho u_i}{\partial x_i} = 0, \tag{2.1}$$

$$\frac{\partial \rho u_i}{\partial t} + \frac{\partial \rho u_i u_j}{\partial x_j} = -\frac{\partial P}{\partial x_j} + \frac{\partial \tau_{ij}}{\partial x_j}, \tag{2.2}$$

$$\frac{\partial \rho h}{\partial t} + \frac{\partial \rho u_j h}{\partial x_j} = \frac{\partial}{\partial x_j}\left(k\frac{\partial T}{\partial x_j}\right) + \tau_{ij}\frac{\partial u_i}{\partial x_j} + \frac{\partial P}{\partial t} + u_j\frac{\partial P}{\partial x_j}, \tag{2.3}$$

$$P = \rho RT. \tag{2.4}$$

Where ρ is density, u_i are the components of velocity, P is the pressure, T is temperature, h is enthalpy, τ is the viscous stress, and R is the ideal gas constant. A total energy equation, instead of the enthalpy equation, could have better conservation properties in the presence of shock waves but it is not considered here as there are no shock waves involved in the low Mach number flows.

2.2.2 Pressure-based Compressible Solvers

Most of the efficient pressure-based solvers employ either the PISO or SIMPLE method. Many hybrid methods have also been inspired by these approaches to enhance the performance of PISO in the low Mach number flow region. In this section, PISO discretization and Karki's approach are explained and Kurganov *et al.*'s finite difference based central scheme is briefly introduced.

Pressure-Implicit with Splitting of Operators (PISO) discretization:

The governing equations (2.1)-(2.4) for compressible fluid have been expressed in difference form for each mesh point as

$$\frac{1}{\delta t}\{(\rho u_i)^{n+1} - (\rho u_i)^n\} = H(u_i^{n+1}) - \Delta_i P^{n+1} + S_i \tag{2.5}$$

$$\frac{1}{\delta t}(\rho^{n+1} - \rho^n) + \Delta_i(\rho u_i)^{n+1} = 0 \tag{2.6}$$

$$\frac{1}{\delta t}\{(\rho e)^{n+1} - (\rho e)^n\} = G(e^{n+1}) - \Delta_i(p u_i)^{n+1} + J(u_i^{n+1}) + Q \tag{2.7}$$

Where n and n+1 denote successive time levels and H(u_i) and G(e) are operators which take the form as

$$H(u_i) = A_m u_{i,m} \tag{2.8}$$

$$G(e) = B_m e_m \tag{2.9}$$

Here, the suffix m is a grid node identifier and summation is all over the nodes involved in the formulation of the finite-difference representation of the spatial fluxes. Issa suggested an improved scheme for better accuracy at corrector stage by splitting off the operators as

$$H'(u_i) = H(u_i) - A_0 u_i \tag{2.10}$$

The details of this splitting of operator can be found here (Issa 1985, Issa, Gosman et al. 1986). Further, a pressure equation is derived by taking divergence of Eq. (2.5), substituting for $\Delta_i(\rho u_i)^{n+1}$ in Eq. (2.6) and rearranging the expression to get

$$\Delta_i^2 p^{n+1} = \Delta_i H(u_i^{n+1}) + \frac{1}{\delta t}\Delta_i(\rho u_i)^n + \Delta_i S_i + \frac{1}{\delta t^2}(\rho^{n+1} - \rho^n) \tag{2.11}$$

It can be seen that the Eq. (2.5) and (2.11) are linearly coupled through the appearance of $p^{n+1}$and u_i^{n+1}. This coupling enables the algorithm to iteratively solve discretisation equations second order accurate (O(2)).

In the final formulation, the splitting of operator is included in the Eq. (2.5), (2.6) and (2.7) to formulate a predictor-corrector scheme. There are two and three stage predictor-corrector methods, the effectiveness and accuracy of which is discussed elsewhere. A typical multi-stage scheme is composed of one predictor step and other corrector steps.

Momentum predictor step: The equation of momentum is solved in this step implicitly using old pressures and densities as

$$\left(\frac{1}{\delta t} - \frac{A_0}{\rho^n}\right)\rho^n u_i^* = H'(u_i^*) - \Delta_i p^n + S_i + \frac{\rho^n u_i^n}{\delta t} \tag{2.12}$$

This equation solves for u_i^*, which is used in the corrector step.

Momentum Corrector step: The momentum equation is then written in explicit corrector form as

$$\left(\frac{1}{\delta t} - \frac{A_0}{\rho^n}\right)\rho^* u_i^{**} = H'(u_i^*) - \Delta_i p^* + S_i + \frac{\rho^n u_i^n}{\delta t} \tag{2.13}$$

Subtracting Eq. (2.12) from (2.13) and invoking the continuity equation and equation of state, the pressure-increment equation is obtained as

$$\left[\Delta_i\left\{\left(\frac{1}{\delta t} - \frac{A_0}{\rho^n}\right)^{-1}\Delta_i\right\} - \frac{\phi(p^n,T^n)}{\delta t}\right](p^* - p^n) = \Delta_i(\rho^n u_i^*) \tag{2.14}$$

This pressure-increment equation is solved to yield p^* field. Equation of state and continuity equations are used to determine ρ^* and u_i^{**}. Similarly the second momentum corrector step and third momentum corrector steps can be implemented to improve accuracy and efficiency. The final corrector step thereby completes the splitting and the latest computed fields are now regarded as the final solution to the original equations (2.1), (2.2), (2.3) and (2.4). The details of this method can again be found here (Issa 1985, Issa, Gosman et al. 1986).

Karki's approach:

In an attempt to construct a procedure for viscous flow at all Mach number flow, Karki and Patankar (Karki, Patankar 1989) put forward a different approach using a compressible form of SIMPLER algorithm. This approach casts momentum equations in terms of the physical velocity components along the grid lines, and keeps pressure as the main dependent variable in preference to density. The mass flux through the control-volume face of each grid is given by

$$\rho^* u_i^{**} = (\rho^n + \rho')(u_i^* + u_i') = \rho^n u_i^* + \rho^n u_i' + \rho' u_i^* \tag{2.15}$$

In Eq. (2.15), the second order term $\rho' u_i'$ is ignored. The velocity changes and density changes respond to the change in pressure as follows:

$$u_i' = d_e(p_p' - p_E'), \qquad d_e = \frac{A_e}{a_e} \tag{2.16}$$

$$\rho' = Kp', \tag{2.17}$$

Here a_e and A_e are the convective and diffusive coefficients. K represents a measure of influence of pressure on density and can be obtained from the equation of state. In a one-dimensional situation, the mass flux on the face can be given by

$$\rho^* u_i^{**} = \rho^n u_i^* + \rho^n d_e \left(p'_p - p'_E\right) + Kp' u_i^* \tag{2.18}$$

The diffusion like term involving d_e is responsible for downstream pressure effects, whereas the convective term involving K exhibits upstream effects. The ratio $\frac{\rho^n d_e}{K u_i^*}$ is inversely proportional to the square of the Mach number. At high Mach numbers, the term involving upstream pressure is dominant and the equation exhibits a hyperbolic nature. However at low Mach numbers, the term

involving pressure differencing becomes dominant and the equation exhibits an elliptic nature. As this algorithm should yield a pressure correction equation that exhibits the correct Mach number dependent behaviour, the present equation exhibits the Mach dependent behaviour through these two convection like and diffusion like terms. The details of this method can be found here (Karki 1986). This idea of yielding a pressure correction equation that exhibits elliptic behaviour in subsonic flow and hyperbolic behaviour in supersonic flow has become the basis of opting for the proposed Mach uniform hybrid algorithm, which also has the robustness of PISO.

2.2.3 Finite-difference-based Central Scheme

As mentioned earlier, finite-difference methods for solving convection-diffusion equations are not tied to specific eigen-structures as most of finite volume methods are, and therefore are universally used for solving convection-diffusion equations. Kurganov and Tadmor's (Kurganov, Tadmor 2000) central scheme uses the idea of constructing a central scheme by using precise information of the local propagation speed to improve the second order Riemann-solver-free NT scheme. The scheme does not require any other characteristic information besides the CFL related speeds. Besides, the realization and generalization of this scheme for complicated multidimensional systems is comparatively easier than those upwind schemes of a similar order. This scheme has far less numerical viscosity than the original NT scheme and it can be written and integrated efficiently in semi-discrete form much more easily than other central schemes.

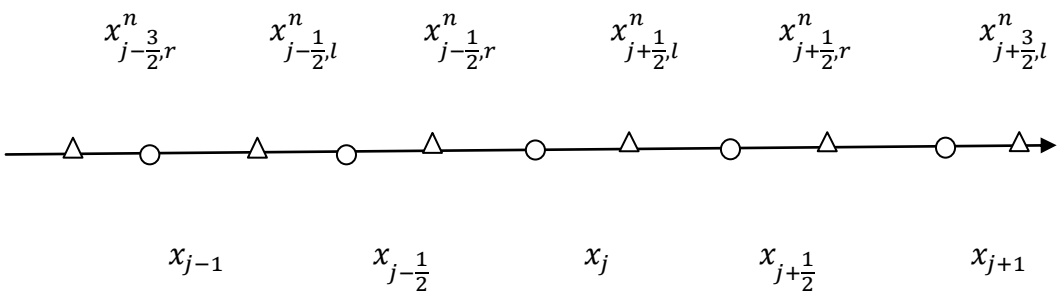

Figure 2.1: *Central scheme proposed by Kurganov and Tadmor.*

This scheme can be represented as the Godunov-type scheme by initially assuming already computed approximation of the piecewise-linear solution at time level t^n, based on cell averages u_j^n and reconstructing approximated derivative $(u_x)_j^n$ using equation,

$$u(x,t^n) = \sum_j \left[\overline{u_j^n} + (u_x)_j^n (x - x_j)\right] I_{[x(j-1/2,)\, x(j+1/2)]} \qquad \text{... (2.19)}$$

The solution evolves in time according to estimated local speed of propagation at cell boundaries, $x_{j+\frac{1}{2}}$: the upper bound is denoted by $a^n_{j+\frac{1}{2}}$ and is given by,

$$a^n_{j+\frac{1}{2}} := max\left\{\rho\left(\frac{\partial f}{\partial u}(u^-{}_{j+\frac{1}{2}})\right), \rho\left(\frac{\partial f}{\partial u}(u^+{}_{j+\frac{1}{2}})\right)\right\} \qquad \text{... (2.20)}$$

Where $u^{\mp}{}_{j+\frac{1}{2}} = u^n_{j+1} \pm \frac{\Delta x}{2}(u_x)^n_j$. A narrower control volume is used where at each time step integration is performed over the intervals $[x^n_{j+1/2,l}, x^n_{j+1/2,r}]\ x\ [t^n, t^{n+1}]$ (as shown in Figure 2.1). The points $x^n_{j+1/2,l} = x_{j+\frac{1}{2}} - a^n_{j+\frac{1}{2}}\Delta t$ and $x^n_{j+1/2,r} = x_{j+\frac{1}{2}} + a^n_{j+\frac{1}{2}}\Delta t$ separate between the smooth and the non-smooth regions and the non-smooth region are then contained inside these narrower control volumes. The exact evaluation of the new cell averages at t^{n+1} is obtained as,

$$w_{j+1/2}^{n+1} = \frac{u_j^n + u_{j+1}^n}{2} + \frac{\Delta x - a_{j+\frac{1}{2}}^n \Delta t}{4}\left((u_x)_j^n - (u_x)_{j+1}^n \right) - \frac{1}{2a_{j+\frac{1}{2}}^n}\left(f\left(u_{j+\frac{1}{2},r}^{n+\frac{1}{2}} \right) - f\left(u_{j+\frac{1}{2},l}^{n+\frac{1}{2}} \right) \right)$$

...(2.21)

Finally, the desired cell averages, u_j^{n+1} for the discrete second-order central scheme are obtained by averaging the approximate solution of the piecewise-linear approximation of Eq. (2.21) as,

$$u_j^{n+1} = \frac{1}{\Delta x}\int_{x_{j-\frac{1}{2}}}^{x_{j+\frac{1}{2}}} \widetilde{w}(\xi, t^{n+1}) d\xi$$

... (2.22)

2.3 Proposed Hybrid Karki-PISO Algorithm

A hybrid algorithm is proposed here which adopts the operator splitting feature of PISO with modified predictor and corrector steps inspired by Karki's derivation of mass-flux at control-volume face represented by equation (2.15), achieving a tighter coupling between predictor and corrector steps. Previously, there have been several attempts to obtain a hybrid algorithm using various known methods. Some of them are mentioned by Barton in his work (Barton 1998) where a hybrid PISO+SIMPLE scheme is also presented. However unlike the present implementation, where a closer coupling has been achieved, the PISO+SIMPLE hybrid algorithm uses one loop of PISO and a consecutive loop of SIMPLE to obtain a final corrected value. This PISO+SIMPLE algorithm has not been tested for low Mach number acoustic simulations. A very similar attempt has also been made by Xu (Xu, Ge et al. 2009) to implement a hybrid SIMPLER+PISO named as SIMPLEXT. All these hybrid algorithms are generally simplistic and have not been specifically tested for low Mach number acoustic simulations. The proposed hybrid Karki-PISO algorithm can be explained in various predictor-corrector steps as follows:

Momentum predictor step: The equation of momentum of this hybrid algorithm is solved in this step implicitly using old pressures and densities as

$$\left(\frac{1}{\delta t} - \frac{A_0}{\rho^n}\right)\rho^n u_i^* = H'(u_i^*) - \Delta_i p^n + S_i + \frac{\rho^n u_i^n}{\delta t} \tag{2.23}$$

Momentum Corrector step: The momentum equation is then written in explicit corrector form as

$$\left(\frac{1}{\delta t} - \frac{A_0}{\rho^n}\right)\rho^n u_i^{**} = H'(u_i^*) - \Delta_i p^* + S_i + \frac{\rho^n u_i^n}{\delta t} \tag{2.24}$$

In the corrector stage, the coupling is required to be established using a pressure-correction equation. As it can be noticed at this stage, the density value from previous iteration is used on the left side of Eq. (2.24), instead of the latest density value. However the pressure differential on the right side of Eq. (2.24) uses the latest density value obtained from solving the pressure corrector equation (Eq. (2.28)) and then applying the equation of state ($\rho^* = p^*\varphi(p,T)$) to finally get the latest pressure value *p**. We can form an incremental form of equation by subtracting Eq. (2.23) from Eq. (2.24) as

$$\left(\frac{1}{\delta t} - \frac{A_0}{\rho^n}\right)\rho^n(u_i^{**} - u_i^*) = -\Delta_i(p^* - p^n) \tag{2.25a}$$

This can also be re-cast as:

$$\rho^n u_i' = -\left(\frac{1}{\delta t} - \frac{A_0}{\rho^n}\right)^{-1} \Delta_i p' \tag{2.25b}$$

Again, we have Karki's formulation in equation (2.15), which can be expressed as follows for the low Mach number flow:

$$\rho^* u_i^{**} = \rho^n u_i^* + \rho^n u_i' + \rho' u_i^*$$

The value for $\rho^n u_i^{'}$ can be substituted from Eq. (2.25) and the value for $\rho^{'}$ in $\rho^{'} u_i^{*\prime}$ can be substituted from Eq. (2.17) to finally obtain the expression

$$\rho^* u_i^{**} = \rho^n u_i^* - \left(\frac{1}{\delta t} - \frac{A_0}{\rho^n}\right)^{-1} \Delta_i p^{'} + K p^{'} u_i^* \tag{2.26}$$

The continuity equation (2.6) can now be expressed as:

$$\Delta_i(\rho^* u_i^{**}) = -\frac{1}{\delta t}(\rho^* - \rho^n) \tag{2.27}$$

Taking the divergence of Eq. (2.26) and substituting it in Eq. (2.27) gives

$$\Delta(\rho^n u_i^*) - \Delta_i \left\{\left(\frac{1}{\delta t} - \frac{A_0}{\rho^n}\right)^{-1} \Delta_i\right\} p^{'} + K \Delta_i p^{'} u_i^* = -\frac{1}{\delta t}(\rho^* - \rho^n)$$

This equation can be rearranged with the help of the equation of state to give

$$\Delta_i \left\{\left(\frac{1}{\delta t} - \frac{A_0}{\rho^n}\right)^{-1} \Delta_i - \frac{\varphi(p,T)}{\delta t}\right\}(p^* - p^n) = \Delta(\rho^n u_i^*) + K \Delta_i (p^* - p^n) u_i^* \tag{2.28}$$

This is termed as the pressure correction equation. This equation is solved to yield the p^* field. Equation (2.25a) may then be used to determine the value of u_i^{**}. Similarly the second momentum correct step can be implemented to improve accuracy and efficiency. The final corrector step thereby completes the splitting and the latest computed fields are now regarded as the final solution to the original equations (2.1), (2.2), (2.3) and (2.4).

It is evident from the direct comparison of Eq. (2.14) and Eq. (2.28) that an additional pressure gradient term has appeared in the proposed hybrid algorithm in contrast to the original PISO algorithm. This resembles very closely to the Karki's derivation of mass flux at the control volume face. However the beauty of this algorithm is that it still keeps PISO's second order accuracy

(O(2)) and operator splitting feature, which is claimed to be responsible for a better accuracy and higher efficiency at the momentum corrector stages, while keeping the low Mach effectiveness of Karki's approach intact. (Issa 1985, Issa, Gosman et al. 1986) The diffusion like term involving $\left(\frac{1}{\delta t} - \frac{A_0}{\rho^n}\right)^{-1}$ is responsible for downstream pressure effects, whereas the convective term involving K exhibits upstream effects. The ratio $\left(\frac{1}{\delta t} - \frac{A_0}{\rho^n}\right)^{-1} / Ku_i^*$ is inversely proportional to the square of the Mach number. At high Mach number, the term involving upstream pressure is dominant and the equation exhibits the hyperbolic nature. However at low Mach number, the term involving the pressure differencing become dominant and the equation exhibits elliptic nature of pressure. As this algorithm should yield a pressure correction equation that exhibits the correct Mach number dependent behaviour, the present equation exhibits the Mach dependent behaviour through these two convection like and diffusion like terms.

The Eq. (2.28) apparently introduces a pressure differential term (term involving K) in the equation, which resembles to the set of equations formed by the asymptotic form of low Mach number semi-implicit implementation by Klein (Klein 1995, Munz, Roller et al. 2003).

2.4 OpenFOAM

The core technology of OpenFOAM (Field Operation and Manipulation) is a flexible set of efficient C++ modules. These C++ modules include **solver**, which simulates specific problems in engineering mechanics; **utilities**, which performs pre- and post-processing tasks like simple data manipulations, visualisation and mesh processing; and **libraries**, which creates toolboxes that are accessible to the solvers/utilities. The idea behind creation of FOAM is to develop a C++ class library that makes it possible to implement complicated mathematical and physical models as

high-level mathematical expressions. This is facilitated by making the high levels of the code resemble as closely as possible standard vector and tensor notation. In this approach tensorial fields (like ρ, U etc) are considered as the solution of a set of partial differential equations rather than viewing the problem as a numerical one in which arrays of floating values are obtained by inverting matrices. An object-oriented programming (OOP) methodology has been adopted, which is easier to write, validate, and maintain than procedural techniques.

FOAM has implemented most of the object-oriented features like abstraction, encapsulation, inheritance and polymorphism to optimise the performance of the tool for computational fluid dynamics simulations. There are numerous uses of data abstraction and data encapsulation to hide the data behind the interface and also to provide a well defined access to encapsulated data. An example of inheritance within FOAM is the use of inheritance to represent conceptual links between turbulence models. Similarly, an example of polymorphism can be witnessed in the implementation of boundary conditions. While a great deal of attention has been paid to the development of new and efficient algorithms for CFD, little has been published about the overall code design. The robust design and efficient algorithms has made FOAM an effective CFD tool which can implement a wide variety of continuum-mechanics modelling techniques, including those of incompressible and compressible fluid flow, multiphase flow, and free surface flow, together with various turbulence modelling techniques.

Implementation of tensor fields: The majority of fluid dynamics can be described using the tensor calculus of up to rank 2*, i.e.,* scalars, vectors, and second-rank tensors. Therefore there have been three basic classes created: scalarField, vectorField and tensorField. These tensor field classes are somewhat different from mathematical tensor field and they do not contain positional information. They are essentially ordered set lists of tensors and so only point-wise operations (i.e. tensor

algebra) can be performed at this level. As C++ allow operator overloading therefore it is possible to resemble tensor algebra to mathematical notation by overloading +, - , *, etc. The next level of tensors is referred to as "geometric tensor fields" and contains the positional information lacking in the previous classes. Again, there are classes for the three ranks of tensor currently implemented, volScalarField, volVectorField, and volTensorField. In addition to the additional metrical information necessary to perform differentiation, which is contributed by reference to a mesh "mesh class" fvMesh, these classes contain boundary information, previous time step necessary for the temporal discretization, and dimension set information. Since every algebraic expression is checked dimensionally before execution, therefore it is impossible to execute any dimensionally incorrect expression in FOAM.

Implementation of partial-differential-equation classes: Computational modelling requires the solution of partial differential equations, which is accompanied by converting them into systems of equations by linearizing them and finally inverting the resulting matrix using a suitable matrix solver. In the case of unstructured meshes, the differential operators$\nabla.$, ∇ and ∇x lead to sparse matrices which have a complex structure requiring indirect addressing and appropriate solvers. FOAM currently uses the conjugate-gradient method, with incomplete Cholensky preconditioning (ICCG), to solve symmetric matrices. For asymmetric matrices the Bi-CGSTAB method is used. The matrix inversion is implemented using face addressing throughout, a method in which elements of the matrix are indexed according to which cell face they are associated with. Both transient and steady state solutions of the equation systems are obtained by time-marching, with time step being selected to guarantee diagonal dominance of the matrices, as required by the solvers.

To address the issue of the matrix representation of a differential equation by mathematical notation, classes of equation object called fvMatrixScalar, fvMatricVector, etc are defined. These classes are defined to handle addressing issues, storage allocation, solver choice, and the solution. The standard mathematical operators + and – are overloaded to add and subtract matrix objects. In addition, all the tensorial derivatives $\partial/\partial t$, $\nabla\cdot$, $\nabla\times$, etc., are implemented as member functions of a class finiteVolumeMethod (abbreviated to fvm), which construct appropriate matrices using finite volume discretization. Numerical considerations are relevant in deciding the exact form of many of the member functions.

Mesh topology and boundary conditions: Geometric information is contributed to the geometric fields by the class fvMesh, which consists of a list of vertices, a list of internal cells, and a list of boundary patches (or cell faces). The vertices specify the mesh geometry, whereas the topology of any cell is specified as an ordered list of indices together with a primitive shape describing the relationship between the ordering in the list and the vertices in the shape. These primitive shapes can be defined at run time and usually consist of tetrahedron, pyramid, prism or hexahedron.

The exterior boundary of the domain is defined by fvMesh, which incorporates a set of patches. Every patch carries a boundary condition, which is dealt with by every fvm operator in an appropriate manner. There are different classes of patch like calculated, fixed value, fixed gradient, zero-gradient, symmetry, cyclic, and other boundary conditions, each of which is derived from a base class, patchField. All boundary conditions have to provide the same types of information, that is, they have the same interface but different implementation, which is actually a good example of implementation of polymorphism in the code. Boundaries suitable for specific situations like inlet, outlet, wall etc can be devised using these basic elements. An additional

patchField processor is also available, which helps in parallel implementation of the code for multi-processor simulation runs.

Turbulence modelling in FOAM: In turbulent flow, there are coherent structures on a variety of spatial scales from the largest, determined by the size of the geometry, down to very small scales where viscous scales dominate. The range of scales involved may be over several decades. There are two approaches to solving for turbulence: either the mesh used is fine enough to resolve all of the flow scales, or the range of scales explicitly simulated must be reduced, with the effect of the unresolved scales being accounted for by modelling. There are different types of Reynolds-Averaged Simulation (RAS) and LES models implemented in FOAM. For RAS, there are various turbulence models available, whereas for LES, the range of possible LES model is even larger. In LES, the turbulence models can be incorporated directly into the momentum equation, or a virtual class hierarchy may be constructed in order to make the model run time selectable. LES uses a three level hierarchy in contrast to the flat hierarchy used by RAS models.

There are different sets of model implementation available. The first of those sets involves models that use Bousinesq hypothesis, in which the effect of unresolved turbulence on the large scale flow is modelled as an increase in viscosity. This is equivalent to model **B** as

$$\boldsymbol{B} = \frac{2}{3}k\boldsymbol{I} - 2\nu_t\overline{D_d} \qquad \text{.... (2.29)}$$

where, $\overline{D_d} = \overline{D} - \frac{1}{3}tr(\overline{D})$, and the models differ in the way the turbulent viscosity is evaluated. The Smagorinsky and One-equation model come into this set of models. A second set of models provides a full solution of the balance equations for B: for example, the model of Deardorff (Deardorff 1970) has the form,

$$\frac{\partial \boldsymbol{B}}{\partial t} + \nabla(\boldsymbol{B} * \bar{U}) - \nabla . \frac{\upsilon_t}{\sigma_B} \nabla \boldsymbol{B} = P - C_1 \frac{\epsilon}{k} \boldsymbol{B} - \frac{2}{3}(1 - C_1)\boldsymbol{I}_{\epsilon}$$

$$-C_2[P - \frac{1}{3}\boldsymbol{I}\, tr(P)] \qquad \text{.... (2.30)}$$

Most of the available CFD codes require the six individual equations for the above equation to be written out separately. However in FOAM these can be expressed as a single tensorial equation:

```
Solve   (
        fvm::ddt(B) + fvm::div(phi, B)
        - fvm::laplacian(nut/sigmaB, B)
= = P - fvm::Sp(C1*epsilon/k, B)
        - (2.0/3.0)*(1.0-C1)*l*epsilon
        - C2*(P-(1.0/3.0)*l*tr(P))
        );
```

A third set of LES model is the scale-similarity model, which introduce further interaction between different turbulent scales by introducing a second level of filtering. These models are usually combined with other models to give a mixed model. The class hierarchy of the LES models in FOAM is based on the relationships, at the base of which is a virtual base class isoLESmodel. Derived from this are intermediate classes: isoGenEddyVisc, isoGenSGSStress, and isoGenScaleSimilarity, which implement Eq. (2.29) and Eq. (2.30) respectively. Finally, details of the models are implemented in the highest level classes. For example, the classes derived from isoGenEddyVisc calculate the value of υ_t is used in eq. (2.29). isoMixedSmagorinsky is a mixture of a scale similarity and an eddy-viscosity model, and so multiple inheritance is used to represent this relationship.

2.5 Test case: Simple Expansion Muffler Simulation

Aiming at sound attenuation in propagating medium of various engineering devices, various acoustic filters have been used. For numerous uses of simple expansion mufflers in exhaust silencers and air conditioning HVAC systems, a simple expansion muffler has been chosen for simulating a pulsating flow to demonstrate the effectiveness of the proposed low Mach hybrid Karki-PISO compressible solver. The details of various aspects of this simulation are provided in Chapter 4 and only necessary information pertaining to the set of results introduced in this chapter is provided here. Second order spatial discretization and temporal discretization are employed in these simulations. An axi-symmetric 5 degree uniform mesh is used as mesh for this simulation as shown in Figure 2.4 (a).

A pure single period sinusoid of 3200Hz frequency and amplitude of 0.05 m/s is imposed at the inlet of the expansion muffler using the proposed Karki-PISO compressible solver. The CFD model has long inlet and outlet, in this simulation fourteen times the length of the expansion section, to ensure a sufficient amount of data to obtain reasonable results.

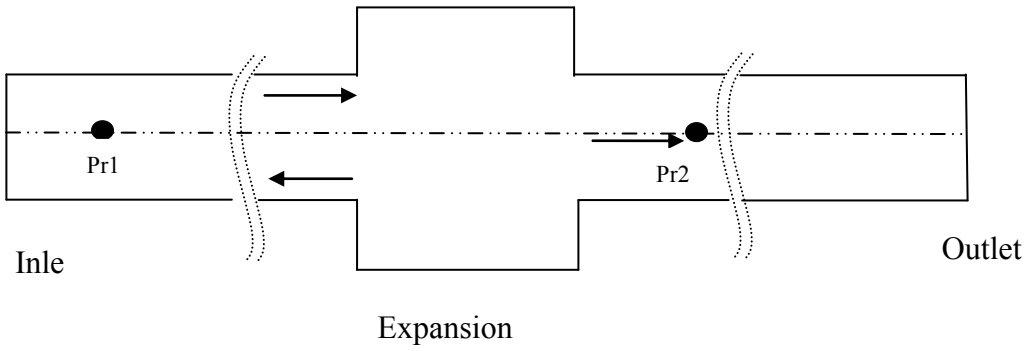

Figure 2.2: *Simple Expansion Muffler CFD model.*

(a)

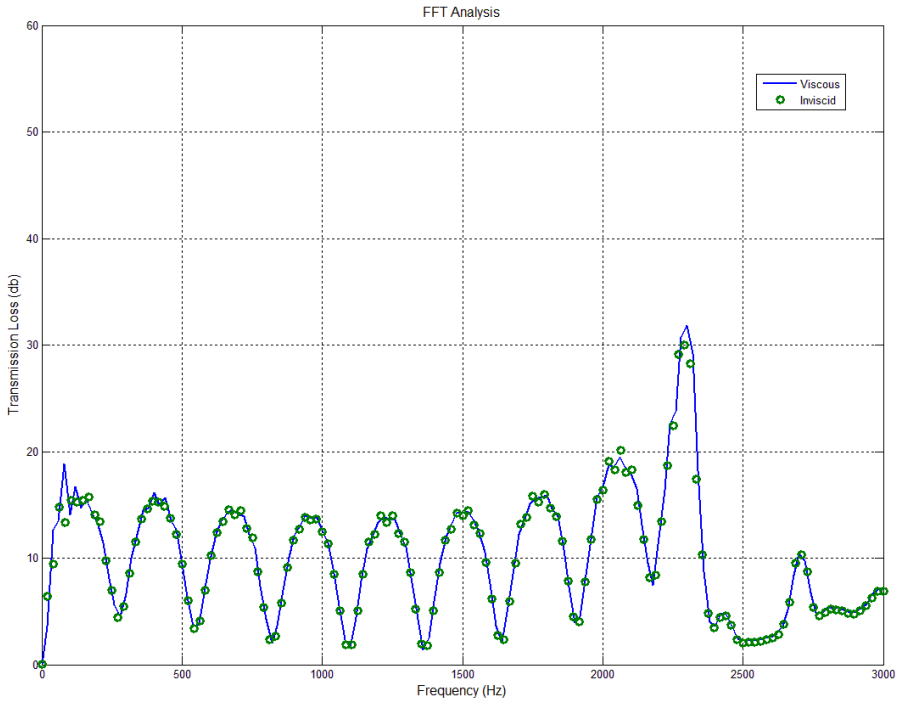

(b)

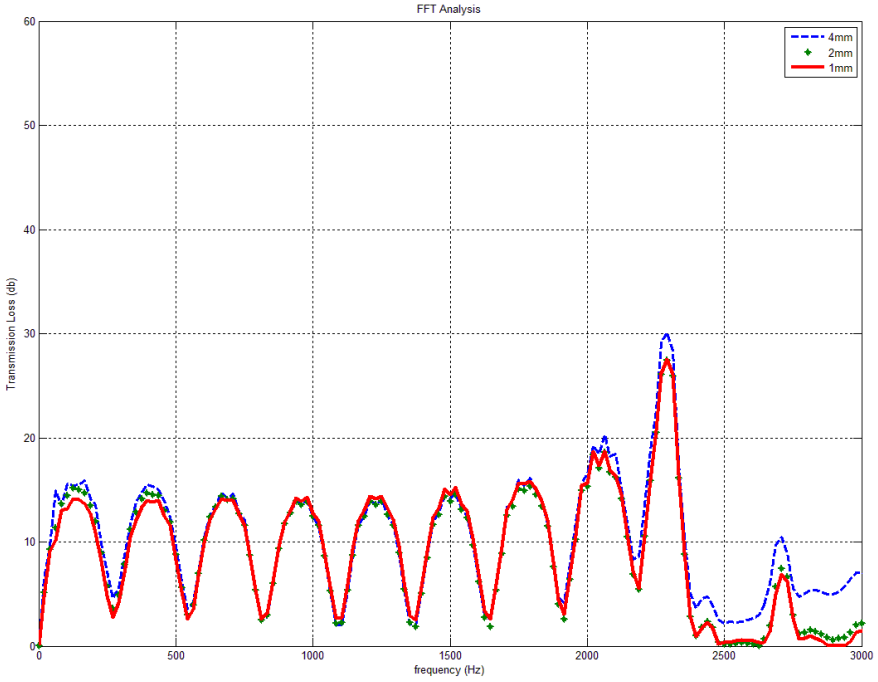

***Figure 2.3**: Comparison of **(a)** viscous and nearly inviscid simulation; **(b)** muffler simulations with different mesh sizes.*

This also avoids reflections from the walls and expansion sections contaminating the monitoring data at probes Pr1 and Pr2, as shown in figure 2.3 (a). The inlet and outlet pipe diameters are chosen so that the diameter of the expansion pipe is three times larger than that of the inlet pipe.

Figure 2.5 (a) shows a 5 degree axisymmetric uniform mesh of a simple expansion muffler, whereas figure 2.5 (b), (c) shows respectively incident pulse and transmitted pulse reaching and passing through the muffler's expansion section. After various reflections from the expansion section, the incident and transmitted pulses are recorded in the inlet and outlet pipes at probe locations Pr1 and Pr2. The reflections from the expansion chamber can be seen in the inlet and outlet pipe section of the CFD simulation of figure 2.5 (d). Figure 2.6 shows the detailed behaviour of the pulse interaction with the expansion. Figure 2.6 (c) and (d) clearly show the generation of reflected waves from the expansion that travels towards the inlet pipe and only a part of it is transmitted through the expansion section. Finally, figure 2.7 provides the velocity distribution of the transmission pulse and its interaction with the interface of the expansion section and outlet pipe. Figure 2.7 (c) and (d) clearly shows the passage of transmission pulse through the outlet pipe and reflection from the expansion section towards the inside of the expansion chamber.

Computational verification: A comparative Fast-Fourier Transform (FFT) analysis is conducted for viscous and inviscid simulation of the simple expansion muffler to analyse the viscous error reflected in transmission loss throughout the frequency spectrum. Figure 2.3 (a) shows perfect agreement between viscous and inviscid simulations. The figure clearly shows that there is not much effect on the frequency analysis of the simulation due to the introduction of viscous forces.

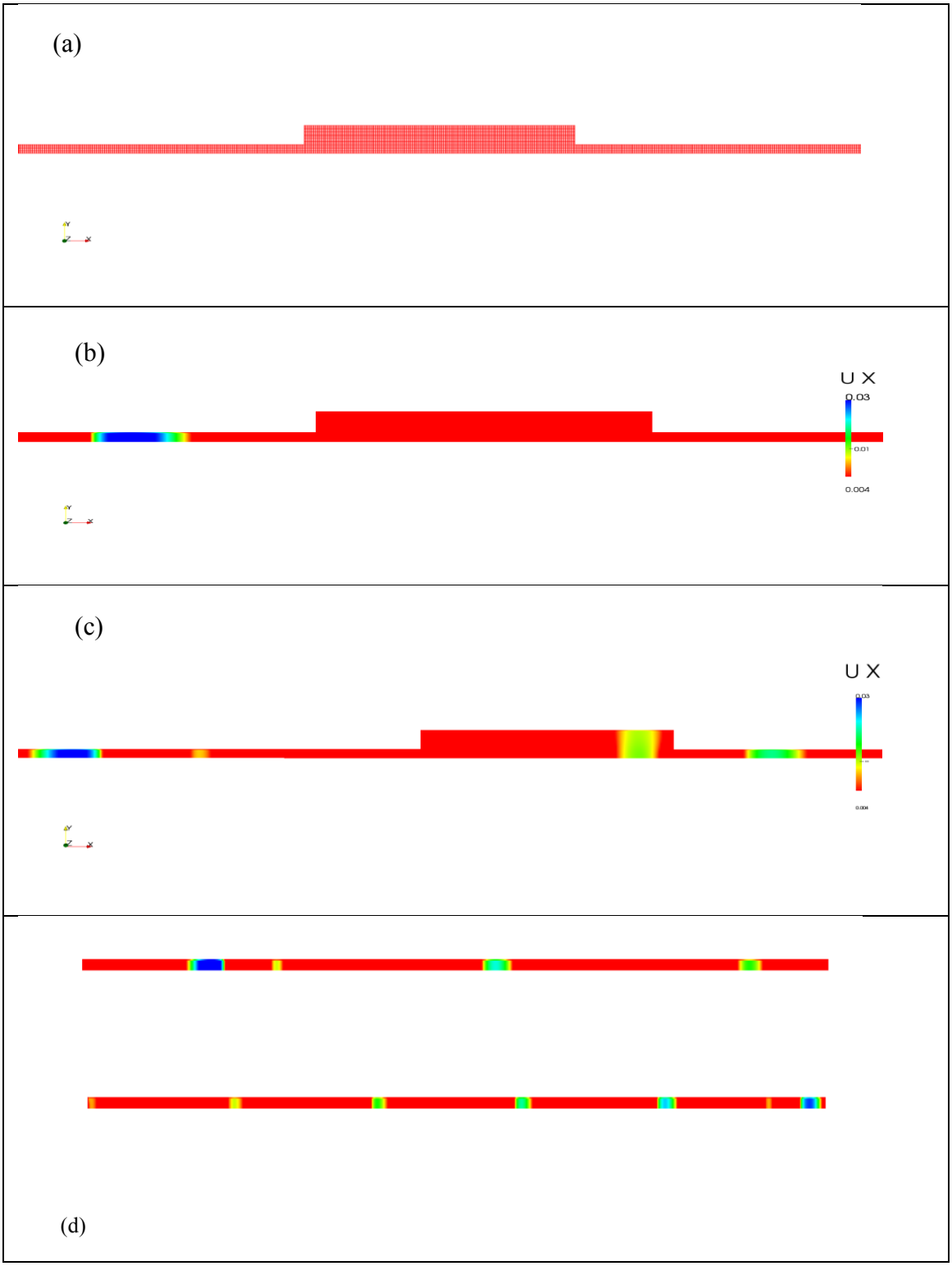

Figure 2.4: *Velocity contours: (a) mesh of section of simple expansion muffler; (b) sinusoidal pulse at the entrance of expansion; (c) Reflections after pulse crosses the expansion sections; (d) Various reflections at the end of simulation in inlet and outlet pipes.*

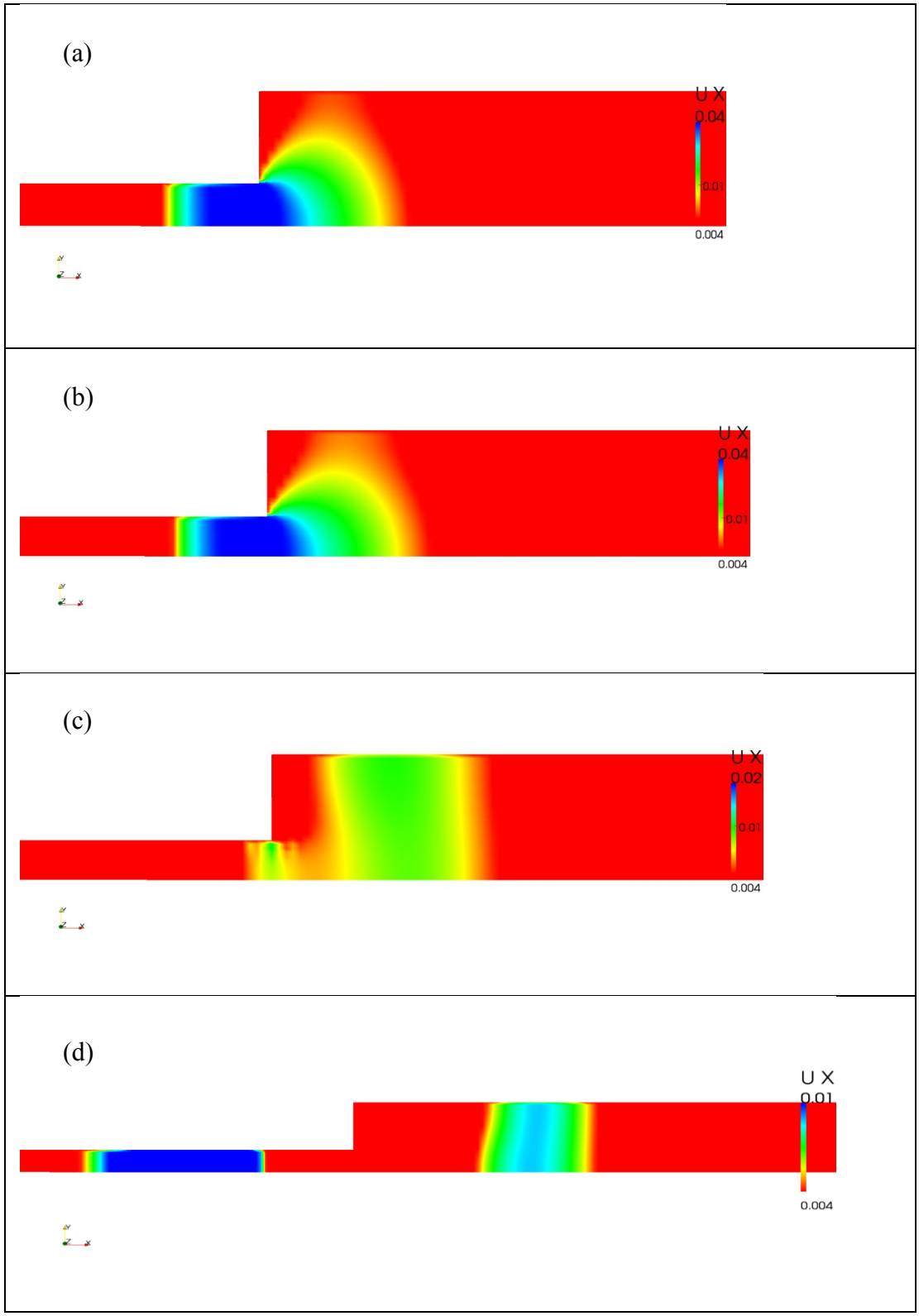

Figure 2.5: *Velocity contours at start of expansion: (a), (b) Sinusoidal pulse reaches at entrance of expansion chamber, (c), (d) Reflection of pulse from the expansion section.*

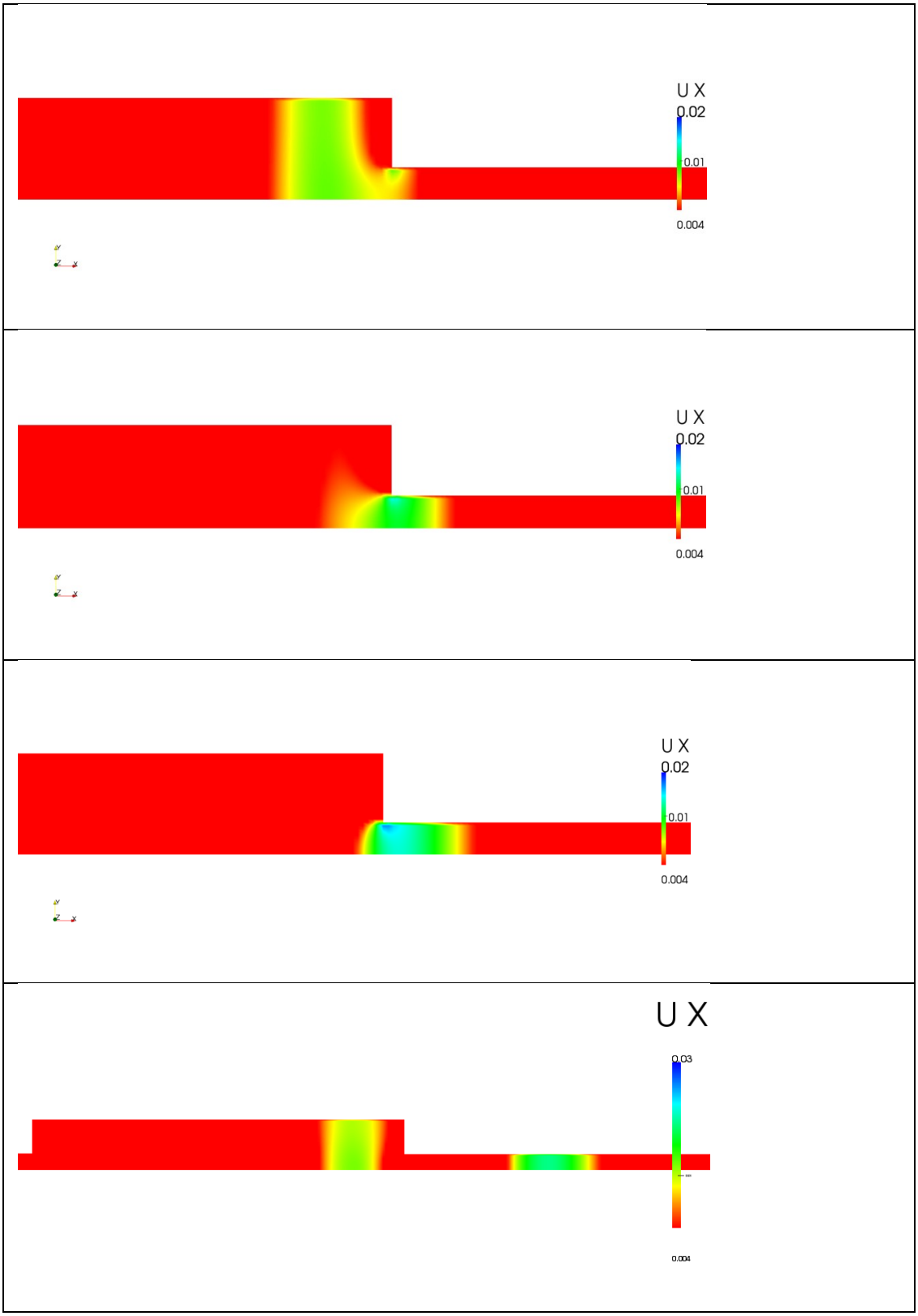

Figure 2.6: *Velocity contour at intersection of expansion and outlet: Sinusoidal pulse transmitted through the outlet pipe.*

Mesh independence: To check for spatial discretization error in the simulation, FFT analysis is performed for a range of mesh sizes; from 4mm to 1mm. Figure 2.3(b) shows no considerable error in the simulation and all the results for various mesh sizes match very well.

2.6 Closure

This chapter has introduced the low Mach compressible Karki-PISO solver for acoustic propagation. The chapter also outlines other related finite-volume and finite-difference methods and discusses the evolution of the Karki-PISO compressible solver. The C++ based OpenFOAM CFD tool kit is also discussed and the implementation of several of its models and features is discussed. A test case of a simple expansion muffler is then taken and the acoustic pulse propagation problem is then solved using proposed Karki-PISO compressible solver. An inviscid simulation is also carried out and the results are satisfactory, compared with the viscous simulation for the validation of compressible solver. Study of mesh dependence also provides good agreement for the frequency-range of our interest. Post processed velocity contours for the simulation of pulses propagation through the expansion muffler show interesting interaction of flow near the expansion and the generation of back pressure and transmission pressure in the inlet and outlet pipes.

Chapter 3

Turbulence Modelling

3.1 Introduction

This chapter aims to provide a brief summary of important aspects of turbulence modelling. Only those aspects of turbulence modelling which are relevant to this thesis are considered in this chapter. The chapter briefly defines turbulence, explains various important parameters of turbulence, discusses near-wall turbulence, outlines scales of turbulence and types of correlation and finally discusses various models of turbulence.

3.2 Introduction to Turbulence

It is known that at low velocities wall bounded flow is smooth and the various layers of fluid flow in an orderly fashion. This flow is called *laminar*. When velocity is increased, the flow becomes intrinsically unsteady and chaotic (even if there is an implementation of constant boundary conditions) and this flow is called *turbulent*. The transition of flow from laminar to turbulent occurs when a certain Reynolds number (usually more than 2000, depending on the flow geometry) is reached. Most industrial fluid flows are turbulent and that makes the process of understanding this phenomenon very important.

Turbulence is one of the least understood topics in fluid dynamics and can be loosely described as irregular motion in rotational flow obeying probabilistic constraints. It has been shown several times in the past that turbulence can only develop and persist in rotational flow or in the presence of shear. The velocity gradient developed due the presence of the shear provides the energy differential that converts the small initial perturbations into large scale coherent structures (Lesieur

1997). The process is only possible when inertial forces overcome the influence of viscous forces which are used to damp down the small initial perturbations (*i.e.* at high Reynolds number). Although there is no strict definition of turbulence present in the literature, turbulence can still be described by the following characteristics:

Randomness: Turbulent flow is random, irregular and chaotic. It consists of a spectrum of different scales known as turbulent eddies. These turbulent eddies have their characteristic velocity and length scales and exist somewhere in space for a certain time and are subsequently destroyed. Although turbulence is chaotic, it is deterministic and can be described by Navier-Stokes equations.

Three-Dimensional: Turbulent flow is always three dimensional and unsteady. However, it can be treated as two-dimensional when equations are time averaged for two-dimension geometries (For example in the RANS simulation). In this case, the fluctuations in time are superimposed upon mean value for each quantity as: $\emptyset(t) = \overline{\emptyset} + \emptyset'(t)$.

Diffusivity: Diffusivity is stronger in turbulent flow than laminar flow. This is very useful because this means that the spreading rate of the boundary layer increases (because of three-dimensional diffusion of turbulent eddies by momentum exchange) as flow becomes turbulent. This strongly enhances the heat transfer, mixing and friction.

Dissipation: Turbulent flows are dissipative. Since the kinetic energies of small eddies are transformed into thermal energy, it makes the flow dissipative. There is an energy cascade which allows the transfer of kinetic energy from larger eddies to the smaller eddies. The smallest eddies receive energy from slightly larger eddies, and the larger eddies receive energy from even larger

eddies and so on. The largest eddy receives its energy from the mean flow. This process of energy transfer is called a cascade process.

Continuum: Turbulence is also a continuum phenomenon. Although the smallest scales of turbulence are extremely small, they are still many orders of magnitude bigger than the molecular length scale. This is followed by the fact that time dependent, three dimensional continuity and Navier-Stokes equations contain all of the physics of a given turbulent flow.

Vortex Stretching: Vorticity is connected to the rotational nature of the fluid and its three-dimensionality. Vortex stretching is the main physical process of spreading the motion over a wide range of wavelengths. The turbulence gains energy if the vortex elements are oriented in a direction in which the velocity gradients can stretch them. The energy cascade which was explained previously can also be explained in terms of vortex stretching. The larger eddies in the flow interact most strongly with the mean flow and carry most of the energy. In turn, vortex elements that comprise most of the smaller eddies are stretched by the larger eddies, transferring their energy to smaller eddies. The energy is dissipated in the shortest wavelengths by viscous forces.

These properties lead to the inference that turbulence is definitely not isotropic, except at the smallest scales, where it is non-directional. The rest of the larger eddies obviously strongly depend on the mean flow direction.

3.3 Turbulent Energy Spectrum

Richardson (Richardson 2007), in his pioneer work explained how the larger scale coherent structures break up into smaller pieces. Later on, Kolmogorov (Kolmogorov 1991) predicted the scale distribution of eddies which surprisingly fits well with Richardson's energy cascade. An

assumption was made in Kolmogorov's theory that the large scale influence of anisotropy is gradually lost, when energy is transferred from larger scale to smaller scales. In the turbulent energy spectrum shown in the Fig. 3.1, Kolmogorov's law is graphically represented by the dotted line, which is derived from dimensional analysis and expressed as:

$$E(k) = C_k \varepsilon^{2/3} k^{-5/3} \quad \text{.... (3.1)}$$

where C_k is a universal constant and experimentally found to be of the order of 1.5. Kolmogorov's law states that, if the flow is fully turbulent then the energy spectrum should exhibit a -5/3 law in the inertial region. The spectrum shown in Figure 4.1 can be broadly divided into three parts I, II, III, generally known as the large eddy region, inertial range and dissipative range respectively.

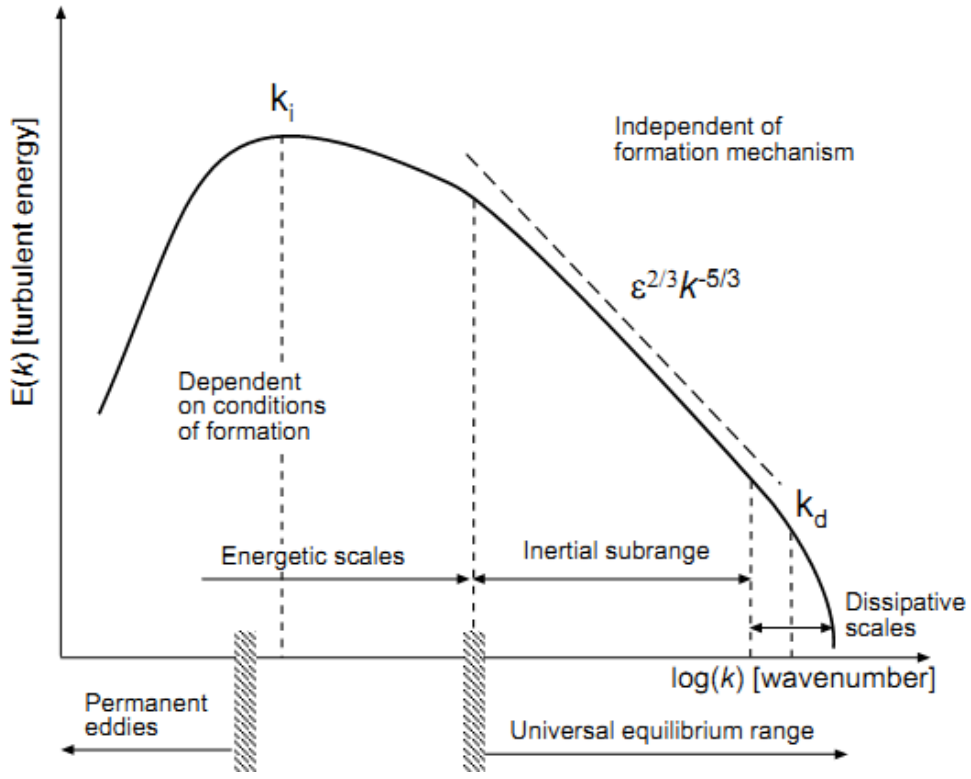

***Figure 3.1**: Turbulent energy spectrum,* (Hinze 1975)

Region I: This region consists of large eddies which carry most of the energy and interact with the mean flow to extract energy from the mean flow. The energy transfer from the mean flow to the larger eddies takes effect via the production term, P^k, in the transport equation for turbulent kinetic energy. The large scale eddies in this region contain most of the turbulent kinetic energy.

Region II: At a sufficiently high Reynolds number, this region, more commonly known as the inertial sub-range, contains transitive scales. These scales obey the Kolmogorov's law mentioned above and are dominated by inertial forces rather than viscous forces. In the cascade process, this region is also known as the "transport region"; it dissipates very little energy and mostly transfers energy from the large scales to the very small scales. Since the assumption in the cascade process is that all the energy from large eddies is transferred to small eddies, it means that the number of small eddies will be greater than that of the large eddies. (i.e $N_k k_k$ is constant, where N_k is number of eddies and k_k is turbulent kinetic energy of the eddies.) The eddy range (wavenumber range) in the inertial sub-range increases with increasing Reynolds number.

Range III: This region in the energy spectrum is called the dissipative range. Eddies in this region are small and isotropic and this is the region where dissipation takes place. The eddy scales in this region are described by Kolmogorov scales ($k_d \propto (\varepsilon/\nu^3)^{1/4}$). The energy transfer from turbulent energy to heat energy is governed by ε in the transport equation for turbulent kinetic energy *k*.

3.4 Wall Bounded Turbulent Flow

The presence of a solid boundary has profound effects on the flow turbulence and is often described as the site of the generation of fresh turbulence. Flows near the wall have a number of distinctive properties that are common to many otherwise dissimilar flows. Thus the channel flow and pipe flow boundary layer have very similar characteristics close to the wall, whereas away

from the wall they have notable differences. Apart from the limiting influence because of the presence of the solid boundary on the growth of the instabilities due to viscous processes, the resulting vortices are restricted in scale to some fraction of the distance to the boundary surface. A variety of studies of wall bounded flows have yielded insights into the analytical, statistical and structural characteristics of this sort of turbulence phenomenon.

Prandtl (Prandtl 1925)assumed in his pioneer work that the inner thin region near the wall characterises the wall bounded flow and the behaviour of turbulence in this inner region is independent of the rest of the flow and only determined by viscosity ν and viscous shear stress at wall τ_w. Characteristic velocity scale u_τ and length scale δ_ν can be obtained for the inner region by dimensional analysis as follows:

$$u_\tau = \sqrt{\frac{\tau_w}{\rho}}, \qquad \delta_\nu = \frac{\nu}{u_\tau}. \qquad \text{.... (3.2)}$$

where the characteristic velocity scale $u_\tau$is also referred to as *fictional velocity* and the length scale δ_ν is referred to as the *viscous length scale*. Various quantities normalised with u_τ and δ_ν are expressed in *wall units*; for example y^+ is normalised as y/δ_ν to define different regions in near-wall flow. The y^+ is similar in expression to the Reynolds number ($Re= ul/v$) as its magnitude also determines the relative influence of inertial and viscous effects.

The flow region where the effect of inertial forces is negligible in comparison to the viscous effects is called *viscous sublayer* and the mean flow velocity in this region has a universal form which follows the *law of the wall:*

$$U^+ = y^+ \qquad \text{… (3.3 a)}$$

This viscous sublayer is confined to the very thin region near the wall, in the range of about $y^+<5$, as shown in Figure 3.2. The thickness of this sublayer decreases with increasing Reynolds number. However, the influence of viscosity becomes negligible away from the wall and the size of the large eddies becomes independent of Reynolds number and characteristic length scale. This is called the outer region or defect region and the velocity profile in this region is not universal. In between the viscous sublayer and outer region, there is an overlap region called the log-law region, where the length scale of the dominant eddies is proportional to the distance to the wall. The *log-law of the wall* for mean velocity profile can be obtained by considering a local equilibrium between production and dissipation in the log-law region, as follows (von Karman 1930):

$$U^+ = \frac{1}{\kappa} log y^+ + A \quad \text{.... (3.3 b)}$$

where A is a dimensionless integration constant and Karman's constant $\kappa \approx 0.4$. For smooth surfaces A≈5. Pope (Pope 2000) later confirmed that Eq. (3.3) is valid for $y^+ >30$, as shown in Figure 3.2.

Another wall unit named the *friction Reynolds number* is defined as the ratio of the size of the large eddies δ in the core of the channel to the size of the large eddies in the near wall region δ_v.

$$Re_\tau = \frac{\delta}{\delta_v} = \frac{\delta u_\tau}{\nu}. \quad \text{.... (3.4)}$$

The friction Reynolds number has the same function for wall turbulence as the turbulent Reynolds number (free shear) has for the Kolmogorov cascade. However there are some marked differences as well, which are worth noticing in the context of large and small eddies.

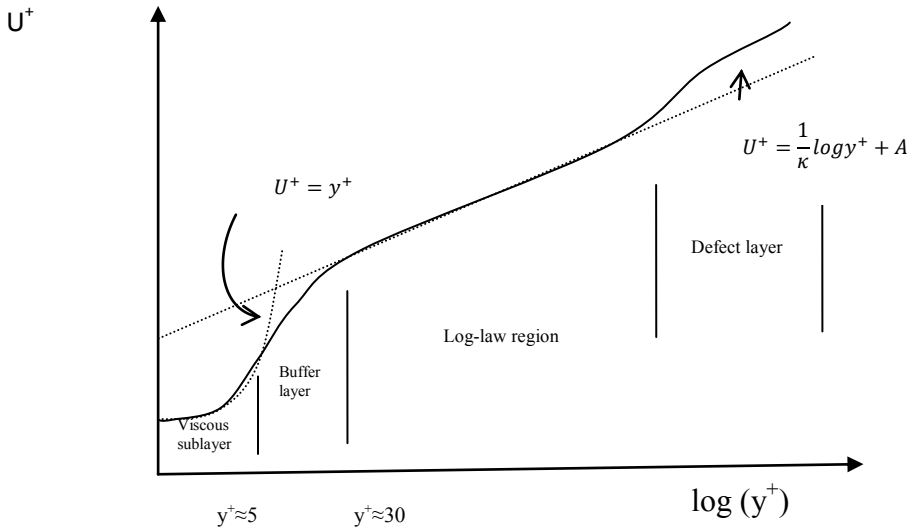

***Figure 3.2**: Velocity profile for turbulent boundary layer.* (Wilcox 2006)

In wall turbulence, large and small eddies are segregated in space due to the presence of the wall and the near-wall area is dominated by the smaller eddies of size δ_ν determined by the viscous effect. On the other hand, further away from the wall, the turbulence of the Kolmogorov cascade has both large eddies and Kolmogorov eddies coexisting at a given space and a full range of length scales is generated. The second difference between free shear turbulence and wall turbulence lies in the way turbulent kinetic energy is transported in the flow. Most of the production of turbulent kinetic energy happens in the near wall region with a peak at y^+=12. (Kim, Moin et al. 1987, Antonia, Kim 1992) The smallest eddies in the near wall region are the major source of turbulence and are consequently transported towards the main flow. Dissipation of the energy in the core flow takes place through a classical Kolmogorov energy cascade. Various attempts have been made to better understand wall turbulence, its structure and dynamics.

Since the 1950s, a number of experiments of increasing sophistication have revealed a degree of connectedness in the motions occurring in wall bounded flows. For example, it has been shown that velocities at different spatial and temporal positions can be highly correlated. (Spalart 1988, Karweit, Blanc-Benon et al. 1991) It is now recognised that there are "structural" features embedded in the randomness of turbulent flow and therefore turbulence is not just random distributions, which is also very clear from the description of turbulence in the previous section. It is also easy to imagine that such a phenomenon is the result of *coherent* events within the seemingly random turbulent fields. Substantial effort has been expended in attempting to get a deeper understanding of the wall-layer physics that might be responsible for these observations. In recent decades, the accumulated knowledge of wall region flow has coalesced around a few rather closely related ideas about the structural composition of the boundary layer. Central of those is the idea that bounded turbulent flows are composed of *coherent structures (CS)*, which are defined as the flow elements or eddies showing a considerable degree of organisation and repetitiveness. The cause of the tremendous increase in drag and heat transfer in the near wall region is also supposed to be because of these coherent structures of turbulent flows. In addition, the transport of energy from these structures to the core flow is the source of the boundary layer's characteristic logarithmic profile. Clearly a better understanding of the underlying mechanisms is important for the improved treatment of the boundary layer.

3.4.1 Near-wall turbulence cycle

A retarding motion tangential to the surface interacts with the wall boundaries via viscous shear and blocks the motion of fluid normal to the interface. Although mean flow properties are largely

influenced by the wall, their categorisation has been generally difficult. However, they have been categorised by some in terms of turbulence properties as local and non-local modes of influence for wall boundaries. Non-local modes are defined as bulk flow phenomena that affect the flow's turbulent characteristics, but are not in close physical proximity to the surface that produces them. Since non-local modes are typically not very Reynolds number dependent, their effects are usually well produced by direct simulations. However the character and extent of these non-local modes must still be taken into account, considering the fact that they can strongly influence the mesh spacing required to resolve a certain flow section. Local modes of wall interactions, on the other hand are defined as the retardation of the flow due to viscous shear and the wall turbulent scale's limiting influence perpendicular to the surface. As described in the previous section, the near-wall shear functions as a source of turbulent energy for coherent structures in the buffer and log-law layers (Figure 3.2) which is produced through various instability mechanisms. Although many prominent features such as low speed streaks, longitudinal coherent structures and a variety of vortical configurations have been listed in the near wall region, their generation mechanisms and mutual interactions have remained ambiguous. Recent works (Le, Coleman et al. 2000, Jeong, Hussain et al. 1997, Schoppa, Hussain 2000, Hamilton, Kim et al. 1995), however, have formulated a more comprehensive theory on wall turbulence production, which is supported by numerical and physical experiments at low Reynolds numbers. The theory describes a self-regenerating cycle of lifted near-wall streaks, longitudinal vortices and internal shear layers and accounts for most of the turbulence phenomenon observed in boundary layers. This theory, named as the *Streak instability theory,* has been further corroborated for low and moderate Reynolds numbers. While the other mechanisms, such as *eddy roll up*, surely contribute to the near-wall turbulence formation, they are not dominant and have been numerically shown to be

unable to sustain the turbulence cycle in isolation. Some evidences also have suggested that the streak instability cycle does not remain the dominant turbulence production mechanism at high Reynolds numbers. This deviation in this theory is attributed to the displacement of coherent turbulence production from the near-wall region to the outer boundary layer, which happens after $\mathrm{Re}_\tau \approx 10000$. However, for the aerodynamic boundary layer the streak instability cycle is considered as the dominant mechanism for coherent turbulence structure production near the wall.

3.4.2 Streak Instability Cycle

It is believed that streaks are generated by the lifting of low speed fluid near the wall by the vertical velocity induced by the streamwise vortices, described by their close proximity in figure 3.3. Recently Schoppa *et al* (Schoppa, Hussain 2000) have proposed that the streak plays a significant and dynamic role in the formation of streamwise coherent structures through the streak instability mechanism. Linear stability analysis shows that typical near-wall streaks are unstable to sinusoidal perturbations in a channel flow solution and therefore a sinusoidal perturbation can initiate an instability which in turn would produce vortices and a shear layer kick-starting the near-wall cycle. A base flow of the following form has been generated to separate the instability of vortex-less streaks:

$$U^+(x^+, y^+) = U_0^+(y^+) + (\Delta u_0^+/2)\cos(b^+ z^+)\left(\frac{y^+}{30}\right)\exp(-c_\sigma y^{+2} + 0.5),$$

$$V^+ = W^+ = 0. \qquad \text{.... (3.5)}$$

where U^+ is the mean velocity profile and Δu_0^+ is the wall normal circulation of streak. Δu_0^+ along with Spanwise wavenumber, b^+ and transverse decay, c_σ are chosen to approximate a typical streak from previous minimal channel simulations (see Figure 3.4).

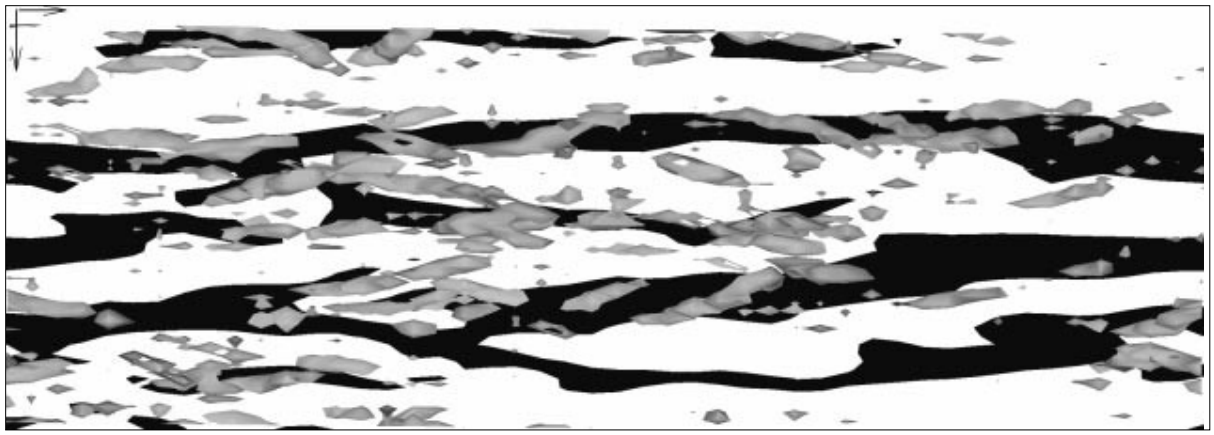

Figure 3.3: *Top view of the near-wall region covering (x^+, z^+) = (1400, 450) in the streamwise and spanwise directions. Lifted low-speed streaks (black) denote $u_0 < 0$ at $y^+ = 20$ and streamwise vortices (grey-shaded) $\lambda_2 < 0$ for $0 < y+ < 60$* (Jeong, Hussain et al. 1997).

The streak waviness in z is applied to investigate the stability of the base flow (Eq. 3.5) and has the form,

$$w(x^+, y^+) = c_\sigma \sin(a^+ x^+)\, y^+ \exp(-c_\sigma y^{+\,2}).$$

$$u = v = 0. \qquad \text{.... (3.6)}$$

where c_σ is the linear perturbation amplitude and a^+ is the x-wavenumber of the perturbation. These initial conditions are shown to evolve by linear instability into a natural instability eigenmode, the growth of which is characterised by an increase in total energy in Fourier modes with a z-wavenumber of 0 (z mean) and an x-fundamental mode proportional to a.

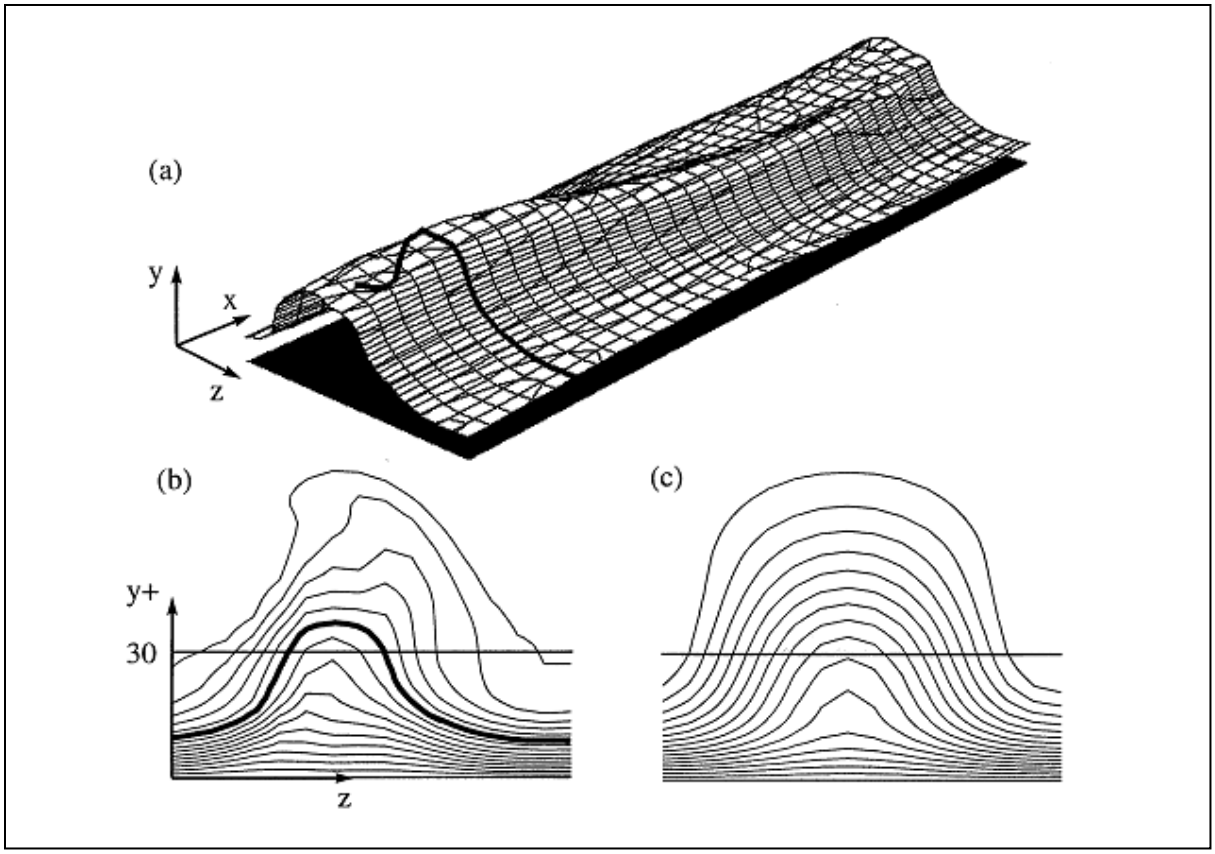

Figure 3.4: *Low speed lifted streak realization in minimal channel flow. (a) 0.55U_c isosurface, (b) typical cross-stream distribution of U(y,z), (c) The analytical base flow distribution of eq. 3.5 at y^+=20* (Schoppa, Hussain 2000).

The streak instability process can be understood in greater detail in the Figure 3.5. In the figure profiles of $\breve{u}_x$, denoting the perturbation velocity normal to the base flow vortex lines, are overlaid with contours of streamwise vorticity w_x at two x (half wavelength apart) and the bold arrows denote the differential streamwise velocity $\breve{u}_x$ of the displaced vortex sheet. The thick lines in Figure 3.5 (a) and (b) indicate the base flow vortex lines, while the dashed counterparts denote perturbed vortex lines. The instability mechanism is dominated mostly by w_x through the induction of $\breve{u}_x$, which displaces the vortex sheet anti-symmetrically in both x and z (see Figure 3.5). The displaced vortex sheet now experiences a differential streamwise velocity, $\breve{u}_x$ at any point on the

sheet, as for example the vortex line at X_0 will move faster at $Z_{\pi/2}$ than at $Z_{3\pi/2}$. This in turn intensifies w_x on top of the streak through vortex line tilting (Figure 3.5 (b)). The enhanced w_x then further accentuates $\tilde{u}_x$, and so on, thereby completing the feedback loop responsible for the instability.

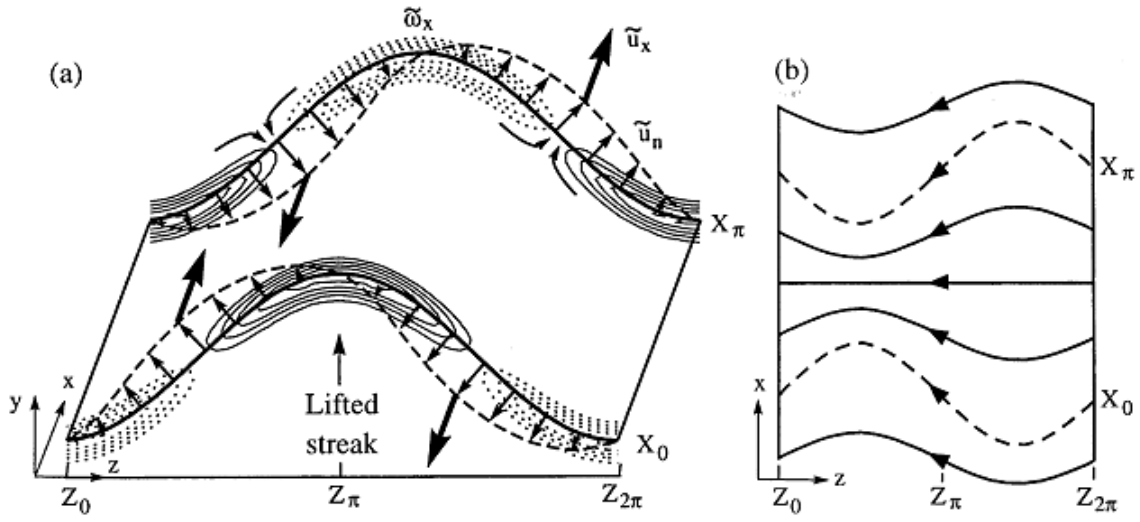

Figure 3.5: Schematic of (sinuous) Streak stability mechanism in (a) perspective view and (b) top view (Schoppa, Hussain 2000).

Schoppa *et al.* (Schoppa, Hussain 2000)further proceed to study the CS's non-linear evolution using Direct Numerical Simulation (DNS). The DNS is initialised using the equations 3.5 and 3.6 to obtain a starting field free from extraneous perturbations. The first observations by Schoppa *et al.* (Figure 3.6 (a)-(c)) shows the direct creation of streamwise vortices due to the growth of the sinuous amplitude of the underlying streak. The streak instability then continues to sustain the streamwise vortex well after initial formation (Figure 3.6 (d)), emphasising the phenomenon's importance to turbulence production.

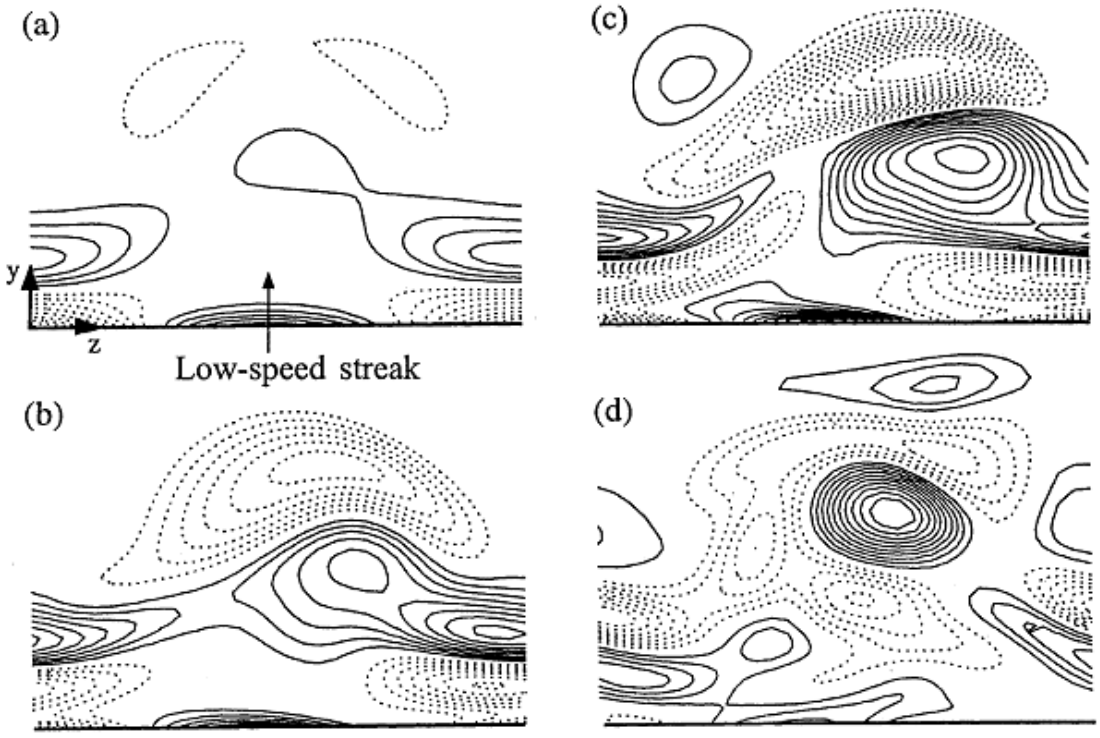

Figure 3.6: *Streamwise vortex formation due to transient streak instability, illustrated by cross-stream distributions of* w_x (Schoppa, Hussain 2000).

3.5 Scales of Turbulence

In a typical turbulent flow, the largest eddies present in the flow extracts their energy from the mean flow. The slightly smaller eddies receive their energy from even larger eddies and the energy transfer process from larger to smaller eddies goes on to the smallest scales. It is these smallest eddies which dissipate and transform their kinetic energy to thermal energy. The whole cascade process creates a spectrum of eddies of various length scales and the largest scale is comparable to the flow geometry. Although frictional forces exist throughout the flow at all scales, they are largest at the smallest scales (eddies). In the idealized model, the frictional losses at all the scales

are neglected, since they are comparably very small. However, more realistic models take into account the small fraction of dissipation at all scales in the flow and it is assumed that most of the energy (90%) carried by the largest eddies is dissipated at the smallest dissipative scales. These smallest dissipative scales where dissipation occurs are known as Kolmogorov scales, as explained earlier.

The dissipation, denoted as ε, is the energy per unit time per unit mass, which is proportional to the kinetic viscosity, ν, times the square of turbulent fluctuating velocity gradient $\left(\frac{\partial v}{\partial x}\right)$. Kolmogorov's velocity scale, u_η, length scale, l_η, and time scale, τ_η are determined by viscosity ν and dissipation ε. The argument is that, since kinetic energy is destroyed by viscous forces, therefore viscosity ν must have a role to play here; similarly, larger the amount of kinetic energy being transformed into thermal energy, the larger the velocity gradient. With these considerations, velocity scale, u_η, length scale, l_η, and time scale, τ_η can be given by dimensional analysis as follows:

$$u_\eta = (\nu\varepsilon)^{1/4},$$

$$l_\eta = \left(\frac{\nu^3}{\varepsilon}\right)^{1/4},$$

$$\tau_\eta = \left(\frac{\nu}{\varepsilon}\right)^{1/2}. \quad \text{.... (3.7)}$$

Integral length scale: As turbulence contains a continuous energy spectrum of different scales, it is often convenient to analyse the flow in terms of spectral distribution of energy. Generally, spectral representation of energy is a Fourier decomposition of energy into domain of wavenumbers κ. Considering the reciprocal of κ as eddy size, an expression for kinetic energy contained between wavenumber κ and $\kappa+d\kappa$ can be obtained as $E(\kappa)d\kappa$, which is further used to obtain the expression,

$$k = \int_0^\infty E(\kappa) d\kappa \quad \text{.... (3.8)}$$

where k is kinetic energy per unit mass of fluctuating turbulent velocity and $E(\kappa)$ is the energy spectral function/density. Considering that the large eddies so strongly influence the turbulence, it follows that energy spectral density $E(\kappa)$ would be a function of larger eddies, l and their dissipation rate, ε. Dimensional analysis for high Reynolds number turbulence established that k can be expressed in terms of ε and l as (Taylor 1935):

$$k \approx (\varepsilon l)^{2/3} \quad \text{.... (3.9a)}$$

which can be rearranged to give:

$$l = \frac{u^3}{\varepsilon} \quad \text{… (3.9 b)}$$

where l is also known as the *integral length scale*.

Another important feature characterising a turbulent flow is *turbulent intensity*. It is usually quantified in terms of specific normal Reynolds stress components, $\overline{u'^2}$, $\overline{v'^2}$ and $\overline{w'^2}$, which could be regarded as the kinetic energy per unit mass of fluctuating quantity in three co-ordinate directions. These turbulence fluctuations are the ones which are imposed on the mean flow in a typical Reynolds Average Navier-Stokes Simulation (RANS) as, $U + u'$ (discussed later). The turbulent kinetic energy, k can be obtained by summing up the squares of all three turbulence fluctuations and multiplying it by ½, as follows:

$$k = \frac{1}{2}(u'^2 + v'^2 + w'^2) = \frac{1}{2}\overline{u_i' u_i'} \quad \text{.... (3.10)}$$

3.6 Two-point Correlation

When averaging a product of those quantities, for instance *u* and *v,* we can write it as a sum of its average and fluctuating part, as

$$\overline{u\,v} = \bar{u}\bar{v} + \overline{u'v'} \quad \text{.... (3.11)}$$

This equation suggests that the mean of the product of two quantities differs from the product of two mean values. The quantities $u' and\ v'$ are said to be correlated if $\overline{u'v'} \neq 0$ or else they are said to be uncorrelated. For example, two points in the near-wall region can be found to be correlated whereas one point near the wall and another far from the wall would not be correlated in a typical channel flow.

In general, there are two types of two-point correlation commonly used in experimental and theoretical turbulence studies:

(a) Temporal two point correlation, and

(b) Spatial two point correlation.

The first involves the correlation of parameters separated in time while the other involves correlation in separation of parameters in spatial position. The basis of the correlation is the pioneer work by Taylor (Taylor 1935) which describes the relation between spatial and temporal separation as follows:

$$\frac{\partial}{\partial t} = -U\frac{\partial}{\partial x} \quad \text{.... (3.12)}$$

However this relationship is only proved to be valid for small turbulent fluctuations. More relevant two point correlations are obtained from extensive analysis of one point time correlation data using autocorrelation functions.

A two point time autocorrelation tensor is defined by considering the correlation of velocities at one point and two different time as follows:

$$R_{ij}(\boldsymbol{x}, t; t') = \overline{u_i'(\boldsymbol{x}, t) u_j'(\boldsymbol{x}, t + t')} \quad \text{.... (3.13)}$$

Similarly a two point velocity (space) correlation tensor is defined by considering the correlation of two point $\boldsymbol{x}$ and $\boldsymbol{x}+\boldsymbol{r}$ in flow**,** as:

$$R_{ij}(\boldsymbol{x}, t; \boldsymbol{r}) = \overline{u_i'(\boldsymbol{x}, t) u_j'(\boldsymbol{x} + \boldsymbol{r}, t)} \quad \text{.... (3.14)}$$

Further discussion in this regard is presented in Chapter 6.

3.7 Models of Turbulence

The presence of wide ranges of length scales and time scales for eddy dimensions require these scales to be computed and solved. Since Navier-Stokes equations exactly compute these wide ranges of scales and the associated turbulence structure in a typical turbulent flow, the computation cost of the simulation is mostly too high for practical applications. In the past, various classes of techniques for simplification of turbulence scales have been employed by choosing different range of scales to model flow simulation. These techniques can be classified as follows:

Direct Numerical Simulation (DNS): DNS is the simulation of Navier-Stokes equations without employing any model. Because no model is employed in the simulation, all scales of flow have to be resolved by the computational grid and that increases the cost of computation to a prohibitive

level for industrial applications. The only source of error in such simulations comes from the discretization error and aliasing error (no dissipation error). However the computational cost rises with Reynolds number; the cost in the near-wall flow is proportional to $R^{3.7}$ and in the

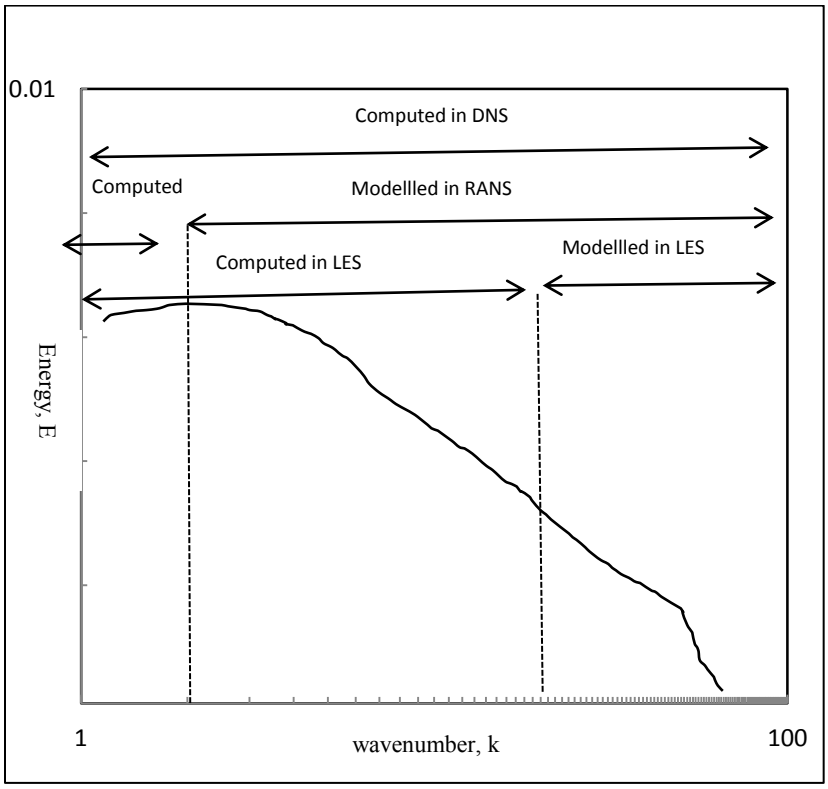

Figure 3.7*: Comparison of computed and modelled scales in RANS, DNS and LES.*

away from wall region is proportional to R^3 (can be derived from equations 3.7 and 3.9). These prohibitively large requirements of computational resources limit the applicability of DNS to low Reynolds number flow and in understanding the turbulence physics. One of the pioneering works in the DNS simulation of wall-bounded channel flow was conducted by Kim et *al.* (Kim, Moin et al. 1987) at a Reynolds number of 3300 with about $4x10^6$ grid points.

Reynolds Averaged Navier-Stokes (RANS): In this method, Navier-stokes equations are averaged in time over a period big enough to capture even the lowest frequency oscillations in the

domain. The averaging almost ignores the unsteady behaviour of turbulent flow and a somewhat steady consideration of turbulence is made while the effect of turbulence on mean flow is evaluated. The Reynolds stress term $\overline{u_i' u_j'}$ appearing in the governing equations for averaging quantities represents the effect of fluctuating velocities on the averaged ones. Taking advantage of the Boussinnesq assumption, Reynolds stress can be considered proportional to the strain rate by introducing eddy viscosity ν_t as:

$$\sigma_{ij} = \overline{u_i' u_j'} - \frac{1}{3}\overline{u_k' u_k'}\delta_{ij} = -2\nu_t \overline{S_{ij}} \quad \ldots (3.15)$$

The problem then shifts to the way of guessing the eddy viscosity ν_t and therefore these models are called eddy viscosity models. Turbulent length and time scale characteristics are calculated through various models to derive the turbulent viscosity field. This can be done using simple algebraic relations such as Prandtl's mixing length hypothesis (Prandtl 1925) or one equation models for turbulent kinetic energy (Kolmogorov 1942)(Kolmogorov 1991) or two-equation models such as the $k - \varepsilon$ model (Jones, Launder 1972). Although the eddy viscosity assumption which implies that the turbulent motion is in equilibrium with the mean flow is not perfect but it is a reasonable approximation considering that the local mean gradient characterises the mean distortion to turbulence in simple shear flows.

Despite inability to handle unsteady flow effectively and not being very accurate in some other cases, RANS are easy to implement, faster to solve and have good accuracy in modelling mean flow. For these reasons, the approach is still widely practised in CFD modelling.

(c) Large-Eddy Simulation (LES): Unlike DNS, LES does not resolve the complete range of turbulent scales and only captures scales as small as practically feasible. In this way LES computes the dynamics of as much of the large energy containing resolved scales of the flow as is economically feasible while modelling only effects of small unresolved phenomenon on the larger

resolved scales with the help of sub-grid models. This method takes into account the fact that energy is mainly contained in the largest scales of flow. The division of the scales of flow into larger resolved and smaller unresolved scales in LES modelling is termed as grid scale (GS) and sub-grid scales (SGS) respectively. The division in scales can be accomplished by convolving the dependent flow variables in Navier-Stokes equations with a predefined kernel, which works like a high-pass filter and separates the GS scale. In traditional methods filtering is applied to the Navier-Stokes equation to obtain a governing relation for filtered velocity. The filtering of the Navier-Stokes equation creates a need for the modelling of sub-grid scale (SGS) stresses and the way this SGS stress is modelled to obtain a closed system of equations distinguishes one LES method from another. In the process of modelling, the GS motion is explicitly simulated whereas the average effect of the SGS motion on GS motion is accounted for by a SGS model. Figure 3.7, illustrates scales computed and modelled by various methods and it clearly shows that LES is an interesting and efficient compromise between DNS and RANS.

The basic equations for LES were first formulated by Smagorinsky in the early 1960's for application in meteorology. (Smagorinsky 1963) The first engineering application of LES was performed by Deardorff (Deardorff 1970) in a channel flow simulation. Since then, LES has become a very attractive research and industrial application tool. LES has been implemented for channel flow (Moin, Kim 1982), isotropic turbulence (Lesieur 1997), free shear mixing layer (Vreman 1995) and flow with separation (Le, Moin et al. 1997). The RANS and LES equations used in this research are provided in the appendix.

3.8 Closure

The phenomenon of turbulence and its characteristics and spectrum were introduced in this chapter. Wall bounded flow and various turbulence generation mechanisms near wall bounded flow were also introduced. Various scales of turbulence and two point correlations were introduced as reference to the generation of synthetic boundary conditions in subsequent chapters. Finally, various available models of turbulence like DNS, RANS and LES were introduced. The chapter concisely has introduced the important information about turbulence which is useful for the current research.

Chapter 4

Simulation of Acoustic Pulse through Muffler

4.1 Introduction

Computational simulation of acoustic propagation and attenuation has always attracted researchers and industries alike for various applications. There has been considerable research done in recent past in the area of turbulence generated noise or noise source identification. The focus of these investigations is predominantly where there is no forced oscillation introduced and only noise due to turbulence or flow characteristics have been important. However, these investigations have been concentrated towards using simplified mathematical models or sets of linear/nonlinear equations for simulation of sound propagation. Therefore, additional research is required in the area of CFD simulation of sound propagation. This chapter will investigate various spatial and temporal discretizations for acoustic simulation, simulate a simple expansion muffler without flow for several structural configurations, and simulate pipe and muffler with flow using the RANS method.

Because of the numerous applications in exhaust silencers and air-conditioning HVAC systems, the expansion muffler has been extensively studied by various authors (Potente 2005, Arenas, Gerges et al. 2004, Munjal 1987, Selamet, Radavich 1997). The acoustic simulation of expansion mufflers has been an essential component of the design and development of noise reduction systems. Some analytical one-dimensional models have also been proposed recently to accurately predict the sound propagation in different expansion mufflers (Yasuda, Wu et al. 2010, Panigrahi, Munjal 2007). A better and more effective mathematical model that has been attempted by some

researchers uses either the Boundary Element Method (BEM) or the Finite Element Method (FEM) to solve a Helmholtz equation to simulate the acoustic propagation (Arenas, Gerges et al. 2004, Selamet, Radavich 1997, Selamet, Radavich 1997, Selamet, Ji 1999, Seybert, Soenarko et al. 1985). Different measurement techniques were proposed for FEM/BEM methods to accurately predict various design parameters like transmission loss or insertion loss in expansion muffler, including four-pole and three-point technique (Arenas, Gerges et al. 2004). Some improvements in the FEM/BEM based methods have also been reported with an enhanced four parameter method (Barbieri, Barbieri 2006, Barnard 2004). Besides these, few attempts to find a simpler, faster and cost effective plane wave models have also been made with some success (Suwandi, Middelberg et al. 2005, Munjal 1997). This model was further improved by Liu (Liu, Lu et al. 2009) to include the effect of high order model waves. There has always been interest in CFD simulation of acoustic pulse but the large disparity between the acoustic and flow scale leads to an enormous computational requirement and this made the CFD simulation of acoustic propagation prohibitively expensive in the recent past, especially for industrial applications. However, with drastic improvements in the computational performance and memory of recent computers/clusters, some successful attempts have been made to computationally simulate the acoustic propagation of acoustic pulse in a laminar flow using CFD.

Recently, two alternative techniques have been proposed to achieve solution convergence in low Mach number flows viz., Asymptotic and Preconditioning. The asymptotic technique uses the perturbed form of equation, which discards specific terms so that the physical acoustic waves are replaced by pseudo-acoustic modes. On the other hand, the Preconditioning technique uses a preconditioning matrix to scale the eigenvalues of the system to a similar order of magnitude. This alleviates the disparity in the wave speeds and leads to a well converging solution. The

pressure-based SIMPLE algorithm has been further extended by different authors using these techniques. A multi-length scale- single time scale asymptotic analysis was done by Klein (Klein 1995) for the full Euler equations which included the influence of long wavelength acoustic waves at leading order in the velocity field. Munz *et al.* (Munz, Roller et al. 2003) further extended Klein's work and proposed a Multiple Pressure Variable (MPV) method, which used the SIMPLE algorithm for simulation of weakly compressible flow. Bijl *et al.*(Bijl, Wesseling 1998)and Webster *et al*. (Webster, Keshtiban et al. 2004) performed similar computations using asymptotic technique on boundary-fitted grids and Cartesian grids respectively.

In an attempt to extend the compressible flow solver to the incompressible range, a hybrid flux-splitting scheme with collocated grid and preconditioning was used by Rossow (Rossow 2000) to simulate airfoil flow using a 5 stage Runge-Kutta scheme. Rossow further extended his work to derive a blended pressure/density-based method based on the SIMPLE method (Rossow 2003). It may be important to note that it has been claimed that when conventional methods without preconditioning are used, false solutions could be obtained due to excessive artificial damping and accumulation of errors. The preconditioning procedure can artificially enhance numerical wave propagation and thus reduce the number of time steps required for acceptable solutions. However, preconditioning methods need to be customised for specific kinds of problem and sometimes it is hard to choose the right preconditioner for a new specific problem, which in turn could be troublesome in developing a more universal and unified numerical solver for low Mach number flow.

Most of the acoustic investigations of muffler with mean flow in the past have unsurprisingly been concentrated towards experimental or one-dimensional analysis. A one-dimensional model has been proposed by Munjal (Munjal 1997) for typically small mean flow in a side-inlet-outlet

muffler. CFD modelling of muffler with mean flow has been done recently by Mohiuddin (Mohiuddin, Rahman et al. 2007) without imposing any acoustic pulse through the muffler. In similar attempts to model high frequency waves of aerodynamic problem, there has been constant development in last few decades in the area of Computational Aero-acoustics (CAA). CFD modelling of expansion muffler with mean flow and with an acoustic pulse imposed at the inlet has mostly been attempted using the Finite difference method (FDM) or FEM/BEM based methods for their dissociation with eigen structure and computational simplification due to analytical models respectively. Therefore, FVM methods have largely been avoided due to their computational complexity and high memory and speed requirements. This certainly limits the study of acoustic modelling and neglects problems where turbulence and mean flow interactions are important. Some high resolution methods have been attempted recently by Hwang *et al.* (Hwang, Lee et al. 2007) to accurately predict the performance of an exponential pipe muffler with mean flow using the finite difference method. The simulation has solved Euler equations using 2^{nd} order Runge-Kutta method for time discretization and MUSCL (Monotone Upwind Schemes for Conservation laws) for space discretization. Later, Obikane (Obikane 2009) has also attempted to simulate a complex muffler configuration using a third order finite difference scheme. The unique feature of this method is that it has solved Navier-Stokes equations instead of Euler equations, using a third order finite difference scheme. The results obtained in this work seem to be promising for a complex muffler structure. However, these results cannot be verified experimentally or with available results in literature for a complex muffler configuration. In the present work, a simple expansion muffler is therefore selected for acoustic simulation so that the results could be verified with analytical or available experimental results.

Many attempts have been made in the past to simulate acoustic pulse propagation in the expansion mufflers of various configurations using commercial CFD codes (DeSpirito, Binseel 2008, Middelberg, Barber et al. 2004). In their initial attempt, Middelberg *et al*. used the Fluent commercial package to simulate the pulse through a muffler but CFD simulation results were still not up to the mark (Middelberg, Barber et al. 2003). They later improved their CFD simulation results by using a second order backward scheme and results were close to the experimental results (Middelberg, Barber et al. 2004). DeSpirito (DeSpirito, Binseel 2008) replicated his work with Fluent software and extended his research for CFD modelling of a specific earplug design. ()Recently, Piscaglia (Piscaglia, Jasak et al. 2010) simulated a similar case using state of the art OpenFOAM (OpenFOAM 2007) software to acoustically simulate a random acoustic pulse through an expansion muffler using a customised acoustic boundary condition with different time varying acoustic inlet perturbations. They implemented numerical filtering along with data smoothing at post processing level to improve the result quality.

An attempt is made in the present work to simulate an acoustic pulse in the expansion muffler using a hybrid low Mach number pressure-based Karki-PISO compressible flow solver (explained in section 2.3). The issues concerning computational acoustic simulation are also reviewed in the light of the present work. Various spatial and temporal discretization methods are investigated for acoustic simulation in the present work. Apart from that, several structural configurations of simple expansion muffler are also investigated to investigate the pulsation response of the muffler. The RANS approach is adopted for obtaining mean flow profile for pipe and muffler configurations, and pulse is thereafter imposed to acoustically simulate the device.

4.2 Computational Aero-acoustics

The CAA community has been mostly working towards obtaining better numerical schemes to solve transport equations to get a more accurate and robust solver for aero-acoustic applications. Since these methods usually solve some form of Euler equation, the solution of these simulations come at expense of ignoring the viscous term in the computational equation, which could be important in certain applications. The other problem with the typical computational aero-acoustics methods is that they usually do not strictly model the turbulence and therefore the study of turbulence and acoustic interaction is very limited in typical CAA studies. Despite that, the contribution of CAA in acoustic propagation and attenuation analysis has been tremendous and various aspect of this research has been shaping the field of computation acoustics for more than 20 years.

The area of Computational Aero-acoustic (CAA) has come to light from the middle of the 1980s and since then it has gained attention of various researchers to study flow with short wavelengths.(Lighthill 1992) However, many date the birth of CAA as recent as the 1993 publication of Tam and Webb (Tam, Webb 1993), highlighting special requirements for efficient finite difference method. The areas of application of CAA have mostly been in the noise generation due to flow, noise radiation from a source or noise propagation into a flow field. In the last three decades, this area has made spectacular progress due to rapid advances in computational resources. On the other hand, it should not be assumed that the CAA methods are completely different from CFD methods. CAA methods are actually very strongly linked to CFD. CAA methods have been developed in a way that it uses specific techniques to resolve wave behaviour well and that's what makes these methods different from typical CFD methods. The issues related to CAA are discussed here in brief:

Broad frequency bandwidth: Typical CAA problems involve widely spread frequency range. The high frequency acoustic waves can coherently cover long distance with negligible attenuation due to the viscous effects. These high frequency waves are also called "spurious waves" and usually arise due to insufficient resolution of relevant length scales of any given problem. Noise in a typical expanded jet consists of frequencies in the range of Strouhal number from 0.01 to 10, which makes a ratio of 1000 between the highest and the lowest frequency. The highest frequency or shortest wavelength in the problem domain decides the spatial resolution requirement of the problem. It has been reported that a general CFD method require a resolution of 18-25 mesh points for typical expanded jet, whereas a CAA method might only need 6 to 8 mesh points. (Tam 2006)A great amount of effort has been put by the CAA community to develop computational schemes which could provide adequate resolution at fewer number of mesh points in computational domain.

Disparity between mean flow and Acoustic wave: It has been found that there is a large disparity between mean flow and acoustic waves. The acoustic waves which are radiated or propagated with the mean flow have fluctuations of the order of around four with respect to the mean flow magnitude. This large disparity between these two parameters presents extreme computational challenges. Putting this disparity in context, it can easily be seen that the small amplitude of the acoustic disturbance is almost comparable to the numerical error, which is the difference between computed mean flow and exact mean flow solution. This leads to the discussion among the researchers to develop high order computational schemes which are robust and correct to greater extent. Some researchers proposed to solve for the perturbation after the mean flow has first been determined, instead of solving the fully non-linear equation to capture the very small amplitude

sound field directly. However the problems related to generation of noise from flow has to solve full nonlinear equation to capture small amplitude sound field directly.

Multiple length scale problem: Most of the aeroacoustic problems are multiple length scale and the length scale of the acoustic source is very different from the acoustic wavelength. Since the growth and decay of the large turbulence structure in the noise source region is dictated by the thickness of mixing layer, there are various length scales available in the inner flow region. In the outer region, the natural length scale of the acoustic field is the acoustic wavelength. A careful consideration of spatial resolution requirement is essential for the simulation of the existing multiple length scales. It has also been reported that the adequate resolution of instability wave in the mixing layer of the jet requires a minimum of 15 mesh points, which makes a spatial resolution in the sound source region 50 times finer than the acoustic field region. The spatial resolution requirement along with the CFL number restriction leads to excessive computational time.

***Numerical dispersion*:** A typical aeroacoustic problem is usually concerned with the directivity, propagation and radiation of sound spectrum. Unlike aerodynamic problem where accurate solution is only required in the vicinity of aerodynamic body, aeroacoustic problem require a computed solution which is accurate throughout the computational domain. Besides, the large distance between the noise source and the boundary make it essential to have a computational scheme which is accurate over such a long propagation distance. Thus, the numerical scheme has to be free from any numerical dispersion, dissipation or anisotropy.

Spatial discretization: Since viscosity terms are usually ignored in a typical computational aeroacoustic problem, the Navier-Stoke equations are replaced by Euler equations to solve compressible problems. The temporal and spatial derivative of these equations has to be approximately discretized and their discretized equations must be solved. It is important to note

that the exact solutions of the discretized equations are not the same as those original partial differential equations. This constitutes an error referred to as the difference between the solution of original partial differential equations and the discretized system. As a simple example, a one dimensional advection equation or first order wave equation can be taken as:

$$\frac{\partial u}{\partial t} + c\,\frac{\partial u}{\partial x} = 0 \qquad \ldots\ldots (4.1)$$

where c is constant and has unit of speed. Fourier-Laplace transform on eq. (4.1) decomposes to their Fourier components in x and *t.* The Laplace transform of a function $g(t)$, denoted by $\tilde{g}(\omega)$, and its inverse, are related by

$$\tilde{g}(\omega) = \frac{1}{2\pi}\int_{-\infty}^{\infty} g(t)e^{i\omega t}dt,$$

$$g(t) = \int_{C} \tilde{g}(\omega)e^{-i\omega t}d\omega \qquad \ldots. (4.2)$$

Where ω is the angular frequency (Laplace transform variable) and C is a contour in the upper half ω-plane parallel to the real axis. The Fourier transforms of Eq. (4.1) leads to,

$$\tilde{u} = \frac{i\,\hat{\phi}(k)}{2\pi(\omega - ck)} \qquad \ldots. (4.3)$$

and then its pole evaluation is obtained by setting denominator to zero. This finally, leads to the dispersion relation,

$$\omega = ck \qquad \ldots. (4.4)$$

which provides a relationship between wave number k and angular frequency ω. Since all the components of the Fourier modes travel with the same speed c, the superimposed waveforms

retain their shape as they propagate. Further discretizing Eq. (4.1) on one dimensional mesh shown in figure 4.1, an approximation of *x*-derivative at *n*th mesh point can be obtained using standard central differencing quotient or Dispersion Relation Preserving (DRP) with a stencil of (2N+1) points as,

$$\left(\frac{\partial u}{\partial x}\right)_n \cong \frac{1}{\Delta x} \sum_{j=-N}^{N} a_j \, u_{n+j}$$

….. (4.5)

where $a_j = -a_{-j}$, and this makes the semi-discretized form of Eq. (4.1) as the system of equations,

$$\frac{\partial u_n}{\partial t} = \frac{-c}{\Delta x} \sum_{j=-N}^{N} a_j u_{n+j}(x + j\Delta x, t)$$

…. (4.6)

Now taking Fourier transform, it can be found that,

$$\tilde{u} = \frac{i\,\hat{\phi}(k)}{2\pi(\omega - ck^*)}$$ ….. (4.7)

This is similar to Eq. (4.3) except that *k* is replaced by *k**. Now inverting the Fourier and Laplace transforms, the exact equation of the discretized equation can be obtained as,

$$u(x,t) = \frac{i}{2\pi} \iint_{-\infty\, C}^{\infty} \frac{\hat{\phi}(k)}{\omega - ck^*(k)} \, e^{i(kx-\omega t)} \, d\omega \, dk$$

…. (4.8)

The dispersion relation is now replaced with the expression,

$$\omega = ck^*(k)$$ …. (4.9)

Eq. (4.8) has a pole at $\omega = ck^*(k)$ which can be picked in the ω-plane by deforming the inverse contour C and using Residue theorem afterwards,

$$u(x,t) = \int_{-\infty}^{\infty} \hat{\phi}(k)\, e^{i(k(x/t)-\omega)t)}\Big|_{\omega=ck^*(k)} dk \qquad \ldots. (4.10)$$

For large values of *t*, the k-integral of Eq. (4.10) may be evaluated by stationary phase point $k = k_s$ which is obtained by zero of the derivative of phase function $\Psi = (k(x/t) - \omega(k))$. This leads to the expression,

$$\frac{\partial \omega}{\partial k} = c\,\frac{\partial k^*(k)}{\partial k}\Big|_{k=k_s} = \frac{x}{t}, \qquad \ldots..(4.11)$$

This expression provides k_s as a function of *x/t.* The term $\frac{\partial \omega}{\partial k}$ is called group velocity and it is also the propagation speed of the component of solution with wave number *k*. As $\frac{\partial k^*}{\partial k}$ is not usually 1, different Fourier components travel with different speed and therefore wave packets of even slightly different wave number propagate with different propagation speeds. A serious dispersion can be witnessed over a long propagation distance even with small differences in group velocity. This is the source of dispersion in computational modelling.

In general, two solutions exist for the dispersion relation, one for long wavelength and another for short wavelength. The group velocity of long wavelength is positive and is well resolved component of the solution, whereas group velocity of short wavelength is negative and poorly resolved which counters the physical phenomena of Eq. (4.1). The long wavelength solutions are referred to as smooth waves whereas short wavelength solutions are referred to as spurious waves

(mentioned above). For second order finite difference scheme, the speed of propagation of spurious waves is equal to that of the smooth waves but in an opposite direction of propagation.

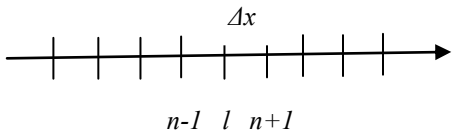

Figure 4.1*: A uniform mesh with spacing Δx.*

Temporal discretization: Besides the spatial discretization, numerical dispersion also comes from time discretization of the partial differential equations. In the semi-discrete formulation, time marching methods can be separated as explicit scheme and implicit scheme. There could also be semi-implicit scheme formation of time discretization. Implicit schemes are solved by iterative or approximate factorization methods and are therefore useful for obtaining solution of a stiff system of ODE. It is especially important when it is required to suppress the component associated with the fastest eigenvalues of the solution. Semi-implicit time schemes are usually used in suppressing high wave number spurious waves, which in turn relaxes the CFL restriction associated with acoustic waves.

In explicit finite difference formulation, the two type of time marching schemes which are most famous are:

- Runge-Kutta method (single-step scheme)
- Linear Multi-step method (multi-step scheme)

The basic difference between these two schemes is in terms of the way flux of information travel forward in time. Runge-Kutta (RK) schemes are single step scheme where integration moves

forward from any point without using previous time-step information of the solution. The resulting system of differential equations can be written as,

$$\frac{\partial u}{\partial t} = F(u, t). \quad \text{…. (4.12)}$$

The explicit *p*-stage RK method for Eq. (12) can be written as,

$$u^n = u^{n-1} + h \sum_{i=1}^{s} b_i k_i,$$

$$k_i = F\left(u^{n-1} + h \sum_{j=1}^{i-1} a_{ij} k_j \ , \ t^{n-1} + \Delta t c_i \right),$$

…. (4.13)

where u^n are dependent variables evaluated at time $t^n$and Δt is the time step. b_i, c_i and a_{ij} are the co-efficients which can be obtained by solving various numerical conditions for a given accuracy level of *p*. The eigenvalues of the right hand side of the linearized Eq. (4.12) determine the stability of the RK methods and the order of accuracy of the method is equal to the number of stage p of the method. For instance, classical RK schemes have accuracy level up to 4 and stability region includes the imaginary axis for 3rd and 4th order RK schemes. In problems associated with very small diffusion (negative real part of the eigenvalue) such as in turbulence and aeroacoustic flow calculations, RK schemes have useful applications. These schemes are obviously restricted by the CFL conditions of the spatial discretization of right side of Eq. (4.12) in finite difference formulation. RK methods have additional dispersion and dissipation (discussion in next subsection) beyond that from the evaluation of spatial discretization and this additional dispersion and dissipation could be reduced by optimizing the co-efficients of the RK methods. Some low dispersion and dissipation (LDD) schemes have also been introduced that have lower formal order

of accuracy (less than p for p-stage RK method) than the usually achievable order (p^{th}-order) with the given classical p-stage RK method. Another advantage of RK method comes from the fact that these methods are very low storage methods which do not use the information from the previous timesteps.

LM methods on the other hand are multi-step methods and information travel forward in time using previous timestep information. The solution obtained is superposition of physically correct solution and spurious solutions. The physically correct solution tends to correct solution as timestep tends to zero, whereas the spurious solution has to be carefully suppressed and damped with time by choosing small enough timestep. Although LM methods are not self starting but a lower scheme can be used for initial steps. Since the LM methods only require one evaluation of *F(u, t)* per time level, these are very efficient. However their spurious solutions can have much stricter CFL constrains than high order RK method. Eventually, it has been found that the RK4 method and LM method have roughly similar computational efficiency and associated cost.

(e) ***Numerical dissipation***: In addition to the numerical dispersion, CAA problems also suffer from other inaccuracies while discretizing partial differential equations, namely numerical dissipation. Again considering the Eq. (4.8) and Eq. (4.10) at $\omega = ck^*(k)$, the extent of damping of numerical solution can be evaluated depending on the kind of stencil used. For a central differencing stencil, $k^*(k)$ is a real function for real *k* and Eq. (4.10) behaves as dispersive wave quanta without being damped in time. For an asymmetric stencil, $k^*(k)$ is complex for real *k* and solution will be damped in time only if $cIm(k^*(k))$ is negative for all *k*. However if the sign of *c* and $Im(k^*(k))$ is same then the numerical result grow exponentially in time causing numerical instability. Therefore the necessary condition for numerical stability can be expressed as:

$$c\ Im(k^*(k)) < 0, \qquad -\pi \leq k\Delta x \leq \pi \qquad \ldots. (4.14)$$

Most of the famous upwind schemes satisfy these criteria. However the drawback of upwind scheme is that there are significant dissipations in the high wave numbers region of the solution. Various artificial damping has been introduced by some researchers to damp out the spurious waves of the computation scheme. In the Eq. (4.1), an artificial selective damping term *D(x)* can be introduced as,

$$\frac{\partial u}{\partial t} + c\ \frac{\partial u}{\partial x} = D(x)$$

.... (4.15)

Further, spatial dicretization using the 7-point optimized stencils can be described as,

$$\frac{\partial u_l}{\partial t} + \frac{c}{\Delta x}\sum_{j=-3}^{3} a_j u_{l+j} = -\frac{v_{ar}}{\Delta x^2}\sum_{j=-3}^{3} d_j u_{l+j}.$$

..... (4.16)

It is also assumed that the discretization of term D_l is proportional to the values of u_l within the stencil. d_j are the damping stencil co-efficients and v_{ar} are the artificial kinematic viscosity. The values of d_j are chosen to selectively damp the high wave number spurious waves only. It has been found that the introduction of artificially selective damping in a computational scheme performed extremely well in eliminating most of the spurious short waves in numerical solution. Besides, artificial selective damping also smoothes out discontinuities over several mesh spacing and is effective in all shock capturing schemes.

(f) Radiation boundary conditions: Since the domain of simulation is inevitably finite, it is necessary to impose outflow and radiation boundary conditions at boundaries of the problem domain. For a highly accurate simulation, it is necessary that these boundary conditions must let

the outgoing disturbances go without getting reflected back into the computational domain. The most frequently used system of equations for aeroacoustic problem is Euler equations, which is formed after ignoring the viscous terms in the Navier-Stokes Equations.

Three type of small-amplitude fluctuations are accounted for solving CAA problem in general Euler equations. These are acoustic fluctuations, vorticity and entropy waves. It is also assumed that the source is far from the problem domain. Tam and Webb (Tam, Webb 1993) derived the expression for asymptotic solution of the outgoing acoustic wave at boundary in polar form as,

$$\begin{bmatrix}\rho\\ u\\ v\\ p\end{bmatrix} \equiv \begin{bmatrix}\rho_a\\ u_a\\ v_a\\ p_a\end{bmatrix} = \frac{F(\frac{r}{V(\theta)}-t,\theta)}{r^{1/2}} \begin{bmatrix}\frac{1}{a_0^2}\\ \frac{\hat{u}(\theta)}{\rho_0 a_0}\\ \frac{\hat{v}(\theta)}{\rho_0 a_0}\\ 1\end{bmatrix} + O\left(r^{-\frac{3}{2}}\right), \quad \text{..... (4.17)}$$

The subscript 'a' indicates that the disturbances are associated with the acoustic waves only. $V(\theta)$ is defined as $V(\theta) = a_0(M\cos\theta + (1 - M^2 sin^2\theta)^{1/2})$ and M is the mean flow Mach number. Eq. (4.17) is then further derived with respect to t and r to obtain the expression which any acoustic disturbances satisfies for arbitrary function F to provide a set of far field radiation boundary condition as,

$$\left(\frac{1}{V(\theta)}\frac{\partial}{\partial t} + \frac{\partial}{\partial r} + \frac{1}{2r}\right)\begin{bmatrix}\rho\\ u\\ v\\ p\end{bmatrix} = 0 + O\left(r^{-\frac{5}{2}}\right). \quad \text{..... (4.18)}$$

This method has been derived by extending for the first term only and therefore can suffer from inaccuracies whenever source is not located near the centre of the computational domain. The reason for the inaccuracies could be the slow convergence of asymptotic expansion.

(g) Outflow boundary condition: The outflow region requires to not letting the outgoing reflections get back into the computational domain. Various Non-reflecting boundary conditions have been developed to accommodate such problems. Non-reflecting boundaries attempt to annul any incoming waves at the boundary. Other approach is Perfectly Matched Layer (PML) where domain is enclosed by a buffer region and terms are added to the governing equations to minimize reflection of outgoing waves. A typical schematic for boundary requirements is showed in the Figure 4.2.

Tam (1993) proposed the asymptotic solution for density, velocity and pressure fluctuations as follows,

$$\begin{bmatrix}\rho\\ u\\ v\\ p\end{bmatrix} = \begin{bmatrix}\chi(x-u_0t,y)+\rho_a\\ \frac{\partial\psi}{\partial y}(x-u_0t,y)+u_a\\ \frac{\partial\psi}{\partial x}(x-u_0t,y)+v_a\\ p_a\end{bmatrix} + \dots , \qquad \dots. (4.19)$$

The explicit terms $(\rho_a, u_{a,} v_a, p_a)$ are explained in Eq. (4.18) and ψ, χ and F are arbitrary functions. These functions are eliminated by a combination of various derivatives and following boundary conditions are obtained,

$$\frac{\partial\rho}{\partial t}+u_0\frac{\partial\rho}{\partial x}=\frac{1}{a_0^2}\left(\frac{\partial p}{\partial t}+u_0\frac{\partial p}{\partial x}\right),$$

$$\frac{\partial u}{\partial t}+u_0\frac{\partial u}{\partial x}=-\frac{1}{\rho_0}\frac{\partial p}{\partial x},$$

$$\frac{\partial v}{\partial t}+u_0\frac{\partial v}{\partial x}=-\frac{1}{\rho_0}\frac{\partial p}{\partial y},$$

$$\frac{1}{V(\theta)}\frac{\partial p}{\partial t}+\cos\theta\frac{\partial p}{\partial x}+\sin\theta\frac{\partial p}{\partial y}+\frac{p}{2r}=0. \qquad \dots. (4.20)$$

Thompson (Thompson 1990, Thompson 1987) has proposed non-reflective characteristic based boundary condition for one dimensional equation which finds characteristic solution easily. However characteristic solutions for three-dimensions are not as promising as one dimensional form of characteristic boundary equations (which is exact). Thompson's characteristic solution is based on local identity and decoupling of left and right going waves across the interface. The three characteristic curves with slopes $\lambda_1 = u,\ \lambda_2 = u + c$, and $\lambda_3 = u - c$, are needed for any characteristic to cross the domain. The integrated values of the dependent variables along the characteristic curve are known as Riemann invariants and these boundary conditions are referred to as *characteristic* Boundary condition. These boundary conditions can be approximated for multidimensional flow to write conservative form of Euler equations as,

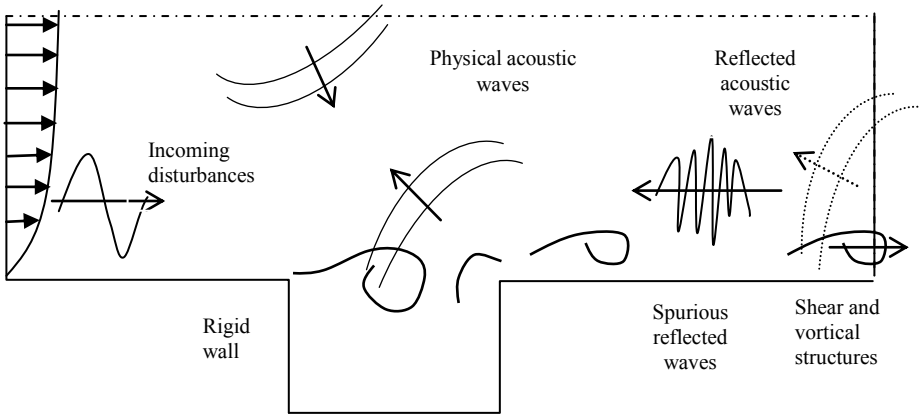

Figure 4.2*: Schematic diagram of boundary condition requirements for expansion muffler flow (one half of the plane-cross-section). cf.* (Colonius, Lele 2004)

$$h_t + P(u)S(u)\Gamma + g(h)_y = 0 \qquad \text{.... (4.21)}$$

where primitive variable $u = (\rho, u, v, p)^T$ and h *and* $g(h)$ are standard conserved variables and their transverse flux to the boundary,- P is the Jacobian matrix that transforms between

conservative and primitive variables $\left(P_{ij} = \frac{\partial h_i}{\partial u_j}\right)$,- S is a matrix whose columns are right eigenvectors A and Γ is a vector with components defined as,

$$\Gamma_1 = \lambda_1 \frac{\partial v}{\partial x}, \Gamma_2 = \lambda_1 \frac{\partial S}{\partial x}$$

$$\Gamma_3 = \lambda_2 \left\{\frac{\partial u}{\partial x} + (\rho c)^{-1} \frac{\partial h}{\partial x}\right\}$$

$$\Gamma_4 = \lambda_3 \left\{\frac{\partial u}{\partial x} - (\rho c)^{-1} \frac{\partial h}{\partial x}\right\}.$$

.... (4.22)

(h) Wall boundary conditions: Wall boundary conditions are necessary to impose the computational representation of the solid surface in the physical problem. For problem related to interior flow like duct flow, turbomachinery noise etc, wall boundary conditions are especially very critical. The representation of zero relative motion at solid rigid wall is generally done by no-slip condition at wall boundary. Mostly rigid walls are assumed to be isothermal or adiabatic in computation. Generally, for the approximation of a set of Euler equations, it is evident that the order of the resulting finite difference equation would be higher than the original partial differential equations. This higher order governing equation requires an extended set of boundary condition and the boundary condition which would work well for partial differential equations would not work well in these cases. The boundary conditions like no-slip boundary conditions are not sufficient in these cases. However, in this chapter the Navier-Stokes equations have been solved which eliminates the difficulty of obtaining specialised boundary condition.

Near the wall boundary log layer, it has been found that the kinetic energy and dissipation are inversely proportional to the distance from the wall. This creates a situation where singular

numerical behaviour presents numerical challenges (Tam 2006). Solving the continuity equation at wall using one-sided differencing for wall normal derivative of velocity and density would not be sufficient as it would create numerical instability and spurious waves in the near wall region. A method for development of technique for discretization of pressure gradient in the wall normal direction is introduced by Tam and Dong (Dong, Lu 2004) in a way to introduce a ghost row in the exterior grid of the body. Other terms in the boundary region are computed after obtaining pressure gradient in consistency with the governing equations accompanied with the isothermal/adiabatic condition or no-slip boundary conditions. Despite all the efforts, even high order schemes in the near wall region have been found to produce spurious waves and create numerical instability in the computational domain. A great deal of research effort is needed to produce wall boundary conditions with minimum numerical instability.

4.3 Computational Methodology

The computational methodology of the simulation constitutes the discretisation of averaged Navier-Stokes equations (described in section 2.2.1), the pressure-velocity coupling, and the numerical solution of the resultant matrices along with other functionalities. Most of the methodologies have been extensively covered in various manuals, text books and other publications and therefore only those portions which are relevant to the current work are reproduced here for completeness. There are several numerical methods available for computational acoustic simulation which includes mainly Finite Element (FE), Finite Difference (FD) and Finite Volume (FV) methods. Unfortunately the FE method configurations do not guarantee local conservation of dependent variables which is one of the most important factors in CFD methods. Therefore, FD and FV methods are more widely used in computational acoustic simulations. Most of the part of this work uses new pressure based finite-volume hybrid

Karki-PISO compressible solver, and the pressure-velocity coupling of this method is discussed in details in section 2.3. Another alternative approach for acoustic simulation uses central differencing based finite difference compressible solver and is discussed in details in section 2.2.3. Discussions throughout this chapter are mostly made in the context of FV methods and only occasional contexts are made to FD methods with specific notes.

Spatial discretisation: The governing equations of flow (described in section 2.2.1) are discretised and applied in an infinitesimal region of space to integrate over a control volume and in time, as shown in Eq. (4.23).

$$\int_V \frac{\partial}{\partial t}\rho\varphi dV + \int_V \nabla.(\rho\bar{u}\varphi)dV - \int_V \nabla.\rho\left(\Gamma_\varphi \nabla\varphi\right)dV = \int_V S_\varphi(\varphi)dV. \quad \text{... (4.23)}$$

The various spatial differencing terms in the final integral form of governing equations are convection term, diffusion term and source terms as shown in Eq. (4.23). Since the overall order of the differential equation is second order (because of second order diffusion term), the order of the discretization should be either equal to or higher than second order. The present spatial discretisation features unstructured boundary fitted meshes with collocated grids. A non-dissipative second order discretisation in space and time is employed in association with fully implicit time-stepping for a good compromise between speed and accuracy. The system of partial differential equations is treated in a segregated manner and an explicit coupling between each result is performed.

The convective term in the equation is integrated over the control volume and linearised as follows,

$$\int_V \nabla.(\rho u\varphi)dV = \int_S dS.(\rho u\varphi) = \sum_f S_f.(\rho u)_f \varphi_f$$

... (4.24)

The face field φ_f can be evaluated using various methods like the Upwind scheme, Central Scheme, Total Variation diminished (TVD) or Normalised Variable diagram (NVD) scheme. The Upwind differencing (UD) determines φ_f from the direction of flow and is bounded at the expense of accuracy.

$$\varphi_f = \begin{cases} \varphi_f = \varphi_P & for\ (\boldsymbol{\rho U})_{\boldsymbol{f}} \geq \mathbf{0} \\ \varphi_f = \varphi_N & for\ (\boldsymbol{\rho U})_{\boldsymbol{f}} \geq \mathbf{0} \end{cases} \quad \dots (4.25)$$

Central differencing (CD) is second order accurate but is unbounded. The face flux is determined as:

$$\varphi_f = f_x\varphi_p + (1 - f_x)\varphi_N \quad ... (4.26)$$

Where $f_x = fN/PN$, as shown in figure 4.3.

TVD and NVD schemes adjust the discretisation of convection term locally based on indicator function that follows the local shape of the solution in a one dimensional analysis. TVD schemes measures total variation of the numerical solution as,

$$TV(u) = \sum_j |u_{j+1} - u_j|$$

... (4.27)

which is standard bounded variation when solution is considered to be piecewise constant function. A scheme is said to be TVD if the solution satisfies,

$$TV(u^{n+1}) \leq TV(u^n) \quad ... (4.28)$$

Where u^n is the solution at time t^n . Some schemes are obtained by blending the central differencing (CD) scheme and upwind differencing (UD) scheme. Self-Filtered Central differencing (SFCD) scheme employs a blended combination of higher order central differencing and upwind differencing with built-in adaptive filter to automatically remove any non-physical spurious waves. The blended differencing preserve boundedness with reasonable accuracy as,

$$\varphi_f = \gamma(\varphi_f)_{CD} + (1-\gamma)(\varphi_f)_{UD} \quad \text{... (4.29)}$$

Where γ is blending co-efficient chosen for specific kind of differencing which forms different schemes with different filters.

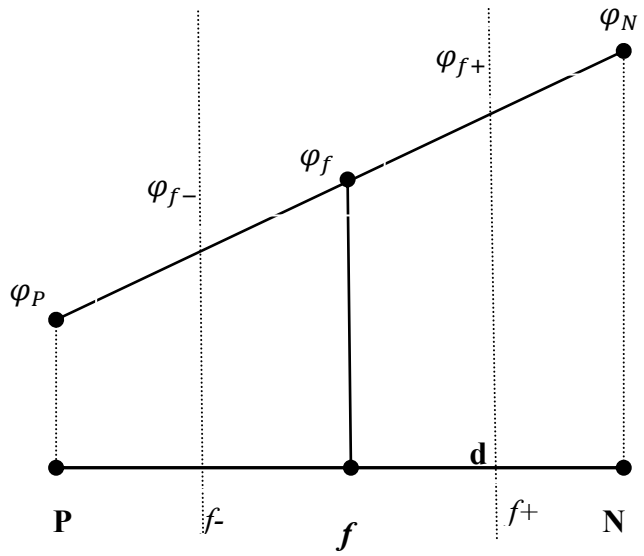

Figure 4.3: *Face interpolation in central differencing scheme.*

A NVD method proposed by Jasak *et al.*(Jasak, Weller et al. 1999) has modified general NVD scheme by changing normalised variables in terms of gradients of the dependent variable to make

it work for unstructured meshes with no increase in computational cost. Face flux can be obtained as follows,

$$\widetilde{\varphi_C} = 1 - \frac{\varphi_D - \varphi_C}{2(\nabla\varphi)_C.d} \quad \text{... (4.30a)}$$

$$\varphi_f = (1 - \gamma(1 - f_x))\varphi_C + \gamma(1 - f_x)\varphi_D \quad \text{... (4.30b)}$$

The blending function γ is calculated according to the local value of $\widetilde{\varphi_C}$ and scheme constant β. Larger the value of β, larger the blending in the scheme and therefore lower value of blending function should be used for higher resolution. Two additional faces are introduced midway between face and other points two obtain local information in this method, as shown in Figure 4.3.

Temporal discretisation: The temporal derivative and integration of the generalised transport equations in time are considered next. First term in the Eq. (4.23) is the temporal discretisation term. The integral equation (4.23) is discretized using various schemes with different terms having different order of accuracies. However, as long as the individual order of accuracy of terms is second order or more, the overall accuracy of the scheme will be second order. Various temporal discretization schemes are available with different accuracies, like first-order Euler scheme, second-order backward scheme and second-order Crank-Nicholson scheme. Present work uses the Crank-Nicholson time scheme and is explained briefly.

Crank and Nicolson (Crank, Nicolson 1947) in his famous work presented temporally discretised numerical solution for approximation of diffusion equation (4.27a) as follows,

$$\frac{\partial\varphi}{\partial t} = \frac{\partial^2\varphi}{\partial x^2} \quad \text{... (4.31a)}$$

$$\left(\frac{\partial\varphi}{\partial t}\right)_j = \frac{\varphi_j^{n+1} - \varphi_j^n}{\Delta t}. \quad \text{... (4.31b)}$$

Keeping a time step of Δt and a spacing of h, the equation (4.27a) can be discretised and rearranged in θ-scheme as,

$$\left(1-\theta\Delta t h^{-2}\delta_j^2\right)\varphi_j^{n+1}=\left(1+(1-\theta)\Delta t h^{-2}\delta_j^2\right)\varphi_j^n \quad \text{... (4.32)}$$

Where $\theta = 1/2$. The eq. (4.27) with $\theta = 0$, corresponds to explicit Euler time-marching, while $\theta = 1$ corresponds to fully-implicit Euler time-marching scheme. An expression similar to Eq. (4.27) can be obtained by using the integral equation (4.23) instead of diffusion Eq. (4.26a). For $\theta > 0$, the scheme forms a tri-diagonal system of simultaneous equation which can efficiently be solved to obtain φ_j^{n+1}. The scheme is unconditionally stable for any value of $\theta \geq \frac{1}{2}$. One can choose to make Δt and h proportional along with second order accuracy this makes the scheme accurate and efficient. The typical problem of stiffness in solution of Navier-Stokes equations with higher resolution persists with this scheme too but a compromise between accuracy and boundedness can be achieved.

Boundary conditions: The working fluid in the study is air and ideal gas properties of air are assumed. The velocity inlet is a time varying single period sinusoid of certain frequency and its amplitude is 0.05 m/s. The velocity outlet is set to a non-reflective boundary condition explained in section 4.2(g) to avoid large velocity reflections from the outlet boundary. The pressure outlet is set to a constant total atmospheric pressure (Dirichlet boundary). The shear stresses due to viscous forces are addressed in the FV based compressible solver calculations and heat transfer at the walls of the model is neglected.

4.4 Acoustic CFD Simulation

The commonly used acoustic filters are *High-pass filter*, *Band-stop filter* and *Low-pass filters*. An acoustic high-pass filter can be constructed simply by inserting a short side branch into the pipe. This acoustic filter blocks the low frequency waves and let pass the high frequency waves. High-pass filter reflects back the energy trapped in the side branch back to the source and is not radiated out of the side branch. The other kind of filter is *band-stop filters*, which absorbs standing waves (or energy) in a band of frequency during one part of cycle and in the later part of the cycle, it returns that energy back to the pipe. The phase relationship is such that all the energy is returned back towards the source. Therefore these filters block any sound within a band around the resonance frequency, and let pass all other frequencies. The last type of acoustic filter named Low-pass filter can be constructed by inserting an expansion chamber in duct, for example, Simple Expansion Muffler. The simple expansion chambers allow passing low frequency waves and blocking high frequency waves. For numerous uses of simple expansion mufflers (low-pass filter) in exhaust silencers and air conditioning HVAC systems, a simple expansion muffler has been chosen for simulating a pulsating flow.

Various parameters have been defined for measurement of specific characteristic of acoustic filters. The difference between the acoustic power radiated without any filter (muffler) and power radiated with the filter (muffler) is called *Insertion loss*.

$$IL = 10log\frac{W_1}{W_2} \quad \text{... (4.33)}$$

Where W_1 is sound radiated without filter and W_2 is sound radiated with filter. The unit of *IL* is dB (decibel).

However the performance characteristic which is getting more favoured among researchers is Transmission loss because mostly researchers are interested in finding acoustic transmission behaviour of the elements. *Transmission loss* is defined as the difference between the sound power incident at the entry of the filter (or muffler) and the sound power transmitted after the filter and is represented as follows,

$$TL = 10log\frac{W_{inc}}{W_{tra}} = 20log\frac{P_{inc}}{P_{tra}} \quad \text{... (4.34)}$$

Where P_{inc} and P_{tra} are the amplitudes of incident and transmitted waves in the muffler and are proportional to the intensities W_{inc} and W_{tra} with the proportionality factor of $1/(2\rho c^2)$. Another important parameter in determining muffler performance is Back-pressure. The returned static pressure exerted by the muffler towards the inlet through restrictions in the flow is called *Back pressure*. The incident, transmitted, reflected or back pressures are depicted in the Figure 4.4. The attenuation in the muffler is achieved by the destructive interference of these incidents, transmitted and reflected waves in the expansion section and elsewhere.

The CFD model has long inlet and outlet (fourteen times the length of expansion section) to ensure sufficient amount of data to obtain reasonable results. It has been found by trial and error that to obtain a reasonable result, a minimum of fourteen reflections from the inside the expansion section has to be included in the time history of the monitoring points near outlet and therefore the length of the inlet and outlet pipe has to be fourteen time the length of the expansion section.

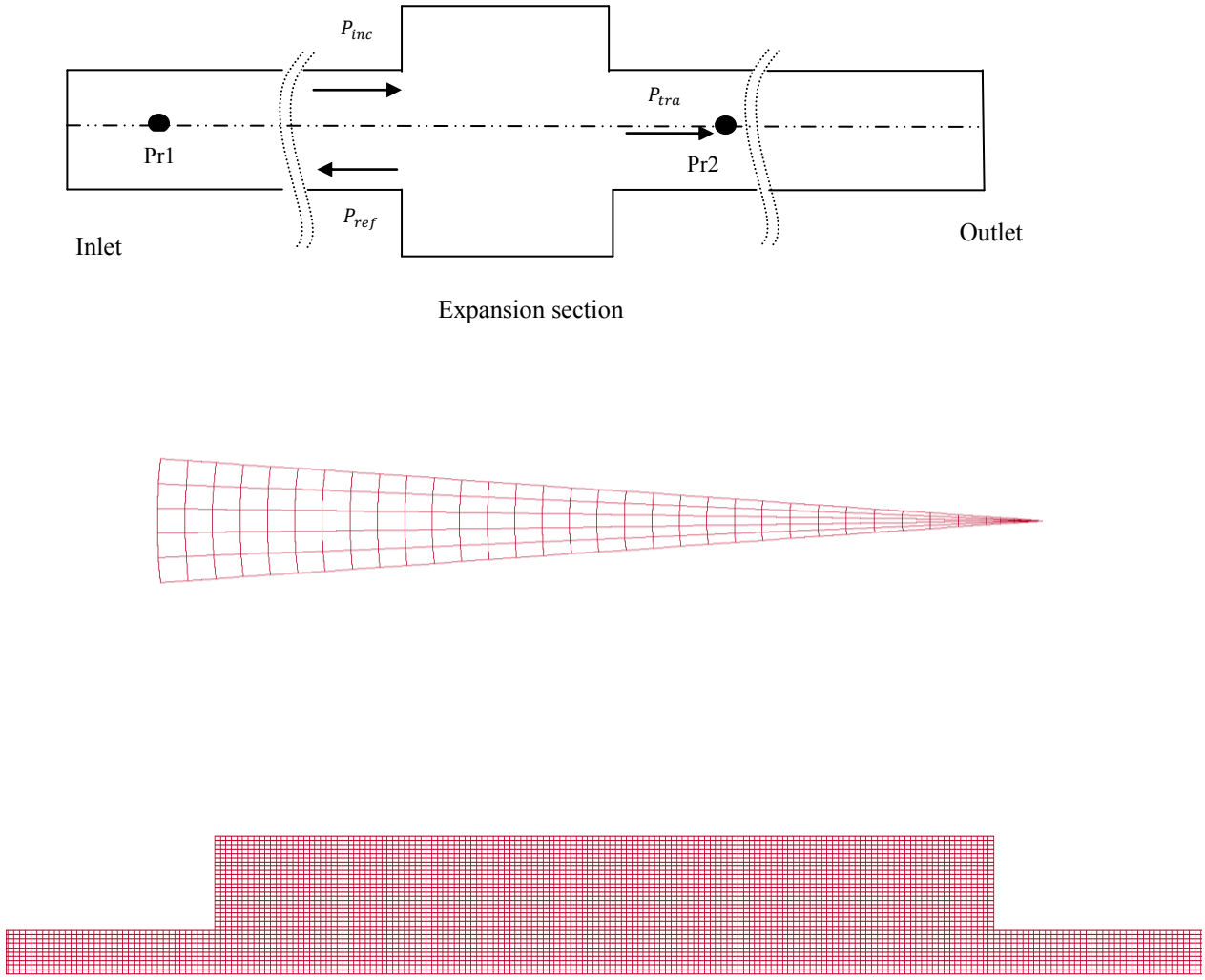

Figure 4.4: *Overview of Simple Expansion Muffler CFD model (top), Sector-mesh for simple expansion muffler: Side View (middle) and Front view (bottom).*

This also avoids the reflections from the walls and expansion sections to contaminate the monitoring data at probes Pr1 and Pr2, as shown in Figure 4.4. A mesh spacing of 4mm or smaller is adopted for most of simulations in this chapter. The simulation requires a time step of 5μs which equates to the sampling frequency of 200 kHz and Nyquist frequency of 100 kHz. The corresponding wavelength to Nyquist frequency is 3.4mm, which is shorter than the mesh spacing for this simulation and therefore solver will be unable to resolve frequencies above Nyquist frequency and aliasing would not be an issue.

4.4.1 Simple Expansion Muffler simulation without mean flow

At first, a simple expansion muffler is considered without any imposed mean flow at the inlet of muffler. The flow is considered laminar and no turbulence model is employed. Only a sinusoidal pulse is imposed at the inlet of muffler and it is allowed to propagate through the expansion section to determine transmission loss. The mesh independence study for a simple expansion muffler is already presented in chapter 2. The simulation performed in chapter 2 is further verified in this section by employing various spatial and temporal discretization schemes. Thereafter, verification of the proposed muffler configuration is done to estimate transmission losses.

Various spatial discretization schemes explained in section 4.3 are employed and their transmission losses are Fourier transformed. The comparative FFT plots for these simulations are presented in Figure 4.5. Although a good agreement can be seen in these simulations, this must be brought to notice that finite volume acoustic simulation is vulnerable to spatial discretization error in higher frequency ranges, as shown in Figure 4.6. The Figure 2.3 (b) is produced in the frequency range of interest 0-3000Hz, whereas Figure 4.6 is produced for much higher frequency range. It can easily be observed that 4mm mesh provides a very good agreement in the range of 0-3000 Hz,

but considerably differs from 1mm and 2mm meshes in the range of 3000-6000Hz. A good agreement between 1mm and 2mm shows that discretization errors are very low for these mesh spacing.

Various temporal schemes like first order Euler scheme, second order backward scheme and second order Crank Nicholson scheme are employed to investigate the propagation of sinusoidal pulse in simple expansion muffler. It has been found that Euler scheme not being stiff captures the propagation of sinusoidal pulse in a straight pipe with no difficulty but with an expansion in the middle (simple expansion muffler); it struggles to capture the higher frequency on the FFT spectrum, as shown in Figure 4.7. Second order backward scheme provides better accuracy in the frequency spectrum and successfully captures higher frequency part of the spectrum.

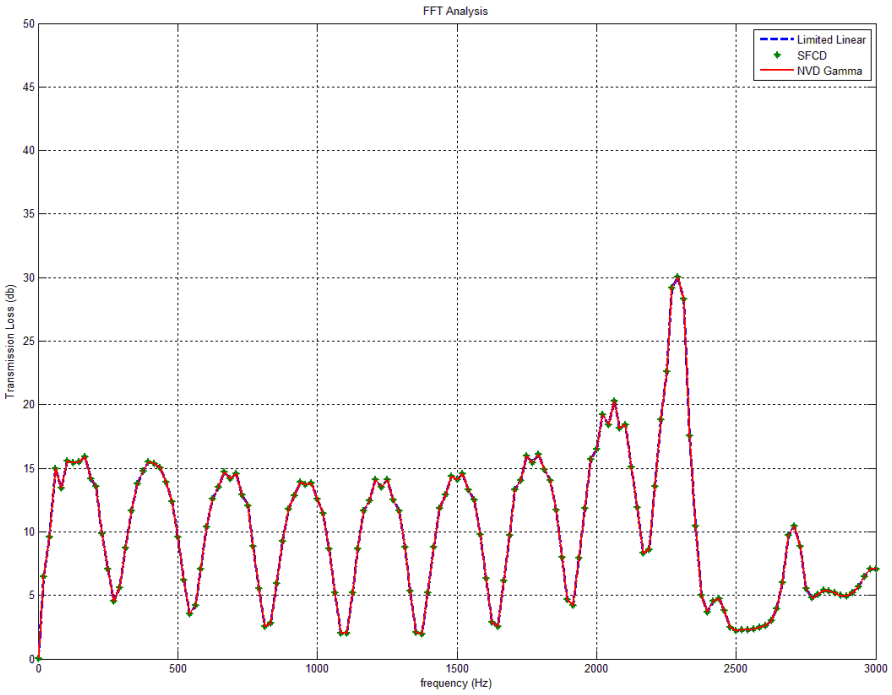

***Figure 4.5**: Comparison of various spatial discretizations for muffler simulation.*

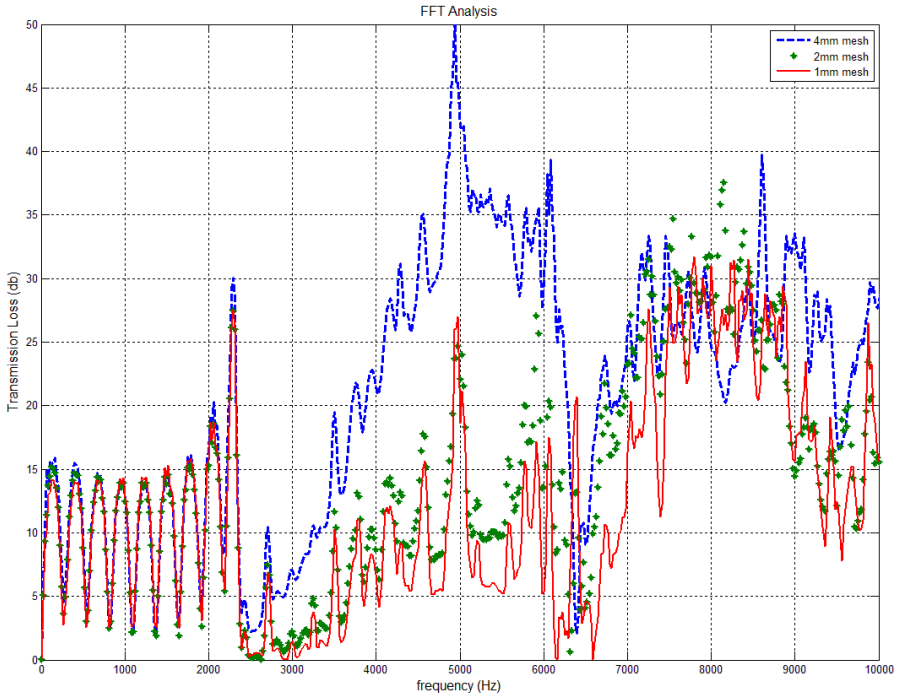

***Figure 4.6**: FFT spectrum of figure 2.3 in an extended frequency range.*

However backward scheme is found to be stiff and could be a problem for the stability of the solver. A better compromise seems to be crank Nicholson scheme which provides compromise between stiffness and accuracy with different θ values and is found to be unconditionally stable for $\theta > 0.5$. Comparison of FFT spectrum with various θ values is provided in Figure 4.8.

Geometric configurations: There have been various analytical studies to model transmission loss (TL) of simple expansion muffler. Wilson (Wilson 1994) proposed the following relation for calculation of transmission loss:

$$TL = 10 \log\left[1 + \frac{1}{4}\left(m + \frac{1}{m}\right)^2 \sin^2 KL\right] \quad \ldots. (4.35)$$

Where $K=2\pi/\lambda$, *and* $m= (d_e/d_i)$.

Transmission loss for simple expansion mufflers of varying inner and outer diameters can be obtained using Eq. (4.35) as shown in figure 4.9. Similarly, transmission loss for varying length of expansion section can be obtained as shown in figure 4.10. Simulation is also carried out to match the trend in transmission loss for varying expansion diameters and expansion length as shown in figure 4.11 and 4.12. The trend in transmission loss of simulated results considerably matches the analytical results, which verifies the new proposed compressible solver for acoustic simulations. Considering the robustness and effectiveness of the finite difference central schemes, the central scheme based finite difference solver of Kurganov and Tadmor (explained in section 2.2.3) is also tested for acoustic propagation of sinusoidal pulse.

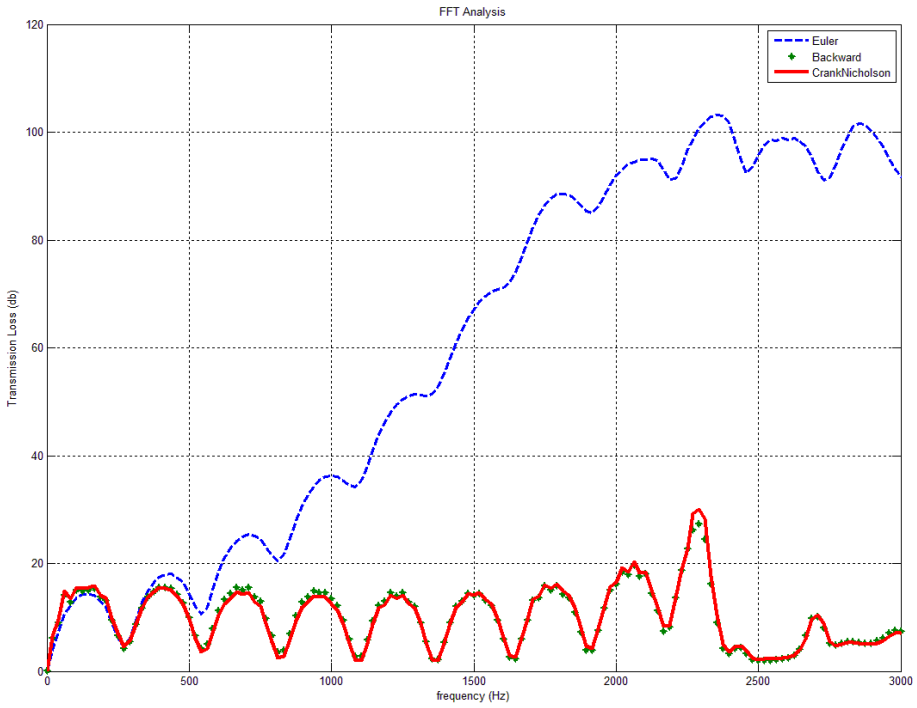

***Figure 4.7**: FFT spectrum analysis for different temporal discretization schemes.*

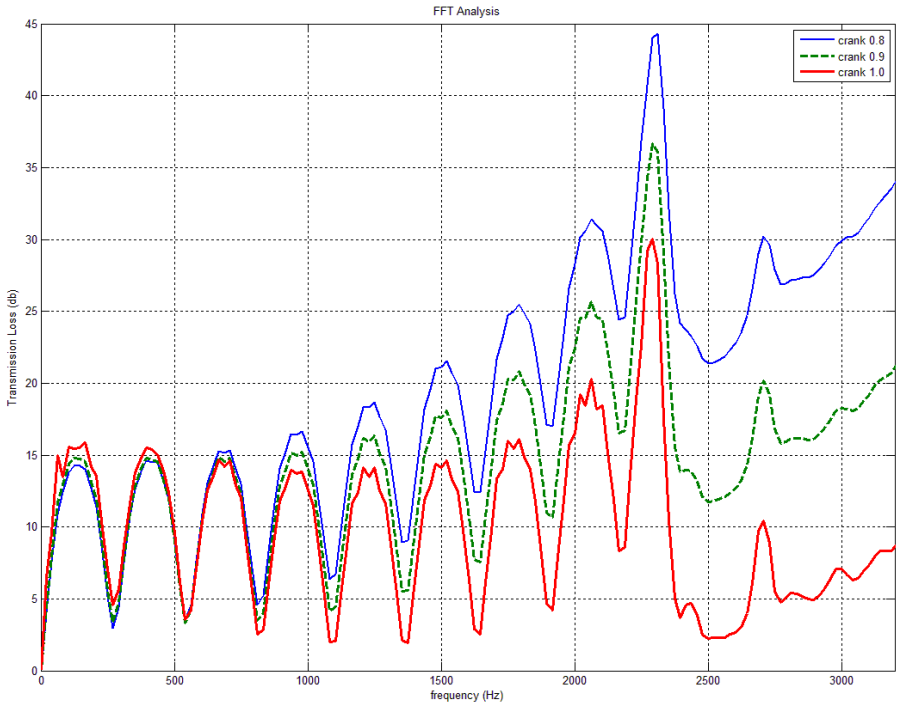

***Figure 4.8**: FFT spectrum for crank Nicholson scheme with different θ values.*

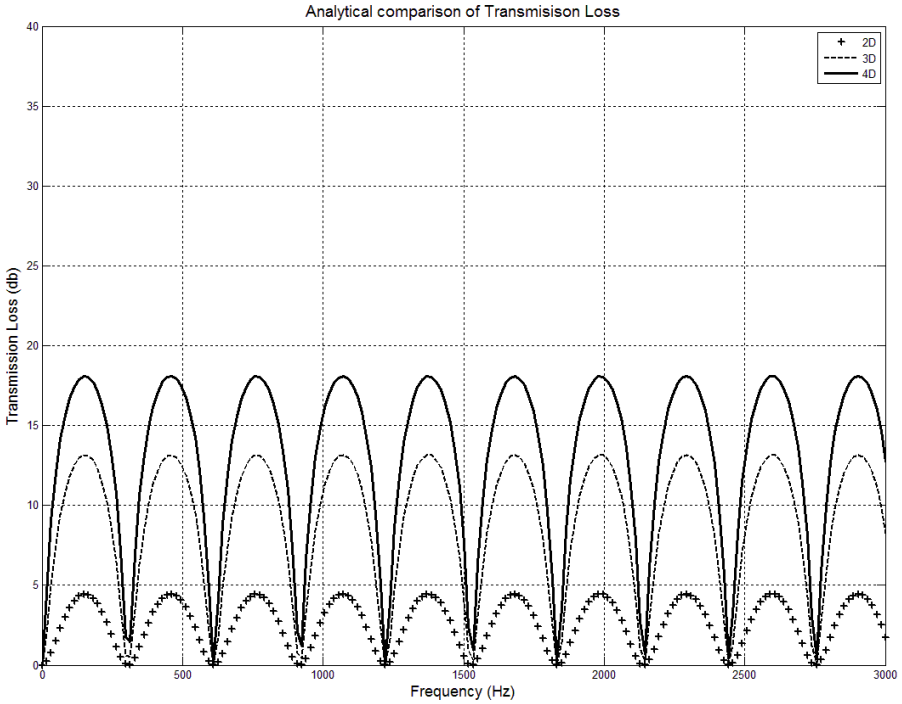

***Figure 4.9**: Comparison of analytical transmission loss for different expansion diameters.*

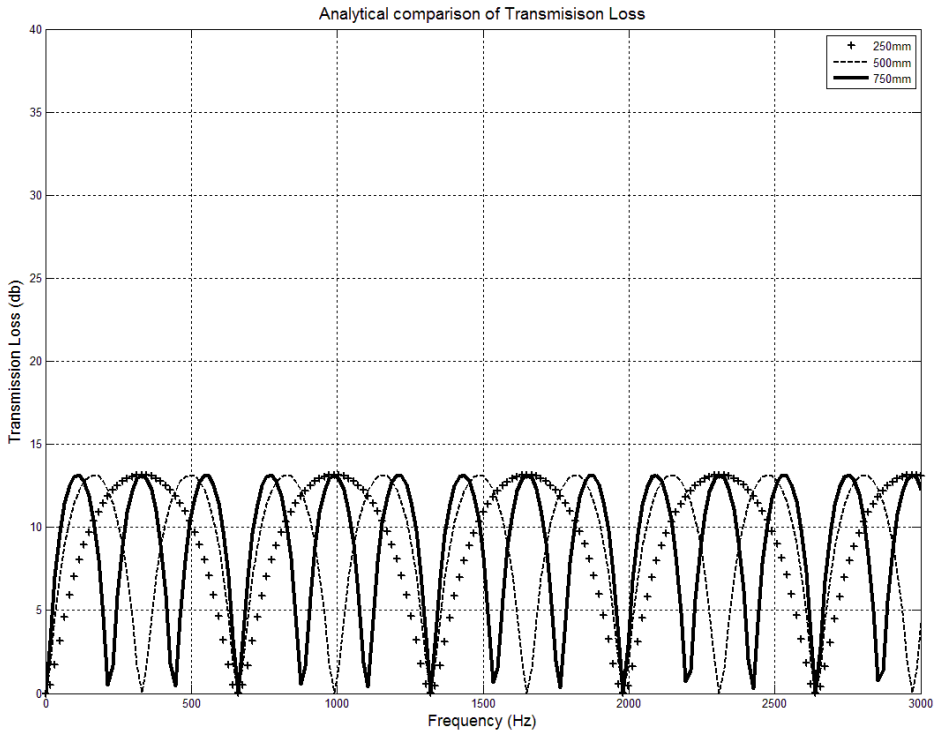

***Figure 4.10**: Comparison of analytical transmission loss for different expansion lengths.*

The result presented in figure 4.13 clearly shows that despite being robust and effective in capturing frequency attenuations, their performance in acoustic propagation is still hardly comparable to the proposed finite volume based Karki-PISO solver for low Mach number flow simulations. Besides, the finite difference based methods are computationally very expensive for its dependence on CFL condition and therefore are ignored in later part of the work. Further, analysis of the simple expansion muffler with $\frac{d_e}{d_i} = 3$, is performed by subjecting the muffler to sinusoidal pulses of different frequencies, extending from lower (200Hz to 500Hz) to the higher ranges (1000Hz to 3000Hz).

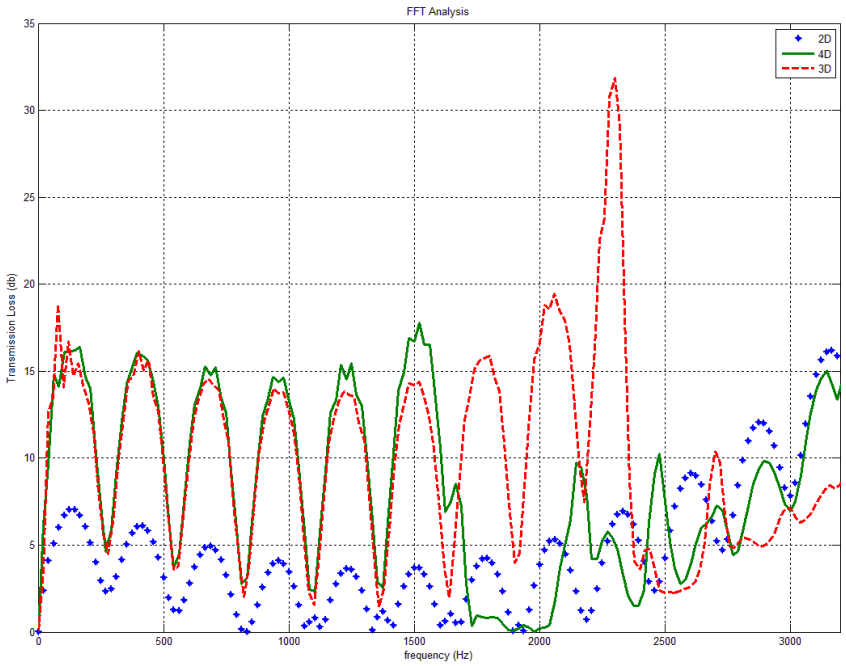

***Figure 4.11**: Comparison of transmission loss in a compressible simulation for different expansion chamber diameters.*

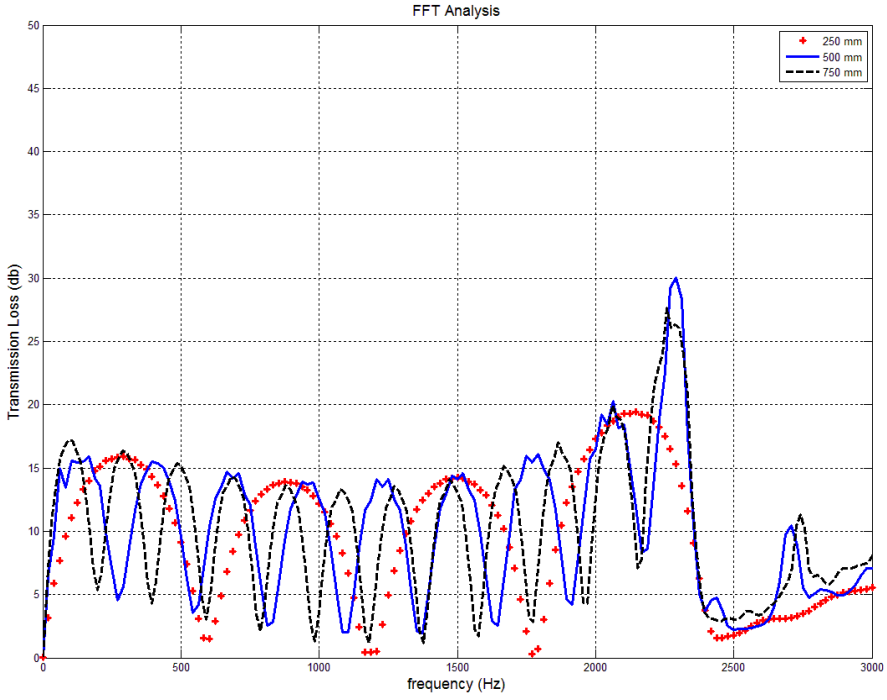

***Figure 4.12**: Comparison of transmission loss for different chamber length.*

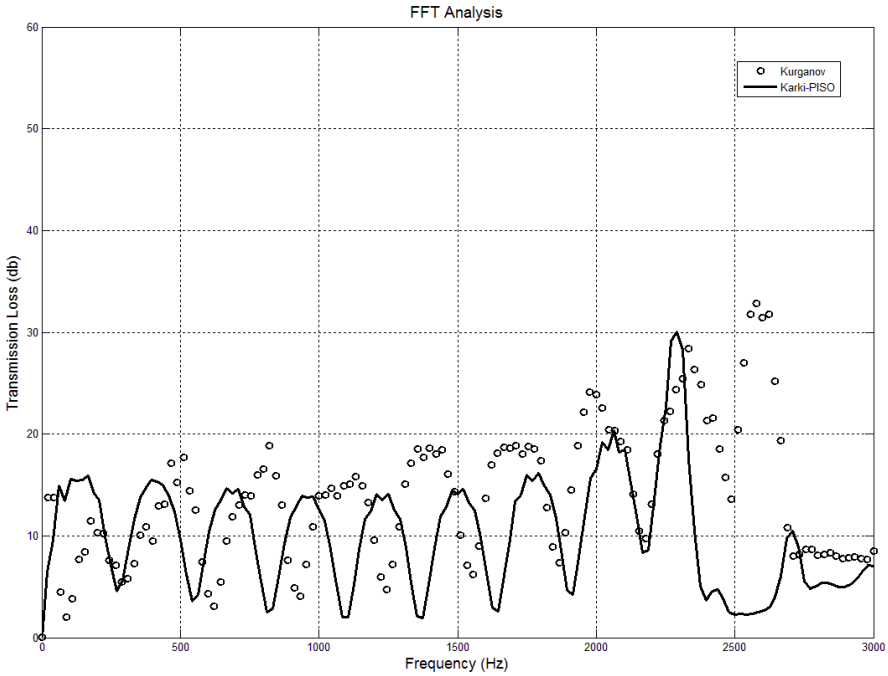

***Figure 4.13**: Comparison of FFT analysis of pressure based Karki-PISO and finite difference based Kurganov & Tadmor simulations.*

Figure 4.14 and Figure 4.15 present the transmitted pulse for lower and higher frequency ranges. A clear development of higher frequency small perturbations can be seen developing for 500Hz frequency in figure 4.14, which further develops in magnitude and oscillation for higher frequency ranges, as shown in figure 4.15. Figure 4.16 and figure 4.17 shows the FFT plot of transmission loss across the muffler. Apart from the abrupt attenuation for 500Hz frequency, the transmission loss spectrum resolves all the relevant scales in the expansion muffler in the desired frequency range.

The frequency analysis of simple expansion muffler shows attenuation due to viscous forces present in muffler flow simulation and when flow is assumed to be laminar. The laminar assumption might not be true for all practical applications but the simulation provides a very interesting set of characteristic of pulse propagation in muffler encompassing effects of important

viscous forces in the muffler. There is no model employed for modelling turbulence in the computational domain. However, to investigate the effect of turbulence on mean flow, there is a requirement of a turbulence model to model length scales of flow and the statistics attached to it. Once an effective turbulence model is employed for the simulation, there can be a detailed investigation of the effects of turbulence on mean flow and acoustic propagation of sound in that flow field has to be considered.

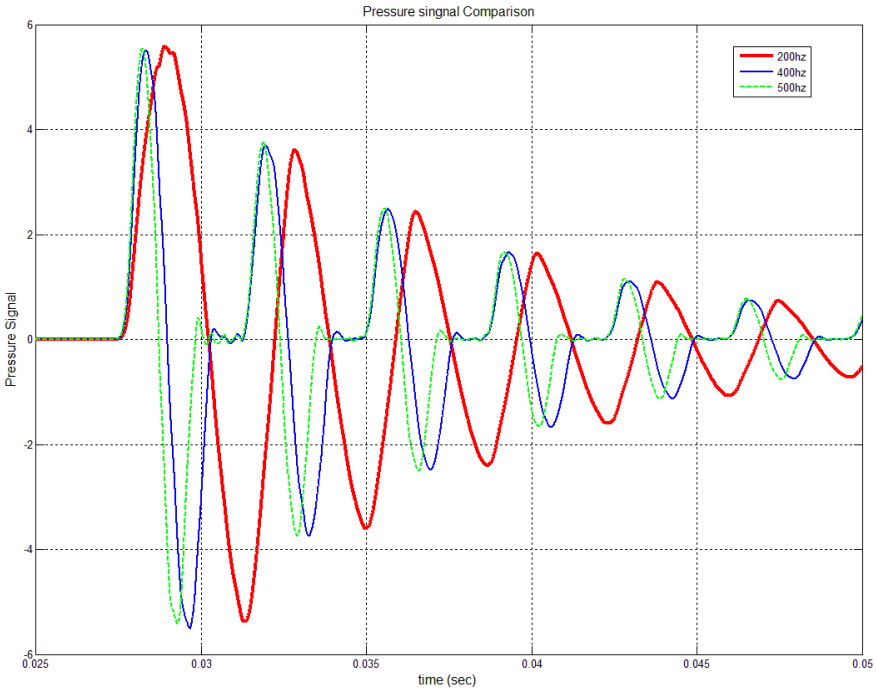

***Figure 4.14**: Transmission pulse through muffler across lower frequency range.*

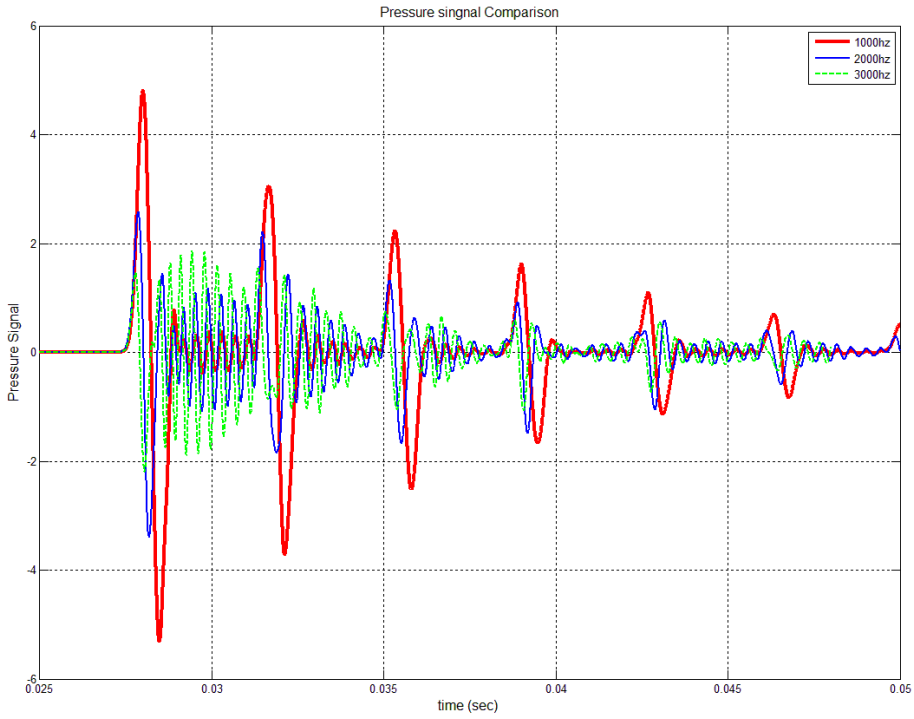

***Figure 4.15**: Transmission pulse through muffler across higher frequency range.*

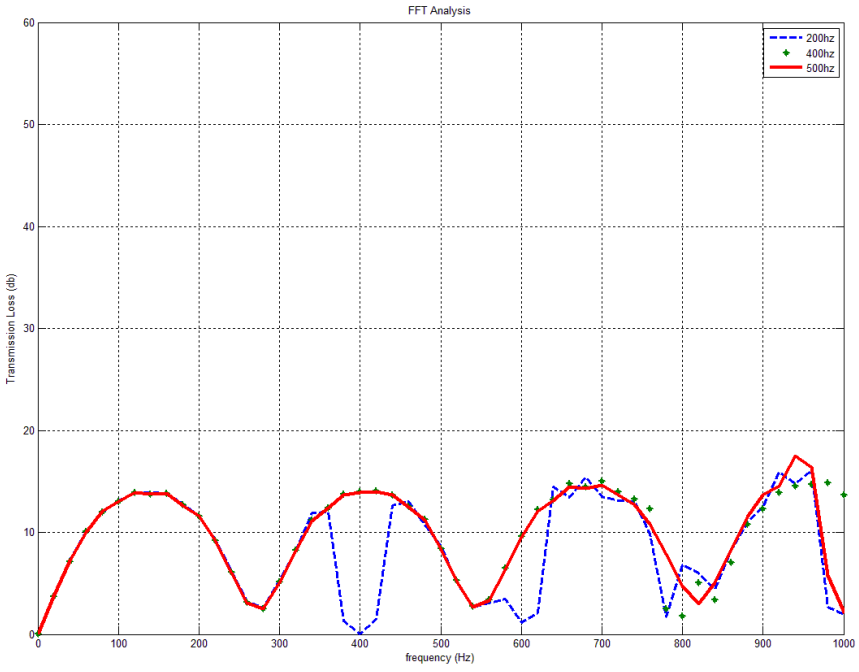

***Figure 4.16**: Transmission loss in expansion muffler across lower frequency range.*

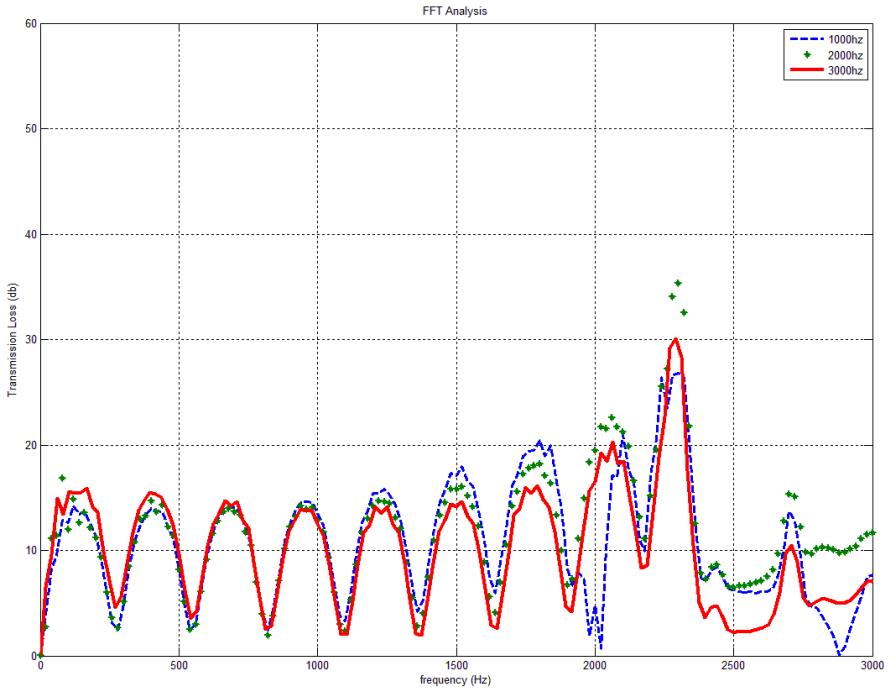

***Figure 4.17**: Transmission loss in expansion muffler across higher frequency range.*

4.4.2 Simulation with Mean Flow

Simulation of acoustic propagation in a turbulent fluid flow is considered to be computationally challenging and complicated in nature. The finite volume methods have certain restrictions in terms of higher stiffness of the Navier-Stokes equations in low Mach number flow simulations. The other issue involved in simulating acoustic problem is related to the length scales of the flow quantities. The smaller length scales involved in these simulations make it further challenging. Some of the challenges involved with mean flow acoustic simulations have also been mentioned in the section 4.2. In the present work, acoustic simulation of a simple circular pipe is made to first check the acoustic propagation capability of the current compressible solver. Later, a two-dimensional simulation of simple expansion muffler is carried out to simulate pulse

propagation through the muffler. For RANS and LES simulations, standard $k-\varepsilon$ turbulence model have been used through out this work to simulate acoustic devices.

4.4.2.1 Simulation of Circular Pipe

Circular pipe is one of the most common elements in the acoustic devices. A mean flow of 10 m/s is obtained in the circular pipe. Once a mean flow profile is achieved with satisfactory statistics, a sinusoidal pulse is forced at the inlet of the pipe. The Karki-PISO solver shows robust performance in the simulation of the forced pulse propagation through pipe and works very well even with the first order temporal discretization. A second order Crank-Nicholson temporal discretization is however adopted for better resolution of the acoustic and flow parameters. A much finer mesh of 2mm has to be adopted considering the circular edges which could either overstretch or narrowed in the computational domain. This mesh seems to resolve the mesh well with the second order limited linear spatial discretization. Figure 4.18 displays the contour of acoustic-pressure, which is the difference of mean and instantaneous pressure profiles, showing sinusoidal pulse propagation through circular pipe. In order to obtain a transmission pulse spectrum and transmission loss spectrum, two probe points near the inlet and near the outlet are chosen and pressure data are recorded at those locations. The transmission pressure pulse and transmission loss are plotted on the frequency spectrum as shown in figure 4.19 (a) and 4.19 (b). The transmission pressure spectrum shows the presence of pressure pulse around the range of 2000-3000 Hz. This can be because of the numerical dispersion of the 3000Hz pulse while it transverse through the pipe.

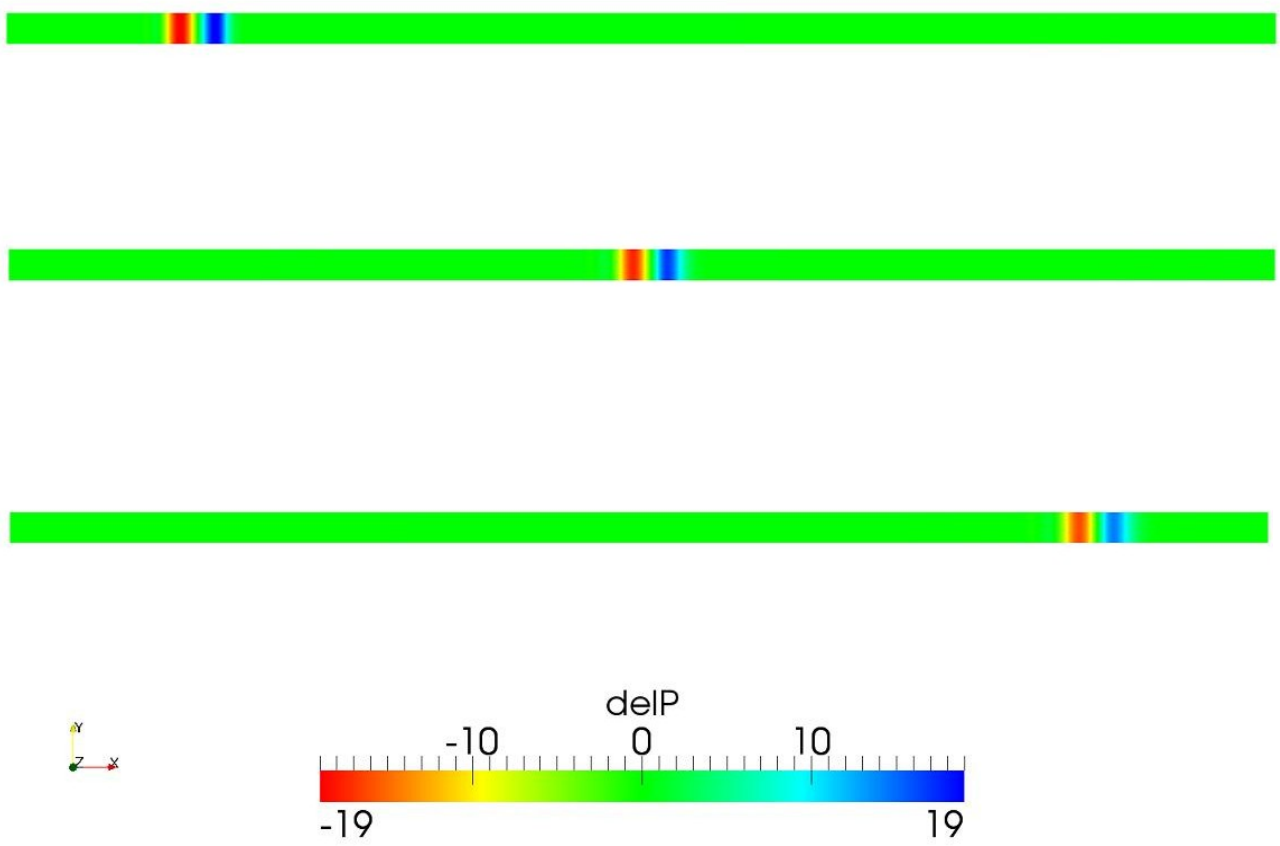

Figure 4.18: *Contour plot of acoustic-pressure (ΔP) showing pulse propagation through the circular pipe.*

The transmission loss in the figure 4.19 (b) shows a peak near the low frequency, which is most likely because of the resolution of large scale of turbulence by the turbulence model. The high peaks at lower frequencies are also congruent with small amplitude pressure signal variations in the transmission pulse spectrum of figure 4.19(a). Another small peak is observed at the frequency of 500 Hz which could be the result of resonance generated in the open pipe. The transmission loss increases linearly thereafter showing that there is transmission loss throughout the higher frequency domain. This transmission loss results from the numerical limitation of the RANS simulation, as it uses the averaging of flow variables inside the computational domain. Any

realistic pressure attenuation in the higher frequency domain would be superimposed by these numerical transmission losses arising from the RANS averaging of flow fields.

4.4.2.2 Simulation of Simple Expansion Muffler

Simple expansion muffler is somewhat different in design and is a bit more complicated in comparison to the simple duct or pipe. The expansion chamber in the middle of the design provides the flow separation which leads to pressure and velocity fluctuations in the chamber. The destructive interference of muffler acoustics makes muffler an important sound- attenuation device. Simple expansion muffler has been studied in the section 4.4.1 for simulations without any mean flow, considering flow to be linear. Now, a mean flow RANS simulation is conducted using standard $k - \varepsilon$ turbulence model to capture length scales of flow and acoustics. A two-dimensional simulation is conducted for a 10 m/s mean flow using Karki-PISO compressible solver with 5 degree mesh of 4mm mesh spacing. The same simulation is then performed using a 3D mesh with same 4mm mesh spacing.

(a)

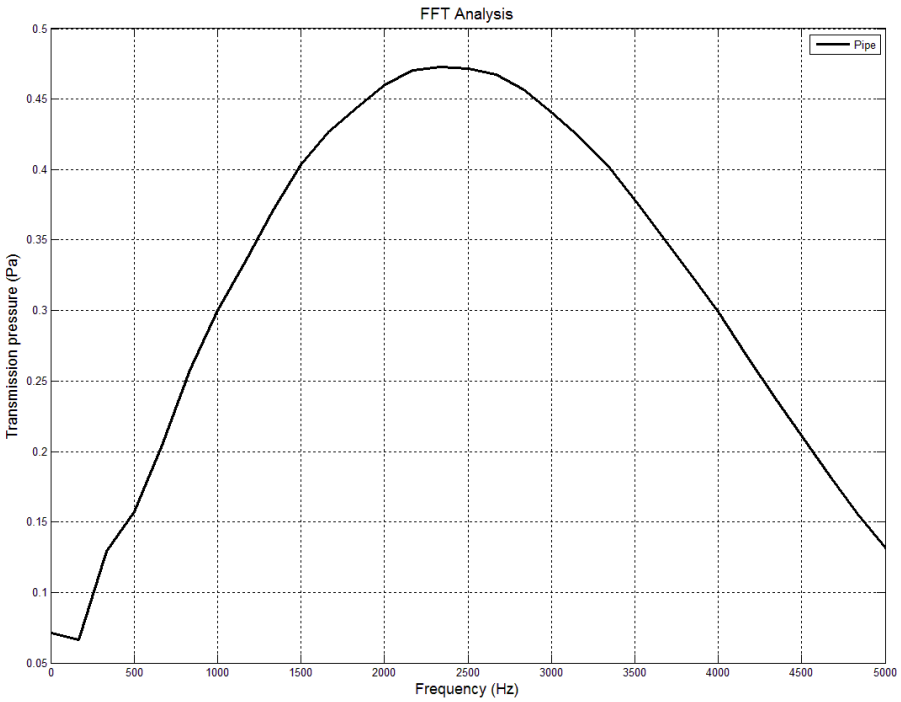

(b)

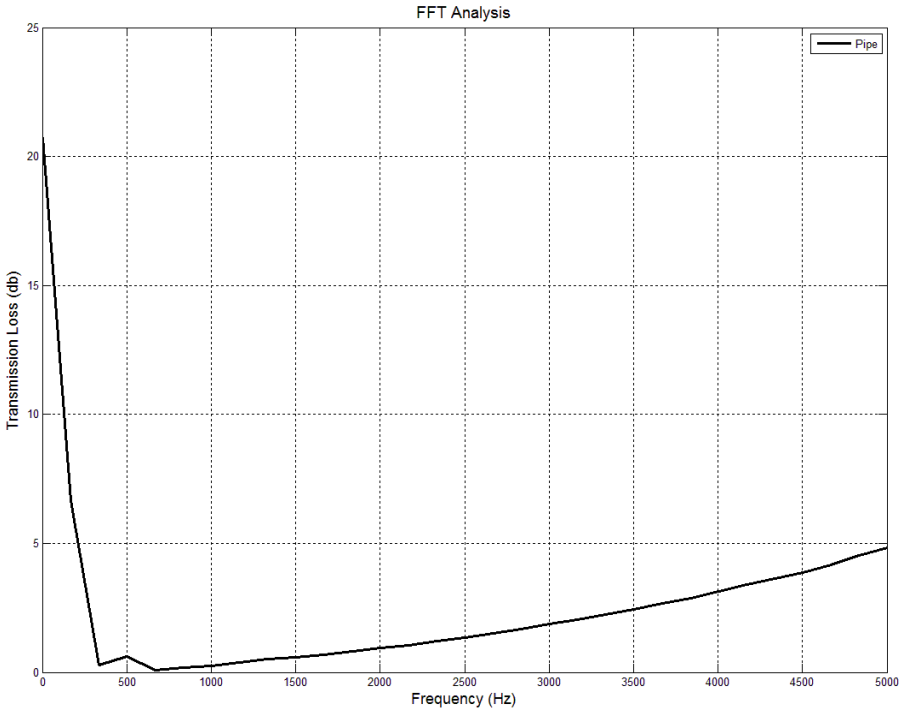

Figure 4.19: ***(a)*** *Transmission pulse spectrum for pulse propagation in circular pipe.* ***(b)*** *Transmission loss spectrum for pulse propagation in circular pipe.*

The large inlet and outlet make the 3D simulation computationally very expensive but the three dimensional simulation provides a good validation for Karki-PISO compressible solver and is generally able to capture more scales and avoid singularity in the solution domain which could arise from the 5 degree mesh.

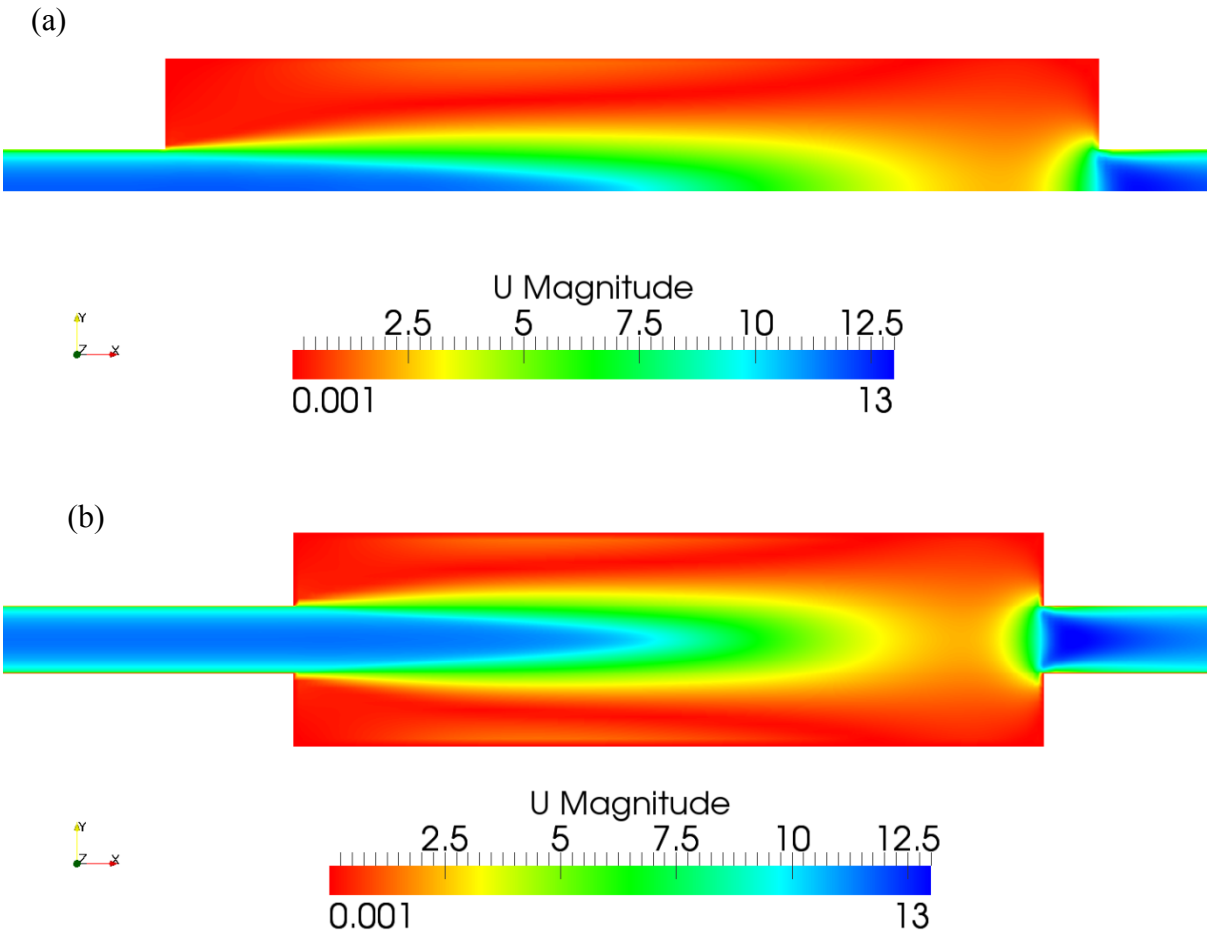

Figure 4.20: *Velocity Contour* ***(a)*** *5^0sector RANS of muffler.* ***(b)*** *3D RANS of muffler.*

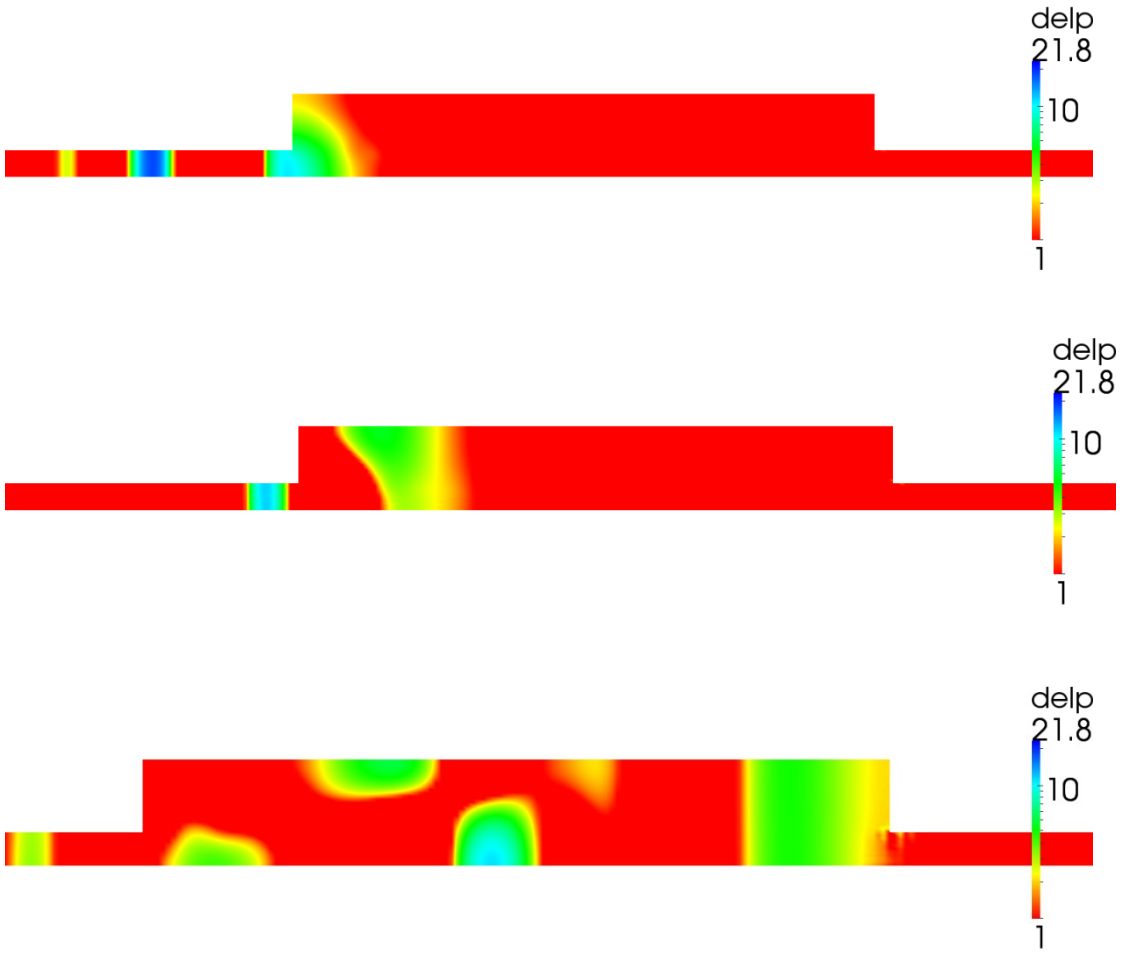

Figure 4.21: *Acoustic-pressure contours showing sinusoidal pulse propagation through the muffler, entering into expansion chamber and creating back-pressure in the inlet pipe (top), travelling inside the chamber (middle) and hitting the rear tailpipe end (bottom).*

A mean flow profile is first obtained for both 2D and 3D meshes and the velocity profile for both cases are shown in figure 4.20 (a) and (b). The mean velocity profile clearly shows the change in Mach number across the length and width of the expansion muffler. The Mach number start to increase near the tailpipe end of the muffler and a great amount of turbulent kinetic energy exchange takes place there.

On top of the mean flow profile, a pure sinusoidal velocity pulse of 3200 Hz is imposed at the inlet of the muffler to simulate the acoustic propagation of pulse through the muffler.

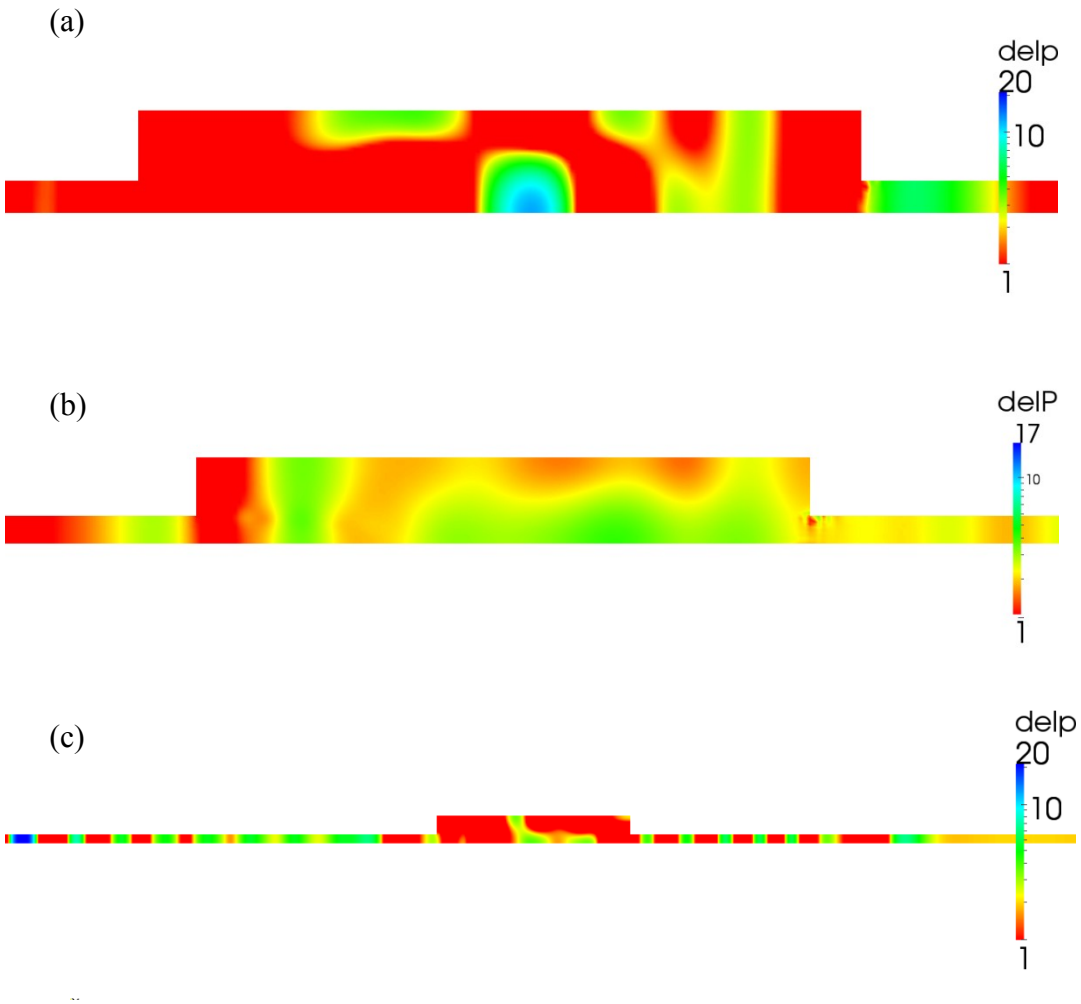

Figure 4.22: *Sinusoidal pulse reflects back from the tailpipe end of the expansion chamber,* **(a)** *Part of the pulse reflect back and part of it transmit through tailpipe,* **(b)** *reflected pulse reaches to the front end of the expansion, where it again get reflected.* **(c)** *After several reflections from inside the expansion, the contour shows the back-pressure and transmitted pulse.*

The pulse propagation can be seen inside the expansion chamber in figure 4.21, where the contour plot of difference between the instantaneous pressure and mean pressure is shown. This

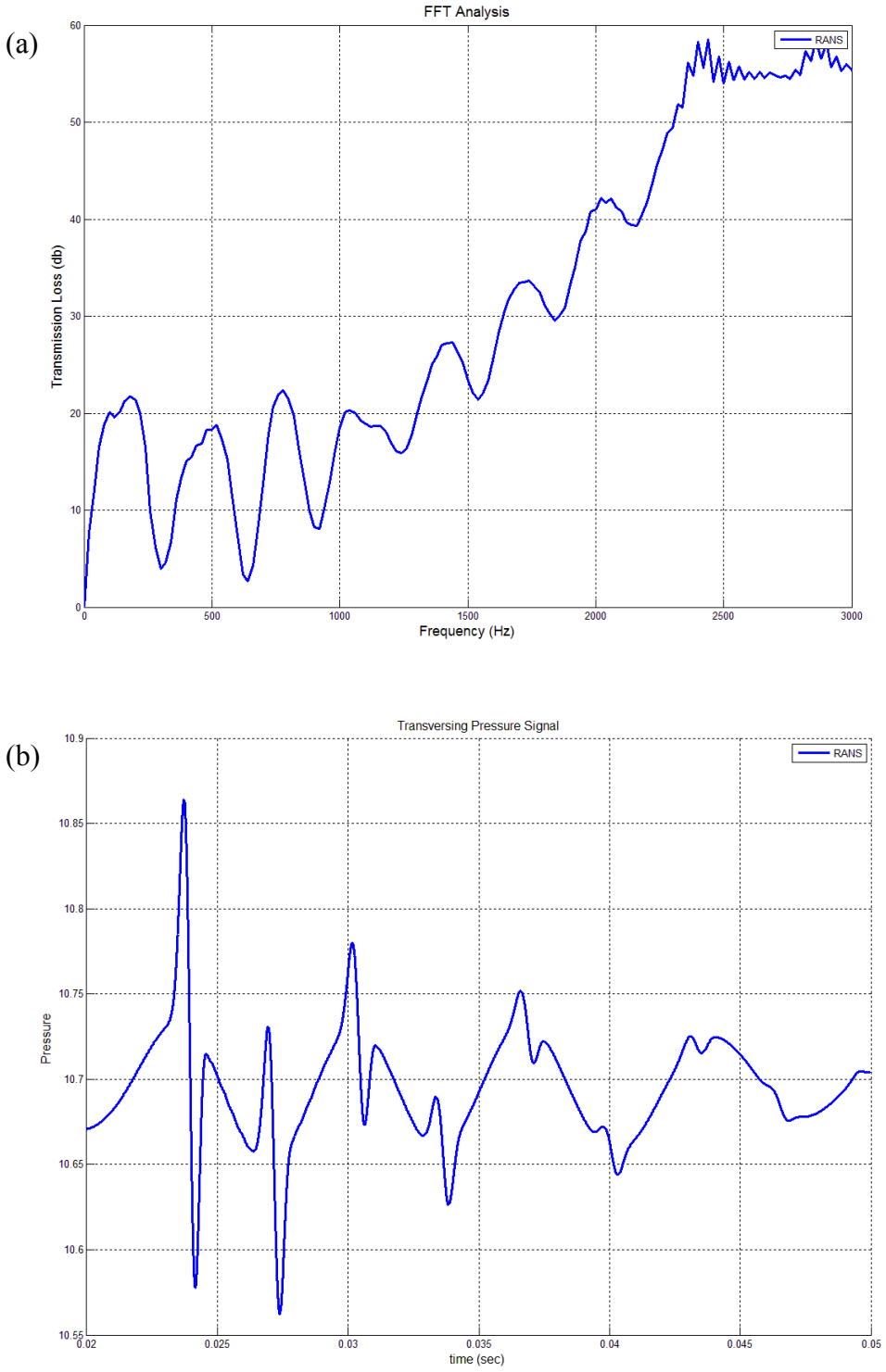

Figure 4.23: (a) *Transmission pressure pulse for pulse propagation in expansion muffler.* ***(b)*** *Transmission loss spectrum for pulse propagation in expansion muffler.*

acoustic-pressure (ΔP) contour shows in figure 4.21 that the pulse enters the chamber and creates a back pressure in the inlet section of the muffler. The pulse then travels across the length of muffler to hit the tailpipe end of the muffler, where it loses its turbulent kinetic energy to the wall. Figure 4.22 shows the pulse reflection at the tailpipe end, where part of pulse is transmit through the tailpipe.

The transmitted pressure waves from the expansion chamber are recorded at a point just after the expansion. The second probe is kept near the inlet to record the pressure waves. These recorded pressure data are Fourier transformed to obtain transmission pressure pulse and transmission loss spectrum as shown in figure 4.23 (a) and 4.23 (b). The transmission loss spectrum shows reasonable attenuation at lower frequency range. The transmission pressure plot also captures the large peaks in the spectrum which corresponds to the lower frequency signals. If a comparison of transmission pressure pulse is made with the laminar case in figure 4.15, it is evident that the high frequency component of the pulse is either lost with the mean flow interactions or gets averaged by the numerical method. So, although numerical method captures all the attenuation peaks in the simulation, there seems to be a trend of increasing attenuation for higher frequency range, which could be either due to discretization error in the numerical method or the dissipation and turbulence modelling error. (Discussed in section 4.2) Despite these slight discrepancies due to numerical averaging in RANS methods, the method provides reasonable agreement in the lower frequency range and also predicts the attenuation frequency at correct level. The averaging in RANS methods method further restrict the scope of the work and is found to be limited to lower frequency analysis.

4.5 Closure

This chapter has further validated low Mach compressible Karki-PISO solver for acoustic propagation. Chapter also outlines various computational issues related to simulation of acoustic propagation. A laminar compressible solver with no flow and a RANS turbulent compressible solver with mean flow, both provide encouraging results for pulse propagation through pipe and simple expansion muffler. The disappearance of some high acoustic frequencies from the computational domain in RANS simulation is also noted to limit the applicability of RANS in acoustic simulations. The detailed study of various spatial and temporal discretization points to some compromise between stability and accuracy by introducing blended discretization methods. Simulation of pulses with different frequencies has also provided some interesting results which would be further discussed in subsequent chapters.

Chapter 5

Numerical and Experimental Investigation of Pulse through Muffler

5.1 Introduction

This chapter introduces experimental and numerical analysis of acoustic propagation in simple expansion muffler in different flow circumstances. The analysis is sub-divided into two parts, one with no considerable mean flow and another with different amounts of mean flows. The chapter also validates the Karki-PISO compressible solver introduced in Chapter 2 for no-flow condition with various random frequency pulses generated in experiment by a signal generator as input signals. A detailed analysis of the recorded pulse is performed, which includes the FFT analysis.

The importance of mufflers in various HVAC and acoustic devices has already been discussed. Mufflers work on the principle of acoustic cancellation of sound waves which reduces the noise radiated by the device to the surroundings. Expansion muffler performance can be evaluated based on insertion loss, transmission loss and back pressure for its optimal design. In general, an exhaust muffler should satisfy basic design requirements such as adequate insertion/transmission loss, low back pressure, modest size and durability. Although insertion loss is the true measure of the muffler performance, as it accounts for losses in radiated power due to insertion of the muffler, transmission loss is favoured by researchers as they are interested in finding acoustic transmission behaviour of the elements rather than absolute attenuation. Most conventional mufflers are round

or oval with an inlet and outlet pipe attached and some mufflers also contain partitions (or baffles) or an extended inlet/outlet to help reduce noise.

Measurements are required to supplement the analysis with known parameters and necessary data from the experimental setup. Measurement of transmission loss is not very difficult and one has to only record sound at two discrete points across the muffler element under investigation. Even though measurements for sound propagation in a muffler without mean flow is very straight-forward, the introduction of mean flow introduces some complications. There is a need for an accurate measurement of dissipation of acoustic energy emerging from the tail pipe end in the shear layer of mean flow and finally the measurement of accurate transmission loss of muffler as required for design specifications. The experimental setup requires alteration for the flow to be incorporated into the experiment, as shown in Figure 5.1. However, this setup makes it difficult to obtain a pure sine pulse and therefore a random pulse of mixed frequencies is considered in this thesis. Different measurement techniques are available for acoustic measurement and only relevant measurement techniques for measuring acoustic parameters are listed here; details of these techniques can be found elsewhere. (Munjal 1987)

The Two-microphone method is one of the most widely used experimental methods so far. The method uses two microphones located at fixed positions to record signals. A random noise generator creates the required signal which is passed through a filter so as to retain only the desired frequency range and which then is power amplified before being fed to an acoustic driver, which creates an acoustic pressure field on a moving medium in the transmission tube. This input signal is picked up by microphone and preamplifier amplifies the signal before feeding it to the FFT analyser (See Figure 5.1) (Selamet, Radavich 1997). This method, however, requires an anechoic termination for reflections not to interfere with the transmitted waves. The method also needs to

feed a continuous signal for attenuation study. The reflection co-efficient of the termination can also be calculated according to this theory. Subsequently, it is found that it is very difficult to obtain a perfectly non-reflecting anechoic termination for acoustic propagation study. Besides, the investigation of propagation of sound in this chapter is aimed at pulse propagation rather than continuous sinusoidal wave. For these reasons, the two-microphone method has not been used in this experimental study and rather a somewhat different setup is constructed for this pulse propagation study without an anechoic termination. The setup uses long inlet and outlet pipes to record sufficient acoustic data before reflection reaches the microphone. The long inlet and outlet pipes ensure that most of the reflections from the expansion chamber can be recorded without interference from the reflections generated at the outlet and inlet. If a smaller outlet pipe were used, it is quite possible that all the reflections from expansion chamber might not be recorded before reflections from the outlet reaches the recording point and therefore unrealistic attenuation might be registered. In case of anechoic termination, it is possible that the low amplitude reflections from the anechoic termination might add to the recorded data and show no attenuation at all where there is indeed some real attenuation.

In the present work, a detailed analysis of frequency responses in a simple expansion muffler for random pulses at various generator frequencies is made in the presence or absence of mean flow. In the case of acoustic simulation without mean flow, numerical validations are also made using a hybrid Karki-PISO compressible solver. Experimental pulses are imposed at the inlet of the muffler and their responses are recorded at designated locations in the muffler for a detailed spectral analysis. The same experimental frequency pulse generated by the signal generator is then fed to the computational inlet of a simple expansion muffler to obtain the simulated response from the compressible Karki-PISO solver. The recorded experimental and computational responses for

the simple expansion muffler are then compared on the frequency spectrum to analyse the attenuation across the frequency range. The study is conducted on a simple expansion muffler with d_e/d_i ratio of 4 with long inlet and outlet pipes attached to it. The experimental study in the presence of mean flow provides a set of benchmark acoustic response data for acoustic simulation without any anechoic termination in the simple expansion muffler. Conclusions are finally drawn based on the observation and obtained results.

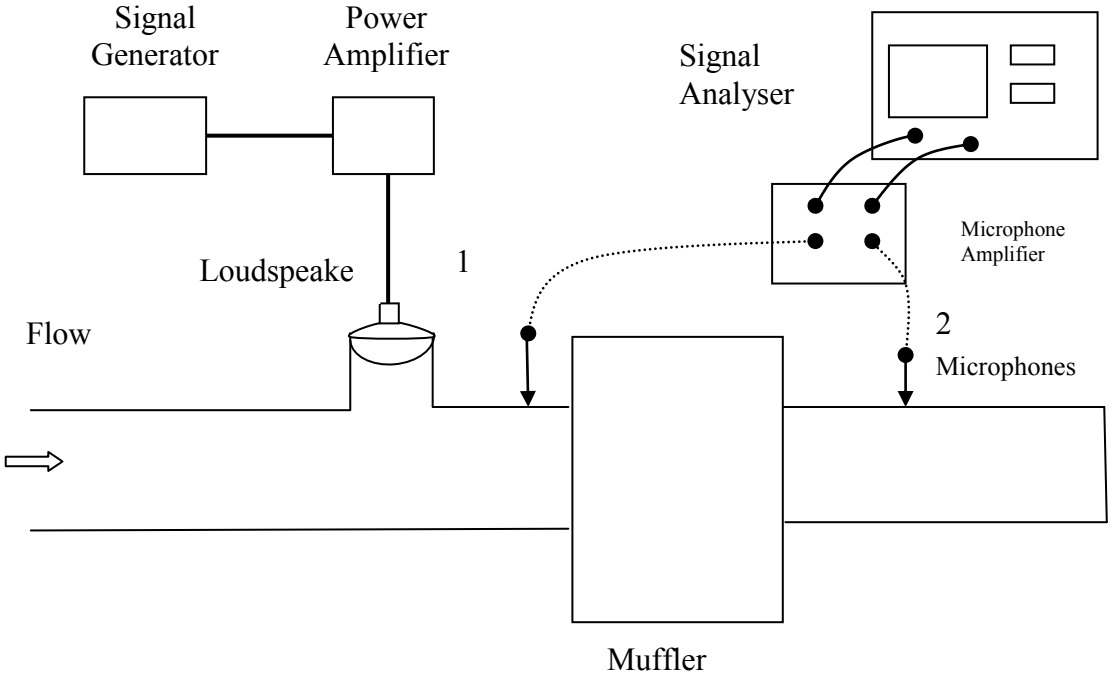

Figure 5.1: *Schematic diagram of experimental setup.*

5.2 Equipment

Various equipment, devices and software used in this experimental investigation can be listed as follows-

Microphone (Brűel & Kjær, Type 4134)

Microphone Amplifier (Brűel & Kjær, Type 2609)

Loudspeaker Amplifier (SONY TA-FE330R)

Signal Generator (RS-Components Ltd, Thandar TG503, 5MHz Pulse generator)

Loudspeaker (8 Ώ)

Digital computer with Labview software as interface for signal analysis

MATLAB software for FFT Analysis.

5.3 Experimental Setup and procedure

An experimental setup for measuring the transmission loss and insertion loss for a continuous pulse with anechoic termination has previously been done by Selamet et al. (Selamet, Radavich 1997).The experimental setup, however, has to be slightly altered in this case because of the involvement of the mean flow in another part of the investigation. Instead of a linear acoustic source, a vertical acoustic source is adopted in this study to avoid interference with mean flow (See loudspeaker in figure 5.1). The experimental configuration constitutes long upstream and downstream pipes to avoid contamination of data at the upstream and downstream probes. Anechoic termination has not been used as it is found that a perfectly anechoic termination is hard to achieve and it is also found that the small amount of energy transmitted from the expansion in consecutive reflection from the inside of expansion chamber is crucial for obtaining the transmission loss spectrum and these small amplitude reflections from the expansion chamber could be hard to distinguish from anechoic reflections from the outlet. Besides, as a final comparison has to be made with the numerical solution, which most certainly would not have the equivalent anechoic numerical termination at its outlet, the current experimental setup seems more

reasonable. The length of the expansion chamber is 100cm and the diameter of the inlet and outlet pipe is about 12 cm.

The current experimental setup constitutes extended upstream and downstream pipes, with a simple expansion muffler placed between them, as shown in Figure 5.1. Two different measurements were conducted for 'pipe without filter (expansion chamber)' and 'pipe with filter (expansion chamber)', with same random pulse generated at a given generator frequency. It was ensured throughout the experiment that the same shape pulse was used as input to both the 'pipe without filter' and 'pipe with filter'. This could also be seen as obtaining an insertion loss rather than transmission loss, considering the nature of measurement. However, the use of long inlet and outlet pipe was adopted with proper care taken in ensuring the same input pulse be imposed in the simple expansion muffler which was imposed in the pipe. This ensures that both insertion and transmission loss could be considered the same for this study.

A signal generator (Thandar TG503, 5MHz Pulse generator) has been used to generate a random sinusoidal pulse which is amplified by power amplifier (SONY TA-FE330R) and passed through the loudspeaker, which creates acoustic pressure field on moving medium. The input signal after getting deflected from the muffler element is transmitted through the downstream pipes, where the microphone picks the signal and the preamplifier amplifies the signal before feeding it to the data acquisition system. Same measurement is conducted without expansion and data is collected for the same. MATLAB software is then employed to Fast Fourier Transform the acoustic data using equation 4.34 to obtain transmission loss spectrum for the muffler element.

For numerical simulation, the responses are recorded for the setup constituting 'pipe without filter' and responses are converted into pressure signals, which is then fed to the computational solver for

simple expansion muffler geometry to obtain pressure data for two probe locations near the inlet and after the expansion chamber. The pressure data is then Fourier transformed to obtain transmission loss spectrum and comparisons are then made with the experimental results to analyse the attenuation due to simple expansion muffler.

5.4 Result and Discussion

Experiments are conducted for simple expansion muffler with various random pulses generated at different generator frequencies by the signal generator as shown in figure 5.2. These signals are imposed at the inlet with or without any mean flow in the experiment.

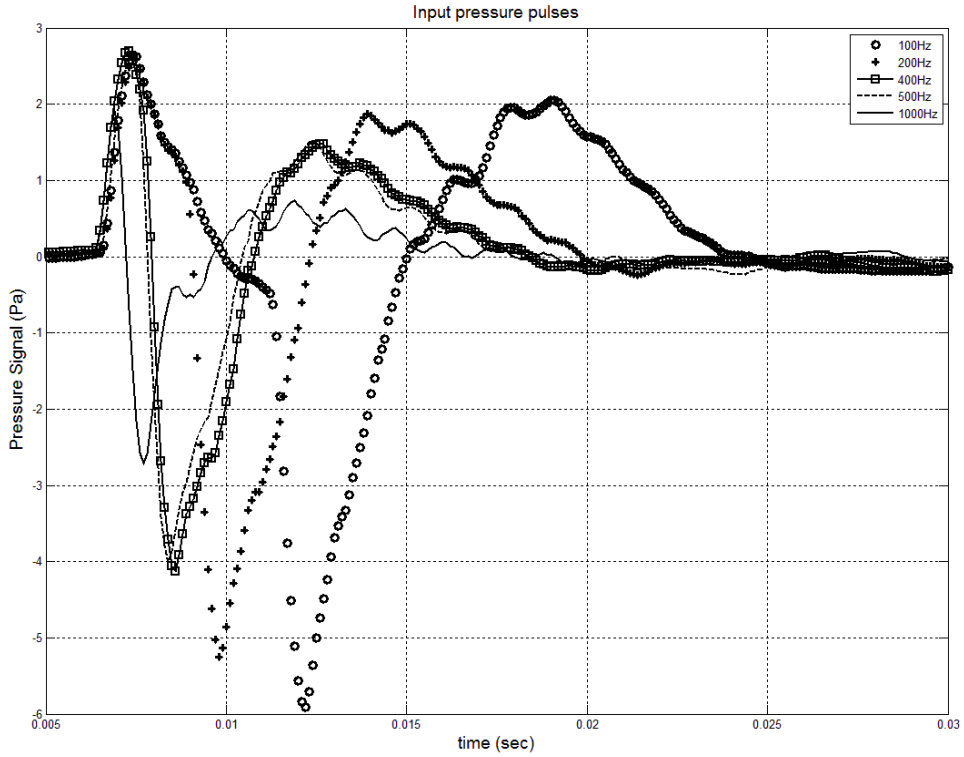

***Figure 5.2**: Comparison of input pressure pulses generated by signal generator at different frequencies ranging from 100Hz to 1000Hz.*

5.4.1 Experimental study of muffler without mean flow

For every pulse generated at various generator frequencies, the input pressure pulse and transmitted pressure pulse are recorded by the microphone and are then Fourier transformed to analyse the attenuation due to simple expansion muffler. The transmitted pulse plot after the expansion and the transmission loss spectrum of the signal attenuation for pulses generated at generator frequencies in the range of 100Hz to 1000Hz are shown in figure 5.3 to figure 5.7. Since all these pulses have mixed range of frequency as it can be seen in figure 5.2, the attenuation in the transmission loss spectrum can be seen to be more in the higher frequency range and considerably less in the lower frequency range. Higher frequency perturbations for transmission pulse at generator frequency of 1000 Hz can be seen in the figure 5.7 (b). These high frequency perturbations are attenuated inside the expansion muffler by the destructive interference and a higher attenuation near 1000Hz frequency is evident from the figure 5.7 (a). It is important to note a low attenuation in the lower frequency ranges in the experimental study of pulse propagation without any mean flow.

(a)

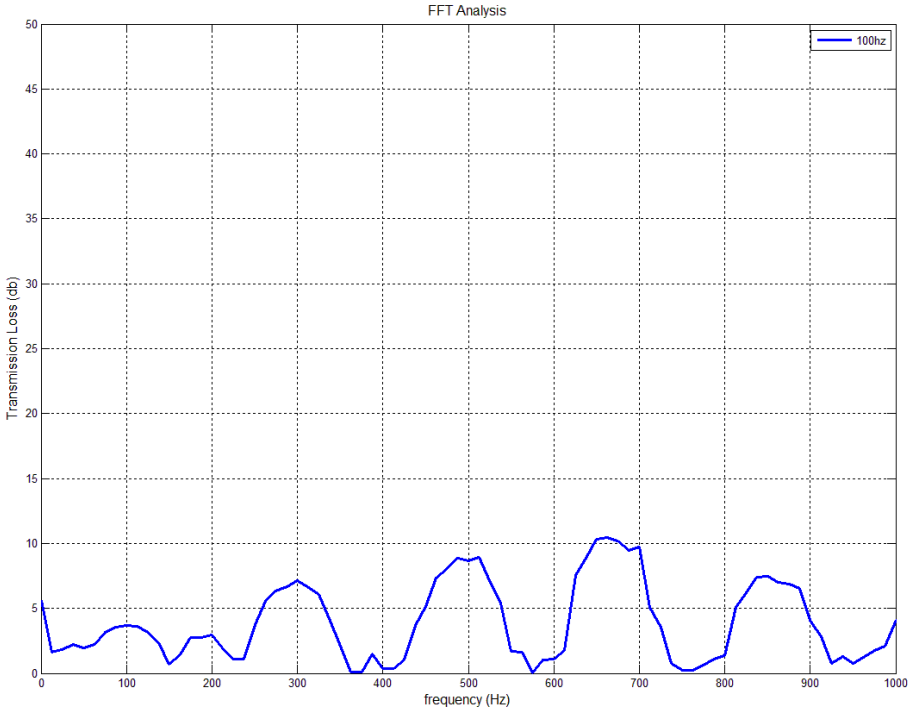

(b)

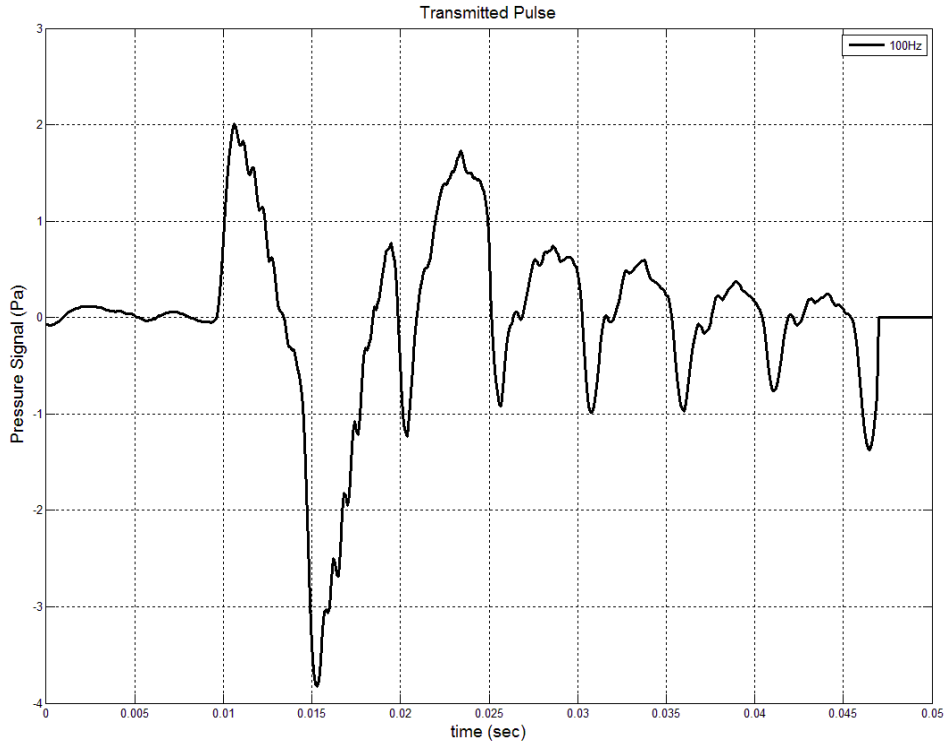

***Figure 5.3**: (a) Transmission loss spectrum at 100 Hz generator frequency. (b) Transmitted pulse plot at 100 Hz generator frequency.*

(a)

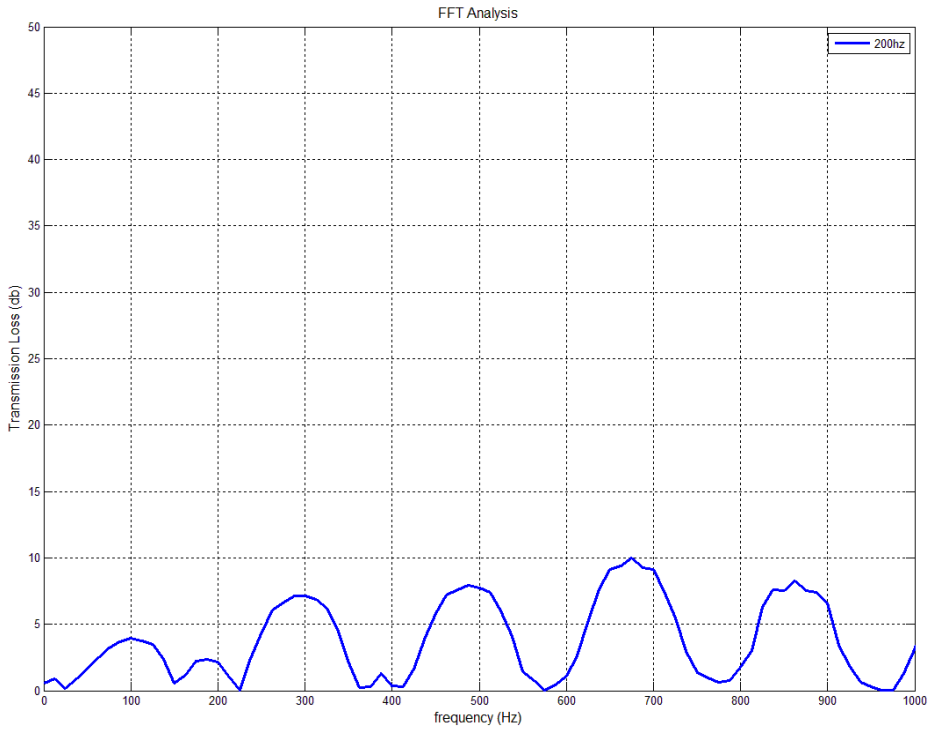

(b)

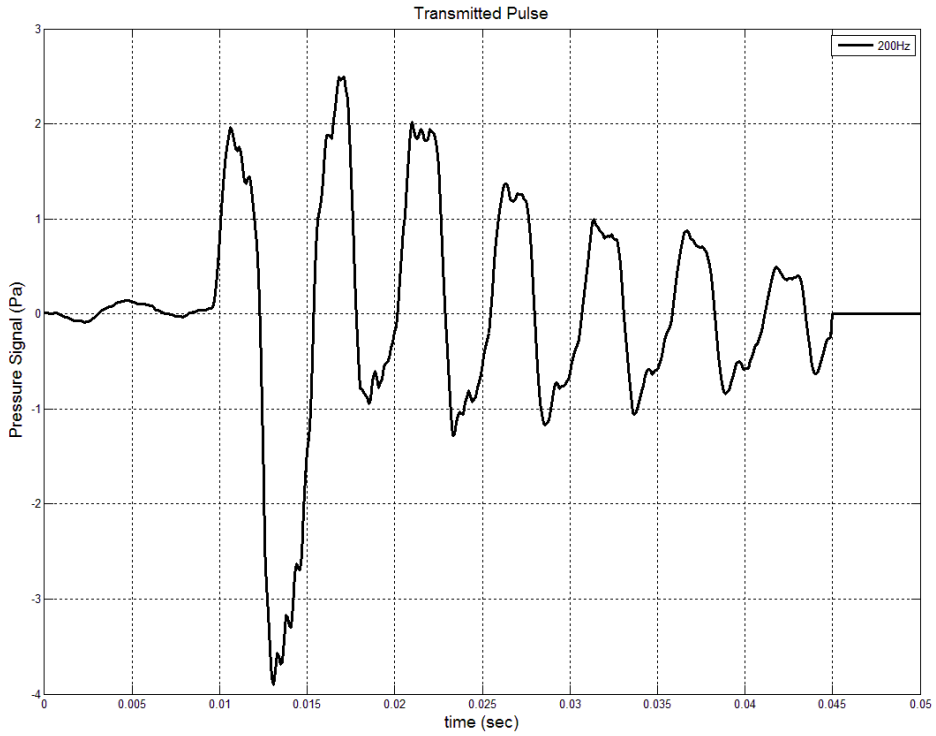

***Figure 5.4**: (a) Transmission loss spectrum at 200 Hz generator frequency. (b) Transmitted pulse plot at 200 Hz generator frequency.*

(a)

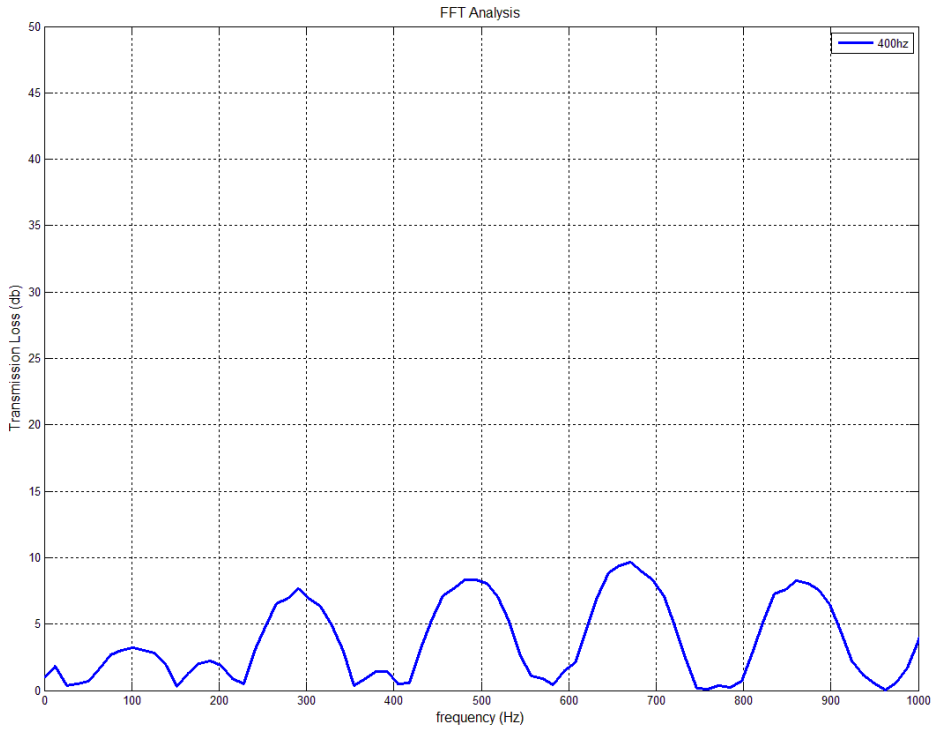

(b)

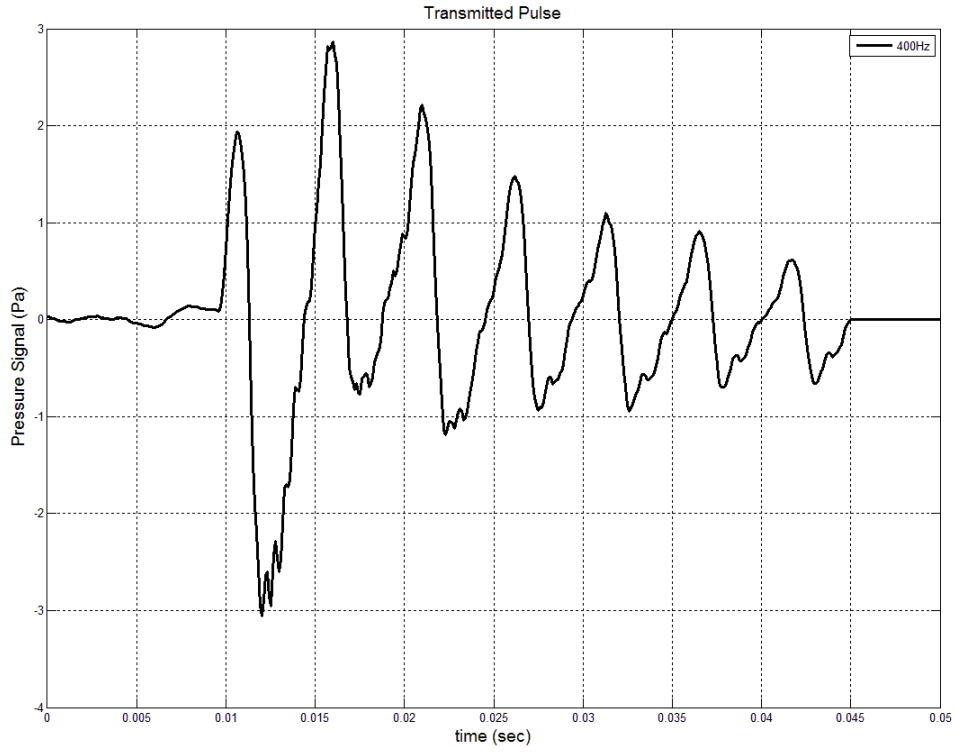

***Figure 5.5**: (a) Transmission loss spectrum at 400 Hz generator frequency. (b) Transmitted pulse plot at 400 Hz generator frequency.*

(a)

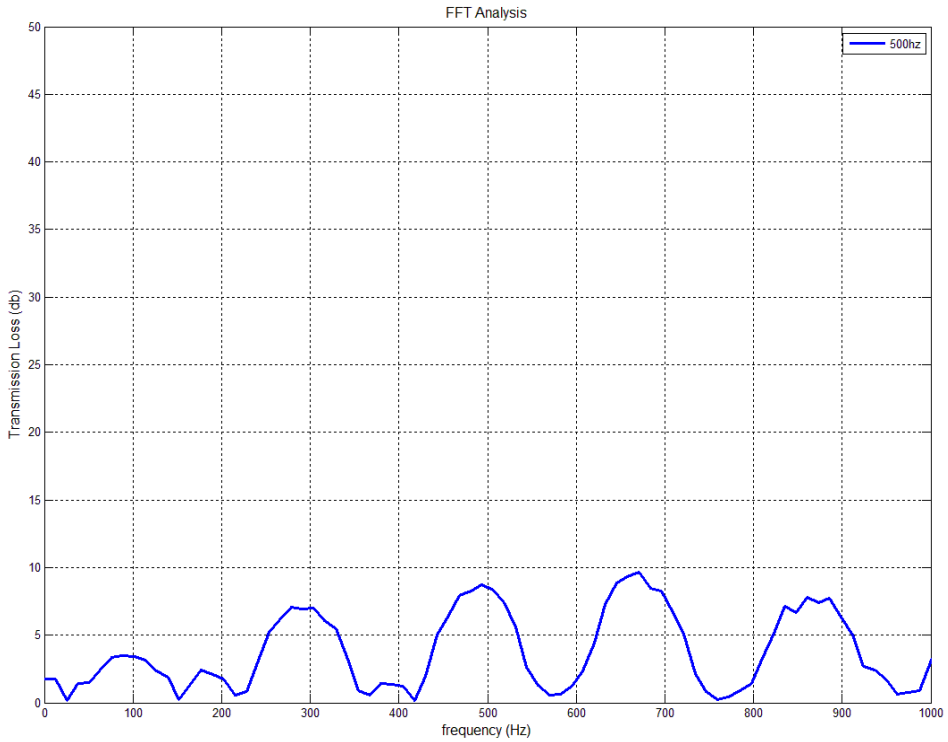

(b)

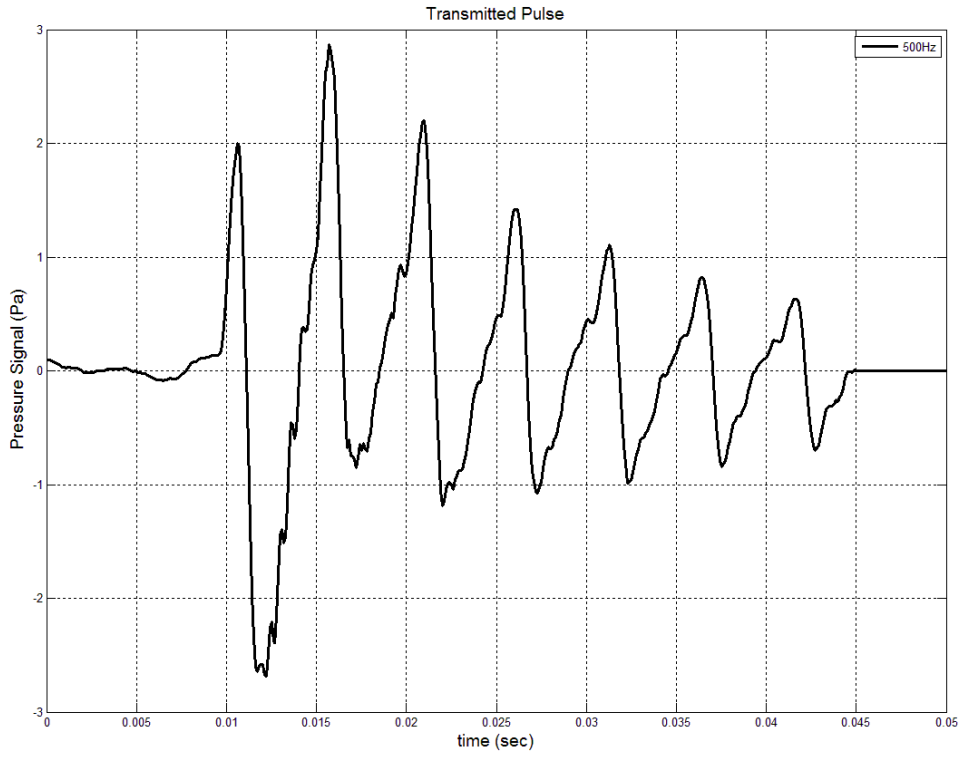

***Figure 5.6**: (a) Transmission loss spectrum at 500 Hz generator frequency. (b) Transmitted pulse plot at 500 Hz generator frequency.*

(a)

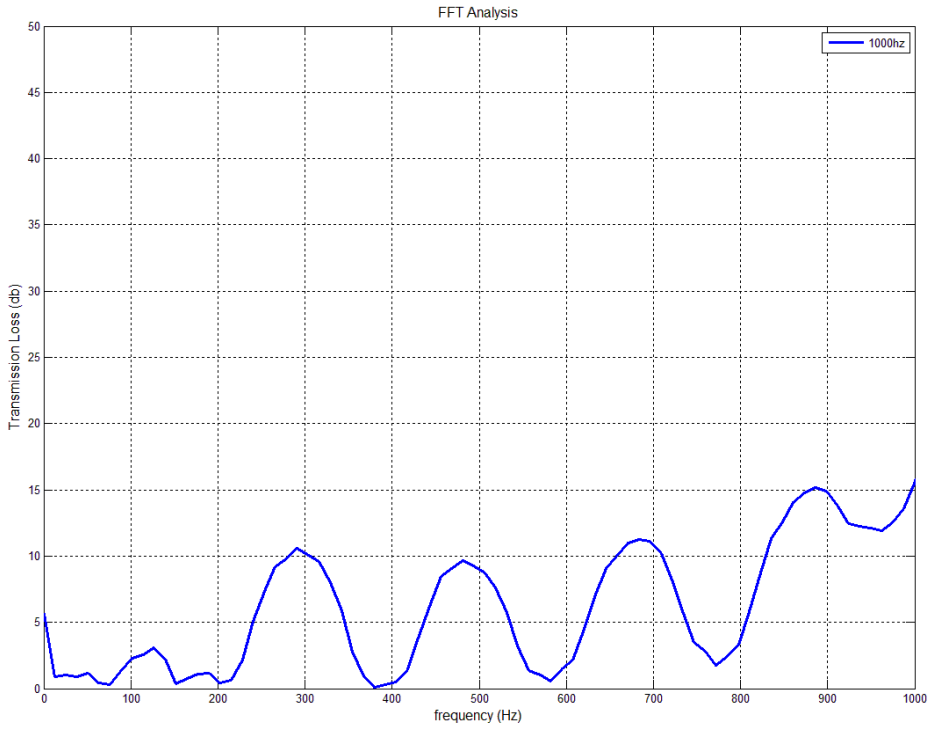

(b)

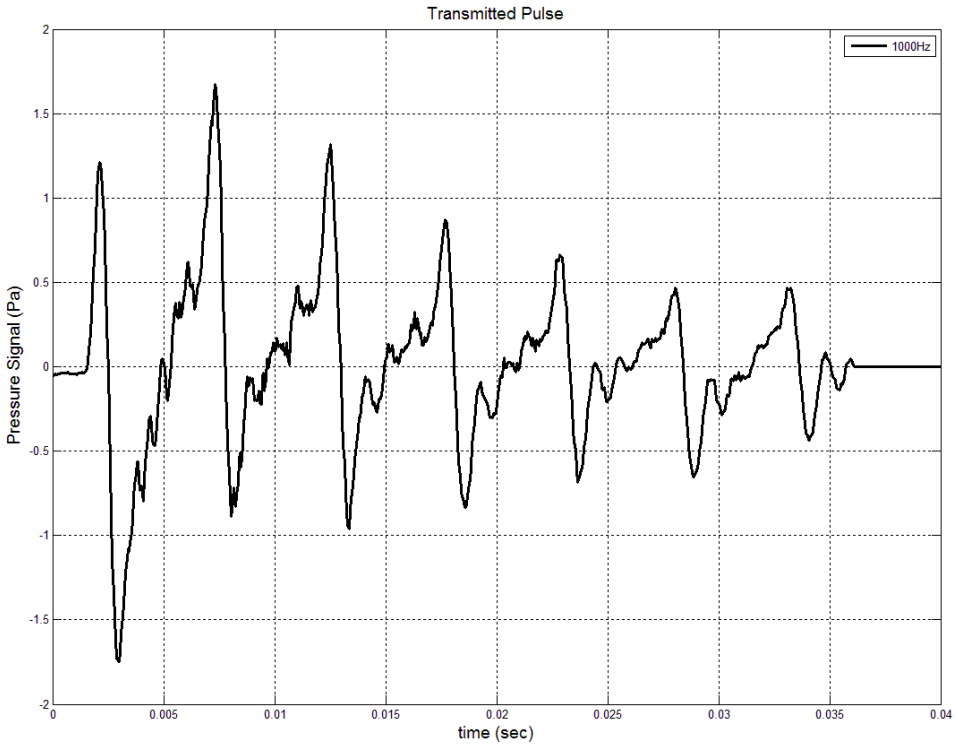

***Figure 5.7**: (a) Transmission loss spectrum at 1000 Hz generator frequency. (b) Transmitted pulse plot at 1000 Hz generator frequency.*

5.4.2 Numerical validation of experiment with no flow

The pressure based Karki-PISO compressible solver with laminar flow considerations is used in this section for experimental validation of the solver. Unlike the previous pulse propagation simulations in chapter 2 and 4, the input pulse in current simulation is not a pure pulse but a mix of various low and high frequency waves. These pulses can also be considered as distorted pulse of a mix of various random frequencies. The pressure based compressible PISO solver seems to struggle in terms of stability and the Navier-stokes equations ultimately diverge. The divergence can only be controlled by using blended discretization for space and time which would result in loss of some of high frequency waves in the domain. The Karki-PISO solver on the other hand provides the required stability by introducing pressure gradient term in the pressure correction equation, as shown in equation 2.28. This solver provides stability by easing the stiffness in the eigen vector of the system of Navier-Stokes equations and enhance the stability of the solver to deal with random pressure fluctuation imposed at the inlet of the expansion muffler.

Mesh independence: Mesh independence study is conducted to ensure minimum spatial discretization error for simulation of mixed-frequency inlet pulse for different mesh. Figure 5.8 shows a very good agreement among the simulations done for the different mesh sizes ranging from a coarse mesh of 4mm to a fine mesh of 1mm. The agreement matches completely in the frequency range of interest 0-3000Hz and the spatial discretization error seems to go away sharply for much finer meshes such as those with size 1mm and 2mm for higher frequency ranges, as shown in figure 5.9.

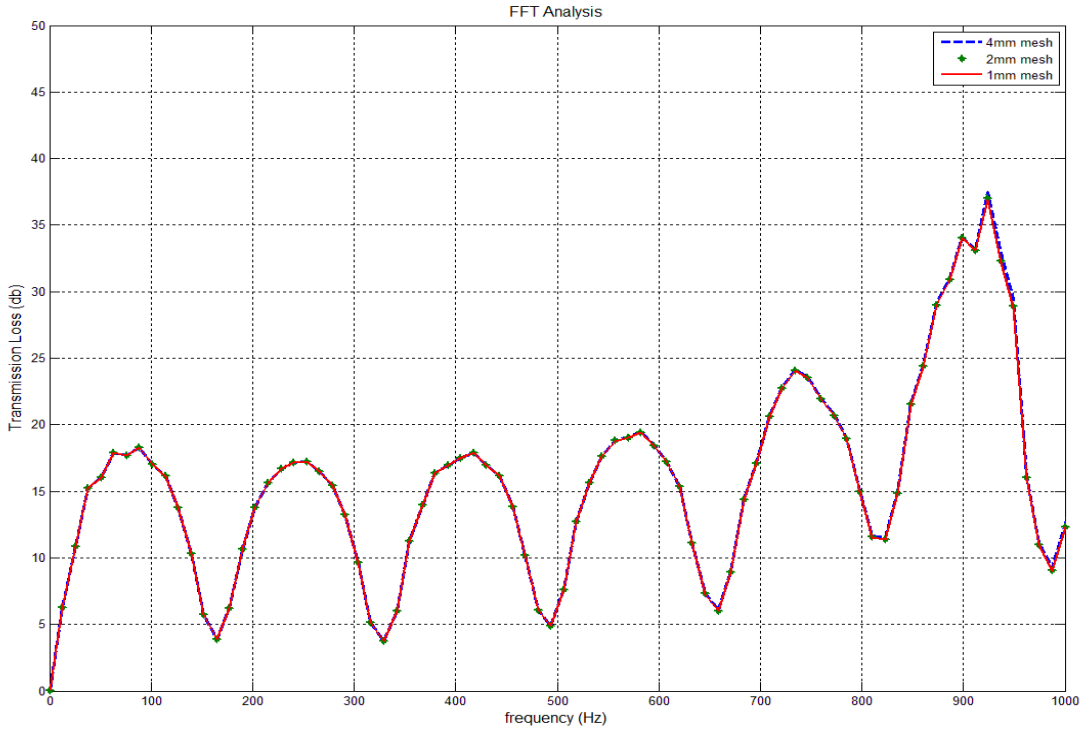

***Figure 5.8**: FFT analysis to show mesh independence of muffler simulation.*

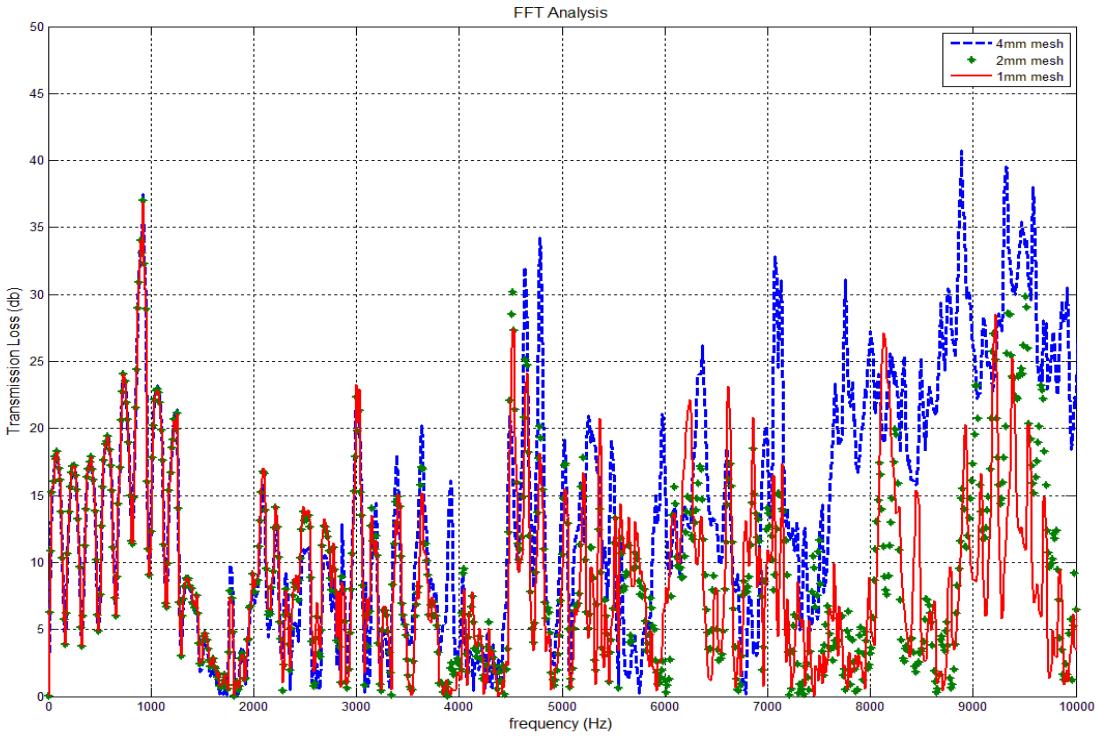

***Figure 5.9**: Broad spectrum of FFT analysis to show mesh independence of muffler simulation.*

Numerical validation: The experimental data collected in section 5.4.1 has been used to validate the Karki-PISO compressible solver with the same set of random mix frequency inputs (shown in figure 5.2) at the inlet. The acoustic measurements in the experiments are done in terms of voltage, mV and these measurements have to be converted into pressure signals, in Pascals. The scaling factor is devised to convert the measurement into comparable units, so that predicted and measured results can be compared. The comparison of the transmission loss spectrum and transmitted pressure pulse for different generator frequencies is shown in Figure 5.10 to Figure 5.14. The transmission loss spectrum predicted by Karki-PISO compressible solver clearly captures all of the attenuation peaks in the frequency domain. The transmitted pressure pulse predicted by the simulation also seems to agree very well with the experimental pulse. As a transient finite volume compressible flow solver, the prediction capability of the solver for a random mix of frequencies as input is very impressive. The stability of the solver is found to be very good throughout the pulse propagation and all the high frequency pressure pulses seems to be captured by the solver. The prediction demonstrates the ability of the Kaki-PISO solver to handle the low Mach number acoustic flow simulation and capture all the available high frequency components in the solution.

Despite using the fully second order temporal and spatial dicretization, there seems to be slight difference in the prediction frequency. It is due to the numerical dissipation in the solution due to instantaneous random changes in the inlet boundary condition which results in stiffness of the system of finite volume Navier-Stokes equations. The Karki-PISO compressible solver clearly handles the challenge in solution stiffness better and provides better predictability in pulse propagation than conventional finite volume subsonic flow solvers.

(a)

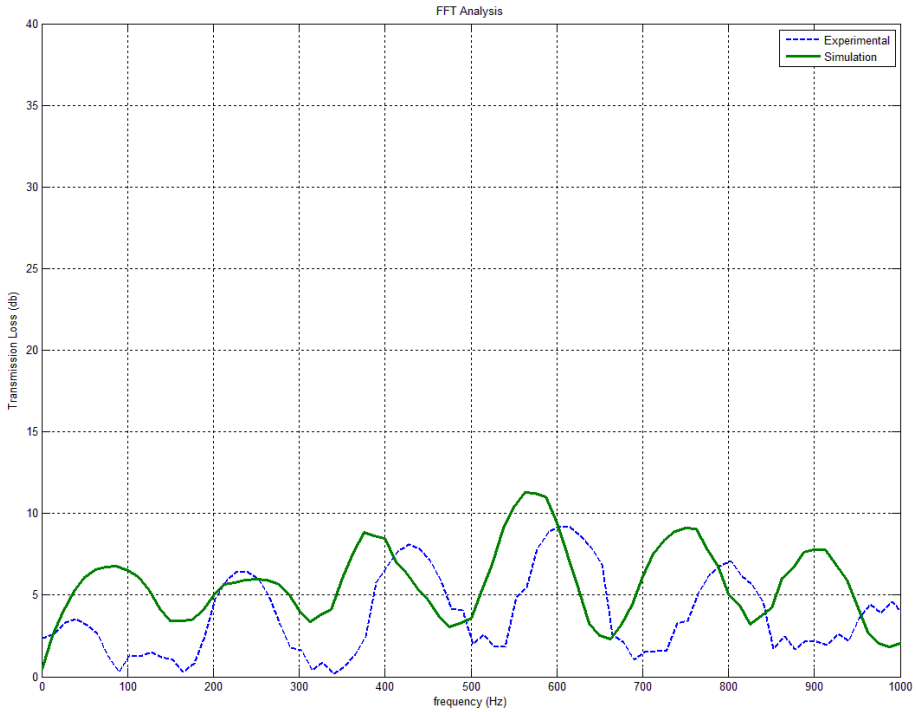

(b)

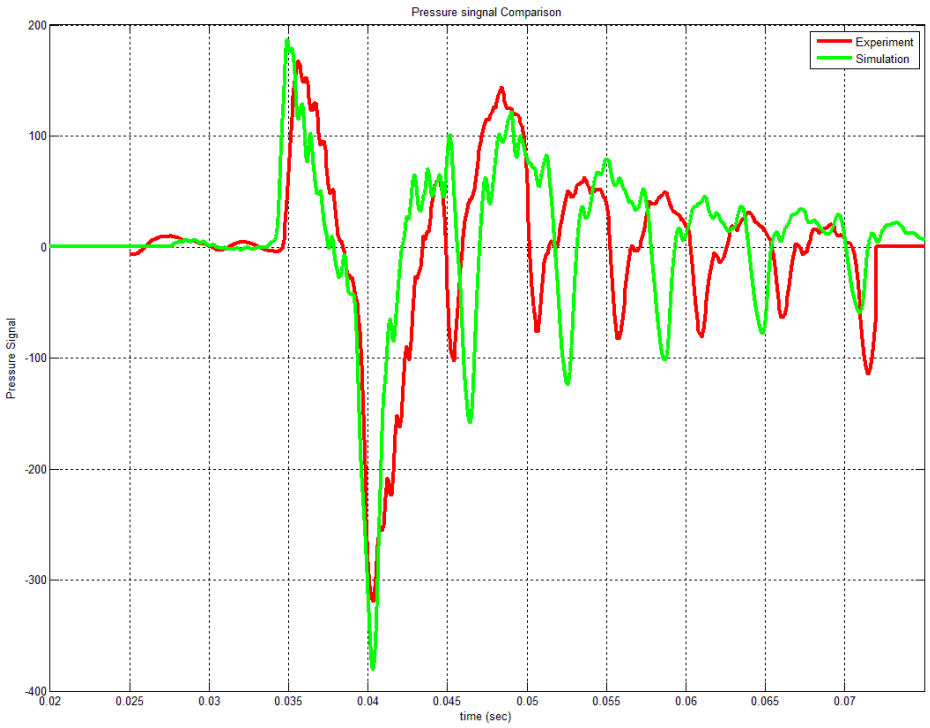

***Figure 5.10**: (a) Comparison of Transmission loss spectrum at 100 Hz generator frequency. (b) Comparison of Transmitted pulse plot at 100 Hz generator frequency.*

(a)

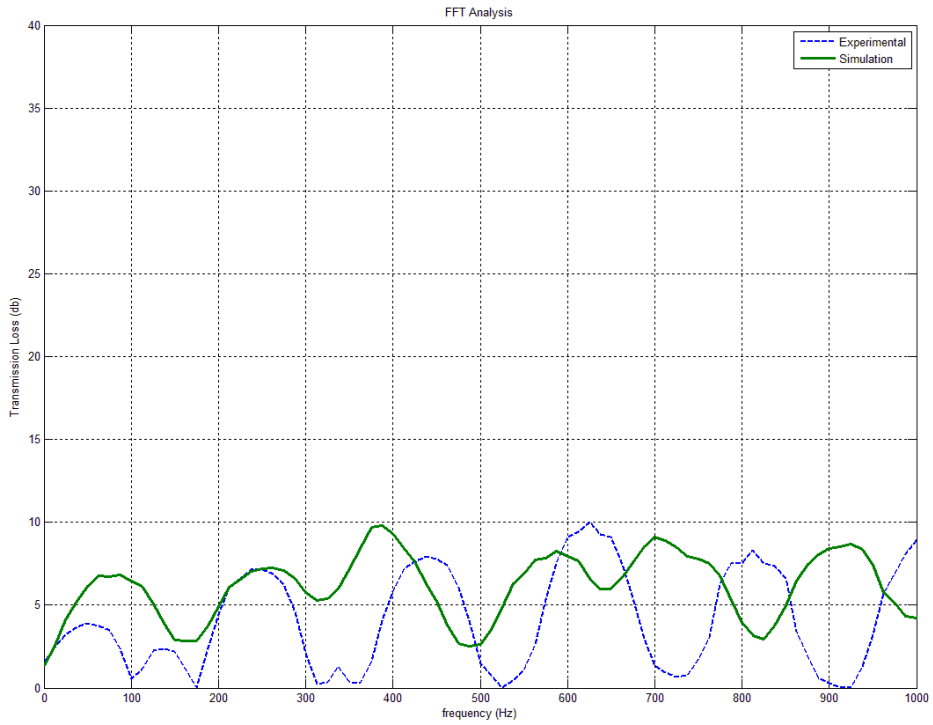

(b)

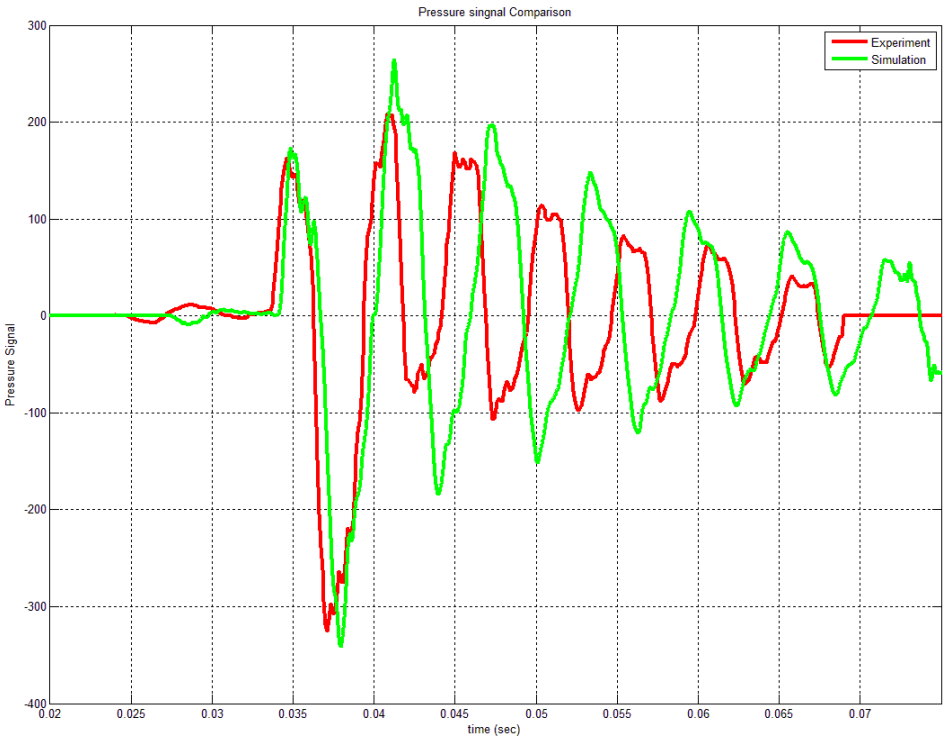

Figure 5.11*: (a) Comparison of Transmission loss spectrum at 200 Hz generator frequency. (b) Comparison of Transmitted pulse plot at 200 Hz generator frequency.*

(a)

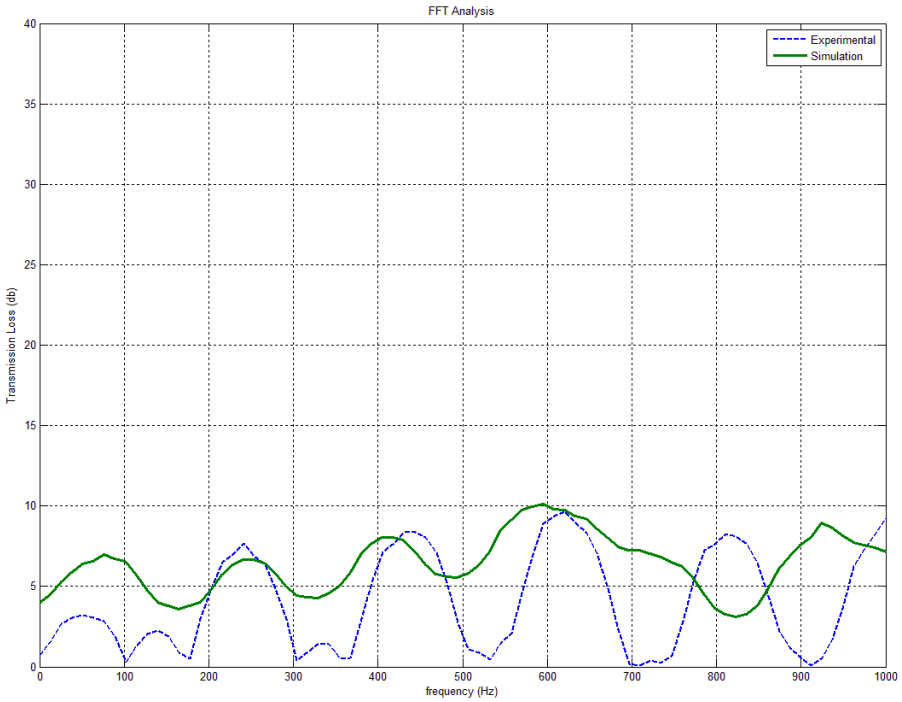

(b)

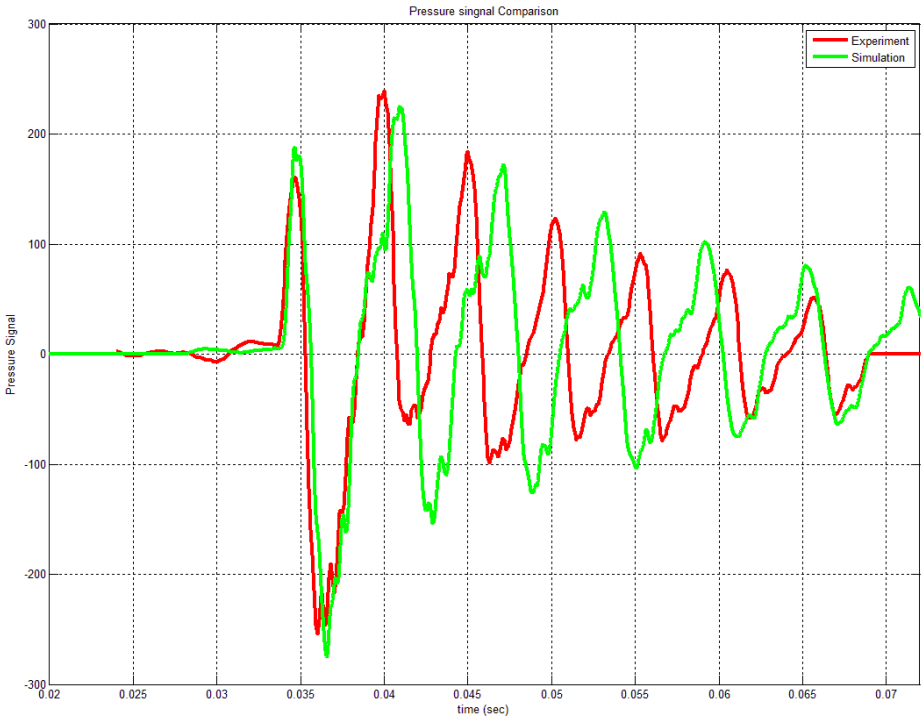

***Figure 5.12**: (a) Comparison of Transmission loss spectrum at 400 Hz generator frequency. (b) Comparison of Transmitted pulse plot at 400 Hz generator frequency.*

(a)

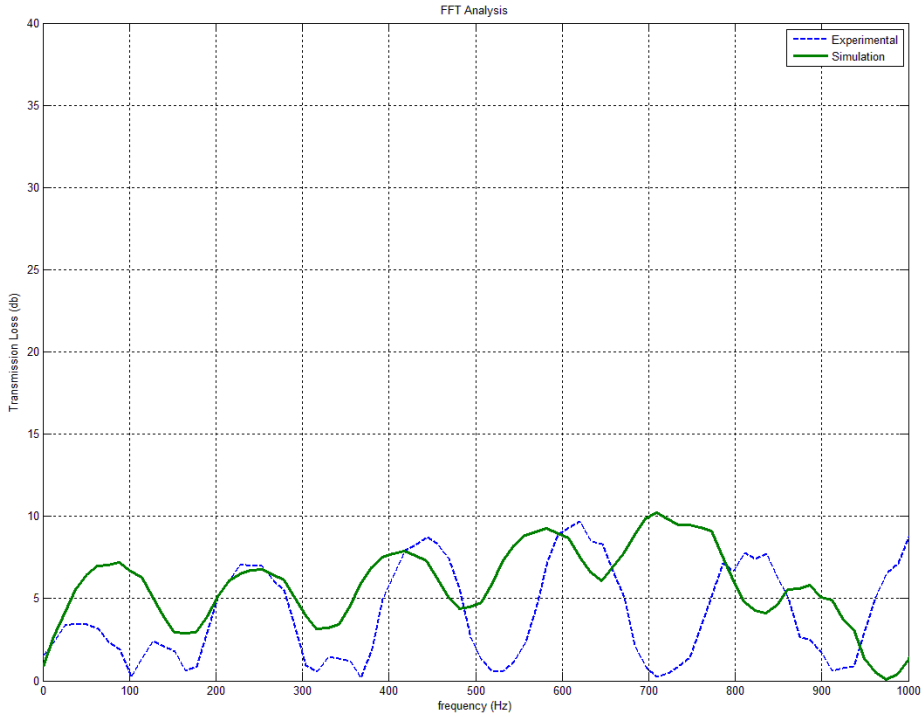

(b)

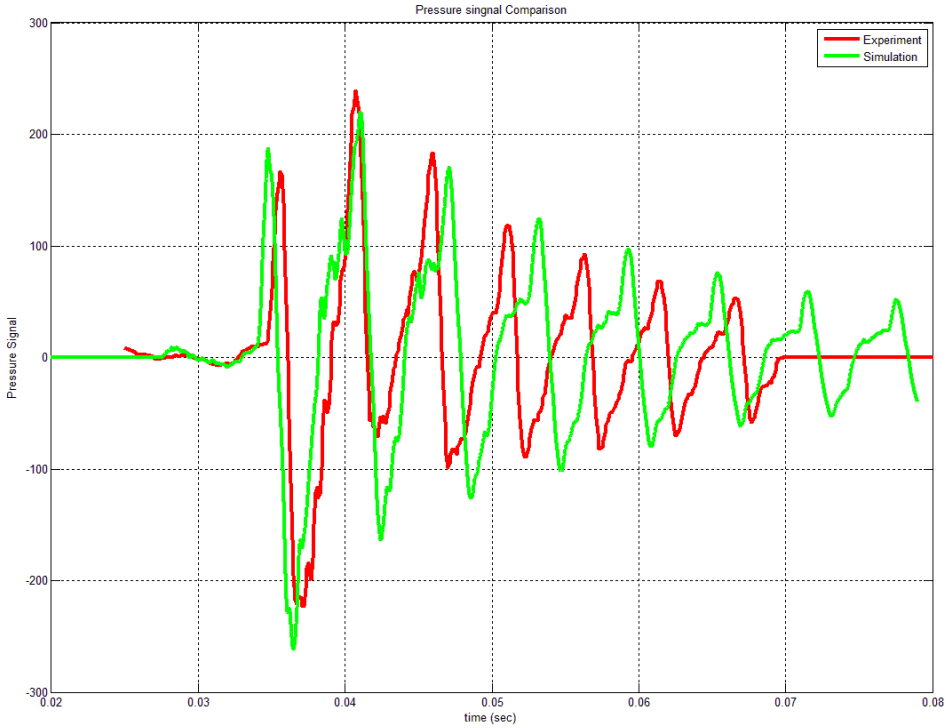

***Figure 5.13**: (a) Comparison of Transmission loss spectrum at 500 Hz generator frequency. (b) Comparison of Transmitted pulse plot at 500 Hz generator frequency.*

(a)

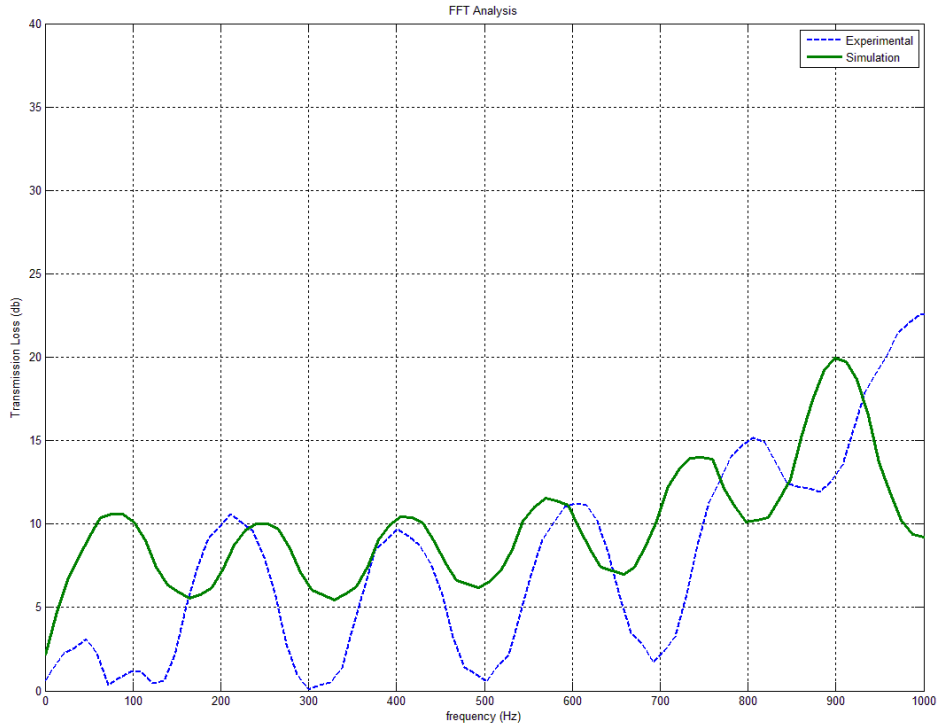

(b)

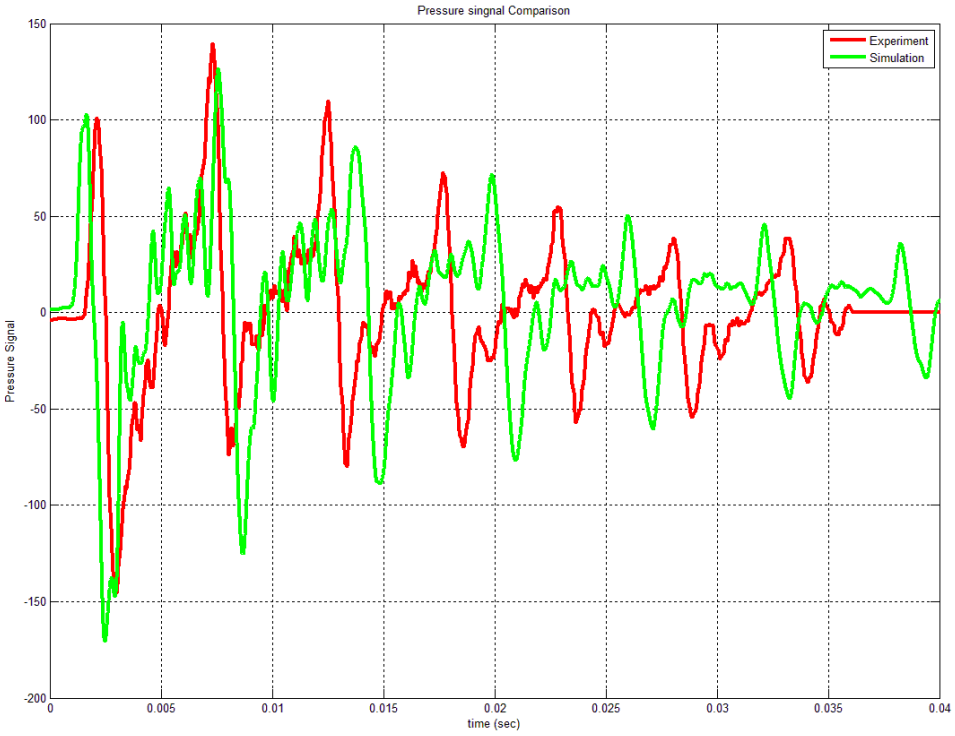

***Figure 5.14**: (a) Comparison of Transmission loss spectrum at 1000 Hz generator frequency. (b) Comparison of Transmitted pulse plot at 1000 Hz generator frequency.*

5.4.3 Experimental study of muffler with Mean flow

The last two sections have dealt with the simulation of pulse propagation in simple expansion muffler without any mean flow inside the muffler. However, in most of the practical situations, the mean flow is necessarily available in the simple expansion muffler during pulse propagation and this makes it very important to study the phenomenon of pulse propagation through the muffler with considerable amount of flow present inside the muffler. In the context of experimental analysis of mean flow effect on the transmission loss, Byrne et al. (Byrne, Skeen et al. 2006) used an inlet pipe of 16mm diameter with expansion cross-section of 50 mm x 50 mm and a length of 100 mm. These diameters are very small in comparison to the present work. Incidentally, Byrne et al did not find much difference in attenuation in the muffler with and without flow for a range of low velocities. Apart from the scale of the geometry, the expansion section used in their experiment is also rectangular and length of expansion is smaller than the present work.

A set of experiments have been conducted for a simple expansion muffler with different amount of mean flow inside the chamber. The same random mix of pressure pulses, used in the last two sections, is imposed over the mean flow at the inlet of the simple expansion muffler. The acoustic data is collected after the expansion chamber of the simple expansion muffler and also separately for a simple pipe without expansion in the presence of imposed mean flow. The recorded data is calibrated and Fourier transformed to obtain transmission loss spectrum. Figure 5.15 shows the comparison of transmission loss spectrum for imposed pulse at 500 Hz generator frequency with 10 m/s flow velocity and without any flow. The comparison shows a consistent level of attenuation throughout the frequency range. However it is important to note that the attenuation at very lower range of spectrum is more pronounced that the higher range of spectrum. In other words, the

attenuation in the lower frequency ranges for the no-flow condition is less pronounced and rather a higher attenuation

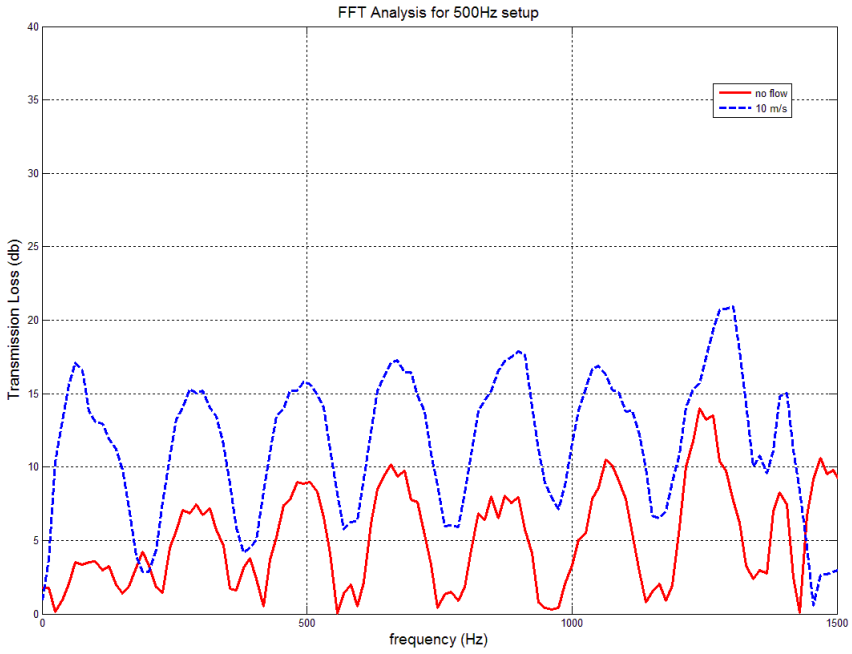

Figure 5.15: *Comparison of FFT of muffler without any flow and muffler at 10 m/s flow for generator frequency of 500Hz.*

in that range is observed due to the consistent attenuation throughout the spectrum after the introduction of mean flow. This is an interesting result which would be discussed in the context of mean flow simulation of simple expansion muffler in later chapters.

Further, the mean flow analysis is extended for the other generator frequencies and different mean flow velocities. Comparisons are made in the presence of three different mean flow velocities of 10 m/s, 12.5 m/s and 15 m/s for different generator frequencies ranging from 200 Hz to 1000Hz. Figure 5.16 and Figure 5.17 shows the comparison for 10 m/s and 15 m/s flow in various range of generator frequencies (200Hz to 1000Hz). It is apparent that there is a slightly

(a)

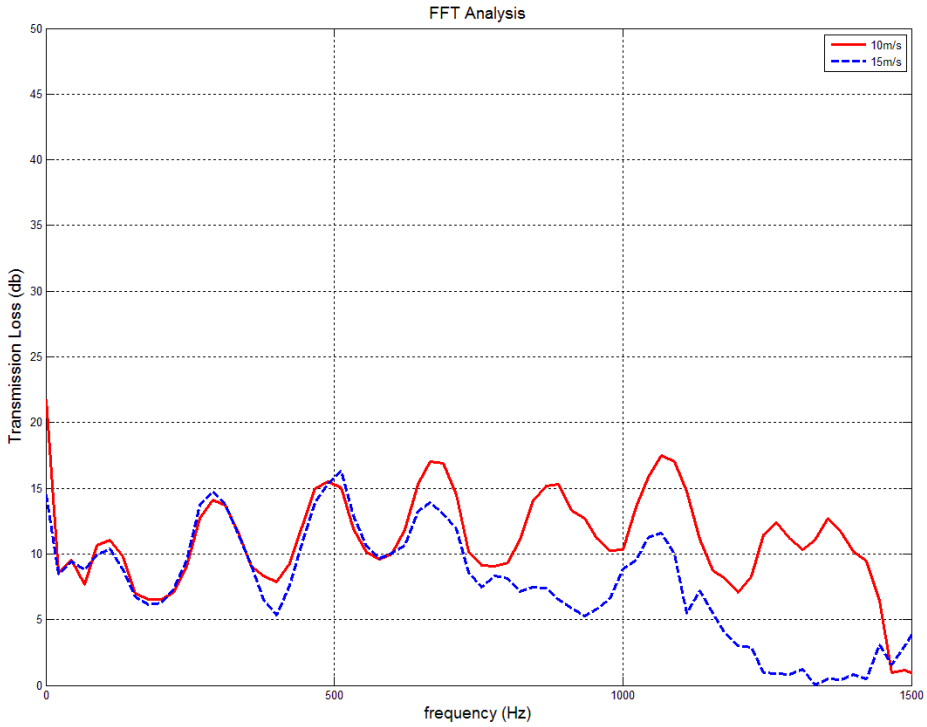

(b)

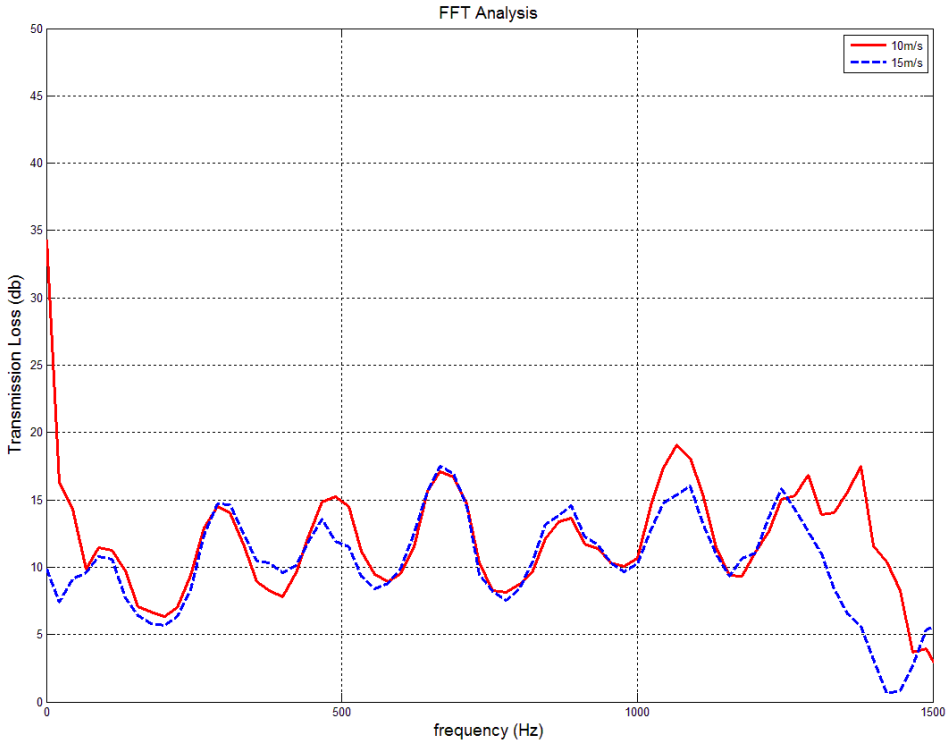

Figure 5.16: *Comparison of FFT at 10m/s and 15m/s at generator frequency of (a) 200Hz and (b) 400 Hz.*

(a)

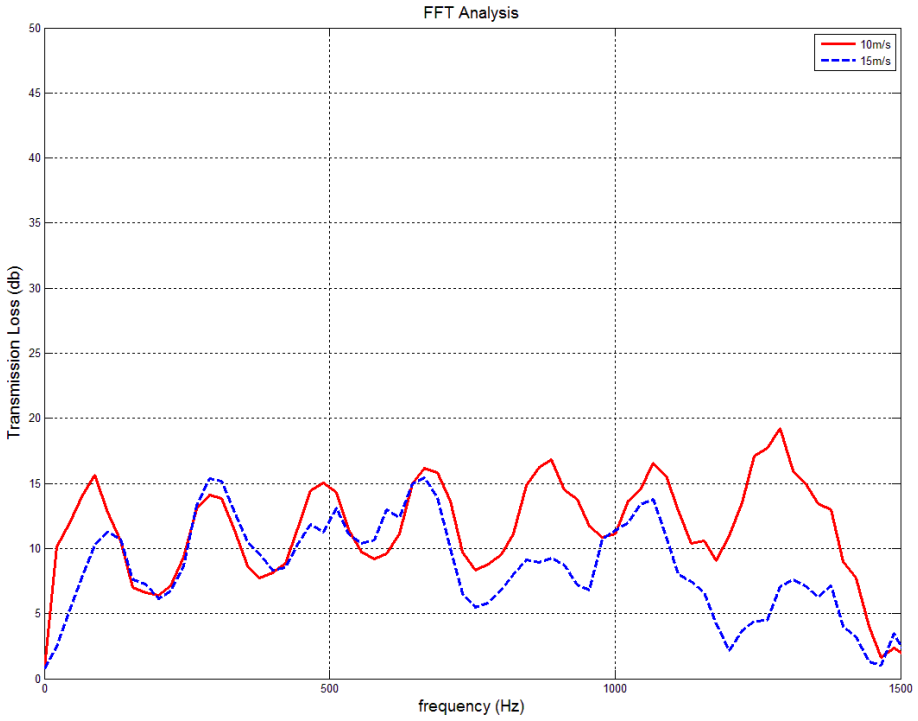

(b)

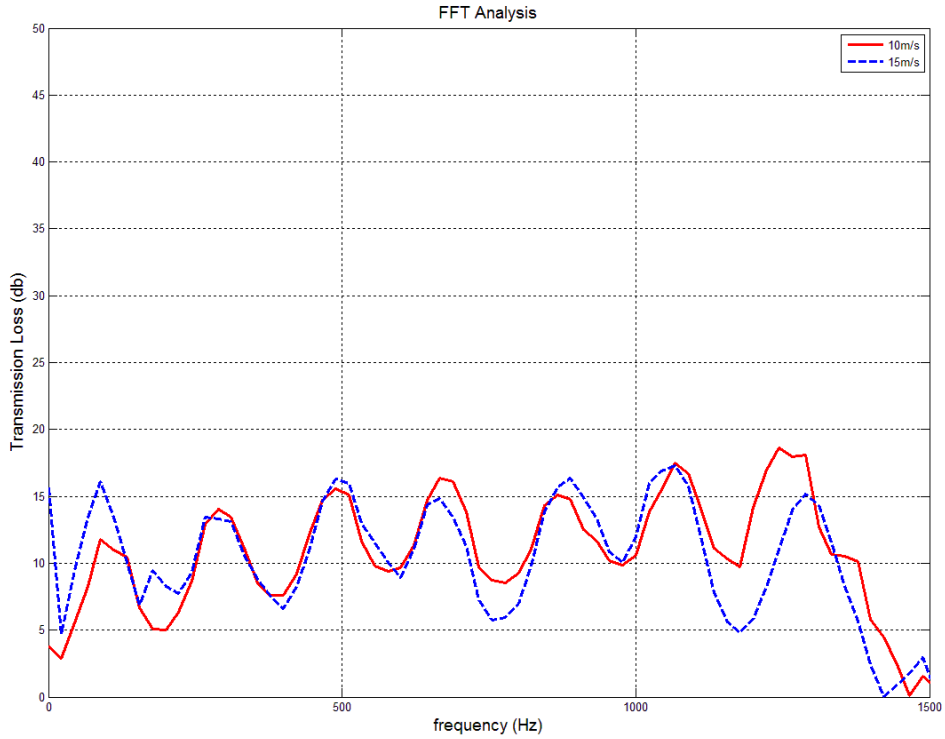

***Figure 5.17**: Comparison of FFT at 10m/s and 15m/s at generator frequency of (a) 500 Hz and (b) 1000 Hz.*

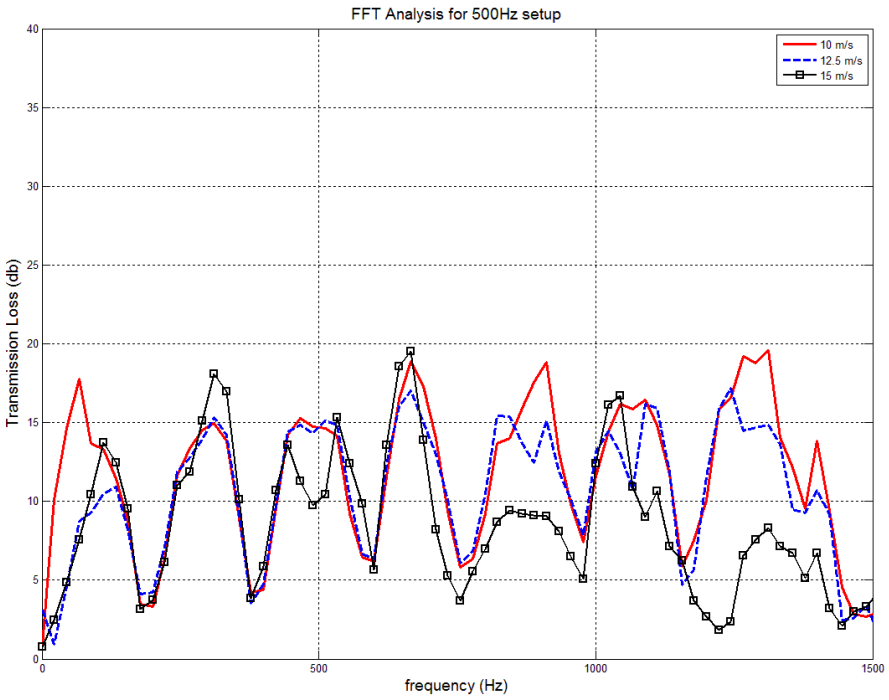

Figure 5.18: *(a) Comparison of FFT at 10m/s, 12.5 m/s and 15m/s for generator frequency of 500 Hz.*

higher attenuation for the lower mean flow (10 m/s) than the higher mean flow (15 m/s). It has also been found that there is considerably lower attenuation at zero mean flow (evident from the figures 5.16-5.18), in contrast to the higher attenuations at lower mean flow of 10 m/s. Therefore, it can be inferred that there must be an optimum mean flow velocity for a given generator frequency which would provide the maximum attenuation in the expansion muffler. However, the study is not focused on finding an optimum flow speed for attenuation and therefore it will not be explored further in this regard. A comparison of transmission loss spectrum for various flow velocities ranging from 10 m/s to 15 m/s at 500 Hz generator frequency is shown in figure 5.18. The overall spectrum supports the argument of having higher attenuation for a considerable lower mean flow value. These mean flow experimental acoustic data for simple expansion muffler provides benchmark transmission loss information for muffler without anechoic termination.

5.5 Closure

An experimental analysis was conducted for a simple expansion muffler both, without mean flow and with considerable mean flow condition. The muffler analysis without any mean flow showed lower attenuation in the transmission loss spectrum at the lower range of frequency. The experimental data was used thereafter to validate successfully the Karki-PISO compressible low Mach number flow solver. The solver captured the attenuation peaks in the transmission spectrum accurately with acceptable shift in frequency value. Finally, the experimental analysis of muffler for various mean flow velocities provided a set of benchmark results which showed higher attenuation in transmission loss for considerable mean flow in the muffler. This higher attenuation was due to the interaction of turbulence with mean flow acoustic. The analysis also provided a comparison for muffler attenuation with various generator pulses under both, with and without considerable mean flow. It was found that after a certain value of mean flow velocity, the trend in attenuation at higher frequency range of the transmission-loss spectrum was reducing.

Chapter 6

Synthetic Boundary Condition for LES

6.1 Introduction

Apart from the direct approaches to inspect instantaneous numerical fields, there are other approaches which use statistical or time averaged mean flow quantity like ρ, *U*, *P* and *T*. These averaged RANS simulations are found to be satisfactory in various applications and reaches universal asymptotic behaviour irrespective of initial boundary condition (George, Davidson 2004). However, LES and DNS approaches are found to require a turbulence representation at the inlet for an accurate simulation. Although an upstream flow condition can ideally provide a good inflow data, the computational boundary cannot, however, be extended upstream indefinitely. The inlet condition should also be consistent with the turbulence model chosen for simulation. In some cases, random fluctuations are superimposed on uniform inlet velocity to achieve turbulent behaviour at the inlet (Rai, Moin 1993). It has also been found that the various flow types have different requirement of inflow condition. For instance, in simulating free shear flow the random perturbation could amplify the disturbances exponentially and inflow condition is believed to be of less importance, whereas in the wall-bounded flow, these random fluctuating inflows are found to be very important.

The generation of random velocity profile for inflow data to match actual turbulent flow field is a difficult and computationally challenging process. It is therefore more preferred to use a lower order description provided by different related turbulent quantities then to use enormous amount of information to describe turbulence. A variety of turbulence methods has been developed for

accurate presentation of turbulence in inflow data (Karweit, Blanc-Benon et al. 1991, Lee, Lele et al. 1992, Bachera, Bailly et al. 1994, Lund, Wu et al. 1998, Billson, Eriksson et al. 2003, Ewert 2005, Jarrin, Benhamadouche et al. 2006, Fathali, Klein et al. 2008). A mixed synthetic boundary condition has been proposed in this chapter and discussion regarding the evolution of this method is also presented.

6.2 Overview of Turbulence Characteristics

6.2.1 Two-point Correlation

Spatial correlation: It has been found that velocities at different spatial and/or temporal positions can be highly correlated. As explained in Chapter 3, turbulent fluctuations are basically characterised by velocity correlations. A two-point velocity (space) correlation tensor has been defined by considering correlation of two points $\boldsymbol{x}$ and $\boldsymbol{x} + \boldsymbol{r}$ in flow**,** as:

$$R_j(\boldsymbol{x}, t; \boldsymbol{r}) = \overline{u_i'(\boldsymbol{x}, t) u_j'(\boldsymbol{x} + \boldsymbol{r}, t)} \quad \text{.... (6.1)}$$

where $\boldsymbol{x}$ is the location and vector $\boldsymbol{r}$ is the displacement vector between two spaces in the flow. R_{ij} would be called statistically steady if it is not the function of time, t and it will be called statistically homogeneous if it is not a function of x. The turbulent kinetic energy can be obtained from R_{ij} as follows:

$$k(x, t) = \frac{1}{2} R_{ij}(x, t; 0).\delta_{ij} \quad \text{.... (6.2)}$$

An *integral length scale*, L can be defined in this context as the integral of normalised space correlation tensor with respect to k over all displacements, as follows,

$$L_{ij}(x, t) = \frac{3}{16} \int_0^{\infty} \frac{R_i(\boldsymbol{x}, t; \boldsymbol{r})}{k(x, t)} dr$$

.... (6.3)

where 3/16 is the scaling factor. This integral length scale is a statistical quantity which provides a convenient measure of the extent of the region within which velocity components are appreciably correlated.

Temporal correlation: Again, in Chapter 3, a two point time autocorrelation tensor was defined by considering correlation of velocities at one point on two different times as:

$$R_{ij}(\boldsymbol{x},;t') = \overline{u_i'(\boldsymbol{x},t)u_j'(\boldsymbol{x},t+t')} \quad \text{.... (6.4)}$$

Here a time averaging of the fluctuating quantities is done at the same point in space but at different times. An *integral time scale*, τ can be defined in this context by integrating normalised R_{ij} over all possible values of t'as follows:

$$\tau(x,t) = \int_0^\infty \frac{R_{ij}(\boldsymbol{x},t;t')}{2k(x,t)}dt'$$

.... (6.5)

The integral time scale denotes the memory time of turbulence. It is often believed to be related to the integral length scale and velocity fluctuations.

In simulating flow problems, not only the statistical, integral or time averaging of flow parameters provide important information but also the mean of the second moment of flow parameters provides important information about the flow characteristics. The second moment defines the root mean square (RMS) as follows:

$$v_{rms} = (\overline{v'^2})^{1/2} \quad \text{.... (6.6)}$$

RMS velocity can also be seen as the standard deviation of the velocity fluctuations which is equal to the square root of the variance.

6.2.2 Probability Density Functions

Probability density functions (PDFs) are a vital statistical tool for detailed analysis and finer description of the turbulence phenomenon. More information can be extracted for a certain parameter to judge its biasness, spread or distribution in space, time and various other domains, if these tools are applied properly. For instance a probability density function f_v can be used to compute mean velocity $\bar{v}$ for a velocity signal v as follows:

$$\overline{v'} = \int_{-\infty}^{\infty} v' f_v(v') dv' \quad \text{…. (6.7)}$$

The probability function has to be chosen and normalised such that

$$\int_{-\infty}^{\infty} f_v(v') dr' = 1 \quad \text{…. (6.8)}$$

PDFs can provide useful representation of the turbulent fluctuations. If the velocity fluctuation is skewed towards the negative or positive side of the mean value, then the PDF plot will also show the skewness toward the right direction. On the other hand, PDF can also provide information about intermittent large fluctuations in the rather flat fluctuation profile. However, instead of looking for PDFs for all fluctuations, there are some terms defined for checking the degree of symmetry of PDF, known as *skewness*. It is defined as,

$$\overline{v'^{\,3}} = \int_{-\infty}^{\infty} v'^{\,3} f_v(v') dv' \quad \text{.... (6.9)}$$

Flatness provides information about any very large fluctuation in a rather flat fluctuation profile. It is defined as,

$$\overline{v'^{\,4}} = \int_{-\infty}^{\infty} v'^{\,4} f_v(v') dv'$$

.... (6.10)

For its applicability, PDFs are an important statistical and analysis tool for turbulent flow simulation.

6.2.3 Velocity Spectrum Function

When we discussed in Chapter 3 the convenience of using frequency or wavenumber space over time domain, we also introduced the energy spectrum to obtain kinetic energy. A hot-wire measurement of time trace velocity components $U_i'(t)$ is shown for the homogeneous turbulence field in Figure 6.2. The PDF of the fluctuation in these velocity components can provide information about the skewness and flatness of these fluctuations.

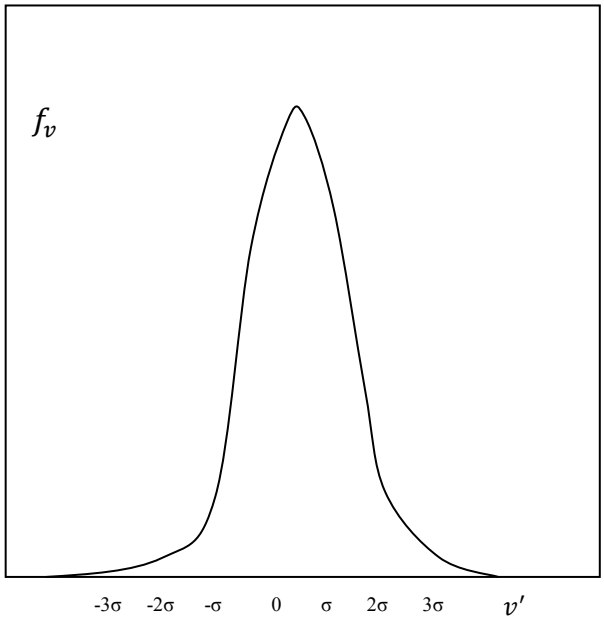

Figure 6.1: A *Probability Density Function.*

However it is also important to understand the velocity and energy spectrum generated by these fluctuations. A Fourier transform of fluctuations can provide information about the structure and size of different eddies through the equation

$$U_i'(x) = \iiint_{-\infty}^{+\infty} u_i(k) e^{i\boldsymbol{k}.\boldsymbol{x}} d\boldsymbol{k}$$

.... (6.11)

where $\boldsymbol{k}$ and $\boldsymbol{x}$ are vector form of wavenumber and space co-ordinates respectively. $u_i(k)$ is the calculated amplitude of the prescribed Fourier coefficient. In order to obtain a symmetric autocorrelation function R_{ii}, an averaged square value of fluctuation velocity's Fourier transforms is performed as

$$\overline{U_i'^{\,2}}(x) = R_{ii}(\boldsymbol{x}, 0) = \iiint_{-\infty}^{+\infty} \psi_{ii}(k) d\boldsymbol{k}$$

.... (6.12)

The autocorrelation tensor R_{ii} is already discussed in Chapter 3, whereas, ψ_{ii}(k) is the velocity spectrum tensor and is also the Fourier transform of the velocity correlation as expressed here.

$$\psi_{ij}(k) = \frac{1}{2\pi^3} \iiint_{-\infty}^{\infty} R_{ij}(r) e^{-i\boldsymbol{k}.\boldsymbol{r}} d\boldsymbol{r}$$

.... (6.13)

The inverse transform of this can be obtained as

$$R_{ij}(\boldsymbol{r}) = \overline{U_i'(\boldsymbol{x}) U_i'(\boldsymbol{x}+\boldsymbol{r})} = \iiint_{-\infty}^{+\infty} \psi_{ij}(k) e^{-i\boldsymbol{k}.\boldsymbol{r}} d\boldsymbol{k}$$

.... (6.14)

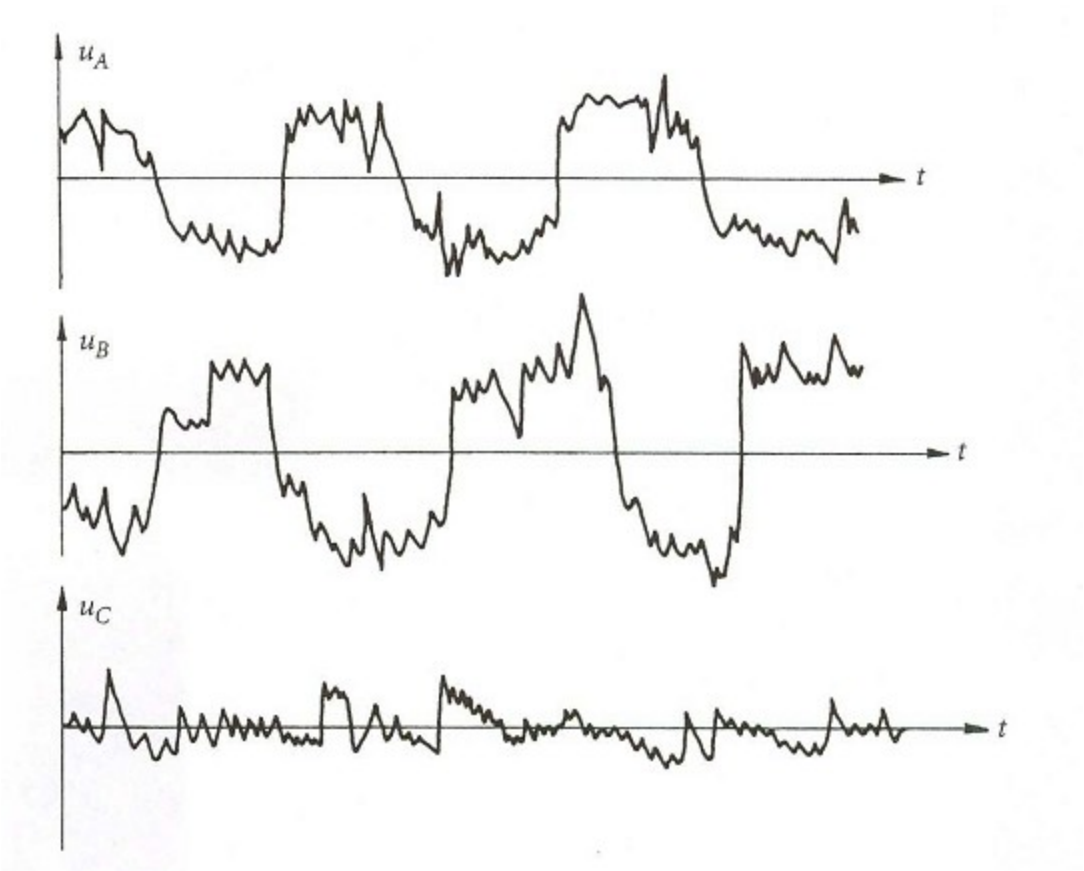

Figure 6.2*: Trace of velocity components in a hot-wire measurement* (Davidson 2004).

At this point, it is important to revisit the energy spectral function, *E(k)* (discussed in chapter 3) in the context of Eq. (5.13). The energy spectrum function vector *E(k)* can be expressed in terms of autocorrelation tensor $R_{ij}(r)$ as (Bradshaw, Ferriss et al. 1964):

$$E_{ij}(k_i) = \frac{1}{\pi}\int_{-\infty}^{+\infty} R_{ij}(r_i)e^{-ik_i.r_i}d\boldsymbol{r_i},$$

i=1, 2, 3. .... (6.15)

And from Eq. (5.15) and (5.13), it is easy to infer the relation between energy spectra function and velocity spectrum function as follows,

$$E_{ij}(k_i) = \iint_{-\infty}^{+\infty} \psi_{ij}(\boldsymbol{k})dk_j dk_k.$$

i=1, 2, 3. .... (6.16)

Eq. (6.15) and (6.16) are referred to as the *Fourier transform pair* for velocity and energy spectrum functions.

6.2.4 Energy Spectrum Function

A detailed discussion about the physical process of generation of turbulent energy spectrum is made in section 3.3. An expression according to Kolmogorov's law for the energy spectrum was presented as $E(k) = C_k \varepsilon^{2/3} k^{-5/3}$. An isotropic behaviour has been adopted for convenience in generation of energy spectrum function, which provides a simplification in generating various components for the velocity correlation tensor $\psi_{ij}(\boldsymbol{k})$, which can finally be expressed as a unique energy spectrum function $E(\boldsymbol{k})$ (see Eq. (6.16)). From Eq. (3.8), kinetic energy expression can now be inferred as

$$k = \frac{1}{2} U_i'^{\,2} = \int_0^\infty E_{ij}(\kappa) d\kappa \qquad \text{.... (6.17)}$$

Further assuming isotropic conditions, the velocity spectrum $\psi_{ij}(\kappa)$ can be assumed to be only dependent upon wavenumber vector $\boldsymbol{k}$ and must have the form,

$$\psi_{ij}(\boldsymbol{\kappa}) = A(\boldsymbol{k})\delta_{ij} + B(\boldsymbol{k}) k_i k_j \qquad \text{.... (6.18)}$$

A spectral incompressibility condition can be imposed to formulate the expression

$$k_i \psi_{ij}(\boldsymbol{\kappa}) = 0 \qquad \text{.... (6.19)}$$

Eq. (6.18) and (6.19), along with Eq. (6.17) and due application of Gauss's theorem, can provide the expression for velocity spectrum function as

$$\psi_{ij}(k_i) = \frac{E(k)}{6\pi k^2}\left(\delta_{ij} - \frac{k_i k_j}{k^2}\right)$$

.... (6.20)

which leads to the energy spectrum function with application of Eq. (6.16) as

$$E_{ii}(k_i) = \iint_{-\infty}^{\infty} \frac{E(k)}{2\pi k^2}\left(1 - \frac{k_i^2}{k^2}\right) dk_j dk_k$$

i=1, 2, 3. .... (6.21)

There have been various implementations of energy spectrum in the past and a few of the important ones are discussed here.

Kolmogorov's 5/3rd energy spectrum: Kolmogorov's energy spectrum is one of the earlier works done in the area of energy spectrum function which depicted the close to ideal picture of turbulence small scales at high Reynolds number. The details of this model and its various scales were explained in the sections 3.3 and 3.5 of Chapter 3. The final energy spectrum is given by Eq. (3.1) and its related scales are listed in Eq. (3.7).

Gaussian energy spectrum: A Gaussian probability distribution of velocity correlation is assumed for the fluctuation in this case. The Gaussian spectrum simplifies the model and provides a bell shape distribution as shown in the case of PDFs (Ghanem 1999). The velocity correlation leads to the energy spectrum function *E(k)* as

$$E(k) = \overline{U'^2}\frac{k^4}{8\sqrt{\pi}}\Delta^5 \exp\left(\frac{-k^2\Delta^2}{4}\right)$$

.... (6.22)

where Δ is proportional to the inverse of the Gaussian distribution spread. However, it has been experimentally found that the real turbulence distribution is far from Gaussian in nature.

Pope's energy spectrum: Pope (Pope 2000) in his work introduced an energy spectrum which provides an accurate representation of turbulence spectra and is found to be very close to the real turbulence spectrum. The spectrum is a mixed model which is derived from both Von-Karman and Kolmogorov spectra and is depicted as

$$E(k) = C_c \varepsilon^{2/3} K^{-5/3} \left\{ \frac{kL}{((kL)^2 + c_L)^{1/2}} \right\}^{\frac{5}{3}+p_0} \exp\left\{ -\beta((k\eta)^4 + {c_\eta}^4)^{1/4} - c_\eta \right\} \quad \text{.... (6.23)}$$

where C_c, c_L, β, c_η are constants and p_0 is a constant with most likely value of 2. L and η are the characteristic length scale for large eddies and Kolmogorov eddies respectively.

Von-Karman energy spectrum: This spectrum is so far the most realistic analytical representation of energy spectrum *E(k).* The spectrum was primarily aimed at smaller and intermediate wave number ranges but is found to work well for even higher wavenumbers, as there is an exponential term added in the spectrum (Hinze 1975). The exponential term in the equation ensures that higher spectral moments converge smoothly in the spectrum. Being one of the most accurate models, it has been modified on various occasions (Goedecke, Ostashev et al. 2004, Bauer, Zeibig 2006) and the latest modified Von-Karman spectrum is as follows:

$$E(k) = C_E \frac{{u_{rms}}^2}{k_e} \frac{(k/k_e)^4}{(1 + (k/k_e)^2)^{17/6}} \exp\left(-2(k/k_\eta)^2\right) \quad \text{.... (6.24)}$$

$$k = (k_i k_i)^{1/2}, \qquad k_\eta = \varepsilon^{1/4} \nu^{-3/4} \quad \text{.... (6.25)}$$

The integration of energy spectrum over all wavenumbers provides the coefficient C_E and is found by the expression,

$$C_E = \frac{4}{\sqrt{\pi}} \frac{\Gamma(17/6)}{\Gamma(1/3)} \approx 1.453.$$

where the gamma function,

$$\Gamma(z) = \int_0^\infty e^{-z'} x^{z-1} dz'$$

.... (6.26)

A comparative study by Ostashev *et al*. clearly suggests the superiority of Von-Karman spectrum over others, as shown in Figure 6.3 (Ostashev, Brähler et al. 1998).

6.3 Recycling Method for Inflow Condition in LES and DNS

The recycling method is one of the most accurate techniques to generate an inflow condition for LES and DNS, where a precursor simulation generates a sufficiently accurate boundary condition for main simulation. There are various ways to generate the library for precursor simulation, for example using periodic boxes of turbulence or cyclic channel flow calculation using periodic boundary condition, as shown in Figure 6.4. It is also important to note that precursor simulation need not necessarily be at the same Reynolds number and is only supposed to provide a realistic scale of turbulence at the inlet.

Breuer and Rodi (Breuer, Rodi 2007)in their precursor method of a periodic channel duct, produced inlet data for a 180 degree bend periodic duct (shown in Figure 6.5). On the other hand, Spalart (Spalart 1988) performed a DNS simulation of a spatially developing boundary layer using zero-gradient boundary by using an additional source term in the Navier-Stokes equation with periodic boundary in a streamwise direction.

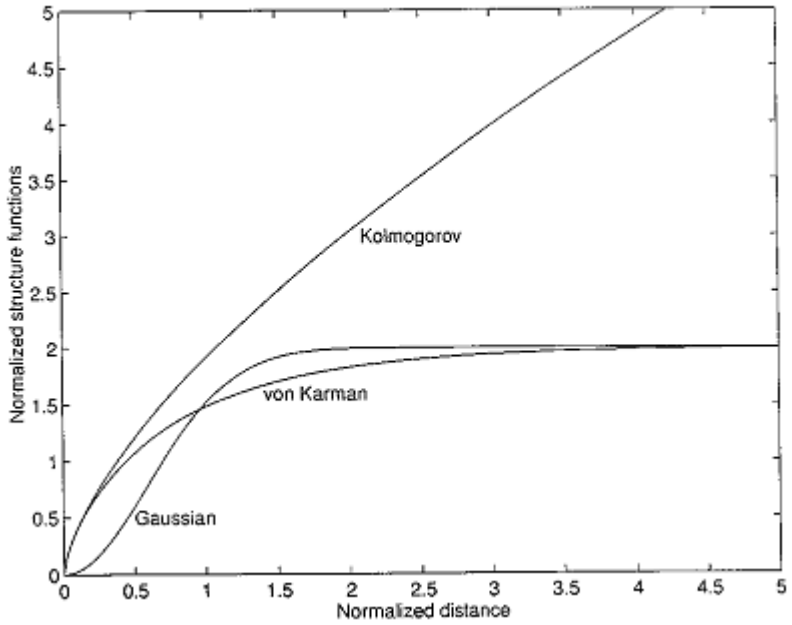

Figure 6.3: *Comparison of three energy spectrum function (Ostashev, Brähler et al. 1998).*

He further modified his work by adding a fringe region in the end of domain to enforce decreased boundary-layer thickness, so that the periodic boundary can be reintroduced at the inlet (Spalart, Watmuff 1993).

Cyclic method: For computing fully developed turbulent pipe flow, it is required that the flow is invariant in the streamwise direction and generally this requires a pipe length of 40 times the diameter. However, the cyclic method can produce invariance with a very short section of pipe and has been extensively been used in LES and DNS study of wall bounded flow (Fureby, Gosman et al. 1997, Lamballais, Lesieur et al. 1997).

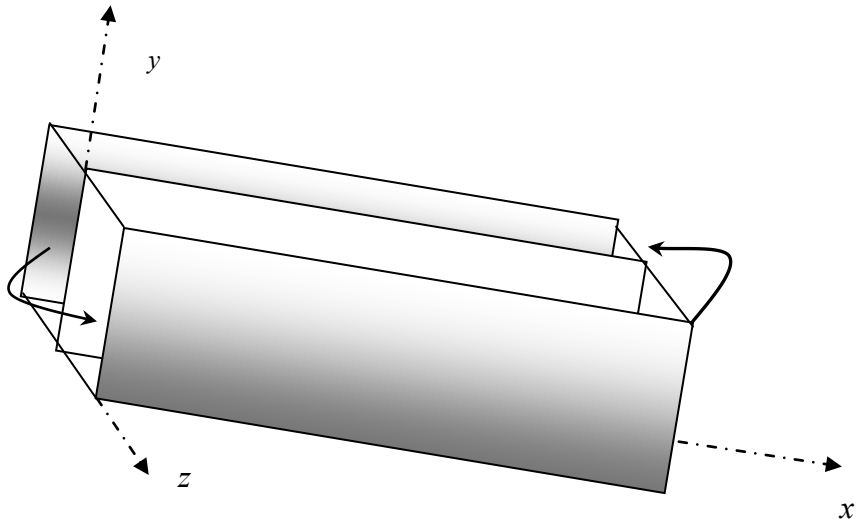

Figure 6.5: *Geometry of the* Breuer and Rodi's *channel with flow in x-direction.*

Mapping method: Precursor calculation is performed at the samples downstream of the inlet and the sample is then mapped back at the inlet (Tabor, Baba-Ahmadi et al. 2004, de Villiers 2006). Chung and Sung (Chung, Sung 1997) in a comparative study of various inflow conditions along with their spatiotemporal inflow condition introduced the spatial and temporal database of cut-plane which sweeps across the length at single time-step. They used Taylor's frozen field hypothesis during sweeping across the cutting planes. Despite the varying flow velocity across channel length, this method produced a reasonable inflow condition.

Although recycling methods are very accurate as an inflow for LES or DNS, these are computationally expensive and are not applicable to most of the flow simulation of practical

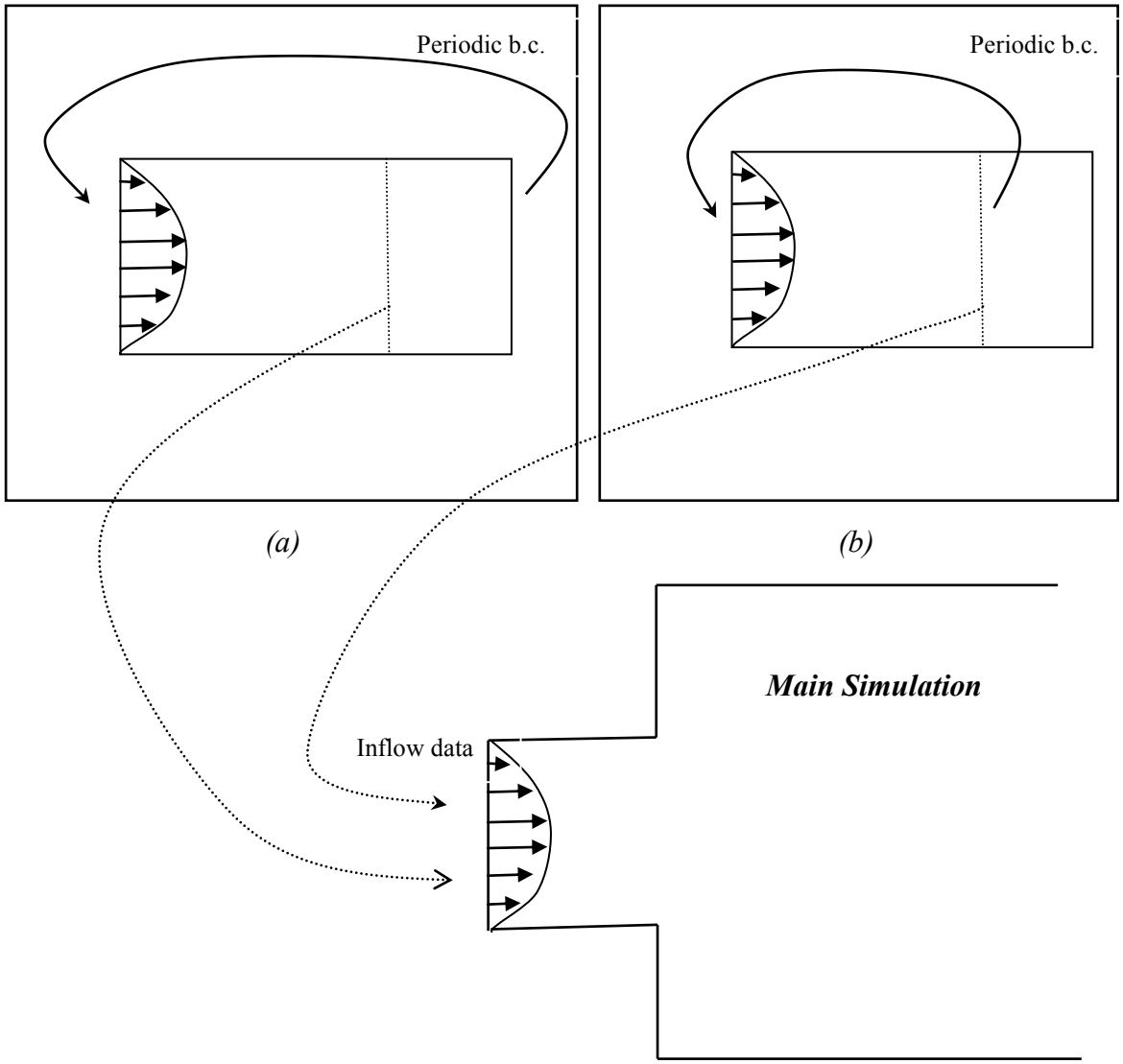

Figure 6.4: *(a) Cyclic inflow generation (b) Mapped or rescaled inflow generation.*

importance. In simulation of acoustic propagation in muffler, for example, in case of longer inlet and outlet makes the computation too expensive and the recycling of the acoustic information from the downstream to upstream flow go against the purpose of simulation to evaluate acoustic attenuation. Synthetic boundary condition is found to be a good alternative for generation of inflow condition for LES or DNS.

6.4 Synthetic Boundary Condition for LES and DNS

It is widely accepted that a realistic inlet boundary conditions are crucial for accuracy of a computational simulation. RANS approaches only require the mean profile for velocity and turbulence variable for an accurate solution but it is not as straight forward for the LES or DNS. The inflow data for LES or DNS require turbulent unsteady inflow conditions. To obtain the turbulent unsteady inflow, there has been a lot of research performed and techniques devised recently.

6.4.1 Random Perturbation Method

This method uses random pattern over inlet boundary in such a way that the pattern matches the turbulence statistics. It is one of the simplest approaches to generating synthetic inflow condition. A Gaussian distribution of zero mean and unit variance is used to generate random fluctuations and is imposed upon the uniform mean inlet velocity as follows:

$$U_i = \overline{U}_\iota + C_r u_i' n_r \quad \text{.... (6.27)}$$

where U_i is the instantaneous velocity, $\overline{U}_\iota$ is the uniform mean velocity, u_i' is the square root of turbulence intensity, n_r is the random number between 0 and 1, and C_r is the parameter which ascertains the amplitude of fluctuation based on the distance of the point from the wall. Clearly, u_i' in this case can be represented in terms of kinetic energy *k* as

$$u_i' = \sqrt{\frac{2}{3}k} \quad \text{.... (6.28)}$$

However it is important to note that there are no significant two-point spatial correlations between velocity components and there is no two-point temporal correlation either.

An effort has been made by Lund *et al.* (Lund, Wu et al. 1998) to bring some correlation between the velocity components by constructing a signal matching the target Reynolds stress tensor using Cholesky decomposition a_{ij} of the Reynolds stress tensor R_{ij}. The turbulent fluctuation are then similarly imposed over mean values, as follows,

$$U_i = \bar{U}_\iota + u_r a_{ij} \quad \text{.... (6.29)}$$

where a_{ij} is given by

$$a_{ij} = \begin{pmatrix} \sqrt{R_{11}} & 0 & 0 \\ R_{21}/a_{11} & \sqrt{(R_{22} - a_{21}^2} & 0 \\ R_{31}/a_{11} & (R_{32} - a_{21}a_{31})/a_{22} & \sqrt{R_{33} - a_{31}^2 - a_{32}^2} \end{pmatrix} \quad \text{.... (6.30)}$$

Although Lund's method provides correlation between the velocity components, it does not really provide any spatial or temporal correlation. This results in uniform spreading of energy across all wavenumbers and therefore contains excess energy at small scale, contrary to the physical turbulence phenomenon.

6.4.2 Streak Transient Growth Method

A typical recycling technique usually takes many flow-through times to start a transition to a real turbulence regime. This is believed to be because of the perturbations produced from the numerical simulation errors after many flow-through times (Schoppa, Hussain 2000, de Villiers 2006). This method is computationally very expensive and sometimes is not useful in propagation problems. On the other hand, algebraic methods like random perturbation methods do not seem to generate turbulence like structure and correlations. A simplistic approach has been adopted by Schoppa *et al.* (Schoppa, Hussain 2000) in their work to produce turbulence structures with proper statistical characteristics of turbulence. This approach has already been described in details in section 3.4.2.

As was explained earlier in section 3.4.2, near-wall streaks are unstable to sinusoidal perturbations in a channel flow solution and a sinusoidal perturbation can initiate an instability which in turn produces vortices and shear layer, which end up kick-starting the near-wall cycle. Therefore it is possible that if these streaks are produced artificially then they would interact with mean flow to cause instabilities which in turn would end up kick starting a near-wall turbulence cycle. In this case, a laminar parabolic profile is used as the initial inflow profile. This parabolic profile (U_0^+) is then superimposed with near-wall parallel streak of slow and fast moving fluids using Eq. (3.5) as

$$U^+(x^+, y^+) = U_0^+(y^+) + (\Delta u_0^+/2)\cos(b^+ z^+)\left(\frac{y^+}{30}\right)\exp(-c_\sigma y^{+2} + 0.5),$$

$$V^+ = W^+ = 0 \qquad \text{.... (6.31)}$$

This mean flow profile (U^+) is then perturbed to give wave character which would produce streamwise vortices using the following equation:

$$w(x^+, y^+) = c_\sigma \sin(a^+ x^+)\, y^+ \exp(-c_\sigma y^{+\,2}).$$

$$u = v = 0. \qquad \text{.... (6.32)}$$

where constant a^+ and $b^+$are chosen to produce sparse streak spacing, constant c_σ is the linear perturbation amplitude and term Δu_0^+ is the wall normal circulation of streak. This method has been used in channel flow simulation with considerable success (de Villiers 2006).

6.4.3 Digital Filter based Methods

Despite providing some correlation and generating turbulence like structure, the streak transient growth method takes a lot of time to achieve steady state and is obviously not universally applicable, considering its wall-bounded genesis. The correlation produced has also not been

found to be very strong in space and time. Klein *et al.*(Klein, Sadiki et al. 2003) and Schluter *et al.* (Schluter, Pitsch et al. 2004) in their work inferred that random inflow methods usually loses its turbulence character immediately downstream and lacks the large scale structures and therefore provides the same result as the laminar inlet profiles do. An approach to produce artificial velocity data to remedy those problems is adopted by Klein *et al.* (Klein, Sadiki et al. 2003) which reproduces the first and second order one point statistics using given autocorrelation function. The random fluctuation fields (Gaussian shaped) in all three dimensions are generated with zero mean ($\mu = 0$) and unit variance ($\sigma = 1$) and are filtered. It was assumed that if r_m is the series of random data then a linear non-recursive digital filter can be defined as,

$$u_m = \sum_{n=-N}^{N} b_n r_{m+n} \quad \text{.... (6.33)}$$

where b_n are the filter co-efficient. The three dimensional filter is then obtained with convolution of these one dimensional filters as,

$$b_{ijk} = b_i . b_j . b_k \quad \text{.... (6.34)}$$

An autocorrelation function is then obtained by transforming the correlated data from an amplitude tensor related to Reynolds stress tensor. A special shape for R_{uu} is therefore considered and it has, for a given time, the form:

$$R_{uu}(k\Delta x) = \frac{\overline{u_m u_{m+k}}}{\overline{u_m u_m}} = \sum_{j=-N+k}^{N} b_j \, b_{j-k} / \sum_{j=-N}^{N} b_j^2 = \exp\left(-\frac{\pi k^2}{4n^2}\right) \quad \text{.... (6.35)}$$

where the desired length scale is $L = n\Delta x$ and filter co-efficient is $\widetilde{b_k} = \exp\left(-\frac{\pi k^2}{2n^2}\right)$. After the filtering operation, a spatially correlated data is obtained for velocity as

$$U_\alpha(j,k) = \sum_{i'=-N_x}^{N_x} \sum_{j'=-N_y}^{N_y} \sum_{k'=-N_z}^{N_z} b(i',j',k') R_i(i', j+j', k+k') \quad \text{.... (6.36)}$$

This is then superimposed on average velocity field to obtain target velocity profile and Reynolds stress profile as

$$u_i = \overline{u_\iota} + a_{ij} U_i \quad \text{.... (6.37)}$$

This velocity profile is then fed into the first layer of the inflow plane. Random fields are generated using Eq. (6.36) and (6.37), which are again fed to inflow before shifting the previous layer to the next layer. There inflow data is generated in these three layers to produce space and time correlated data. The coefficient a_{ij} is obtained by Eq.(6.35). Klein *et al.* tested this method for direct simulation of a turbulent jet (Klein, Sadiki et al. 2003). Veloudis *et al.* (Veloudis, Yang et al. 2007) used digital filter for a repeating periodic channel flow simulation. In the investigation, they estimated length scale based on streamwise direction and found that improved results could be obtained with varying length scale in the filtering process. In contrast, di Mare *et al.* (di Mare, Klein et al. 2006) attempted to achieve filter coefficients b_k by inverting Eq. (6.35). The coefficient for the two point correlation tensor is extracted and decomposed as

$$b_{ik} = \sqrt{\lambda_k \nu_{ik}} \quad \text{.... (6.38)}$$

where ν_{ik} are the eigen vectors of the correlation tensor and λ_k are the corresponding eigen values. The coefficients b_{ik} are considered as characteristic eddies of physical space and these methods

are usually referred to as Proper Orthogonal Decomposition (POD). Although these methods are deployed for large eddy simulation of boundary layer flow, they are found to be difficult to implement in coupled RANS-LES solvers. Ewert (Ewert 2005, Ewert, Emunds 2005) also proposed a method inspired from digital filter using space correlation, where a solenoidal (divergence free) velocity field was considered for a computational aeroacoustics (CAA) noise identification problem. The argument was made that the non-solenoidal velocity field would give rise to spurious wave which would contaminate the flow solution (Ewert, Emunds 2005). A stream function is generated by random field filtering (Eq. 6.39) which is later correlated in lateral and longitudinal direction for true representation of turbulence:

$$\psi(x,t) = \int_{-\infty}^{\infty} G(x-x').r(x')dx' \qquad \text{.... (6.39)}$$

where G has the same form as filter coefficient b_k. The divergence free guaranteed solenoidal field can be achieved in tems of stream function as

$$U_1' = \frac{\partial \psi}{\partial y}\ ,\ U_2' = -\frac{\partial \psi}{\partial x} \qquad \text{.... (6.40)}$$

Recently a modified form of this method named the Random Particle-mesh (RPM) method was also introduced by Ewert (Ewert 2008) where a temporal correlation is also introduced in the inflow condition of CAA simulation. Ewert's method is found to be very effective in noise identification problems in CAA.

Recently, Fathali *et al.* (Fathali, Klein et al. 2008, Fathali, Meyers et al. 2008, Fathali, Klein et al. 2009) have further extended the work of Klein *et al.*(Klein, Sadiki et al. 2003) by introducing velocity field as the linear combination of individual uncorrelated filtered random fields. These

related linear combinations provide a multi-correlation among different velocity components, which produces different integral scales, cross-integral length scales, and correct Reynolds stress values. Velocity components as a linear combination of different uncorrelated random field f_{ij} can be given as

$$u = a_{11}f_{11} + a_{12}f_{12} + a_{13}f_{13}$$

$$v = a_{21}f_{12} + a_{22}f_{22} + a_{23}f_{23}$$

$$w = a_{31}f_{13} + a_{32}f_{23} + a_{33}f_{33} \quad \text{.... (6.41)}$$

Clearly, the presence of f_{13} and other similar terms in expression of u and w (and u) introduces a cross-correlation between these components. These velocity fields are related to Reynolds stress via autocorrelation function as

$$R_{uu} = (a_{11})^2 r_{11} + (a_{12})^2 r_{12} + (a_{13})^2 r_{13}$$

$$R_{vv} = (a_{21})^2 r_{21} + (a_{22})^2 r_{22} + (a_{23})^2 r_{23}$$

$$R_{ww} = (a_{31})^2 r_{31} + (a_{32})^2 r_{32} + (a_{33})^2 r_{33}$$

$$R_{uv} = (a_{12})(a_{21}) r_{12}$$

$$R_{uw} = (a_{13})(a_{31}) r_{13}$$

$$R_{vw} = (a_{23})(a_{32}) r_{23} \quad \text{.... (6.42)}$$

The presence of cross integral length scale and corresponding Reynolds stress scales provides a better estimate of local length scale and local Reynolds stress. Although this method is slightly

more expensive than Klein *et al.*'s original digital filter, the accuracy obtained is found to be worth the extra computational cost in various applications.

6.4.4 Spectral Methods

Spectral methods are one of the most extensively used and easy to implement methods for inflow in LES and DNS simulation. These methods provide the most sought for temporal and spatial correlation in turbulence characteristic at the inlet. Fourier synthesis techniques are among the most important attempts in generating spectral method for inflow turbulence generation. Since a Fourier series can be expressed in terms of any periodic function, therefore an estimated mean velocity profile in *x*-direction can be decomposed as

$$\overline{U}_x = U_m \left(\frac{\overline{a_0}}{2} + \overline{a_1} \cos ky + \overline{a_2} \cos 2ky + \cdots + \overline{b_1} \sin ky + \overline{b_2} \sin 2ky \ldots \right) \quad .. (6.43)$$

where U_m is the maximum flow velocity and the shape of the velocity profile is govern by the Fourier series. The coefficients of the series are replaced with the stochastic random variables to generate a new series for original mean value as

$$U_x = U_m \left(\frac{a_0}{2} + a_1 \cos ky + a_2 \cos 2ky + \cdots + b_1 \sin ky + b_2 \sin 2ky \ldots \right) \quad .... (6.44)$$

where coefficients are obtained from Uhlenbeck-Ornstein process with original mean value, μ along with specified variance, σ. Therefore the new Fourier series with coefficients related as $a_i = a_i(\mu = \overline{a_i},\ \sigma^2)$ produces a spatially coherent velocity field. A fluctuation field around the mean can be obtained by subtracting Eq. (6.44) and (6.43) as follows:

$$U'_x = U_m \sum_{i=1}^{N} a'_i \cos iky$$

.... (6.55)

where $a_i' = a_i - \overline{a_\iota}$, and is a stochastic variable with zero mean and finite variance. This method was first attempted to generate synthetic velocity by Kraichnan (Kraichnan 1969) for a three-dimensional homogeneous and isotropic flow (Eq. 6.11). For three-dimensional space, velocity spectrum function Eq. (6.11) can be modified to include the random phase angle ϕ_k to obtain an approximation of the modified velocity spectrum as

$$U'(x) = \sum_{k=1}^{N} U_k e^{i(\boldsymbol{k}.\boldsymbol{x}+\phi_k)},$$

.... (6.56)

Rogallo (Rogallo 1981) used this method to map velocity field for study of turbulence decay. Amplitude of the velocity field in this case was obtained from the simple consideration of energy spectrum function ($U_k = r\sqrt{E|k|}$). Bachera *et al.*(Bachera, Bailly et al. 1994) have also established a spatially correlated turbulent field with no actual temporal correlation. A time series of independent spatially correlated velocity fields is filtered in a frequency domain with a dominant frequency at $f_0 = \epsilon/K$. For that purpose, an inverse Fourier transform of function $\tilde{G}(f)$ (Gaussian distribution centred at f_0) is calculated and defined as

$$\tilde{G}(f) = e^{-\frac{(f-f_0)^2}{a^2 f_0^2}} \quad \text{.... (6.57)}$$

Besides this method being computationally expensive, the convectional effect in typical shear flow is not found to have been accounted for in this method.

Karweit *et al.* (Karweit, Blanc-Benon et al. 1991*)* have provided a distinct representation of Kraichnan's formulation and expressed wavenumber modes in vectorial form as

$$U'(x) = \int_{-\infty}^{\infty} (U_k \sigma(\boldsymbol{k})) e^{i(\boldsymbol{k}.\boldsymbol{x}+\phi_k)}$$

.... (6.57)

where $\sigma(\boldsymbol{k})$ is the direction of each mode number. Eq. (6.57) can be simplified and expressed for the real part of Eq. (6.57) in terms of a finite sum of modes as

$$U'(x) = 2\sum_{r=1}^{N} U_r \cos(\boldsymbol{k_r}.\boldsymbol{x} + \phi_r)\, \boldsymbol{\sigma_r}$$

.... (6.58)

where U_r are amplitudes, ϕ_r are phase angles and $\boldsymbol{\sigma_r}$ are the direction of the r^{th} Fourier mode. U_r is obtained from the energy spectrum for that particular wavenumber range Δk as

$$U_r = \sqrt{E(k)\Delta k.} \quad \text{.... (6.59)}$$

The vector $\boldsymbol{k_r}$ is a random selection of vectors in a spherical wave space of radius $\|k_r\|$. From the Fourier expansion Eq. (6.44) it is clear that all modes in the frequency domain have to satisfy following restriction for incompressibility consideration:

$$\boldsymbol{k_r}.\boldsymbol{\sigma_r} = 0 \quad \text{.... (6.60)}$$

So it can be inferred that the vector k_r and the direction of the turbulent fluctuation mode σ_r are perpendicular to each other. This method has been particularly successful in noise propagation problems. However the temporal correlation has found to be missing in this implementation, which rules out a very crucial implementation, hence it was later modified for temporal correlation to be successfully implemented in problems involving noise identification.

Bailly *et. al.* (Bailly, Lafon et al. 1995, Bailly, Juve 1999) attempted to alleviate the problem encountered by Bachera *et al.* in relation to convectional effect in typical shear flows. The sum of

the finite Fourier series in their implementation consist of a local convection velocity term U_c to obtain an isotropic velocity spectrum as

$$U'(x,t) = 2\sum_{r=1}^{N} U_r \cos(\boldsymbol{k_r}.(\boldsymbol{x} - t\boldsymbol{U_c}) + \phi_r + \omega_r t)\,\boldsymbol{\sigma_r} \quad \text{.... (6.61)}$$

where ω_r is the angular frequency of rth mode and is a random Gaussian distribution in probability density function. This is expressed as

$$P(\omega_r) = \frac{1}{\omega_{0r}\sqrt{2\pi}} \exp\left\{-\frac{(\omega-\omega_{0r})^2}{2\omega_{0r}^2}\right\} \quad \text{.... (6.62)}$$

where $\omega_{0r} = k_r\sqrt{2K/3}$, is function of wavenumber and K is usually obtained from RANS simulation. Considering the isotropic assumption, the Von-Karman spectrum explained in section 6.2.4 is considered in this method.

$$E(k) = C_E \frac{{u_{rms}}^2}{k_e} \frac{(k/k_e)^4}{(1+(k/k_e)^2)^{17/6}} \exp\left(-2(k/k_\eta)^2\right)$$

where k_e is the wavenumber at which maximum spectral energy is found in the energy spectrum curve. This value of k_e is found by considering the length scale L as the integral equation as

$$L = \frac{1}{\overline{U_r'^2}} \frac{\pi}{2} \int_0^\infty \frac{E(k)}{k} dk \quad \text{.... (6.63)}$$

This integral equation provides the constant k_e on calculating maxima as,

$$k_e = \frac{9\pi}{55}\frac{C_E}{L}. \quad \text{.... (6.64)}$$

Although this method is computationally cost effective and memory efficient, these methods still overestimate the noise prediction. This method has been used in noise prediction of both external flow like the circular jet (Bailly, Lafon et al. 1995) and internal flow like the diaphragm duct (Bailly, Lafon et al. 1996). However this method, like many other methods, also lacks time correlation which reduces the value of this method for noise prediction calculations.

Meanwhile, Lee et al. (Lee, Lele et al. 1992) proposed a spectral method with spatial correlation using Taylor's hypothesis in low Mach number compressible flow. This spectral method was later modified by rescaling the fluctuation magnitude as in Eq. (6.29) by Le et al. (Le, Moin et al. 1997) to match the desired Reynolds stress tensor. The modified method is then used to generate inflow condition in simulation of backward facing step problem. However, not only this method lacks the temporal correlation but also it is computationally complex in compared to Lee et al. (Lee, Lele et al. 1992), considering the inverse Fourier transform in the near-wall region is complex. Blom et al. (Blom, Verhaar et al. 2001) and then Snellen et al. (Snellen, Lier et al. 2003) proposed a spectral method based on Karweit et al. (Karweit, Blanc-Benon et al. 1991) which uses the velocity spectrum

$$U'(x,t) = 2\sum_{r=1}^{N} U_r e^{\boldsymbol{i}(\boldsymbol{k_r}.\boldsymbol{x}+\omega_r t)}\boldsymbol{\sigma_r}$$

The method uses the so-called moving axis spectrum $\psi_r(\omega)$ to take into consideration the convection effect on turbulence by mean flow. The term $\psi_r(\omega)$, however, is similar to the Bailly et al.'s (Bailly, Lafon et al. 1995) probability density function (Eq. (5.62)) and only differs in implementation. The method filters the energy spectrum with $\psi_r(\omega)$ to obtain velocity spectrum amplitude U_r as

$$U_r = \sqrt{\tilde{E}(k_r, \omega_r)\Delta k},$$

$$\tilde{E}(k_r, \omega_r) = E(k_r)\psi_r(\omega),$$

$$\psi_r(\omega) = \frac{1}{\omega_{0r}\sqrt{2\pi}} \exp\left\{-\frac{(\omega-\omega_{0r})^2}{2\omega_{0r}^2}\right\}. \quad \text{.... (6.65)}$$

where $E(k_r)$ employs the Von Karman spectrum explained in Eq. (6.24). Despite a different implementation of convection of turbulence, this method is still no better than Bailly et al.'s approach. Smirnov et al. (Smirnov, Shi et al. 2001) modified Karweit et al.'s formulation based on local time and length scale to generate a non-homogeneous, anisotropic turbulence by explicit diagonalisation of the Reynolds stress R_{ij}. The modifield velocity signal is expressed as

$$U'(x,t) = \sqrt{\frac{2}{N}} \sum_{r=1}^{N} a_r \cos(\boldsymbol{k_r}'.\boldsymbol{x}' + \omega_r t') + b_r \sin(\boldsymbol{k_r}'.\boldsymbol{x}' + \omega_r t')$$

$$x' = \frac{x}{L}, \qquad t' = \frac{t}{\tau}, \qquad k_r' = k_r c'$$

.... (6.66)

The energy spectrum used in this method has the form

$$E(k) = 16\frac{\sqrt{2}}{\sqrt{\pi}} k^4 \exp(-2k^2) \quad \text{.... (6.67)}$$

The method can be used for anisotropic turbulence length scale and has been used as the inflow condition for LES.

In order to provide an effective scheme with temporal correlation, Billson et al. (Billson, Eriksson et al. 2003) put forward a method which synthesizes isotropic fluctuation at each time step *m* using an asymmetric filter as follows:

$$U'_i(x)^m = \boldsymbol{a}\, U'_i(x)^{m-1} + \boldsymbol{b}\, \widetilde{U'}_i(x)^m$$

$$\boldsymbol{a} = \exp\left(\frac{-\Delta t}{\tau}\right) \quad , \quad \boldsymbol{b} = \sqrt{(1-\boldsymbol{a}^2)}$$

.... (6.67)

where $\widetilde{U'}_i(x)^m$ generates velocity field for time step *m* using Karweit et al.'s (Karweit, Blanc-Benon et al. 1991) method expressed in Eq. (6.58). The value of **a** and **b** are kept such that the RMS value of $U'_i(x)^m$ and $\widetilde{U'}_i(x)^m$ still remains the same but at the same time provides the correlation between instances in time. The time scale τ in this case is obtained from the RANS simulation by calculating the average kinetic energy as follows:

$$\tau = f\frac{\bar{K}}{\epsilon} \qquad \text{.... (6.68)}$$

Davidson and Billson (Davidson 2007b, Davidson, Billson 2004, Davidson, Billson 2006) have further attempted to simulate a hybrid LES-RANS with the same time correlation, but with different set of boundary methods for near wall space. The method employs Karweit et al.'s spectral equation (6.58) with fluctuations generated in all three dimensions as follows:

$$U'(x) = 2\sum_{r=1}^{N} U_r \cos(\boldsymbol{k_r}.\boldsymbol{x} + \phi_r)\, \boldsymbol{\sigma_r}$$

It is important to remember that the wavenumber k_r is a random selection of vector about a sphere of radius equal to $\|k_r\|$ as shown in Figure 6.6. The expression satisfies the criteria of Eq. (5.60) to ensure that the direction of wavenumber k_r and direction of fluctuation mode σ_r remain orthogonal (perpendicular to each other). U_r is again obtained from the energy spectrum for a particular wavenumber range Δk using expression

$$U_r = \sqrt{E(k_r)\Delta k.}$$

The wavenumber vector k_r can then be defined in its components with different random selection of angles as

$$k_{rx} = \sin\theta_r \cos\varphi_r$$

$$k_{ry} = \sin\theta_r \sin\varphi_r$$

$$k_{rz} = \cos\theta_r \quad \text{.... (6.69)}$$

The unit vector σ_r which lies in a plane normal to the waveumber vector $\boldsymbol{k_r}$ can be obtained as its components as

$$\sigma_{rx} = \cos\varphi_r \cos\theta_r \cos\alpha_r - \sin\varphi_r \sin\alpha_r$$

$$\sigma_{ry} = \sin\varphi_r \cos\theta_r \cos\alpha_r + \cos\varphi_r \sin\alpha_r$$

$$\sigma_{rz} = -\sin\theta_r \cos\alpha_r \quad \text{.... (6.70)}$$

The direction of vector σ_r is randomly chosen in the plane through α_r, as shown in Figure 6.7. The associated probability distribution of random variables can be listed as in Table 6.1.

$P(\varphi_r) = 1/2\pi$	$0 \leq \varphi_r \leq 2\pi$
$P(\phi_r) = 1/2\pi$	$0 \leq \phi_r \leq 2\pi$
$P(\theta_r) = 1/2\sin\theta_r$	$0 \leq \theta_r \leq \pi$
$P(\alpha_r) = 1/2\pi$	$0 \leq \alpha_r \leq \pi$

Table 6.1: *Probability distribution of random variables.*

They also used Von Karman energy spectrum (*E(x)*) discussed in section 6.2.4 and expressed in Eq. (6.24) and (6.25) as,

$$E(k) = C_E \frac{{u_{rms}}^2}{k_e} \frac{(k/k_e)^4}{(1 + (k/k_e)^2)^{17/6}} \exp\left(-2(k/k_\eta)^2\right)$$

$$k = (k_i k_i)^{1/2}, \qquad k_\eta = \varepsilon^{1/4} \nu^{-3/4}$$

where C_E is estimated to be around 1.453 (Section 6.2.4). The parameter k_e (wavenumber with maximum spectral energy) is obtained from Eq. (6.64). Figure 6.7 explains the geometry of the r^{th} mode vector σ_r and wavenumber vector k_r.

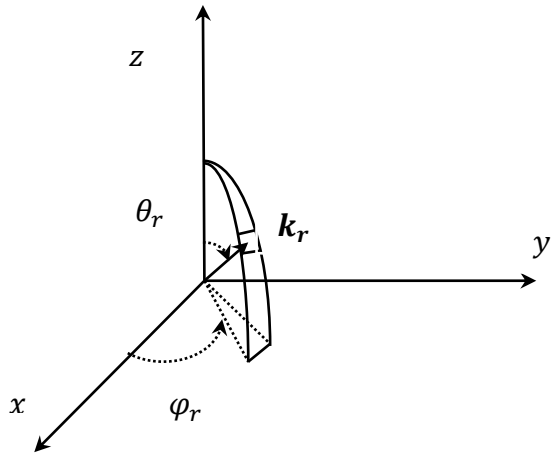

Figure 6.6: *Probability distribution of wavenumber vector k_r.*

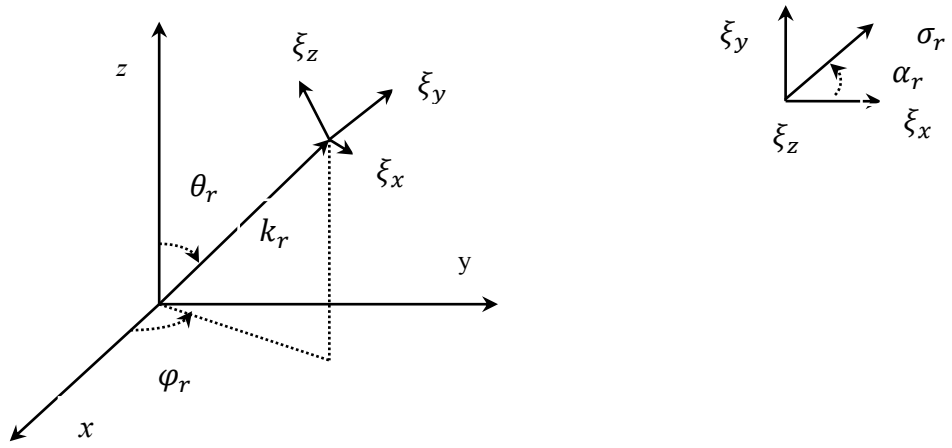

Figure 6.7: *Wavenumber vector k_r and velocity unit vector σ_r for r^{th} mode.*

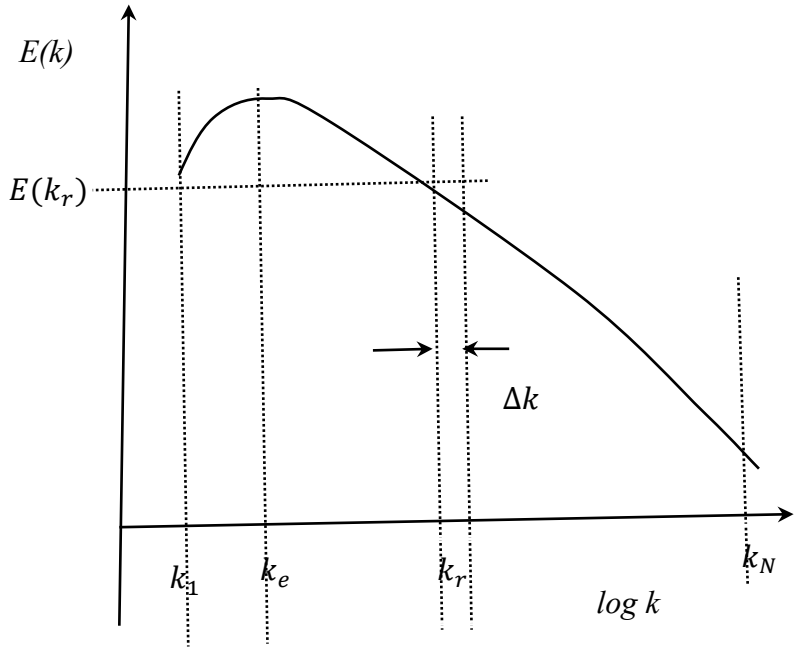

Figure 6.8: *Von Karman spectrum showing minimum and maximum wavenumber.*

The energy spectrum $E(k_r)$ is subdivided into *N* equidistant points with wavenumbers ranging from the minimum k_1 to the maximum k_N. Selection of these two parameters is done considering the energy spectrum shown in Figure 6.8 as follows:

$$k_N = \frac{2\pi}{2\Delta} \quad , \quad k_1 = \frac{k_e}{p} \qquad \text{.... (6.71a)}$$

where Δ is the grid spacing and can be obtained in all three dimensions as

$$\Delta_i = \frac{x_i}{N_i} \quad , \quad i = x, y, z. \qquad \text{.... (6.71b)}$$

The value of k_e can be obtained by knowing the value of *L,* as C_E values are already known to be 1.453. The length scale L can be found from RANS simulation as proportional to the inlet boundary layer thickness δ. In literature it is found that L is 10% of δ (Davidson, Billson 2006, Davidson 2007a, Davidson, Dahlstrom 2007).

$$L \approx 0.1\delta \qquad \text{.... (6.72)}$$

The value of *p* in Eq. (6.71a) is found to be suitable as 2 in most applications.

Besides these, there are some other recently commendable attempts made in the direction of synthetic boundary inflow generation. Jarrin et al. (Jarrin, Benhamadouche et al. 2006, Jarrin, Prosser et al. 2009) proposed a unique method for inflow generation technique based on consideration of turbulence as superimposition of coherent eddies. Coherent structures are generated by a predefined shape function encompassing the spatial and temporal nature of turbulence. A new eddy is generated at the inlet with compact support in the domain $[-r_x, r_x] \times [-r_y, r_y] \times [-r_z, r_z]$. Each eddy is convected by the mean velocity into the inlet and once the old eddy is

out of the domain, a new eddy is generated and convected through the inlet. The turbulent field can be written as the finite sum of *N* eddies as,

$$U_r = U_i + \frac{1}{N}\sum_{k=1}^{N} a_{ij}\epsilon_j^k f_\sigma(x - x^k)$$

.... (6.73)

where *f* is a simple tent function and σ is the length scale for eddies. The velocity signal is then rescaled with Lund's transformation described in Eq. (6.29) and Eq. (6.30) using Cholesky decomposition a_{ij} of the Reynolds stress tensor R_{ij}. This technique has also been employed in various applications of interior and exterior flows for LES simulation (Poletto, Revell et al. 2011, Uribe, Jarrin et al. 2010). Despite its anisotropic characteristic, its application being only found in a few areas. Nevertheless, the method seems to provide good prediction of first and second order statistics and two point correlations for noise prediction applications.

Kornev et al. (Kornev, Kroger et al. 2007, Kornev, Hassel 2007, Kornev, Kroger et al. 2008) have proposed another inhomogeneous turbulence generation method which considers turbulence as random spot distributed in an unknown form evaluated by a prescribed autocorrelation function. The fluctuating velocity components at the nth instant of time can be given as the finite sum of velocities at each spot as

$$U_r(x) = \sum_{i=1}^{M}\prod_{k=1}^{3} f_k(x_{s\,i}, x_k, \rho_{ik})\; sign(d_i - 0.5)$$

... (6.74)

where $x_{s\,i}$ is the centre of the i^{th} spot, d_i is the random number and ρ_i is the length scale of i^{th} spot. The function $f_k(x_{s\,i}, x_k, \rho_{ik})$ is unknown and has to be determined with the help of a prescribed autocorrelation function given by

$$R_{ii}(x, x+\eta) = \frac{\overline{U_\iota(x,t)U_\iota(x+\eta,t)}}{\overline{U_\iota(x,t)^2}} \quad \ldots. (6.75)$$

The velocity signal is then rescaled with Lund's transformation described in Eq. (6.29) and Eq. (6.30) using Cholesky decomposition a_{ij} of the autocorrelation function R_{ii}. Eq. (6.74) provides the two point correlation and temporal correlation whereas Eq. (6.75) provides the one point cross-correlation. These velocity fluctuations are then fed to the inflow of LES simulation. The significance of this formulation of this method is that it is inhomogeneous, exact and anisotropic and provides a more realistic approach to turbulence generation.

6.5 Mixed Spectral Inflow Boundary Condition for LES and DNS

A mixed synthetic inflow boundary condition can be obtained by selecting appropriate correlation function for space and time and also by selecting a true analytical representation of turbulence. Unlike the most recent methods such as those proposed by Jarrin et al. (Jarrin, Benhamadouche et al. 2006), Fathali et al. (Fathali, Klein et al. 2008) and Kornev et al. (Kornev, Kroger et al. 2007) , Davidson et. al.'s (Davidson, Billson 2006) method lacks the cross correlation term in the synthesis. A mixed spectral method is proposed to generate a turbulent velocity field with a designated temporal correlation, two points spatial correlation and one point cross correlation. The method is described as follows:

1) A turbulent velocity field is generated with *N* random Fourier modes with the help of Eq. (6.58) as

$$U_r'(x) = 2\sum_{r=1}^{N} U_r \cos(\boldsymbol{k_r}.\boldsymbol{x} + \phi_r)\,\boldsymbol{\sigma_r}$$

where k_r and σ_r are obtained from Eq. (6.69) and Eq. (6.70). The amplitude of fluctuation U_r is obtained from Eq. (6.59). Angles ϕ_r, α_r, φ_r and θ_r are obtained by random probabi lity distributions (Table 6.1).

2) A Von-Karman spectrum is chosen as given in Eq. (6.24) and is subdivided into *N* equidistant points with wavenumer ranging from $k_1$to k_N, given by Eq. (6.70).
3) The energy spectrum is then summed up with the help of Eq. (6.58) to obtain the three-dimensional velocity fluctuations.
4) At this point, a cross correlation term is introduced by employing Lund's transformation on the velocity components by constructing a signal matching the target Reynolds stress tensor using Cholesky decomposition a_{ij} of the Reynolds stress tensor $R_{ij}$with the help of the equation

$$v'_i = U_r a_{ij} \qquad \ldots. (6.76)$$

where a_{ij} is again given by a normalised form of Eq. (6.30) as:

$$a_{ij} = \frac{1}{\sqrt{R_{11}}} \begin{pmatrix} \sqrt{R_{11}} & 0 & 0 \\ R_{21}/a_{11} & \sqrt{R_{22} - a_{21}^2} & 0 \\ R_{31}/a_{11} & (R_{32} - a_{21}a_{31})/a_{22} & \sqrt{R_{33} - a_{31}^2 - a_{32}^2} \end{pmatrix}$$

5) A temporal correlation of Billson et al. (Billson, Eriksson et al. 2003) is then employed to obtain synthesised turbulent fluctuation:

$$v'_i(x)^m = \boldsymbol{a}\, v'_i(x)^{m-1} + \boldsymbol{b}\, \widetilde{v'}_i(x)^m$$

$$\boldsymbol{a} = \exp\left(\frac{-\Delta t}{\tau}\right) \quad , \quad \boldsymbol{b} = \sqrt{(1 - \boldsymbol{a}^2)} \qquad \ldots. (6.77)$$

This is the final turbulent velocity fluctuation field which is superimposed on the mean inflow field.

Steps (1) and (2) are continuously repeated on various spectrum stages of generation of Fourier modes. Eq. (6.76) provides an extra cross-correlation term which has been found to be very crucial in getting better results in a few recent works (Jarrin, Benhamadouche et al. 2006, Fathali, Klein et al. 2008, Kornev, Kroger et al. 2007, Mesbah 2006). The method is thereforesomewhat more expensive than Davidson et al.'s (Davidson, Billson 2006) method. Synthetic boundary conditions have been generated for various geometries in this study using this method. A typical synthetic boundary inflow condition profile generated by this technique for plane channel flow is shown below in Figure 6.9.

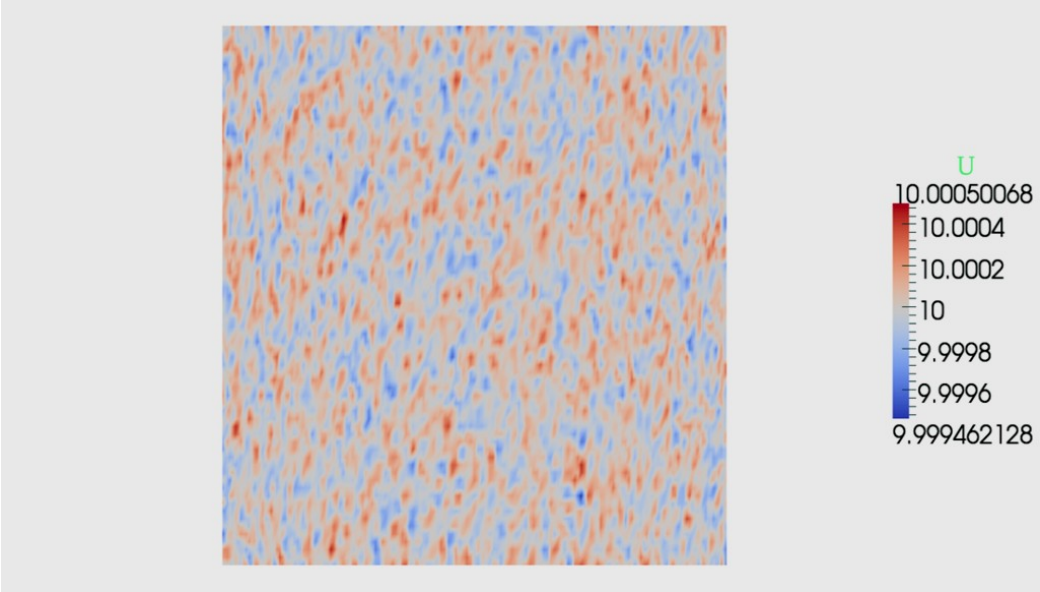

Figure 6.9: *Synthetic boundary inflow profile generated by proposed mixed synthetic boundary condition.*

6.6 Closure

A mixed synthetic boundary condition for inflow turbulence was introduced in this chapter. The evolution of the mixed synthetic boundary generation method was presented and a comparison made with other methods. An overview of turbulence characteristics was picked up from Chapter 3 and further extended with introduction of velocity and energy spectrum. After explaining the recycling method for inflow condition and other synthetic boundary condition methods in LES and DNS, the mixed synthetic spectral inflow boundary condition was introduced. This is further validated for channel flow simulation in Chapter 7 and for a simple expansion muffler in Chapter 8.

Chapter 7

LES Simulation of Pulsating Acoustic Flow through Channel or Duct

7.1 Introduction

In the last few decades, computational simulations of turbulent flow problems have become an important research tools in understanding the physics of turbulence. The last two decades in particular have seen the rise of Large Eddy Simulations (LES) in calculation of traditionally difficult turbulent flow cases such as unsteady and re-circulating flows and for Computational Aero-acoustic applications. The accuracy of the LES simulation of turbulent flows comes at an expense of considerable computation cost as compared to the conventional RANS method. RANS solves ensemble averaged mean flow with an appropriate model used to describe the effect of fluctuations around this mean, whereas LES solves filtered average of large scale motion of flow and models small scale of flow. Despite that, LES is still much less expensive than Direct Numerical Simulation (DNS), which needs to resolve the full range of scales available in the flow and therefore requires more computational resources. As LES occupies a middle ground between DNS and RANS, it has received growing interest among researchers for turbulent engineering applications over the last decade and is becoming an important tool for industrial applications with increasing computational advances in recent years.

For its geometrical simplicity, a fully developed channel flow has been extensively studied by various authors to clearly understand the complex turbulence phenomenon near the wall. Different

incompressible and compressible flow LES solvers have been employed to simulate plane channel. For the incompressible flow cases, the pioneer work is done by Deardorff (Deardorff 1970) and Schumann (Schumann 1975) in simulating plane channel flow. Detailed analysis with accurate wall resolution and turbulence statistics are produced later by Moin and Kim (Moin, Kim 1982) and Kim et al. (Kim, Moin et al. 1987) respectively. Different approaches have also been used for incompressible simulation of channel flow for different configurations (Jarrin, Benhamadouche et al. 2006, Bauer, Zeibig 2006, Bauer, Zeibig 2006, Fureby, Gosman et al. 1997, Breuer, Rodi 2007, de Villiers 2006, Davidson 2007a, Ducros, Comte et al. 1996). Recently, some high resolution methods have also been attempted to investigate the source of error and scope of improvement in the incompressible solver for channel flow (Laizet, Lamballais 2009). In the compressible flow case, the compressibility effect comes into the effect in modelling SGS stress. Since SGS models were originally derived for incompressible solvers, an additional physical mechanism needs to be considered particularly in the implementation of the energy equation. Various attempts have been made to address the issues concerning SGS modelling of compressible flow (Vreman 1995, Ducros, Comte et al. 1996, Erlebacher, Hussaini et al. 1992, Fureby 1996) . Channel flow has been studied by various authors in different ranges of flow speed, which include subsonic to moderate and supersonic flow (Lenormand, Sagaut et al. 2000, Moser, Kim et al. 1999, Suh, Frankel et al. 2006, Pantano, Pullin et al. 2008). Recently an argument has also been made in favour of universality of compressible flow for wall bounded flows (Brun, Haberkorn 2008). High resolution methods have also been implemented to obtain solvers with better accuracy in compressible flow simulations (Suh, Frankel et al. 2006, Nagarajan, Lele et al. 2003, Knight, Zhou et al. 1998, Rizzetta, Visbal et al. 2003). Although there have not been many investigations in compressible pipe flow simulation, there has been some interest in this area among some

researchers (Rudman, Blackburn 1999, Eggels, Unger et al. 1994, Eggels, Westerweel et al. 1993, Xu, Lee et al. 2005) .

Various sub-grid-scale models have been derived for different applications in LES simulation. The most popular of them is Smagorinsky's SGS model (Smagorinsky 1963), which has been used by Moin and Kim (Moin, Kim 1982) for wall bounded channel flow. Knight and Okong (Knight, Zhou et al. 1998) also employed the Smagorinsky model using unstructured finite volume grid for compressible channel flow. However, these studies have also identified the shortcomings of the Smagorinsky model; e.g., it's over dissipative characteristic; limiting behaviour for wall bounded flow; unaccounted backscattering of energy from small scale to large scale; and unaccounted compressibility effects. Some of these shortcomings have been addressed with enhanced perturbation at the inlet for synthetic boundary conditions. A more recent introduction is the dynamic sub-grid scale model by Germano et al (Germano, Piomelli et al. 1991), which is implemented by Piomelli (Piomelli 1993) for simulating high Reynolds number flow. An improved near wall performance has been achieved with one equation sub-grid scale model in simulating compressible wall bounded flow (Fureby, Gosman et al. 1997, Fureby 1996). Mixed sub-grid scale models have been employed by Lenormand et al (Lenormand, Sagaut et al. 2000) to simulate both subsonic and supersonic compressible channel flow. A detailed comparative study has also been made by Fureby et al (Fureby, Tabor et al. 1997) to investigate the sensitivity of different SGS models to simulation results. In a high order compact finite difference setup, a low Mach number LES channel flow simulation is performed by Rizzetta et al (Rizzetta, Visbal et al. 2003) using both Smagorinsky and dynamic SGS models with low-pass operators to obtain agreeable results.

Out of various LES simulation setup for channel flow simulation, LES technique with no-slip boundary condition without a wall model is found to be most successful. However, much finer grids are required in the wall normal direction for capturing an acceptable fraction of near wall energy for simulation at practical Reynolds numbers. This further increases the computational cost of LES simulation. There have been attempts to provide the approximate boundary condition near the wall to avoid increased computational cost. The first of such pioneer works, where wall-normal derivatives of the wall-parallel velocity was constrained to obtain logarithmic profile was carried out by Deardorff (Deardorff 1970) and Schumann (Schumann 1975). Some hybrid RANS-LES methods have also been used where simplified wall laws are imposed with the help of blending functions to diminish the effect of eddy-viscosity near the wall. (Davidson, Dahlstrom 2007, Jarrin, Prosser et al. 2009) Another approach known as detached-eddy simulation does not adopt any explicit blending function but a transport equation for turbulent kinetic energy close to the wall is solved and blended with the LES in resolved flow (Nikitin, Nicoud et al. 2000). However the approximation of the near-wall boundary condition introduces numerical error in the computational domain which requires to be thoroughly considered and kept under control. Various analyses have been done in regard to various errors like discretization error, aliasing error, and dissipation error and their effect on the accuracy of the simulation has been discussed in recent investigations (Geurts, Vreman et al. 1993, Ghosal 1996, Glendening, Tracy 2001, Chow, Moin 2003, Blaisdell, Spyropoulos 1996) .

Pulsating flow has been experimentally and numerically studied by various authors to gain insight into the sound propagation and attenuation phenomenon in pipe and duct. Preliminary investigations in pulsating channel flow have been focused on measurement of wall shear stress and near wall region parameters (Ronneberger, Ahrens 1977, Mao, Hanratty 1986, Binder, Tardu

et al. 1985, Tardu, Binder et al. 1994). Tardu *et al.*(Tardu, Binder et al. 1994) forced a range of frequencies and amplitudes (0.1-0.7 times the mean velocity) in the pulsating flow and found that the fluctuations generated by pressure gradient in the near wall region do not propagate beyond a certain distance l_t (dimensionless stokes length) from the wall. Similar observations are also made by Scotti and Piomelli (Scotti, Piomelli 2001), who adopted LES for pulsating channel flow simulation and validated previous experimental finding in the near-wall region. Scotti and Piomelli (Scotti, Piomelli 2002) also investigated various RANS turbulence models for turbulence to estimate their effectiveness for pulsating channel flow. Recently, Comte et al. (Comte, Haberkorn et al. 2006) also adopted the LES method to simulate pulsating channel flow to investigate the origin of the critical Strouhal number range for near-wall shear impedance lower than the laminar regime. More recently, a spectral dynamics study of pulsating pipe flow is made by Manna and Vacca (Manna, Vacca 2008) to investigate the effect of pulsation on near wall coherent structures for a fixed frequency with ratio of amplitude of oscillation and mean flow in the range of 1 to 11. However most of the pulsating channel and pipe flow studies have been mainly focused on near wall region and propagation of sound in the central region still needs further investigations.

This chapter presents the LES of Channel flow and validates the simulation with the DNS results of Kim *et al*. (Kim, Moin et al. 1987). The research also investigates various LES sub-grid models for channel flow using a cyclic boundary condition. Moreover, LES is performed for channel flow using the mixed synthetic boundary condition introduced in Chapter 6. Later on, a forced pulsation is introduced at the inlet in a steady mean flow profile of the channel and pulse propagation through the channel is analysed to observe the attenuation in the channel.

7.2 Large Eddy Simulation

Unlike DNS, Large Eddy simulation (LES) does not resolve the complete range of turbulent scales and only captures the scales as small as practically feasible. In this way LES computes the dynamics of as much of the large energy containing resolved scales of the flow as is economically feasible while modelling only effects of small unresolved phenomenon on the larger resolved scales with the help of sub-grid models. The division of the scales of flow into larger resolved and smaller unresolved scales, termed grid scale (GS) and sub-grid scales (SGS) respectively, can be accomplished by convolving the dependent flow variables with a predefined kernel, which works like a high-pass filter. In traditional methods, filtering is applied to the Navier-Stokes equation to obtain a governing relation for filtered velocity. The filtering of the Navier-Stokes equation creates a need for the modeling of sub-grid scale (SGS) stresses and the way this SGS stress is modelled, resulting in a closed system of equations, distinguishes one LES method from another. In the process of modeling, the GS motion is explicitly simulated whereas the average effect of the SGS motion on GS motion is accounted for by a SGS model.

The basic equations for LES were first formulated by Smagorinsky in the early 1960's.(Smagorinsky 1963) A need for an alternative method for resolving all the scales of motion was realized as the computational resources were severely limited at that time. It was known from the theory of Kolmogorov that the smallest scales of motion are uniform and that these small scales serve mainly to drain energy from the larger scales through the cascade process, it was felt that they could be successfully approximated. The larger scales of motion, which contain most of the energy, do most of the transporting and are affected strongest by the boundary conditions should therefore be calculated directly, while the small scales are represented by a model (called SGS models). Although the main features of the GS flow appear independent of the SGS models,

different SGS models predict the mean effect of the SGS motion on the GS motion differently. In Large Eddy Simulation of flow with very high or low grid Re numbers ($Re_G = \Delta^2 D/ \upsilon$, where Δ is the grid spacing, υ the viscosity and D the rate of strain), the SGS model must incorporate the effects of the viscous sub-range and full inertial range, respectively. The grid filter width Δ mentioned above facilitates the filtering operation. It retains scales larger than Δ and filter out the smaller scales, which are modelled with SGS models.

Formally, any flow variable, *k*, in LES is composed of a large scale and a small scale contribution as:

$$\bar{k} = k - k'. \qquad \ldots (7.1)$$

The prime denotes the small SGS scale and the overbar denotes the larger grid scale. To extract the large scale components a filtering operation is applied, which is defined as:

$$\bar{f}(x) = \oint G(x, x'; \Delta) f(x') dx' \qquad \ldots (7.2)$$

Where Δ is the filter width and is also proportional to the wavelength of the smallest scale retained by the filtering operation. G (x, x'; Δ), the filter kernel, is a localized function or function with compact support (*i.e.* the function is large only when x and x' are not far apart), that satisfies the condition:

$$\oint G(x, x'; \Delta) dx' = 1 \qquad \ldots (7.3)$$

The most commonly used filter functions are the sharp Fourier cut-off filter, best defined in wave space as

$$\bar{G}(k) = \int_{\boldsymbol{D}} G(x')e^{-ikx'}dx' = \begin{cases} 1 & if\ k \leq \pi/\bar{\Delta}, \\ 0 & \text{otherwise,} \end{cases}$$

… (7.4)

the Gaussian filter,

$$G(x) = \sqrt{\frac{6}{\pi\bar{\Delta}^2}\exp\left(-\frac{6x^2}{\bar{\Delta}^2}\right)},$$

… (7.5)

and the tophat filter in real space:

$$G(x) = \begin{cases} \dfrac{1}{\bar{\Delta}} & if\ |x| \leq \bar{\Delta}/2, \\ 0 & \text{otherwise,} \end{cases}$$

… (7.6)

When this filtering process is applied to the Navier-Stokes equations, one obtains the filtered equations of motion. Provided that the filter commutes with differentiation, these appear at first glance to be very similar to the RANS equations. For incompressible flow they are:

$$\nabla \cdot \bar{u} = 0$$

$$\frac{\partial \bar{u}}{\partial t} + \nabla \cdot (\overline{uu}) = -\frac{1}{\rho}\nabla \bar{p} + \nabla \cdot (\nabla \bar{u} + \nabla \bar{u}^T)$$

… (7.7)

Although the definition of the velocity appearing above differs from that in the RANS equation, the issues of closure are conceptually very similar. Since $\overline{uu} \neq \bar{u}\bar{u}$ a modelling approximation must be introduced to account for the difference between the two sides of the inequality:

$$\tau = \overline{uu} - \bar{u}\bar{u} \quad \text{… (7.8)}$$

In LES the term τ is known as the sub-grid scale stress and has the property that $|\tau| \to 0$ as $\Delta \to 0$, so that in the limit of small mesh spacing a DNS solution is returned. It is functionally similar to the Reynolds stress in RANS modeling but predictably the physics of the problem is different in LES. The SGS stresses represent a much smaller part of the turbulent energy spectrum than the RANS turbulent energy, so that the accuracy of the stress model may be less crucial than in RANS computation. However if the turbulent dissipation in the small scales is not accurately represented by the SGS model it can lead to a build-up of energy in the resolved scales and computational instability.

After decomposition of the velocity field *i.e.* $u = \bar{u} + u'$, the SGS stress can be decomposed into three separate terms as,

$$\tau = \overline{(\bar{u} + u')(\bar{u} - u')} - \bar{u}\bar{u} = (\overline{\bar{u}\bar{u}} - \bar{u}\bar{u}) + (\overline{\bar{u}u'} + \overline{u'\bar{u}}) + \overline{u'u'}. \qquad \ldots (7.9)$$

Each term has its physical significance. The first term in the equation is known as Leonard term, which can be computed from the resolved velocity field and represents the interaction of resolved eddies to produce sub-grid turbulence. The second term is known as cross term, which is related to the energy transfer between the resolved and unresolved scales. Energy can be transferred in either direction, but generally move from the larger to the smaller eddies. This term physically represents the interaction between unresolved and resolved eddies. The last term represents the effect of small eddy interaction and is generally known as the SGS Reynolds stress. The SGS stress as a whole is a Galilean invariant and therefore is independent of frame of reference, whereas the cross stresses and Leonard stresses are not Galilean invariant. Also, the correlations that are used to model these stresses are approximations and therefore contain errors that defeat any attempt at precision. For

these reasons the decomposition of SGS stress has largely been abandoned in favour of modelling the SGS term as a whole.

7.3 Sub-Grid Scale (SGS) Modelling

As we know that the dissipative scales in LES are generally not resolved and therefore the main role of the SGS model is to extract energy form the resolved scales, mimicking the drain associated with the energy cascade. This can be accomplished in a very similar way to the RANS model, where there was an eddy-viscosity model. However the eddy viscosity model used in LES is based on the hypothesis that the non-uniform component of the SGS stress tensor is locally aligned with the resolved non-uniform part of the rate of strain tensor. The normal stresses are taken as isotropic and can therefore be expressed in terms the SGS kinetic energy.

$$\tau - \frac{1}{3}tr(\tau)I = \tau - \frac{2}{3}kI = -\nu_{SGS}(\nabla\bar{u} + \nabla\bar{u}^{T}) = -2\nu_{SGS}\bar{S}, \quad \ldots (7.10)$$

Where for incompressible flow, $\bar{S}$ is the large scale strain rate tensor,

$$\bar{\mathrm{S}} = \frac{1}{2}(\nabla\bar{u} + \nabla\bar{u}^{\mathrm{T}}) \quad \ldots (7.11)$$

The isotropic part of the stress tensor, $\frac{1}{3}tr(\tau)$ is either modeled or expressed in the filtered pressure.

Smagorinsky model: Smagorinsky model was first proposed sub grid scale eddy viscosity model to be proposed, which was derived from the simplifying assumption that the small scales are in equilibrium and dissipate entirely and instantaneously all the energy received from the resolved

scales. (Smagorinsky 1963) There are other similar methods to derive the eddy viscosity but they all usually produce the algebraic Smagorinsky model of the form:

$$\vartheta_{SGS} = (C_s\,\Delta)^2\,|\bar{S}|$$

$$K = (C_I\,\Delta)^2|\bar{S}|^2$$

$$|\bar{S}| = (\bar{S}:\bar{S})^{1/2} \qquad \ldots (7.12)$$

where C_s is the Smagorinsky constant and the value of this parameter has been determined from the isotropic turbulence decay and ranges between 0.18 and 0.23 for such flows. This model however is excessively dissipative in laminar or high shear regions (caused by high $\bar{S}$) and therefore C_S parameter must be decreased in these situations. This serious deficiency of such models in laminar or high shear region is dealt with some success for near wall flow by using the van Driest damping function which reduces the sub-grid eddy viscosity as a function of wall-normal distance. This is however somewhat undesirable, as the SGS model should preferably depend exclusively on local flow properties. Also, since the assumption in Smagorinsky models that deviatoric SGS stresses and resolved stain rates align does not normally hold true therefore the correlation between the model and the actual turbulent stress behaviour is quite low. Despite these drawbacks, this model is relatively successful because of the reason that it dissipates energy at approximately the right overall rate.

One Equation model: As the Smagorinsky model is based on the assumption of small scale equilibrium, it therefore becomes correspondingly less accurate as the condition moves farther from equilibrium. Unfortunately, non-equilibrium conditions commonly occur in free shear layers, separating flows, boundary layers and wall dominated flows like pipe and channel flows and are thus too common to dismiss out of hand. The problem can be addressed by adding transport

equations for one or more of the sub-grid turbulence characteristics to the model. The simplest such approach is One-equation model.

Most one-equation models are also based on eddy-viscosity concept and in addition solve a transport equation for a sub-grid scale quantity on which the eddy viscosity depends. One such quantity is the sub-grid scale kinetic energy, defined as

$$K = \frac{1}{2}\sum_{i}(\tau_{ii}\,) \qquad \ldots (7.13)$$

which provides a SGS velocity scale. Other possibilities include transported SGS viscosity or vorticity. One variant One-equation turbulent energy model is given by Yoshizawa (Yoshizawa 1986),

$$\frac{\partial K}{\partial t} + \nabla.(K\bar{u}\,) = \nabla.[(\nu + \nu_{SGS})\nabla K] - \epsilon - \tau{:}\bar{S} \qquad \ldots (7.14)$$

Where the SGS eddy-viscosity ν_{SGS}, and the dissipation, ϵ, can be found from,

$$\nu_{SGS} = C_K K^{1/2}\Delta$$

$$\epsilon = \frac{C_\epsilon K^{\frac{3}{2}}}{\Delta} \qquad \ldots (7.15)$$

However one-equation model itself is not free from deficiencies. These models do not address the problem of discrepancy between the principle axes of the SGS stress and the rate of strain tensor. This problem is attributed to the fact that even this model is based on eddy-viscosity concept and therefore similar problems were also encountered by the earlier models such as Smagorinsky

model. Although under similar equilibrium conditions one-equation model should not perform any better than Smagorinsky model, but they provide a more accurate time scale through the independent definition of velocity scale and have also shown better results when used to model transitional flows or flow with large scale unsteadiness. Fureby *et al*. (Fureby 1996, Fureby, Tabor et al. 1997) in particular, have studied performance of different SGS models in channel flows and shown the one-equation model to be quite effective and superior to Smagorinsky and other algebraic models under those circumstances.

Scale Similarity and Liner Combination (mixed) models: Although eddy-viscosity models are able to model global dissipative effect, their correlation between strain rate and sub-grid stress and their energy transfer from small scales to large scales (backscatter) are poor and therefore the model is unable to produce local energy exchange correctly.

A scale similarity model by Bradina *et al.* (Bardina, Ferzinger et al. 1980) is based on the idea that the smallest resolved eddy of size O(Δ) interacts with the SGS eddies in a very similar way to which the slightly larger resolved eddies interact with those of size O(Δ). This can also be conceived as a sort of extrapolation procedure from the smallest resolved to SGS scales, an approach which will generally work if there is a regular pattern in the data over the range extrapolated. The largest sub-grid scale can be obtained by filtering the SGS velocity $u' = u - \bar{u}$ to give $\bar{u'} = \bar{u} - \bar{\bar{u}}$. Now following Bradina's assumption and equation obtained for τ gives:

$$\tau = \overline{u}\overline{u} - \bar{u}\bar{u} \approx \overline{\bar{u}}\overline{\bar{u}} - \bar{\bar{u}}\bar{\bar{u}} \quad \ldots (7.16)$$

In this case the correlation between the scale similarity model and the exact SGS stress is relatively high and it predicts important turbulent stress structures at correct locations. It is also found to transfer energy from the smallest to the larger resolved scales. Unfortunately it hardly dissipates

any energy and therefore it could not be used as an independent SGS model. This problem can be alleviated by combining it with eddy-viscosity model to produce the linear combination or mixed model,

$$\tau = \overline{\bar{u}\bar{u}} - \bar{\bar{u}}\bar{\bar{u}} - 2\nu_{SGS}\bar{S} + \frac{1}{3}tr(\tau) \quad \ldots (7.17)$$

which lacks the stability problems and has been shown to produce improved results compared to Smagorinsky model.

Dynamic Models: The concept Dynamic models are considered to be a one step further to scale similarity model. It was first proposed by Germano *et al.* (Germano, Piomelli et al. 1991) as a procedure, which can apply to most of the models described before. The coefficients procedures are, based on energy content of the smallest resolved scales, rather than a *priori* input as in Smagorinsky model. This is accomplished by assuming that the behaviour of these scales is very similar to the sub-grid scales, which is very analogous to the Scale similarity model. A self-contained sub-grid scale model is produced by calculating the SGS model coefficients for these small scales and applying it to the LES.

To formally describe the procedure, we recall the equation described in scale similarity model with second or 'test filter', with a filter width $\widetilde{\Delta}$ that is larger than and equal to the original filter width Δ. If this test filter is applied to once filtered Navier-Stokes equation, the final sub-grid stress that must be modeled in the test-filter level LES is given by,

$$T = \widetilde{\bar{u}\bar{u}} - \tilde{\bar{u}}\tilde{\bar{u}} \quad \ldots (7.18)$$

At this stage the large scale part of SGS stress at the test filter level can explicitly be computed from the LES field from the following relation,

$$L = \widetilde{\tilde{u}\tilde{u}} - \tilde{\tilde{u}}\tilde{\tilde{u}} \quad \ldots (7.19)$$

It follows directly from definitions above that,

$$L = T - \tilde{\tau} \quad \ldots (7.20)$$

This equation is known as Germano identity and forms the basis of the dynamic model. The use of identity to calculate the model coefficients is illustrated in following derivation by Piomelli (Piomelli 1993).

Consider a generalized eddy-viscosity model to relate both sub-grid and sub-test grid stresses to their respective resolved fields, α and β.

$$\tau = -2C_v\alpha, \qquad T = -2C_v\beta \quad \ldots (7.21)$$

On substituting this equation into Germano identity, it is found that the identity can be satisfied only approximately, since stresses are replaced by modeling assumptions, and the system is over determined (five independent equation to determine one coefficient). It was proposed that the error produced by approximation be minimized in accordance with the least-squares method. The error is given by:

$$e = L - T - \tilde{\tau} = L + 2C_vM \quad \ldots (7.22)$$

Where M=$\beta - \tilde{\alpha}$ and C_v is assumed to be smooth on the scale so that it can be extracted from the filtering operation. The least square minimization is then applied to give,

$$\frac{\partial \langle e.e \rangle}{\partial C_v} = 0$$

… (7.23)

This simplifies to give required coefficient,

$$C_v = -\frac{1}{2}\frac{\langle L:M \rangle}{\langle M:M \rangle}$$

… (7.24)

Where < > denotes an appropriate ensemble averaging. This model can be applied to mixed models and models with two or more coefficients as well. The ensemble averaging has the purpose of removing very sharp fluctuations of the coefficients, which would otherwise destabilize numerical calculations and make the model inconsistent, since coefficients cannot be removed from the filtering operation. This averaged version of the procedure has also removed spurious large and negative eddy viscosities. Several other approaches have also been tried with varying success. One of these, the one used by Germano, was to average the coefficients C_L and C_v over all homogeneous directions. However this is only possible for flow with some degree of homogeneity. Another attempt made by Ghosal (Ghosal 1996) used an integral formulation of the Germano identiy (described above), that rigorously removes the mathematical inconsistency. The expense of this added confidence is the solution of an integral equation at each time step.

The introduction of dynamic models has caused significant progress in the sub-grid scale modeling of transitional flows and has removed many of the traditional problems encountered with static models. In free shear and channel flows the dynamic model automatically adjusts, by lowering the coefficient in areas of high shear and near the walls, a function which is normally performed by the van Driest damping function. Another advantage is that the eddy viscosity automatically goes to zero in laminar regions of the flow.

There are still some drawbacks of these approaches, which includes the requirement of additional averaging, either in homogeneous direction, along the streamline or in local region of the flow, is necessary to avoid excessive fluctuations in model coefficients. In addition to this, unless the scheme is somehow additionally bounded, the dynamic procedure occasionally produces negative dissipation, which if left unchecked, could violate the conservation of energy law and leads to unphysical results.

7.4 Incompressible Channel Flow Simulation using Periodic Boundary

In order to demonstrate the ability of OpenFOAM to perform LES simulation, an incompressible channel flow simulation is carried out using cyclic method, introduced in section 6.3. The distance between the two parallel walls of the channel is 2δ, where δ is referred to as the channel half width. If the flow is developed, there is a constant mean pressure gradient in the streamwise direction which is directly related to the friction velocity u_τ at the wall by,

$$\frac{dp}{dx} = \frac{u_\tau^2}{2\delta} \qquad \text{... (7.25)}$$

The general consensus for the adequate overall dimension for the computational domain for cyclic channel flow simulation seems to be about $2\pi\delta \times 2\delta \times \pi\delta$ in the streamwise, wall normal and spanwise direction respectively. However, there have been encouraging results from by Fureby *et al.* (Fureby, Gosman et al. 1997) using minimal channel approach with a smaller computational domain of $4\delta \times 2\delta \times 2\delta$ to minimise computational cost. The geometric set-up for channel is similar to the figure 6.5 of chapter 6.

Although the domain seems to be slightly smaller to capture all the scales, but it is found that it performs an accurate LES when compared to the DNS results. The DNS simulations performed by

Kim *et al*. (Kim, Moin et al. 1987) have been used to compare all the LES channel flow simulation in this work at frictional Reynolds number of 395. The simulation is carried out at the streamwise velocity of 0.1335 m/s to ensure that the DNS situation of Kim *el at*. is maintained. The offset in the velocity and pressure value due to recycling value from outlet to the inlet, is compensated by adjusting streamwise velocity and pressure gradient *dp/dx*, given by equation 7.25. The simulation is performed for 400 flow-through times to ensure that the LES statistics matches to the DNS statistics. The instantaneous velocity contour for channel flow is shown in figure 7.1. The vorticity contour is shown in figure 7.2, which demonstrates the generation of longitudinal streaks in the computational domain. These streaks are unstable to the perturbation produced at inlet and this instability kick starts a streak instability cycle which is said to be responsible for near wall turbulence cycle. Mesh points of $64 \times 64 \times 64$ with wall gradient is maintained throughout the computational domain.

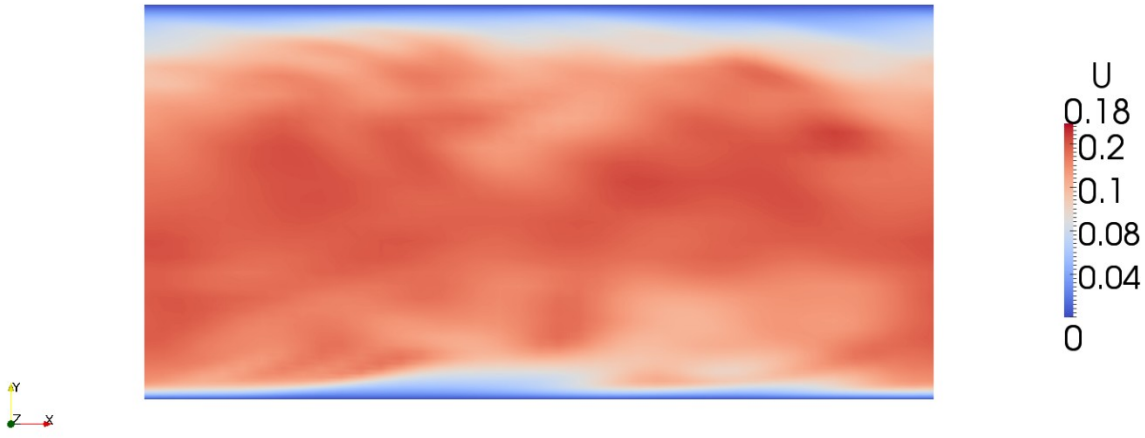

Figure 7.1: *Instantaneous velocity contour in channel flow.*

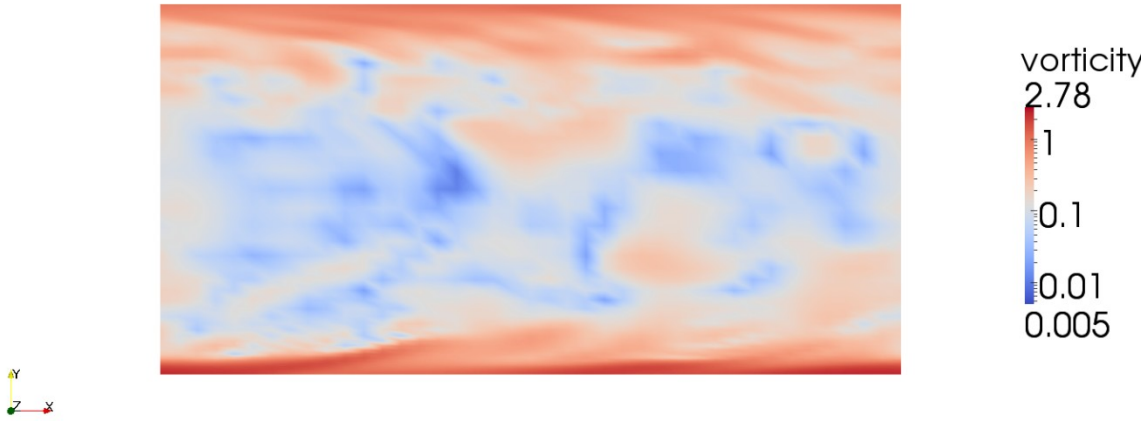

Figure 7.2: *Vorticity contour in channel flow.*

The comparison of mean velocity profile along wall normal direction is shown in the figure 7.3. The figure compares velocity profile for various sub-grid models for LES to demonstrate the effectiveness of sub-grid model in comparison to DNS. It can be seen that a very good agreement with DNS is achieved for all the sub-grid models away from the wall but the dynamic sub-grid model provides better solutions near the wall. The comparison of cross Reynolds stress along wall normal direction is shown in figure 7.4. The comparison shows that the stresses are very close to DNS away from the wall but the dynamic model performs better near wall. One-equation model provides a better compromise between the Smagorinsky and the dynamic model. Since the investigations in this research are mostly concerned at away from the wall, this research has adopted Smagorinsky sub-grid model for its numerical stability and accuracy away from the wall.

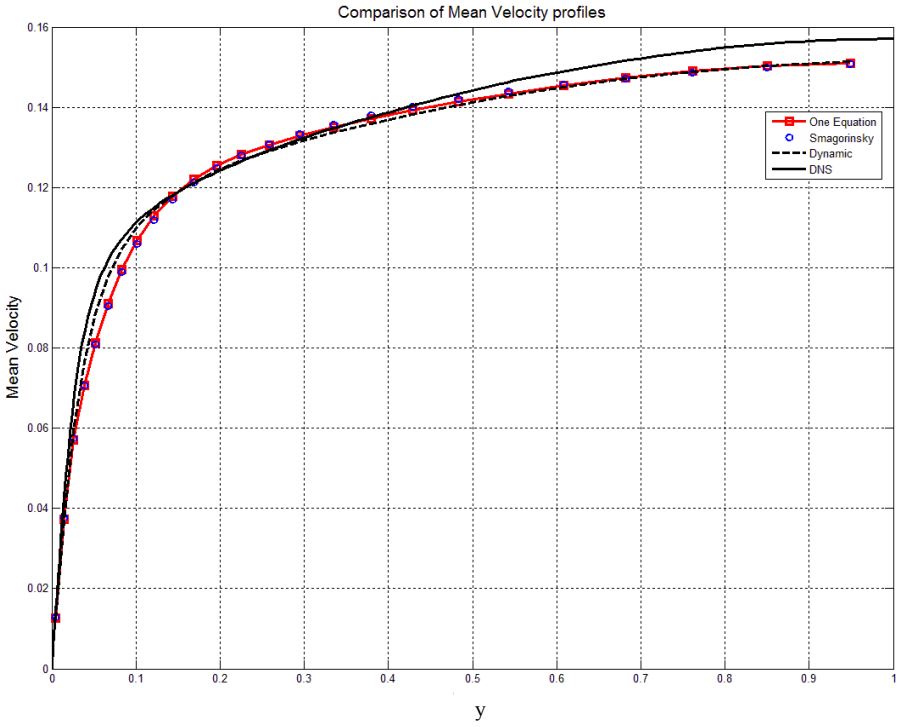

Figure 7.3: *Comparison of different sub-grid models for mean velocity profile.*

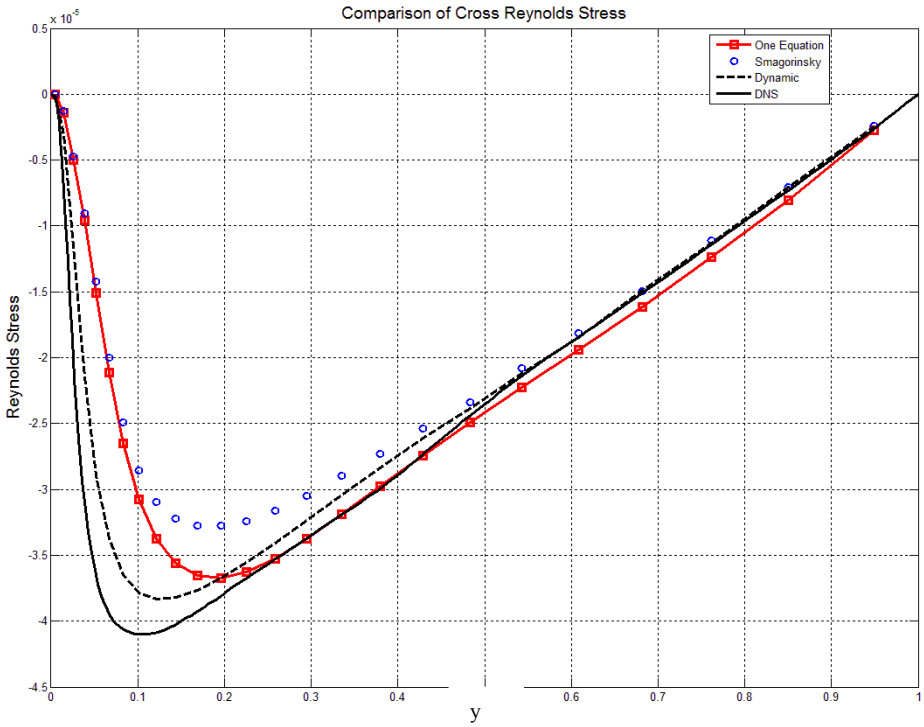

Figure 7.4: *Comparison of different sub-grid models for Cross-Reynolds Stress profile.*

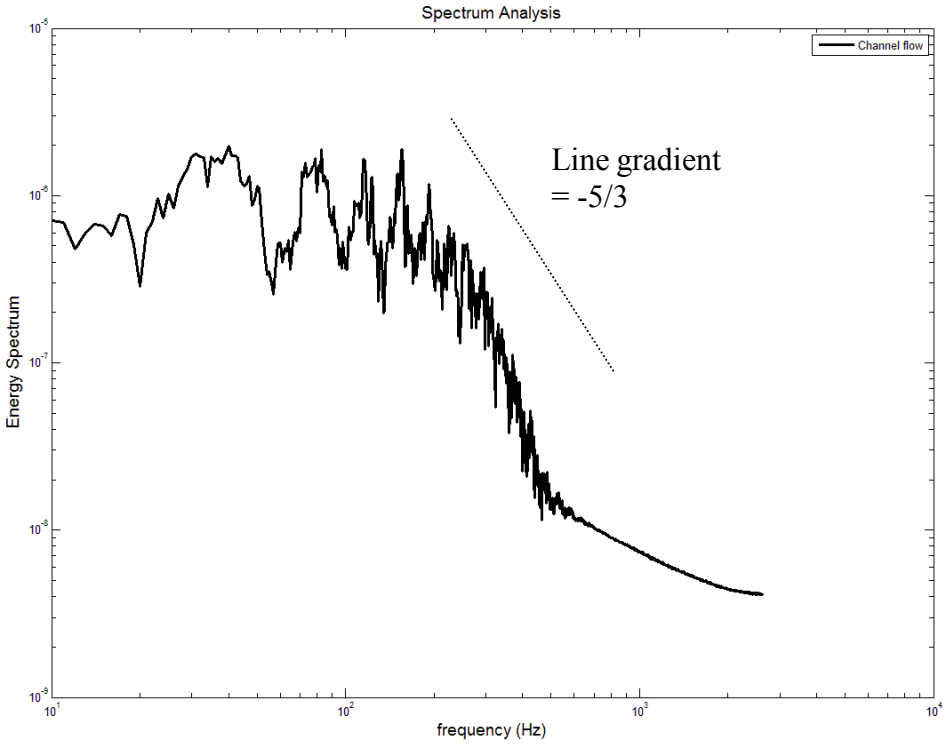

Figure 7.5: *Energy spectrum for LES of channel flow using cyclic boundary condition.*

The energy spectrum generated for LES of channel shown in the figure 7.5 demonstrates that the spectrum follows the -5/3 law of Kolmogorov spectrum.

7.5 Compressible Channel Flow Simulation using Synthetic Inflow Boundary

A simulation of compressible flow in a long channel is elucidated in this section using the mixed synthetic boundary condition developed in section 6.5. The channel dimension is $20h \times h \times h$. The synthetic boundary condition help provide turbulence like structure as an initial inflow condition for LES simulations. The steady profile for velocity for the mixed synthetic boundary condition is quickly achieved in a channel flow simulation. The time taken to achieve steady

profile is only 20-25 flow-through times, in comparison to the 200-400 flow-through times taken by periodic boundary conditions.

The vorticity profile developing along the length of the channel is shown in figure 7.6 (a). The figure shows the generation of longitudinal streaks in the computational domain as flow progress along the length of the channel.

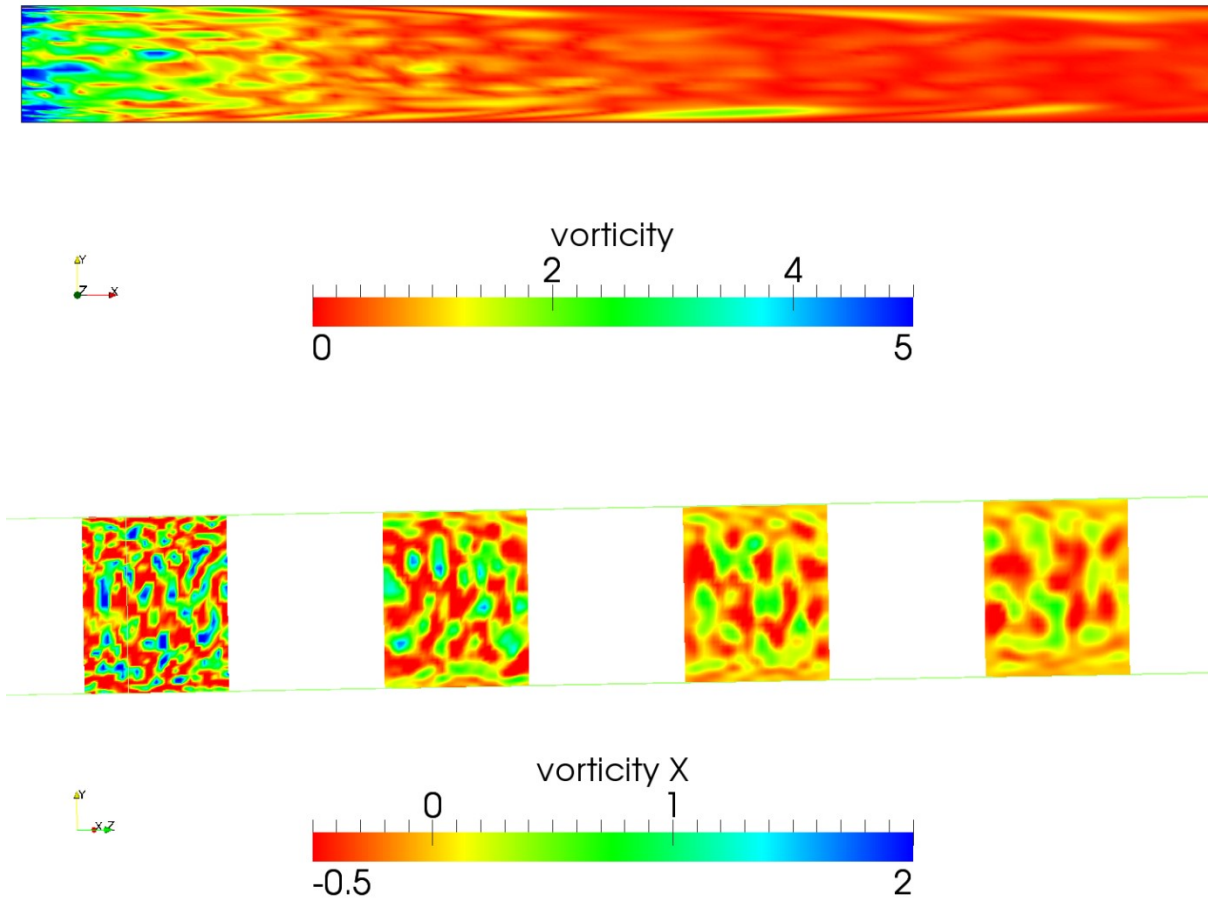

Figure 7.6: (a) *Vorticity contour for long channel along the length of the channel.* ***(b)*** *Vorticity cross-section contour along x-axis (at 1m, 6m, 12m and 16m away from inlet) .*

These streaks are unstable to the synthetic fluctuations produced by the von-Karman spectrum involved in the generation of fluctuation part in the synthetic boundary condition at the inlet and this instability initiates streak instability near wall turbulence cycle. Figure 7.6 (b) shows the vorticity planes generated by synthetic inflow across the length of the channel. The mean flow profile seems to develop quickly from the RANS mean flow profile in the near-wall region but the development of flow in the bulk flow region took considerable amount of time (20-25 flow-through times). This is consistent with the observation made by Jarrin et al. (Jarrin, Benhamadouche et al. 2006) in the development of his Synthetic-Eddy Method. The mean velocity profile and Reynolds-stress profile are compared with the DNS results obtained from Moser et al. (Moser, Kim et al. 1999) with necessary scaling for the current simulation of 10 m/s mean flow. The mean flow profile satisfactorily agree with the DNS profile in the bulk flow region and matches the trend reasonably in the near-wall region, as shown in Figure 7.7 (a). The Reynolds-stress profile seems to match the trend of DNS profile satisfactorily, as shown in Figure 7.7 (b).

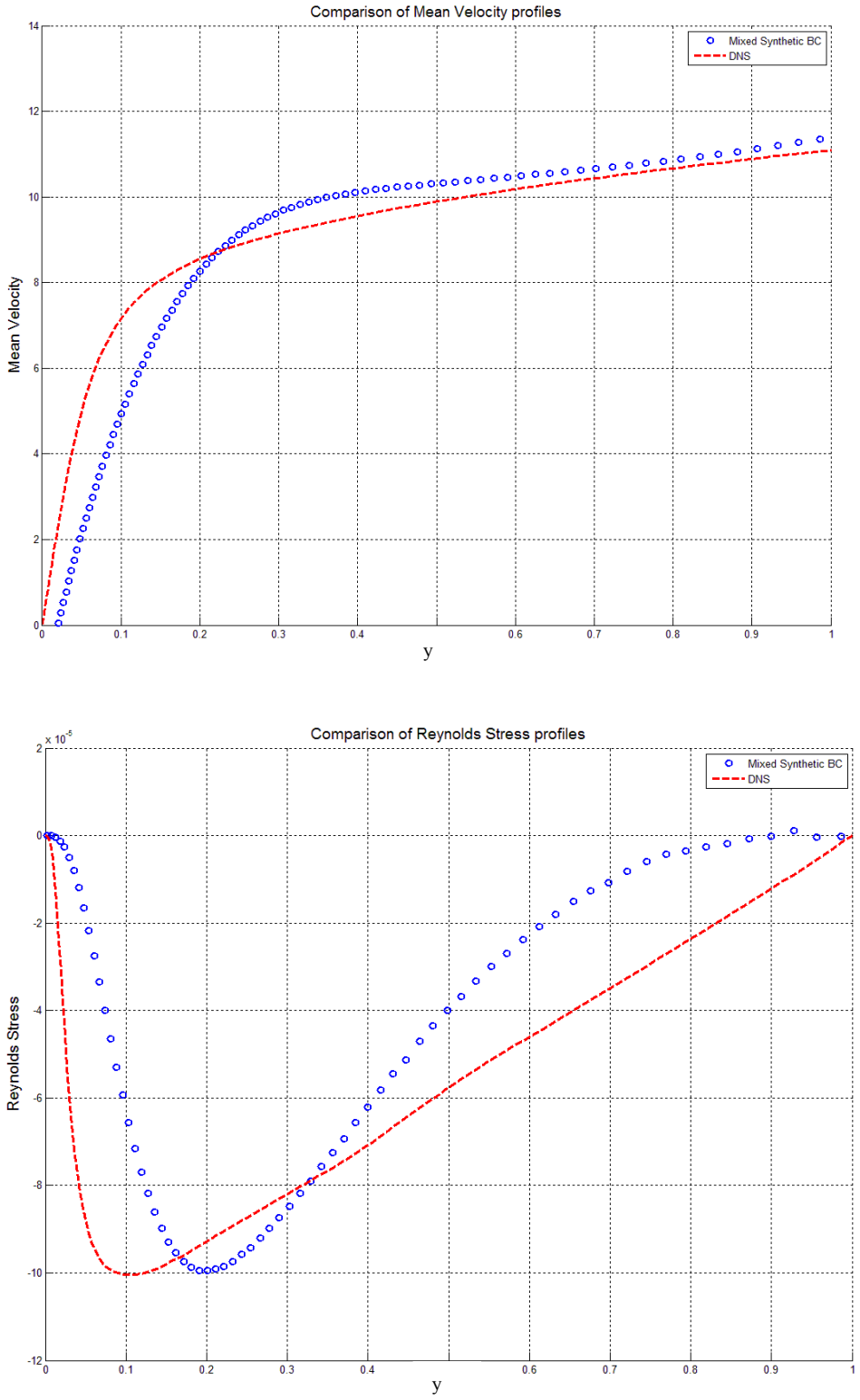

Figure 7.7: *Comparison of mixed synthetic boundary with DNS:* ***(a)*** *Mean velocity profile.* ***(b)*** *Reynolds Stress profile.*

The energy spectrum generated for LES of channel using synthetic boundary inflow condition shown in the figure 7.5 demonstrates that the spectrum reasonably follows Kolmogorov's law. Besides that, the spectrum also shows some particular dissipation in the high frequency, smaller energy containing scales inside the channel due to the Von-Karman spectrum used in generating the turbulence scales in the development of synthetic boundary condition.

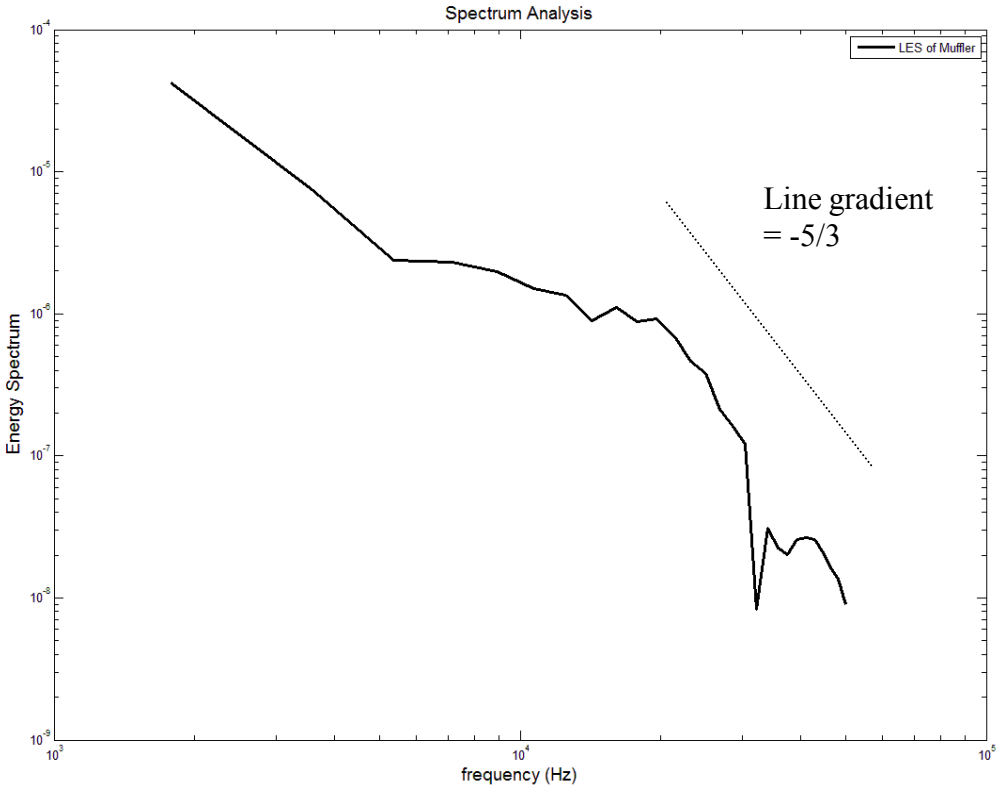

Figure 7.8: *Energy spectrum for LES of channel flow using mixed synthetic boundary condition.*

7.6 Acoustic Pulse through a Long Channel

The CFD simulation of propagation of acoustic pulse with considerable mean flow has put forward some serious computational challenges for the CFD community. The introduction of acoustic pulse to mean flow simulation presents an important scenario for understanding the physics of interaction between turbulence and acoustic pulses. This understanding could help attenuate sound propagation in turbulent flow, like in the case of various applications in the past.

The pressure based compressible flow solver for laminar flow simulation usually consists of some built-in errors in the simulation, such as the error due to 1) the presence of wall; 2) the reflections from the wall of computational boundary; 3) the disparity in the acoustic scale and flow scale; 4) numerical aliasing; and 5) the numerical discretisation/dispersion. Despite the presence of these errors, general compressible solvers usually found fit-to-use for most of applications and provide good agreement with the experimental results as well. However, the study of acoustic propagation and acoustic noise source prediction involves the wave or perturbations of very small scale and therefore the solver for the acoustic simulation need to be very robust and extremely accurate.

Mean flow simulation introduces an additional error due to the modelling of turbulence in the simulation, which makes it even more important for the solver to be more robust and accurate. There will also be an additional dissipation error which would arise with the introduction of turbulence model in the mean flow simulation. RANS simulation of pulse through a pipe has been demonstrated in section 4.4.2.1. It can easily be seen that due to the very nature of the RANS modelling, the turbulent scales of the simulation have been averaged and whole energy spectrum is modelled rather than computed, which results in some arbitrary pressure equalisation in the

domain during simulation. LES provides an interesting opportunity to simulate pulse propagation with greater accuracy.

In order to obtain a transmission pulse spectrum and transmission loss spectrum for LES of long channel, two probe points near the inlet and near the outlet of the channel are chosen and pressure data are recorded. The transmission pulse spectrum and transmission loss spectrum are obtained on the frequency spectrum as shown in figure 7.9 (a) and 7.9 (b). The transmission pulse spectrum shows the presence of pulse 2000-3000Hz, along with some perturbations, which was not present in the RANS simulation of circular pipe in section 4.4.2.1. (See Figure 4.19) These perturbations are captured accurately by the LES, and are produced due to the turbulence interaction with the scales of mean flow. A low frequency peak is observed in the transmission loss spectrum shown in figure 7.9 (b), which is likely to be originated from the resolution of large scales of turbulence by turbulence models. Unlike the RANS simulation of circular pipe, where the large scale turbulence scales in the simulation are underestimated due to averaging, the LES provides more realistic large scale attenuation. Subsequent to the first peak, there are other peaks at 450 Hz, 1250 Hz and so on, which corresponds to the chamber resonances generated in the long channel. It is important to compare the RANS simulation of pipe in this context where the first mode of resonance is not obtained with high accuracy. The RANS simulation of pipe showed a linear increase in transmission loss throughout the higher frequency domain due to the averaging of flow variables inside computational domain and therefore the chamber resonances below certain frequency range were found to be lost due to superimposition with those scales, as shown in Figure 4.19 (b). However, LES captures these high frequency scales accurately and captures the higher modes of resonance in the channel.

(a)

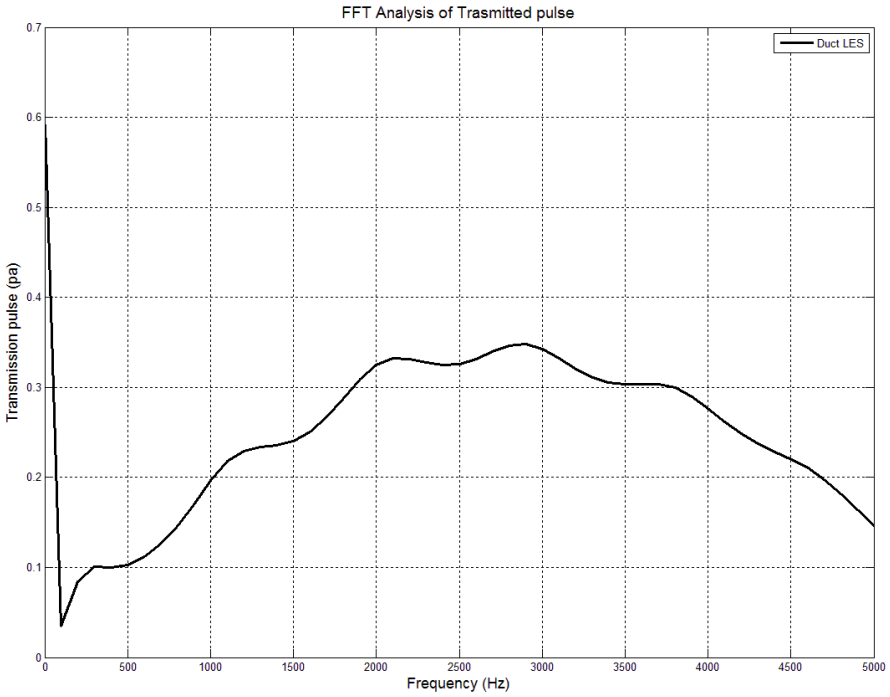

(b)

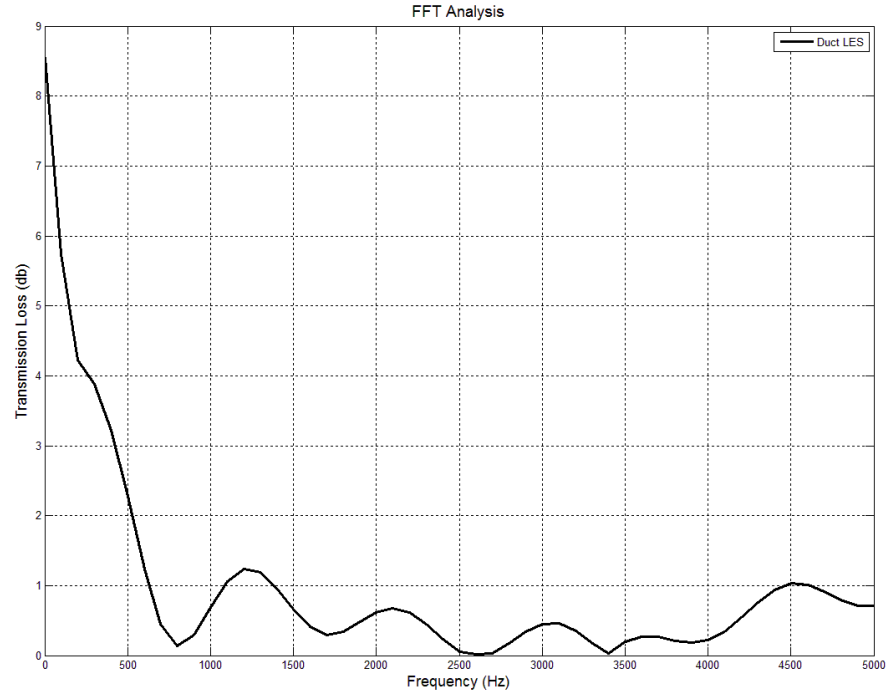

Figure 7.9: (a) *Transmission pulse spectrum for pulse propagation in long channel.* ***(b)*** *Transmission loss spectrum for pulse propagation in long channel.*

7.7 Closure

In this chapter, the ability of OpenFOAM to perform LES of channel flow using cyclic boundary condition has been demonstrated and the channel flow simulation is validated with DNS results available in literature. Various other LES sub-grid models are also investigated in the context of accuracy and compared with the DNS results for channel flow. Besides, the synthetic boundary condition as inflow condition for simulating channel flow is also validated in this chapter. A forced pulsation through the channel over a steady mean flow profile is successfully simulated to obtain a better resolution of large scale of mean flow. The LES of forced pulsation in channel is found to compute the scales related to channel resonance more accurately then the RANS simulations.

Chapter 8

LES Simulation of Pulsating Acoustic Flow through Muffler

8.1 Introduction

The need of a robust and accurate compressible solver for acoustic propagation simulation has already been stressed. Moreover, it has been pointed out that turbulence modelling of -mean flow introduces additional numerical inaccuracies in terms of dissipation error due to modelling assumptions. Because of its unique shape, the simple expansion muffler introduces further numerical challenges arising from the production of various reflected and transmitted waves from the expansion chamber inside the domain of mean flow simulation.

Because of the inherent limitations in RANS methods such as averaging of the length-scales and modelling of the full spectrum instead of computing the broad length spectrum, accurate acoustic simulation using RANS methods are rather difficult. RANS modelling is also not very effective for the same reasons in separating flow cases including expansion muffler, cavity and resonators. DNS can provide accurate results in separating flow cases but it comes at very high computational cost and is mostly not feasible for industrial applications. LES, on the other hand provides a very interesting opportunity for the CFD community to explore the area of Computational Aeroacoustics (CAA) to study sound propagation. Although LES is computationally less expensive than DNS, it is still much more expensive and exhaustive than RANS methods.

However, with recent advances in computational capacity, several attempts have been made by the CFD community to simulate such flow cases.

Most of the research in the past has been conducted towards noise source identification or noise source prediction. A lot of work has been carried out to extend the near-field acoustic data to the distance farther away. A simpler domain extension method usually uses uniform cartesian mesh and employs analytical integral formulation methods such as Kirchhoff surface (Freund, Lele et al. 1996) and more refined Ffowcs Williams and Hawkings (FW-H). Gloerfelt *et al*. (Gloerfelt, Bailly et al. 2003, Gloerfelt, Bailly et al. 2001) conducted DNS simulation for flow over cavity using compressible Navier-Stokes equations to obtain radiated noise directly and used it as a benchmark to compare with hybrid methods using mean-flow profile with different integral formulations of Kirchhoff surface and FW-H (Gloerfelt, Bailly et al. 2003). Some hybrid methods for noise prediction use LES or DNS with acoustic analogy. LES or DNS is used to compute the sound sources in the well known acoustic analogy such as Lighthill's analogy. A DNS simulation with Lighthill analogy for sound radiation by turbulence is conducted by Whitmire et al. (Whitmire, Sarkar 2000) Ali *et al.* (Ali, Escobar et al. 2008) implemented LES with Lighthill's analogy for flow induced sound from fluid-structure interaction. Seror *et al.* (Seror, Sagaut et al. 2001) compared DNS and LES results with Lighthill's analogy and found some discrepancies in acoustic spectrum.

In another approach to predict noise propagation in an extended domain, a set of Linearised Euler Equations (LEE) are solved around a known stationary mean flow. Bailly et al (Bailly, Juve 2000) have computed LEE using dispersion-relation-preserving (DRP) spatial scheme along with fourth-order Runge-Kutta (RK4) temporal discretization. Astley (Astley 2009) has also implemented LEE for a subsonic flow case in turbofan aeroengines. Bogey et al (Bogey, Bailly et

al. 2002) have also used LEE along with aerodynamic source term obtained directly for reference from solving Navier-Stokes equations. LEE has also been used as hybrid model where mean flow is supplied by RANS equations (Lummer, Grogger et al. 2001). Addad et al (Addad, Laurence et al. 2003) have also successfully conducted LES for forward-backward facing step along with LEE for noise source prediction.

Although there have been very few investigations in the area of high fidelity simulation of a simple expansion muffler, there is a lot of research work reported with other similar geometries and applications. A DNS study has been conducted to investigate resonant instability in a cavity by Rowley et al. (Rowley 2002, Rowley, Colonius et al. 2002), who hypothesized that the presence of backflow in cavity flow simulation leads to an absolute instability in the wake mode. In DNS simulation of slit resonators in a normal incidence, Tam *et al* (Tam, Ju et al. 2003, Tam, Kurbatskii et al. 2001) observed that at high sound pressure intensity, vortex shedding is the dominant dissipation mechanism. Recently, they performed three dimensional simulations to correctly predict the trend in measured impedance using slits with different aspect ratios but failed to predict the exact linear evaluation to acceptable tolerances. (Tam, Ju 2009) A band-stop filter, Helmholtz resonator has been simulated by Roche et al (Roche, Vuillot et al. 2010) using direct simulation of Navier-Stokes equations and compared with the simulation using Euler equations. The simulations were conducted both with and without mean flow, to compare the attenuation due to viscous dissipation and vortex shedding. Their results also support the nonlinear absorption of resonant liner at higher sound intensities. Mendonca et al (Mendonca, Read et al. 2005) have performed detached eddy simulation (DES) on a double diaphragm orifice of an aircraft climate control system to detect the noise signature using Lighthill's analogy and the noise detected has been correctly validated with the experimental measurements conducted by microphone.

Despite the availability of various analytical sound prediction methods, LES has been considered to be a very reliable tool for design and development of sound attenuation systems. Since the Navier-Stokes equations consider viscous effects, some attempts have been made to simulate acoustic propagation using Navier-Stokes equations without any acoustic analogy (explained before) in various attenuation devices to get deeper understanding of the physics behind sound-mean flow interaction. A pressure based semi-implicit compressible Navier-Stokes solver has been presented by Wall et al. (Wall, Pierce et al. 2002) This method is similar to the pressure-correction method but requires iterative steps at every time step to stablise the solution for low Mach number flows. The method also claims to have a large (2.6 times) efficiency gain and much smaller (15 times) computational expense in performing LES at low Mach number flow. Such low Mach compressible LES solvers have also been found to be an effective tool in handling combustion instability problems. Roux et al (Roux, Lartigue et al. 2005) conducted compressible LES investigation in a complex swirled premixed combustor and found very good agreement with experiments in cold and reacting cases. Usually the acoustic analysis of the noise is calculated on wavenumber-frequency space; however Roux et al (Roux, Gicquel et al. 2008) in their recent LES simulations of mean and oscillating flow have used Proper Orthogonal Decomposition (POD) along with spectral maps to show all unsteady modes in the simulation. In another attempt to simulate an automobile muffler with a resonator attached in the expansion section, an exact compressible Navier-Stoke solver has been used by Obikane (Obikane 2009) to simulate low speed forcing oscillation at the inlet of the muffler. Rubio et al (Rubio, Roeck et al. 2006a) have recently attempted a 2D LES of simple expansion muffler to predict tonal noise. They further extended their investigation in three dimensions to predict both tonal and broadband noise produced near the expansion section of a simple expansion muffler (Rubio, Roeck et al. 2006b).

However, none of the investigations reported so far has covered the LES of forced oscillations/pulsation at the inlet of a simple expansion muffler.

This chapter presents two-dimensional and three-dimensional LES simulation of muffler flow acoustic and forced pulsation of a simple expansion muffler for different ranges of frequencies. Unlike Rubio et al (Rubio, Roeck et al. 2006b) this work employs long inlet and outlet ducts for the muffler configuration to ensure that no reflections contaminate the interaction of different acoustic waves in the domain during the acoustic flow simulation. Besides, a longer expansion chamber (10 times the expansion) has been used and the flow Mach number is 0.03, which is realistic for practical applications. The chapter also observes the physics of flow-turbulence-acoustic interaction in the muffler which is said to be responsible for tonal and broadband noise. This work also forces a pulse at the inlet of muffler to observe its interaction with flow acoustic. The chapter also highlights the advantages of the Karki-PISO algorithm (proposed in Chapter 2) for LES simulation in the context of acoustic propagation simulation.

8.2 Computational Setup

The LES simulation is carried out for two-dimensional and three-dimensional meshes. The two-dimensional simulation saves time but does not capture small scale turbulence and its effect on mean flow and acoustic pulse. On the other hand, three-dimensional simulation captures smaller scales of turbulence but it is computationally very expensive. Keeping this in mind, at first a two-dimensional LES is carried out to ensure good agreement with theory and statistics and then- a three-dimensional LES simulation is carried out for detailed analysis of the muffler. A mean flow of 10 m/s (M=0.03) is considered throughout the simulations and in the later part, a positive

sinusoidal pulse is forced on the inlet. Positive sinusoidal is considered to clearly analyse the flow-acoustic effect in the computational domain on the travelling pulse. In simulating simple expansion chamber, *Acoustic Pressure* can be defined as the difference of total pressure and mean pressure inside the chamber. This acoustic pressure provides interesting visualisation of pressure pulse propagation inside the simple expansion muffler.

Numerical schemes: A second order limited linear blended differencing scheme explained in section 4.3 is used for spatial discretization for this work. The Crank and Nicholson's second order temporal discretization with different θ values (equation 4.32) is used for all the simulations. The blended spatial differencing and mixed Crank-Nicholson scheme helps in stabilising the stiffness produced in solving Navier-Stokes equations when solving a compressible set of equations. The hybrid Karki-PISO algorithm proposed in Chapter 2 further enhances the robustness of the solver and extends the temporal discretization to operate at fully-implicit time marching scheme. This is particularly helpful in reducing temporal discretization errors introduced during simulation of forced pulse propagation in muffler, as shown in figure 4.8 of chapter 4.

Mesh refinement: The mesh size for the large domain should be kept at minimum possible to provide accurate results. A 4mm mesh is again used due to acoustic and LES simulation requirements for better resolution of length scales. With Karki-PISO algorithm, it is found that the 4mm mesh along with synthetic boundary condition for LES model provides accurate result for acoustic propagation in simple expansion muffler. The wall grading is used near wall and no-slip condition is used instead of any wall function. No-slip condition is used to avoid any error introduced into the solution domain due to the wall-function modelling. A total number of 2.5 million mesh points are used for the 3D simulation on 24 cores for a period of 1500 hrs time (more than 2 months) on 2.00 GHz Xeon processor to reach a steady state in the LES simulation.

Boundary condition: The boundary conditions in these simulations are very much the same as in chapter 4, except the inlet velocity boundary. The new boundary condition is not only the time varying sinusoidal pulse but a mixed form of synthetic turbulence boundary and synthetic pulsating boundary. This mixed form of inlet boundary is formulated keeping in mind the initial boundary requirements for LES simulations in such a developing flow. The synthesised turbulent fluctuations generated in section 6.5 of chapter 6 can be given by Eq. (6.77) as,

$$v'_i(x)^m = \boldsymbol{a}\, v'_i(x)^{m-1} + \boldsymbol{b}\, \widetilde{v'}_i(x)^m$$

This turbulent fluctuation along with forced pulse is superimposed on the mean flow. The forced pulse is given by,

$$u_f = A\, sin\,(2\pi f t) \qquad \ldots (8.1)$$

The final fluctuation is given by considering the turbulent intensity for the pulsating sinusoidal and imposed on mean flow as follows,

$$U = U_0 + u_f + (1 + \xi)v'_i \qquad \ldots (8.2)$$

Where U_0 is the mean-flow velocity and ξ is the turbulent intensity. The amplitude of forced pulsation A is kept at 0.5 m/s. A non-reflective boundary condition is adopted at the outlet. Rest of the setup is same as the RANS simulations in chapter 4.

8.3 Two-dimensional Simulation of Simple Expansion Muffler

The ineffectiveness of RANS modelling in simulating separating flows is evident from the simulation of simple expansion muffler in section 4.4.2.2. The pressure-difference contour in section 4.4.2.2 shows that the pulse bifurcates near the expansion of muffler because of the averaging of the dispersing pulse- that moves forward to create unphysical pressure differentials in the expansion chamber due to pressure-fluctuation averaging. These problems can be alleviated by using LES models which computes most the larger length scales rather than modelling all the length scales like RANS models. As mentioned before, acoustic propagation simulation deals with much smaller amplitude of oscillations in comparison to the mean flow and therefore the numerical solver should have very low numerical noise. On these ground, LES stands a better choice and provides a much accurate and robust technique for abovementioned reasons. The requirement of turbulence like inlet boundary condition is achieved by the introduction of a new variant of mixed synthetic boundary condition introduced in chapter 6 and explained in previous section. First, LES simulation of simple expansion muffler is performed to achieve a steady state flow and then, a forced pulsation is imposed in the later part of the work. After obtaining the results for a stable LES simulation in simple expansion muffler, the simulation is processed to analyse flow-acoustic interactions inside the expansion chamber and in the tailpipe.

Noise generation: The noise generation due to turbulence inside the muffler has quadrupole nature and is not a very prominent noise source in muffler. However the monopole and dipole noises produced by flow-acoustic feedback-coupling in expansion chamber or by the acoustic resonances excitation in chamber and tailpipe, are more effective source of noise generation in simple expansion muffler. The mechanism of acoustic feedback-coupling has been studied in the context of flow over cavity by various authors. The flow separation at sharp backward facing edge forms

thin shear layer or vortex sheet. These unstable vortex sheets quickly roll up to form a train of vortices. The vortex sheets are perturbed by acoustic waves reflected at the downstream edge of the expansion muffler and cause chamber resonance.

Acoustic simulation: LES simulation is carried out with the same 5 degree sector mesh, which was used in chapter 2 and 4. Mesh spacing of 4mm is maintained inside the computational domain. The mixed synthetic boundary condition is used with rest of the boundary conditions similar to muffler simulation of chapter 4. Besides, the boundary conditions at sides are set to symmetry boundary conditions. The blended second order Crank-Nicholson time discretization is employed in combination with the spatial limited linear second order discretization scheme. Since the analysis of simple expansion muffler simulation in this study is not concerned about the near wall scales, the Smagorinsky sub-grid scale turbulence model has been adopted over other more accurate sub-grid models (discussed in section 7.4) for the LES simulations in this chapter. It can be seen in section 7.4 that most the statistics for Smagorinsky model in a flow way from wall matches very well with the DNS statistics. Apart from that, the Smagorinsky model has also been found to be very stable in comparison to the other more accurate models.

As it is evident from the velocity contour and streamline of Figure 8.1 and Figure 8.2, even at very low Mach number, the shear layers or vortex sheet start to roll up quickly and break down into periodic vortex shedding. This is supported by the vorticity contour of Figure 8.3 as well, where the vortex roll up can be seen in the expansion section of the muffler. These periodic vortex shedding has also been witnessed by Rossiter (Rossiter 1966) in his experimental cavity noise investigation and he has described the periodic noise as similar in mechanism to edge-tone noise generation. Inside the expansion chamber, these vortices are convected downstream to the tailpipe end of the expansion-wall, where it hits the wall and breaks down into smaller vortices.

However, the unsteady compressible LES of the sector-mesh carried out in this section does not appropriately describe the turbulent flow field and its related dissipation. The simulation can only be considered to model the largest eddies in the 5 degree sector geometry accurately and therefore sector-mesh simulation should reasonably predict the low frequency tonal components.

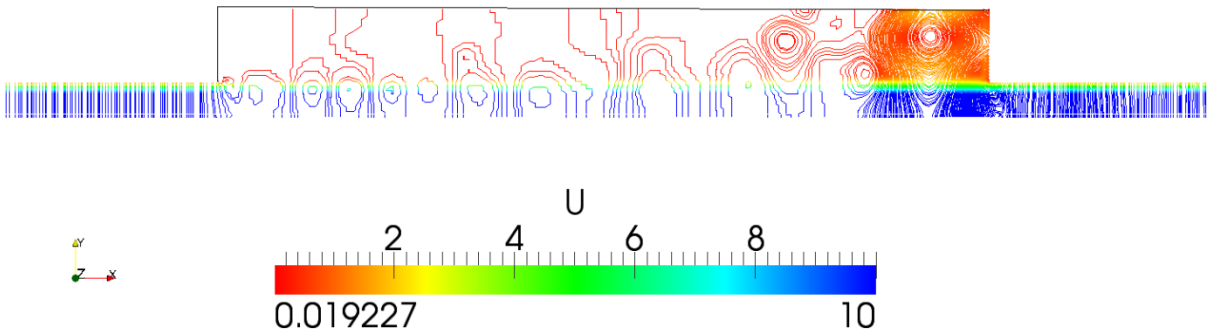

Figure 8.1: *Pressure contour coloured by velocity, showing vortex roll-up.*

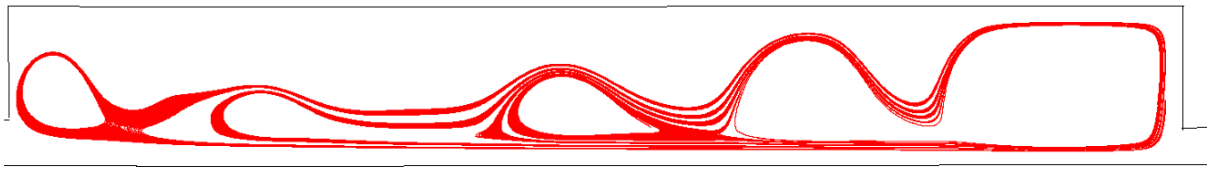

Figure 8.2*: Velocity streamlines for simulation of simple expansion muffler, showing vortex roll-up.*

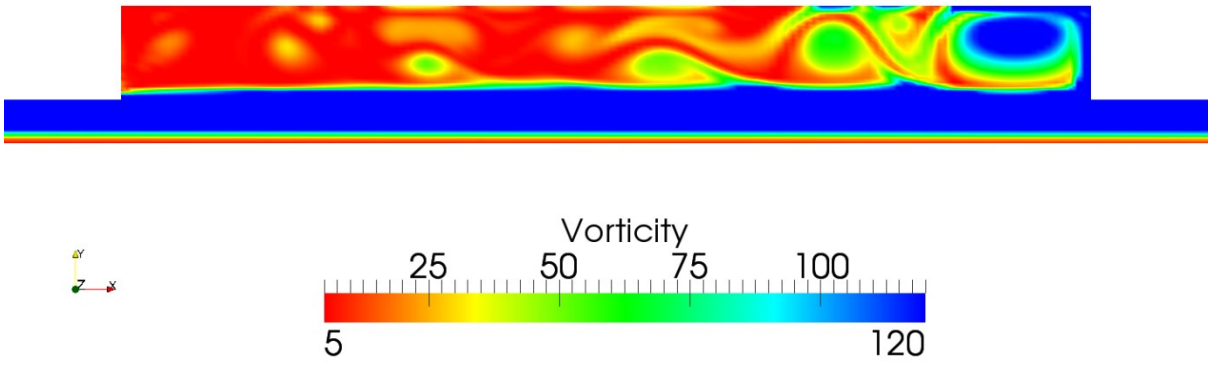

***Figure 8.3**: Vorticity contour for simulation of simple expansion muffler, showing vortex roll-up.*

In addition, the broadband components of the flow which are responsible for turbulence generated noise cannot be predicted with the sector-mesh models accurately and therefore a truly three-dimensional analysis needs to be done.

8.4 Three-dimensional Simulation of Simple Expansion Muffler

Three-dimensional compressible LES simulation is carried out to compute flow-acoustic interactions and to estimate the effect of flow-acoustic on forced pulse propagation. In the previous section, the three types of noise sources in the muffler have been explained. The noise generated due to chamber resonance excitement, noise generated by flow-acoustic feedback-coupling and noise generated by turbulence. The first noise source is obtained due to the rolling up of vortices in shear layer, when flow separation takes place at the entrance of the expansion chamber. Considering that the vortex shedding process happens due to flow-acoustic interaction at certain specific frequency, this source is perhaps the major contributor for tonal noises inside the muffler. The second noise source is obtained at the rear wall of the expansion chamber near the entrance of

tailpipe. The rolled up vortices hit on these walls, breaking up into smaller vortices and generating heavy exchange of energy between flow vortices and breakup vortices. The second source is believed to contribute mostly in broadband noise inside muffler.

Computational setup: The computational setup in the three-dimensional simulation is almost the same as in the two-dimensional simulation except that there is no symmetry boundary needed three-dimensional mesh, as boundary is closed. The same mixed synthetic boundary condition is used for generating better inlet inflow condition. The length of the tailpipe is shortened (halved) to reduce computational cost. Mesh spacing of 4mm is maintained in this simulation as well. However some refinements near the wall has been made to capture better flow parameters. Numerical schemes in this simulation are same as sector-mesh simulation.

Acoustic Simulation: Rossiter (Rossiter 1966) has derived a semi-empirical formula for the Strouhal number *St* in their experimental investigation of first type of noise in cavity flow as follows,

$$St = \frac{fD}{U_\infty} = \frac{n - \varsigma}{M + {}^{1}/_{k}} \quad \ldots (8.3)$$

Where f is frequency, D is the height of the inlet pipe, U_∞ is the free-stream velocity, n is the mode number, M is the Mach number, k is the ratio of convection velocity of the vortices to the free stream velocity and ς is a factor to account for the time lag between of a vortex and the emission of a sound pulse at the trailing edge of cavity. In another approach to find out the tonal noise inside exhaust chamber, Desantes et al (Desantes, Torregrosa et al. 2001) pointed to the acoustically excited resonance in exhaust and obtain the formula for acoustic resonance frequency as,

$$St = \frac{fD}{U_\infty} = nD\frac{(1-M^2)}{2ML_c} \quad \ldots (8.4)$$

Where L_c is the characteristic acoustic length of expansion chamber and is given by $L_c = (L + 0.525D)$, where *0.525D* is the end-correction in the pipe.

For a simple expansion muffler considered in this work, where flow velocity is at *M*=0.03 and inlet pipe diameter is D=0.048m, the first acoustic chamber resonance is expected at Strouhal number of 1.1, given by equation 8.4. On the other hand, equation 8.3 provides the Rossiter frequency for tonal noise which occurs at a Strouhal number of 0.225. To demonstrate the acoustic behaviour, the time history of pressure, density and velocity are recorded by putting probes at four distinct points inside the expansion chamber. Out of these four probes, the first probe is located near the inlet of the expansion wall inside chamber at (7.6, 0.04, 0), the second probe is located at the other end of the expansion wall inside the chamber at (8.0, 0.04, 0), the third probe is located at centre of middle of the expansion at (7.8, 0.004, 0) and the fourth probe is located in the tailpipe of the muffler at (8.2, 0.001, 0).

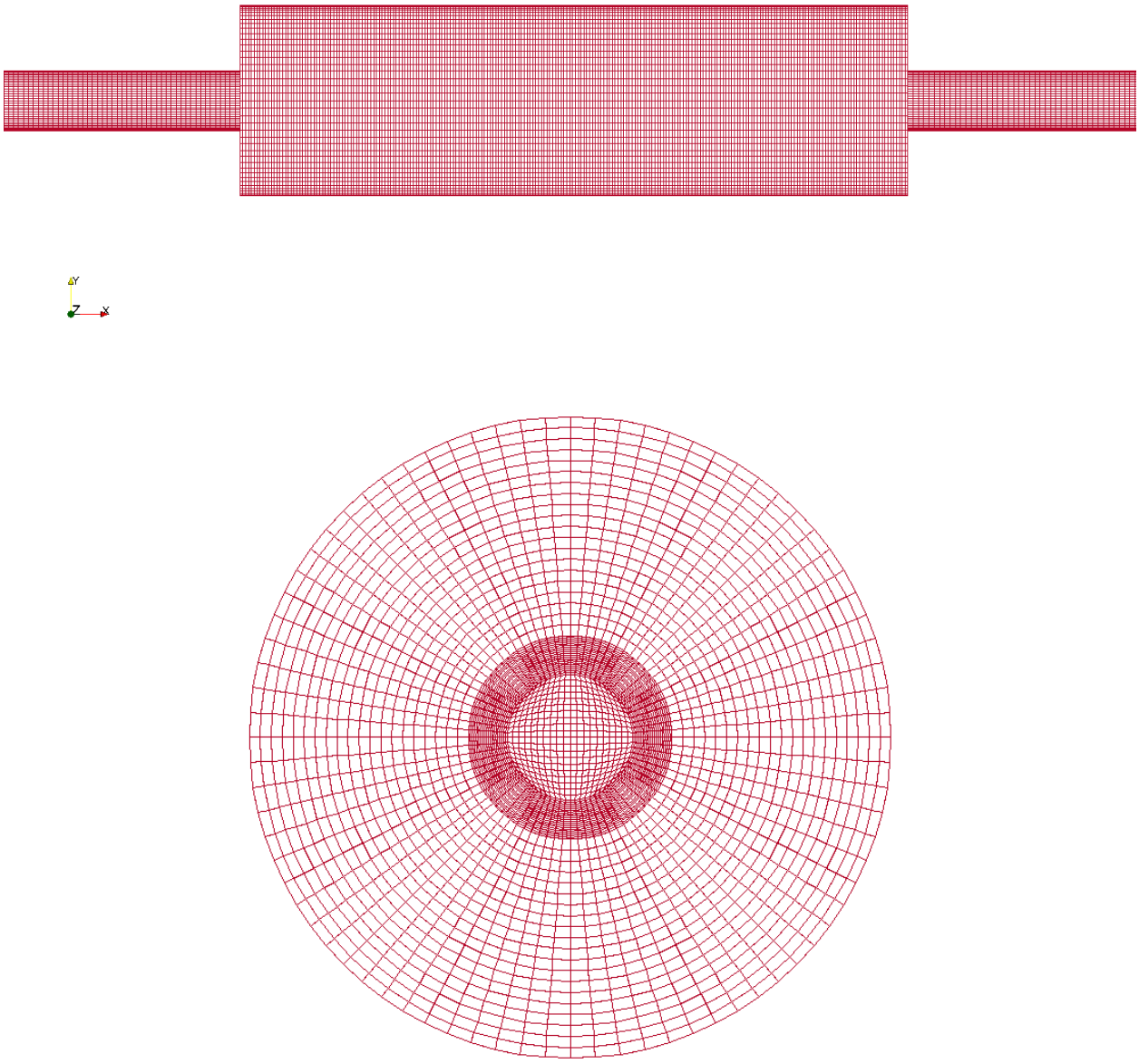

Figure 8.4: *Simple Expansion Muffler 3D Mesh: Front View (top) and Side View (bottom)*

(a)

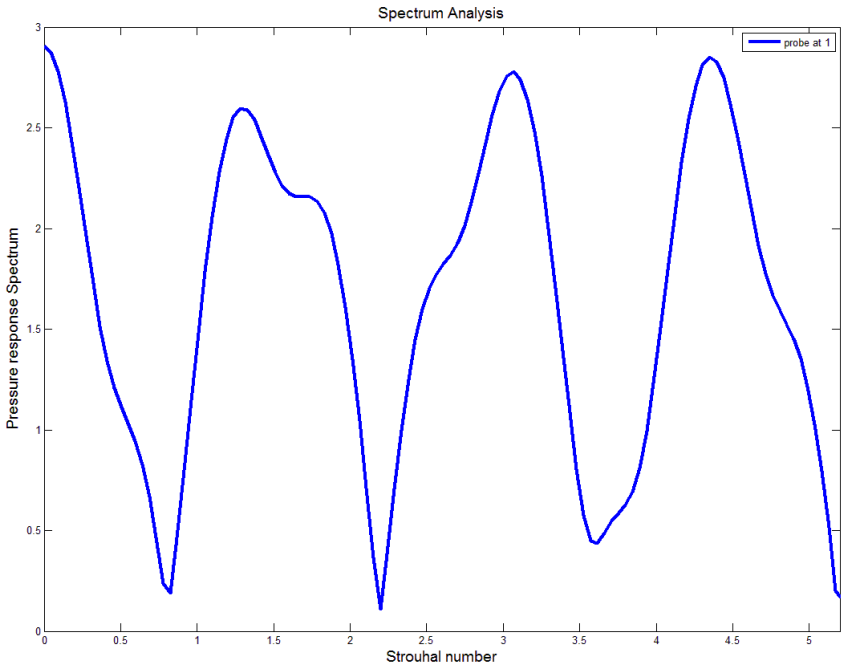

(b)

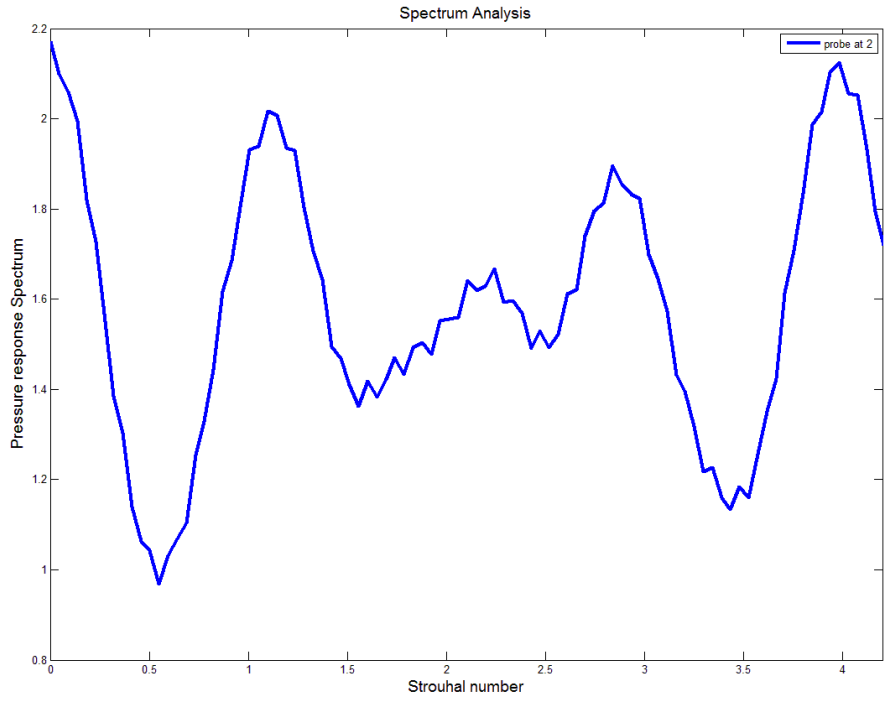

Figure 8.5: **(a)** *Pressure response spectra at probe location 1.* **(b)** *Pressure response spectra at probe location 2.*

The recorded data from the first two probes inside the expansion chamber provides a pressure response spectrum $\left(\frac{p^2}{\rho U^2}\right)$ with a chamber resonance around Strouhal number of 1.1. This is shown at Strouhal number 1.1 in Figure 8.5 (a) and Figure 8.5(b) with spectrum peaks. Some degree of distinction in the location of peaks can be explained with the dependence of the analytical formulation of on Mach number, which considerably fluctuates inside the expansion chamber. It can also be noted in this context that the Mach number of 0.03 at inlet decelerate inside the expansion chamber to a lower than 0.03 average Mach number and therefore analytical formula do not predict the exact location of Strouhal number. Figure 8.9 shows the average mean velocity inside the expansion chamber, which can provide an approximation for Strouhal number at various locations inside the chamber. The non-periodic frequency present in the pressure spectrum of second probe is perhaps due to the interaction of vortex coming toward the wall and the break-up vortex returning after the impact. These vortex interactions can be better explained with the velocity iso-surfaces presented in the figure 8.11 and figure 8.12. The frequent reflections near the tailpipe end of the expansion chamber can be seen in figure 8.12. The figure 8.11 and figure 8.10 clearly shows the rolling up of vortices and their breaking up after they hit the wall and interact with the incoming waves.

The third probe located at the centre of the pipe has a weaker magnitude of resonance chamber at Strouhal number of 1.1. However there is another frequency present in the chamber which occurs at Strouhal number of 0.5, as shown in figure 8.6. This is most likely the vortex shedding frequency. However there is some discrepancy in determination of analytical Strouhal number in the middle of the expansion chamber, which can be explained with the previous explanation of change in Strouhal number with lowering Mach number inside chamber. The fluctuation in Mach number inside expansion chamber can be estimated from the velocity contour in expansion

chamber shown in figure 8.8. The fourth probe located in the tailpipe shows the vortex shedding frequency at Strouhal number of about 0.2, which is close to the analytical approximation. This also supports the argument regarding change in predicted Strouhal number with lowering Mach numbers. The resonance frequency for this simulation is seen to be weak but can be seen at Strouhal number of around 1.1, as shown in figure 8.7. It is important to note that the analysis done by Rubio et al. (Rubio, Roeck et al. 2006a) do not use practically relevant Mach number and uses a short channel instead of long pipe (to save computational time and resource) which tends to make the computational domain susceptible to the contamination from the reflection of waves in flow acoustics.

It is believed that the most important sources of turbulent kinetic energy arise from the shear layer created from the interaction of the flow coming from the inlet pipe with the stagnant flow inside the expansion chamber. A local maximum turbulent kinetic energy is reached near the entrance of the inlet into expansion chamber, as shown by the first peak in figure 8.14. However the most dominant source of turbulent kinetic energy is the rear chamber wall (tailpipe end) where the vortex hits the wall and breaks down into smaller vortices. A global maximum is reach at the rear end as shown by the second peak in figure 8.14. So, unlike the previous assumption that most of the turbulent energy exchange happens at the front end, it can be seen that a stronger exchange of energy takes place at the rear wall if the length of the chamber is long enough. In that contest, it must be noted that the acoustic impedance inside the expansion chamber is found to be very high near the front end of the expansion chamber in comparison to the rear end of chamber, as shown in figure 8.13.

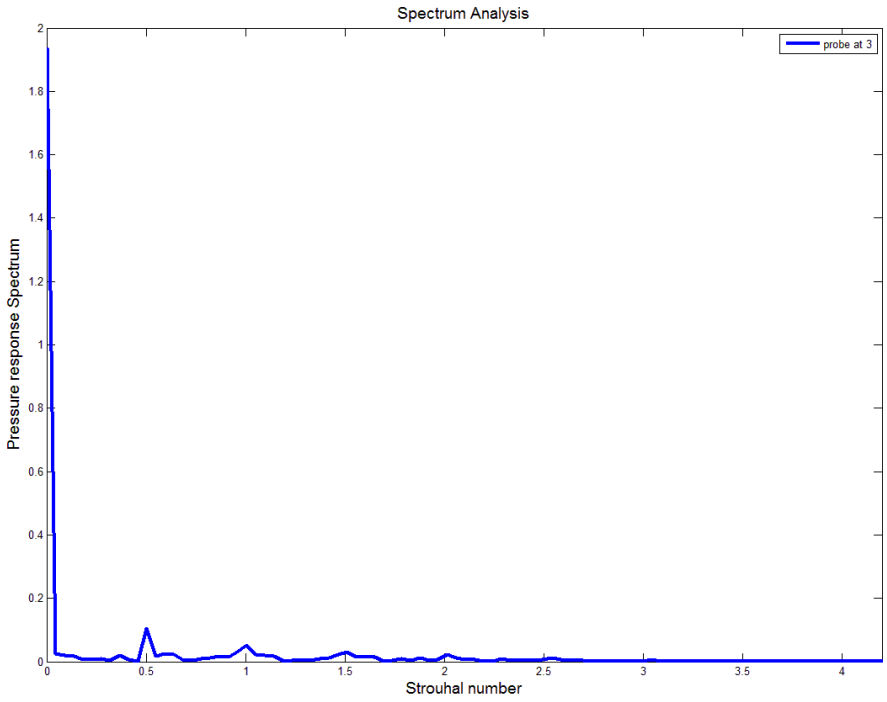

Figure 8.6: *Pressure response spectra at probe location 3.*

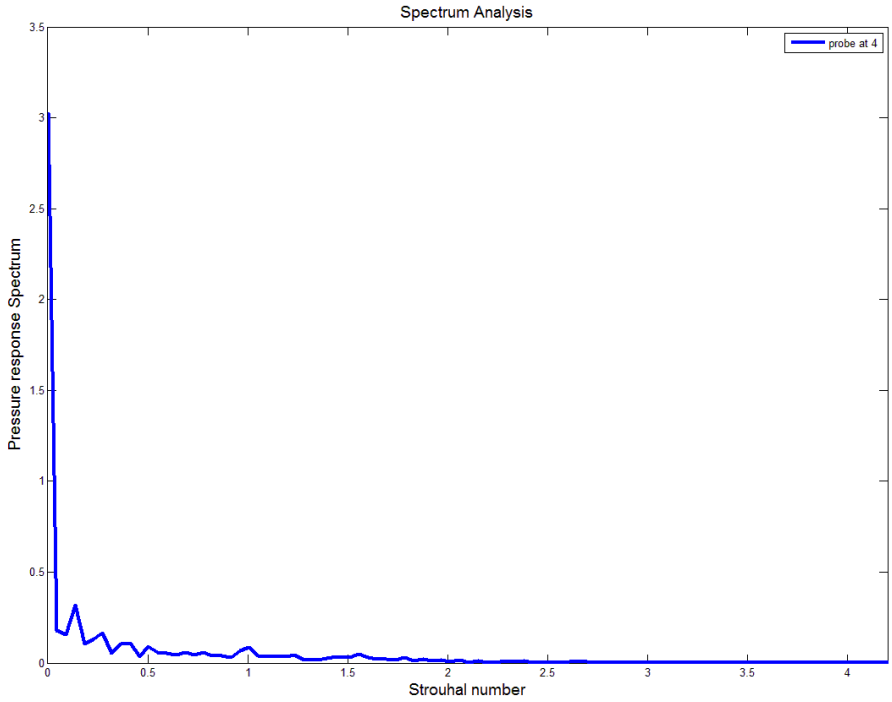

Figure 8.7: *Pressure response spectra at probe location 4.*

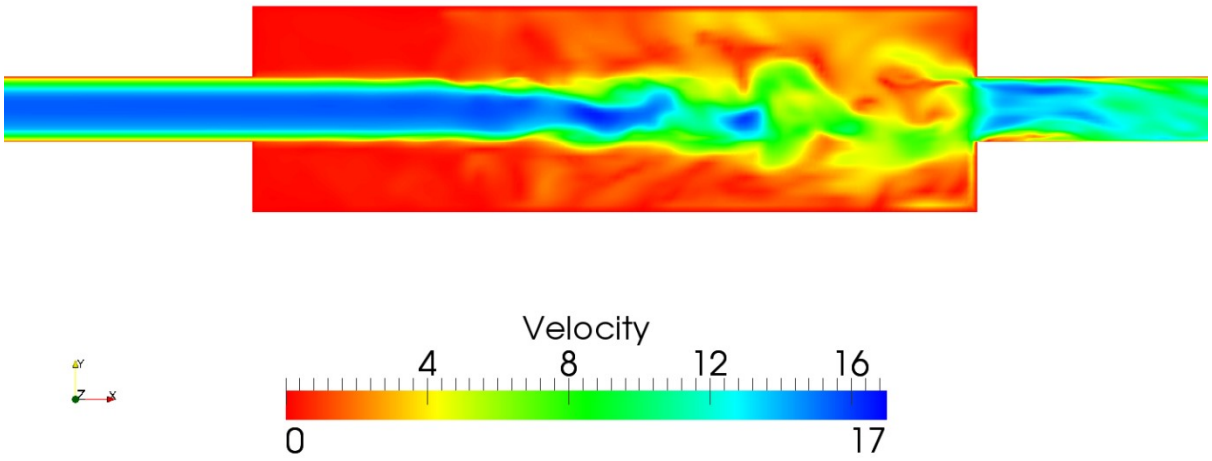

Figure 8.8: *Instantaneous velocity contour inside expansion chamber.*

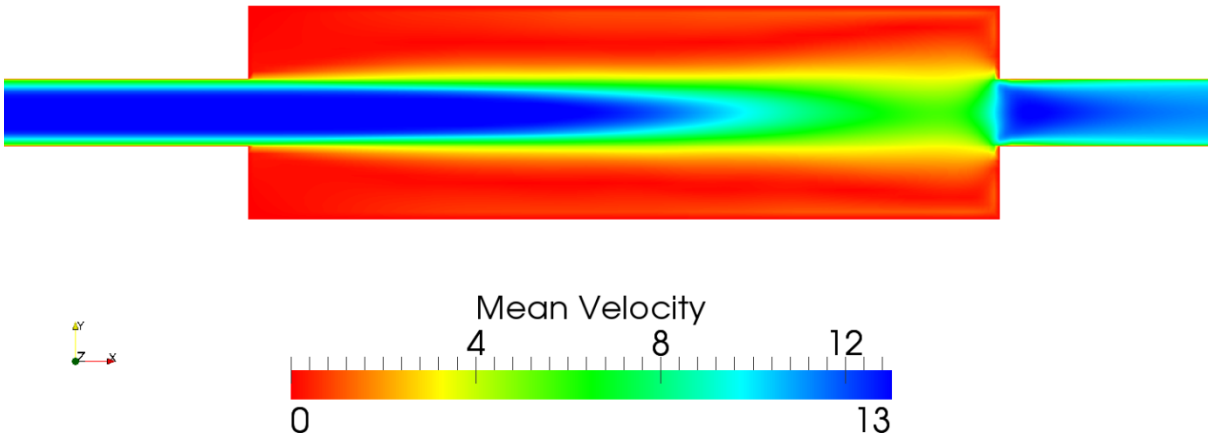

Figure 8.9: *Mean velocity contour inside expansion chamber.*

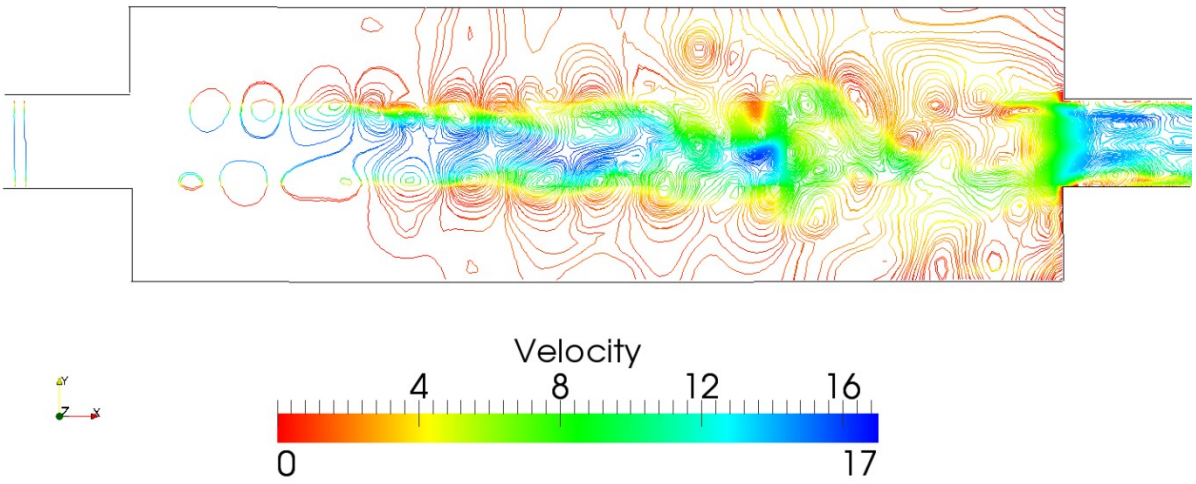

Figure 8.10: *Pressure contour coloured by velocity inside expansion chamber showing vortex roll-up.*

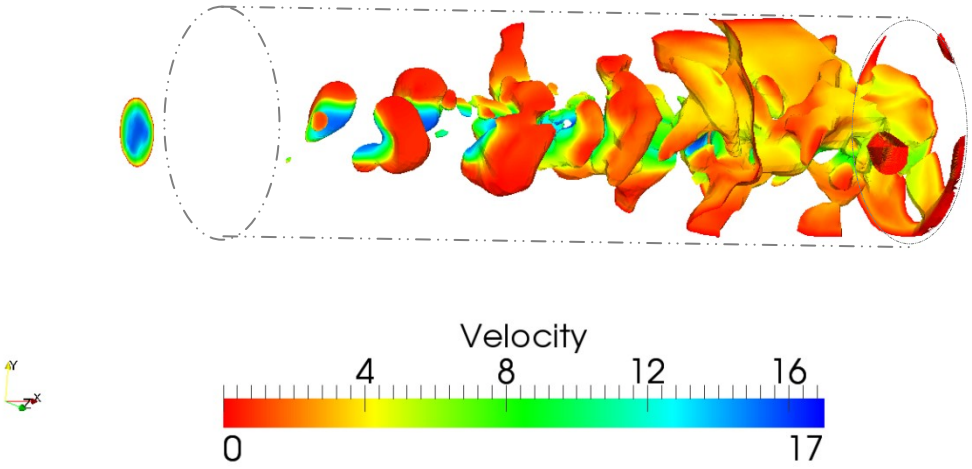

Figure 8.11: *Pressure isosurface coloured by velocity in the range of 100150 pa to 101210 pa inside expansion chamber, showing velocity.*

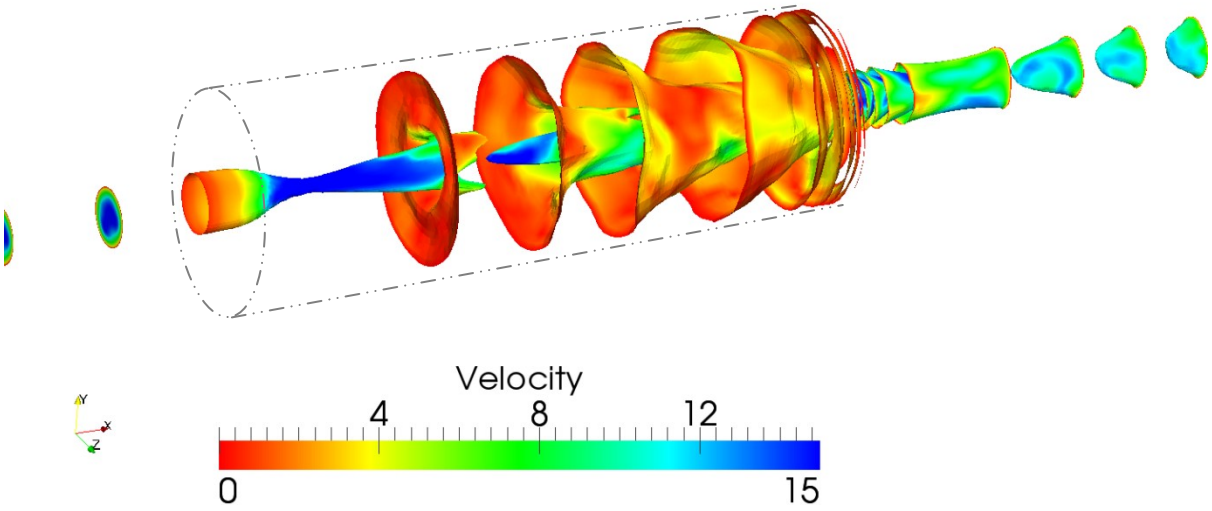

***Figure 8.12**: Acoustic pressure ($p - p_0$) isosurface in the range of 99960 pa to 100216 pa, showing velocity.*

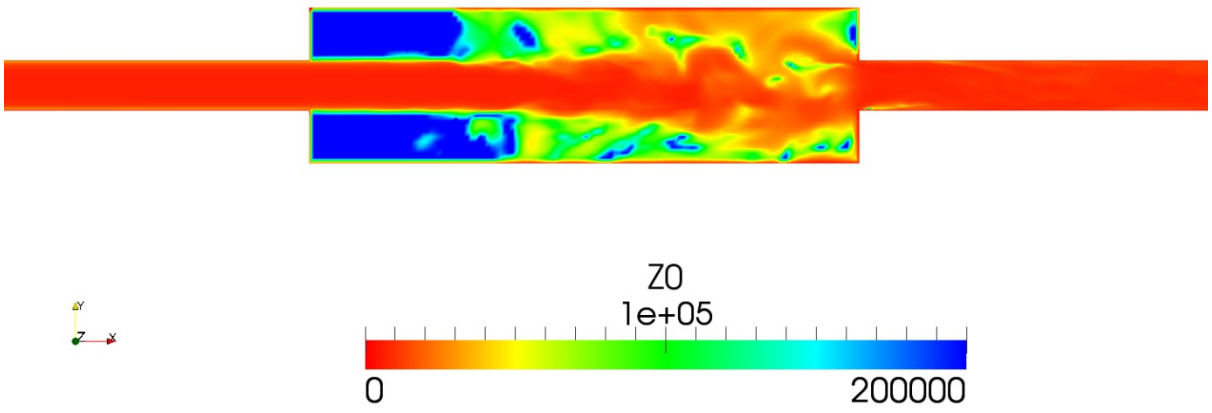

***Figure 8.13**: Acoustic impedance inside the expansion muffler.*

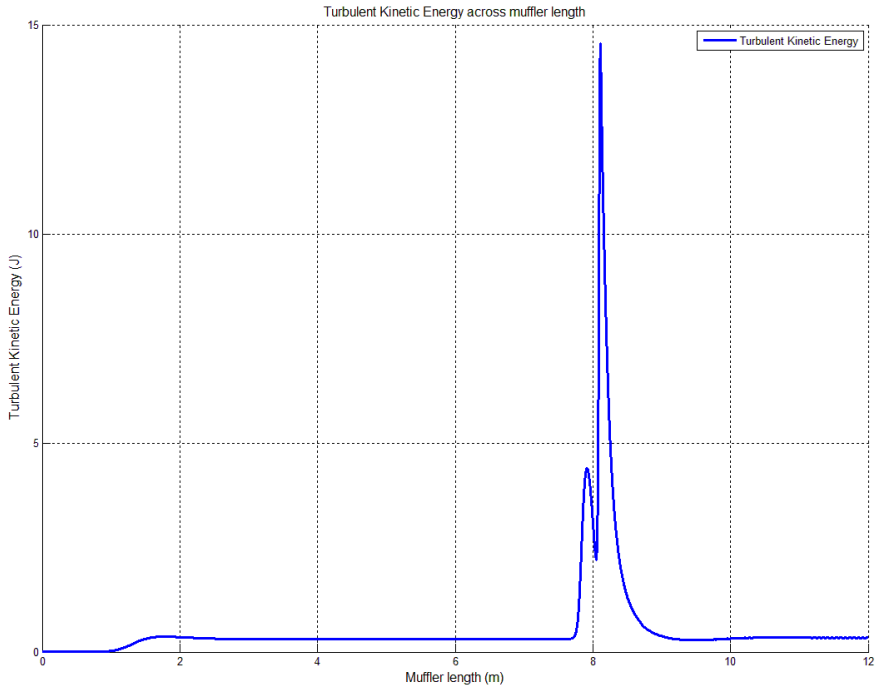

***Figure 8.14**: Turbulent Kinetic energy profile across the length of muffler.*

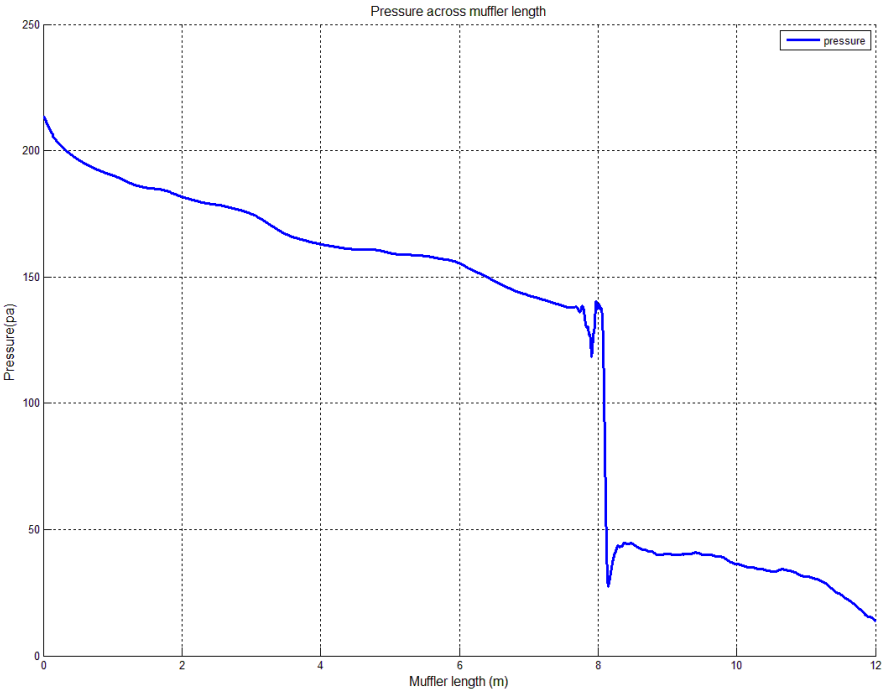

***Figure 8.15**: Pressure profile across the length of expansion muffler.*

The pressure plot in figure 8.15 shows a linear decay and as the flow enters expansion chamber the flow expands and pressure drops at constant value until flow reaches the rear end of expansion chamber. The pressure in the inlet and tail pipe decay as expected in duct type of flow.

8.5 Forced Pulsation at the Inlet of Simple Expansion Muffler

To investigate the propagation of sound inside an expansion muffler, a sinusoidal pulse is forced at the inlet of simple expansion muffler. The forced oscillation is combined with the synthetic boundary condition according to equation 8.2 to keep realistic turbulence along with pulsation in the inflow condition. In case of forced oscillation, it has been noted that more high frequency waves can be captured with fully implicit Crank Nicholson scheme. The Karki-PISO algorithm provides the computational flexibility to adopt fully implicit Crank Nicholson scheme without any stability issue in simulation of forced pulsation over mean flow profile obtained from three-dimensional compressible simulation. The rest of the computational setup is kept similar to the one uses for previous three dimensional simulations.

Acoustic Simulation: Acoustic simulation of forced pulsation has already been studied in chapter 4 with regards to the no-flow laminar condition. Muffler was also simulated with mean flow using RANS to obtain spectral analysis of attenuation in muffler. However, it was found that RANS usually tends to loses high frequency waves in the computational domain, leading to disparity and discrepancies in the predicted attenuation for higher frequency ranges. In last section, three-dimensional simulation of muffler flow acoustics is achieved using LES sub-grid model. On the top of the flow profile achieved in last section, a 3000Hz sinusoidal pulse is imposed at inlet of muffler. The mesh spacing and numerical schemes are same as in the last section.

A similar flow acoustic analysis is made in the domain of the computation by choosing same four probes at same location in the muffler. The pressure, density and velocity data are recorded throughout the period of pulse propagation at these four probe locations, near the front wall of expansion, near the rear wall of the muffler, in the middle of the muffler and in the tailpipe immediately after expansion. The pressure spectrum for probe 1 at the front wall of the expansion in figure 8.16(a) shows that the chamber resonance at the location has shifted to 1.6 from the previous 1.1. The peaks in figure 8.16 (a) seems to be a bit smoother, signalling the cancellation of few perturbations occurring in figure 8.5, where only flow acoustics were considered in the simulation. The shift in Strouhal number of the chamber resonance and the smoothening of certain perturbations are due to the presence of forced pulsation and their subsequent reflections inside the chamber. The pressure spectrum for probe 2 at the rear wall of the expansion in figure 8.16(b) shows the presence of other frequency modes occurring primarily at Strouhal number of 0.4. These frequency modes are different from the chamber resonance which can also be seen occurring there in the spectrum. These mode frequencies are the frequencies at which the vortex near the rear wall of chamber sheds or interacts and get pushed by the incoming forced pulse and subsequent reflections. The velocity contour in figure 8.18 and vorticity contour in figure8.20 clearly indicates the formation of vortex rolls very close to the rear wall of muffler after the pulse crosses the expansion inside the muffler. A comparison between the velocity contour before pulsation (figure 8.10) and velocity contour after pulsation (figure 8.18) also supports the formation of vortex at the corner of rear wall. A closer look at the isosurfaces shown in figure 8.19, highlight the presence of high velocity, closely spaced isosurfaces near the rear wall of the expansion chamber, which also supports the presence of these frequency modes. This spectrum also consists of the frequency of interaction of flow acoustic shedding and pulse propagation in the muffler.

The pressure spectrum for probe 3 in figure 8.17 (a), on the other hand dominantly shows the presence of pulse propagation frequency and the frequency of their subsequent reflections from the expansion walls. The pressure spectrum for fourth probe in the tailpipe shown in figure 8.17 (b) shows the presence of all the frequency modes, including the Rossiter frequency, vortex shedding frequency, vortex interaction frequency and the turbulent frequency, altogether.

In order to perform the analysis of effect of forced pulsation in the muffler, on a similar note to the analysis in section 4.4.1, two probes are again located in the simulation domain of the simple expansion muffler, one near the inlet and another immediately after the expansion chamber. The frequency analysis of pressure spectrum is performed to obtain transmission loss spectrum and pressure pulse spectrum. The transmission loss spectrum for LES simulation in figure 8.21 shows the pulse attenuation in the simple expansion muffler at various frequencies. Figure 8.20 also compares the transmission loss spectrum for RANS and LES simulation in expansion muffler at forced inlet frequency of 3200Hz. It can easily be seen in the figure that there are some discrepancies at the higher frequency range of the transmission loss in RANS simulation of expansion muffler. The discrepancy is supposed to be due to the averaging in RANS simulation which results in smoothening out of the high frequency oscillations.

(a)

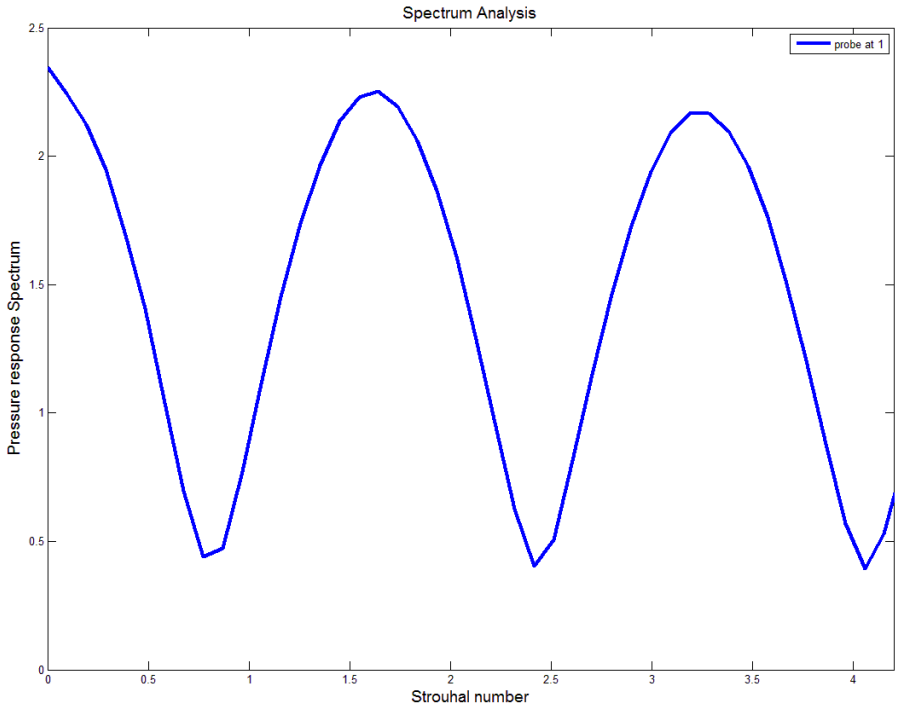

(b)

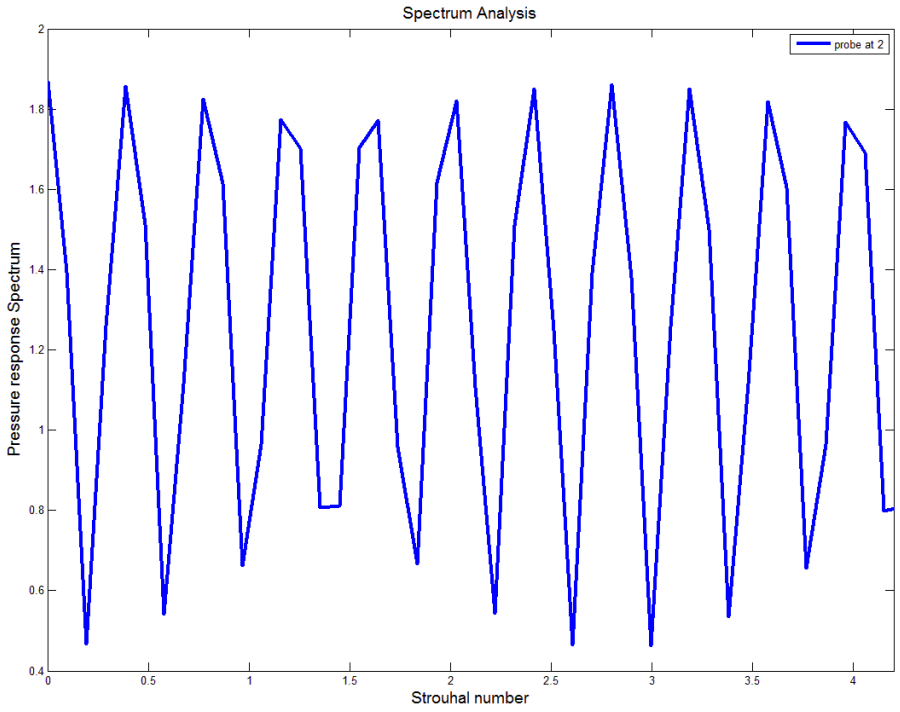

Figure 8.16: (a) *pressure response spectra at probe location 1.* **(b)** *Pressure response spectra at probe location 2.*

(a)

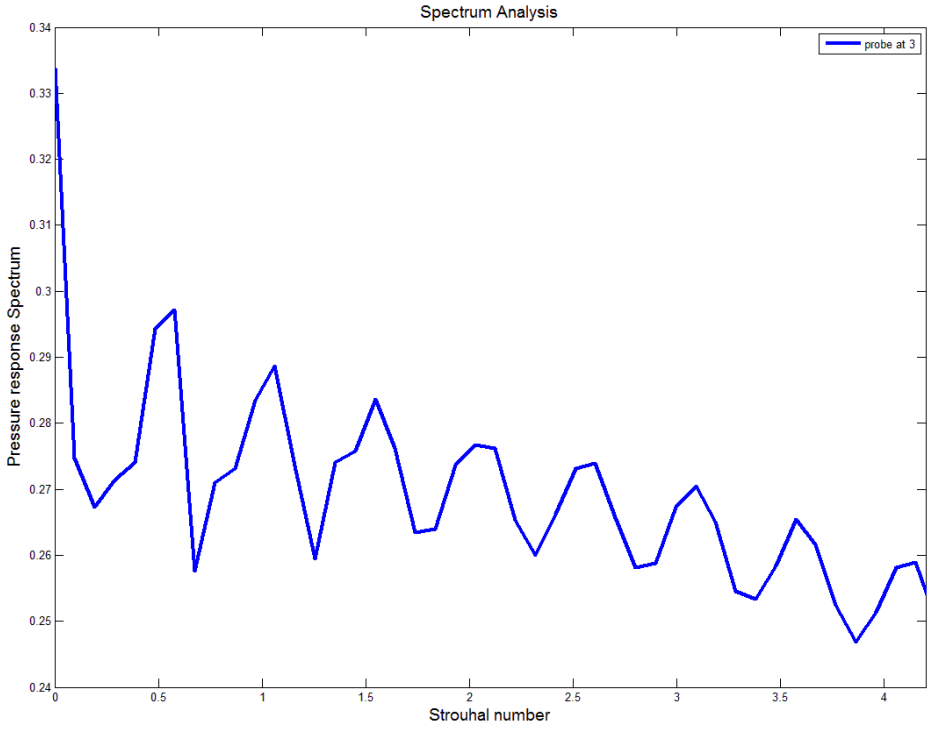

(b)

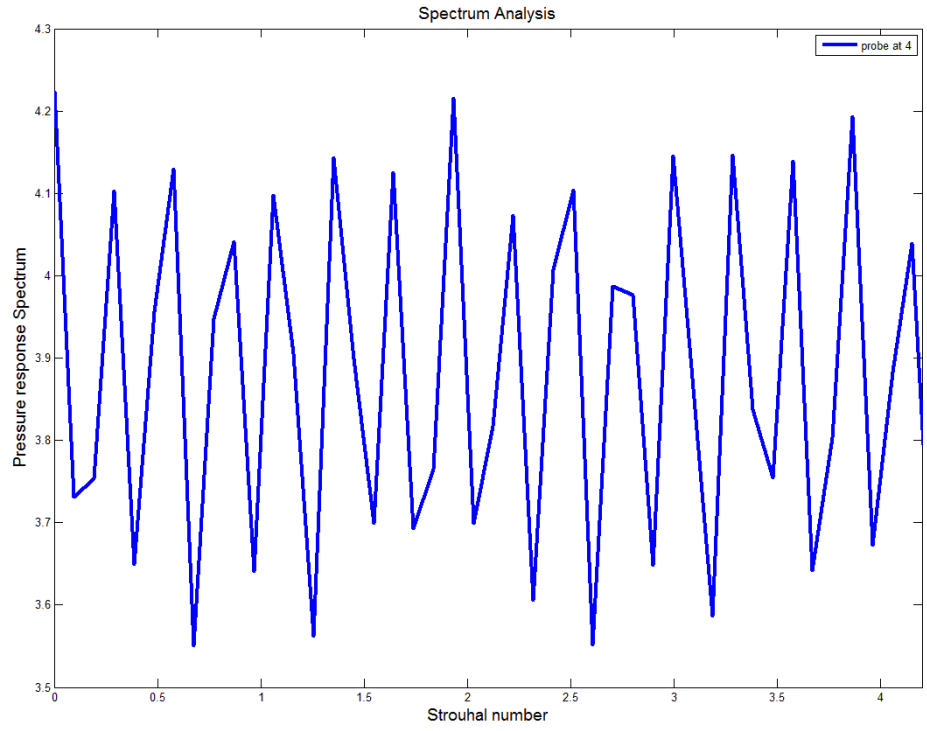

Figure 8.17: **(a)** *pressure response spectra at probe location 3.* **(b)** *Pressure response spectra at probe location 4.*

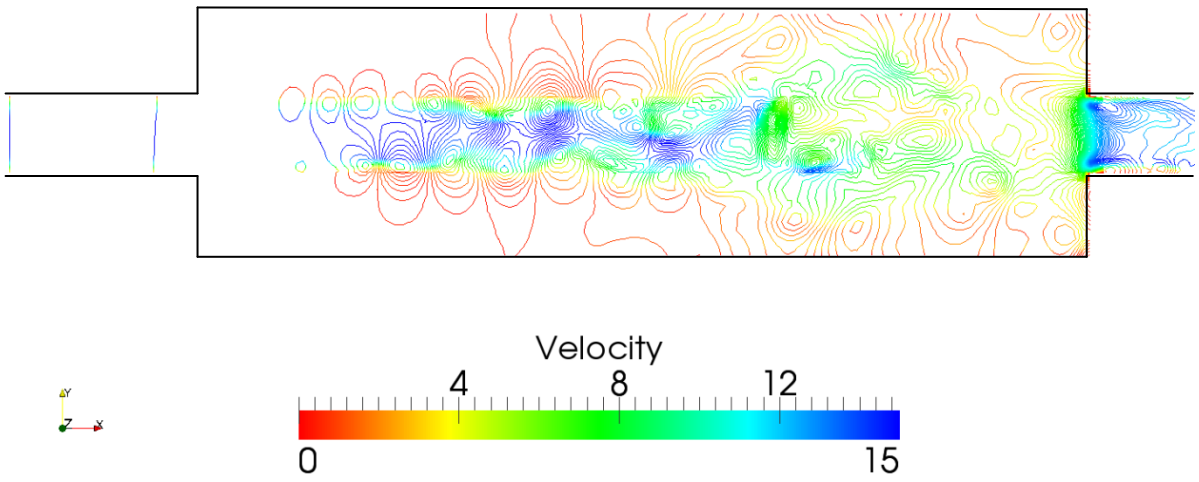

***Figure 8.18**: Pressure contour coloured by velocity after pulse crosses the muffler and their reflections interacts with the flow acoustics.*

This can be better understood, if a comparison between the RANS transmission pulse plot (figure 4.23(b)) and LES transmission pulse plot (figure 8.22) are made. The comparison clearly shows the missing high frequency oscillations in the RANS simulations. It is well known that the LES adopts the Kolmogorov's theory of self-similarity and predicts the transient flows better than RANS. RANS on the other hand uses statistical averaging and model most of the scales in the computational domain.

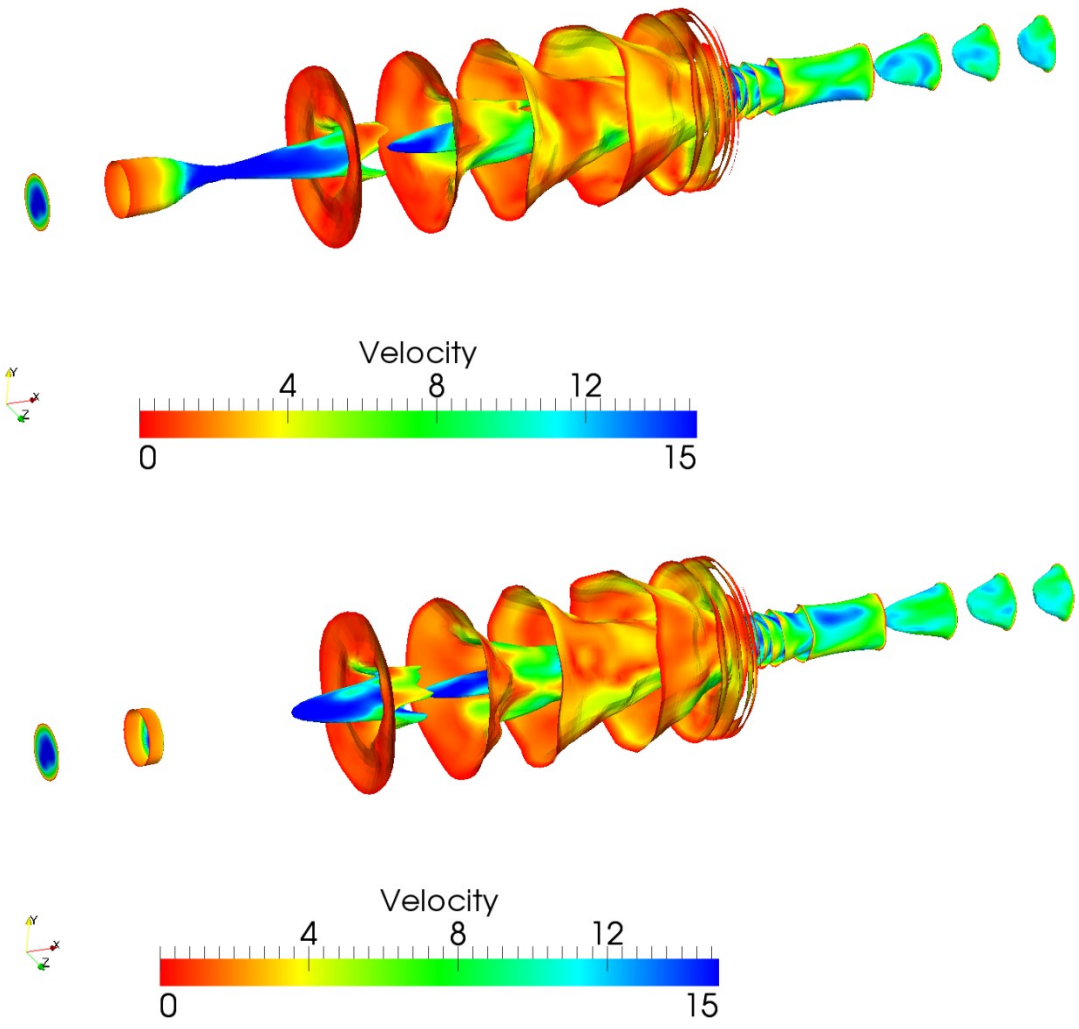

Figure 8.19: Acoustic pressure ($p - p_0$) isosurface in the range of 99960 pa to 100216 *pa, showing velocity profile at start (top), after pulse and their subsequent reflections propagate through the expansion muffler (bottom).*

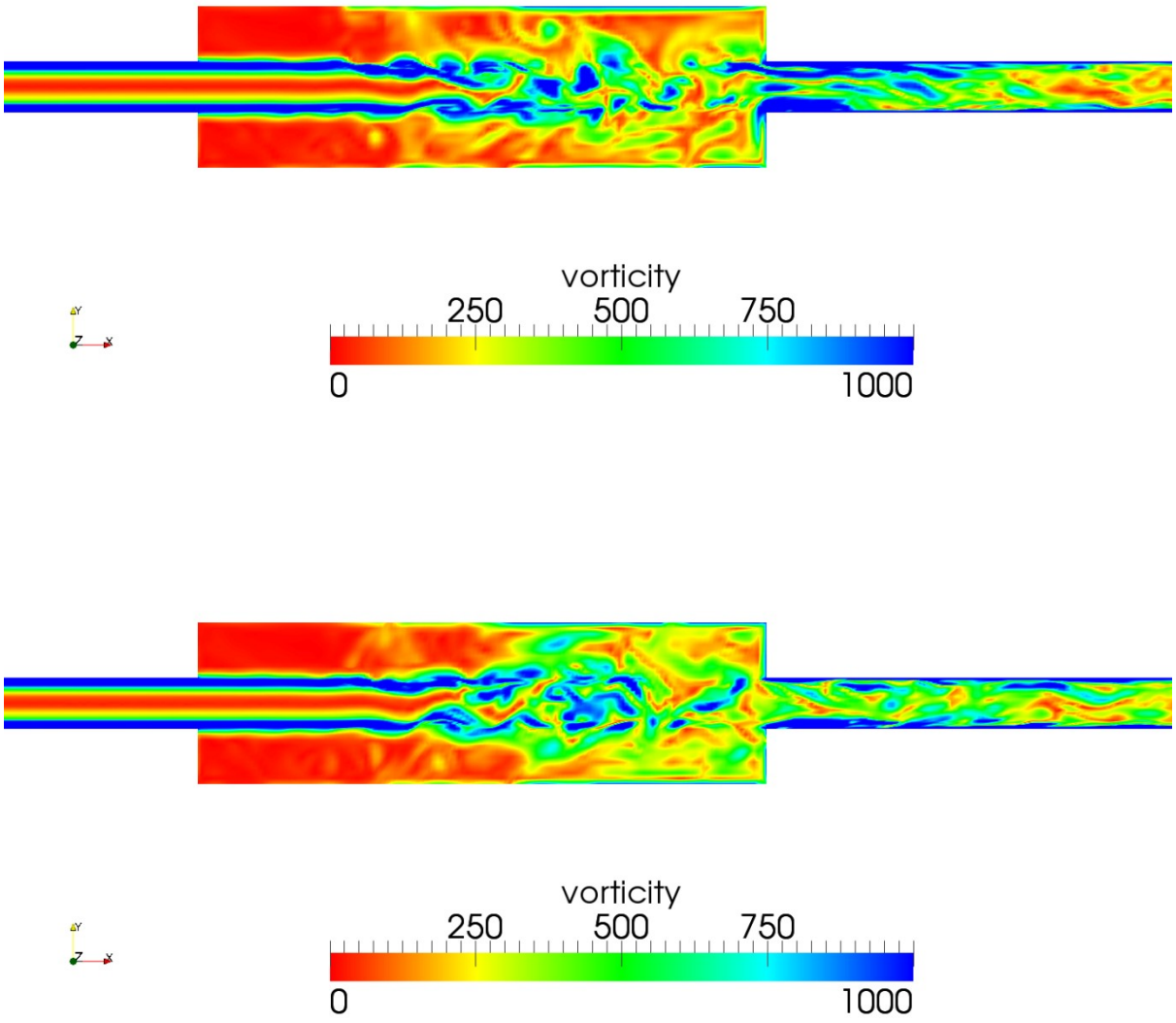

***Figure 8.20**: Vorticity contour at start (top); and, after pulse and their subsequent reflections from expansion chamber propagate through the expansion muffler (bottom).*

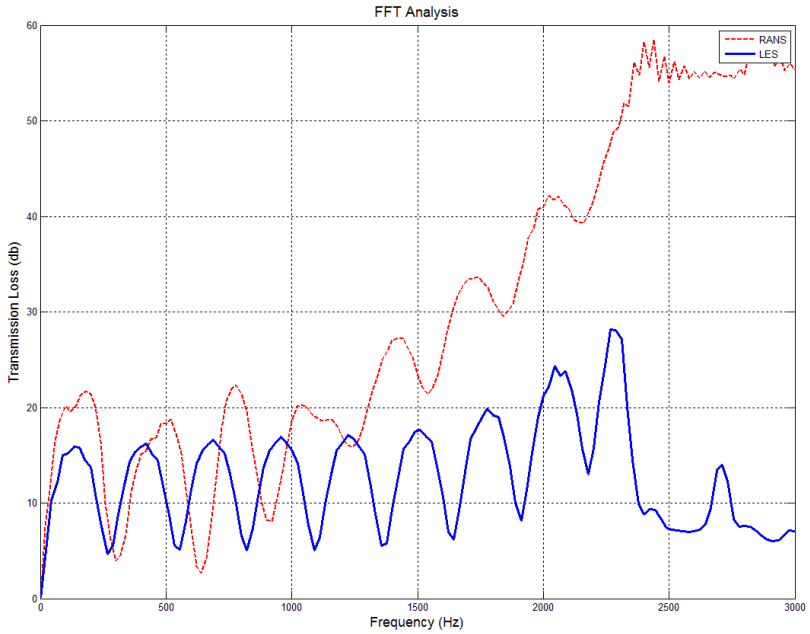

***Figure 8.21**: Comparison of transmission loss spectrum for RANS and LES in simple expansion muffler.*

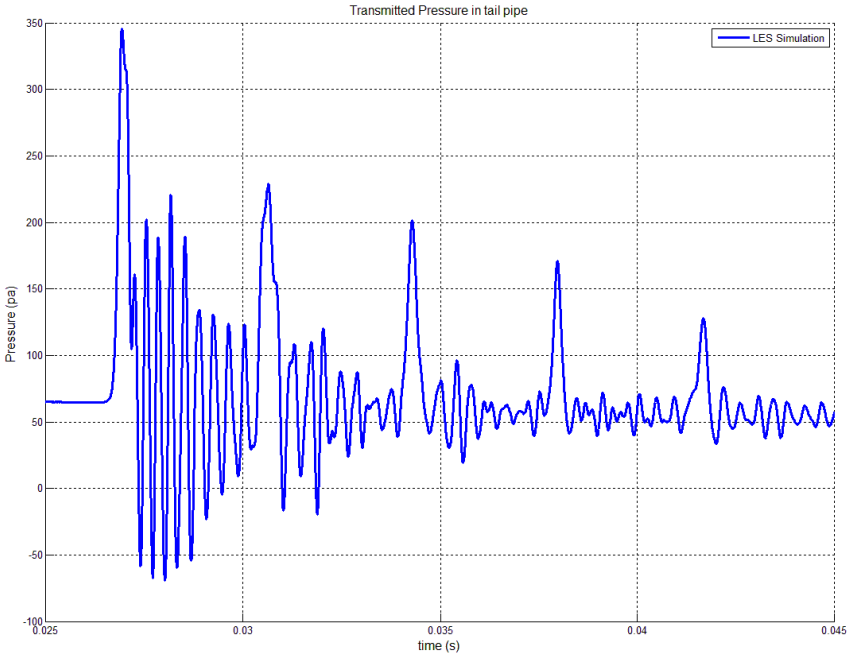

***Figure 8.22**: Transmission pressure spectrum of tailpipe pressure in a LES simulation of simple expansion muffler.*

The ability of LES to compute most of the large scale eddies and only model the small scale eddies through sub-grid scales provides it an edge over RANS, where most of scales are modelled. These attributes of the two methods justify the missing high frequency modes in the RANS results, shown in figure 8.22. The propagation of pressure pulse in the inlet pipe for higher frequency ranges is shown in figure 8.23. The stretching of pulses during the propagation can be observed by comparing the pulse at 1m, 3m and 5m away from the inlet. The pulse propagation for lower frequency range is shown in figure 8.24. The pulse stretching and perturbation seems to be more affected in these lower frequency ranges. The stretching of pulse could be due to the superimposition of turbulence scale and back-pressure over the forced pulsation profile. It is important to note that the back-pressure profile remains effectively constant throughout the simulation and the stretching in the pulse is primarily the effect of turbulence length scales on pulse propagation. In this case also, LES is capturing the effect of back-pressure and turbulence better than RANS methods and demonstrate the pulse and turbulence interaction for a range of frequencies.

To better understand the acoustic response of simple expansion muffler for a range of frequencies, a detailed acoustic response analysis is performed. The mean flow profile of simple expansion muffler is forced with a range of pulsating flow of varied frequencies, and their acoustic responses are recorded at certain points for obtaining a transmission loss spectrum and transmission pulse plot in the tailpipe. Figure 8.25 shows the transmission loss spectrum and transmission pulse plot for frequencies ranging from 500Hz to 2000Hz.

(a)

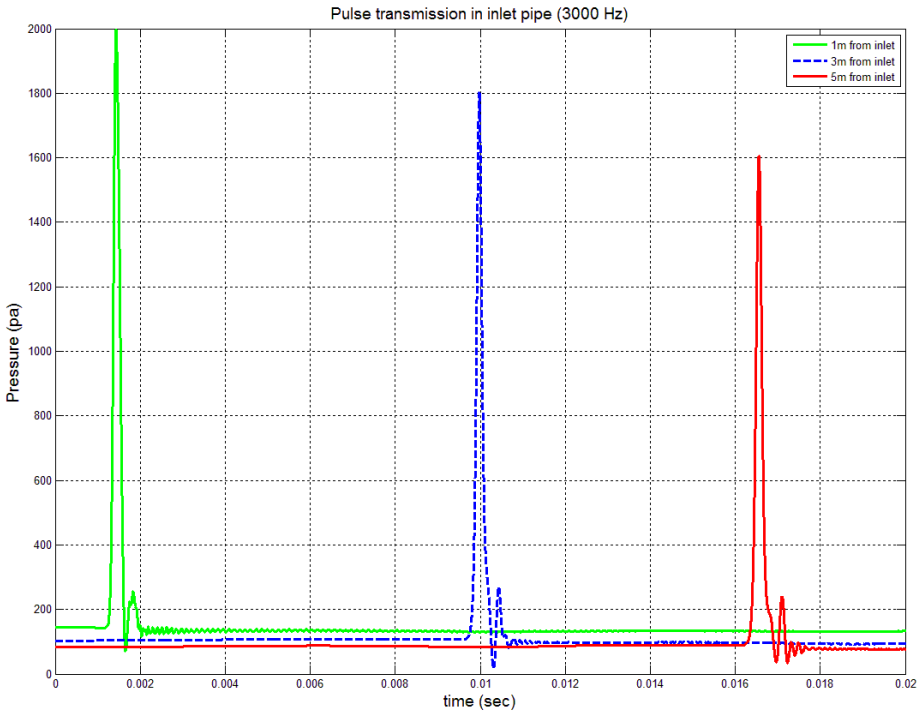

(b)

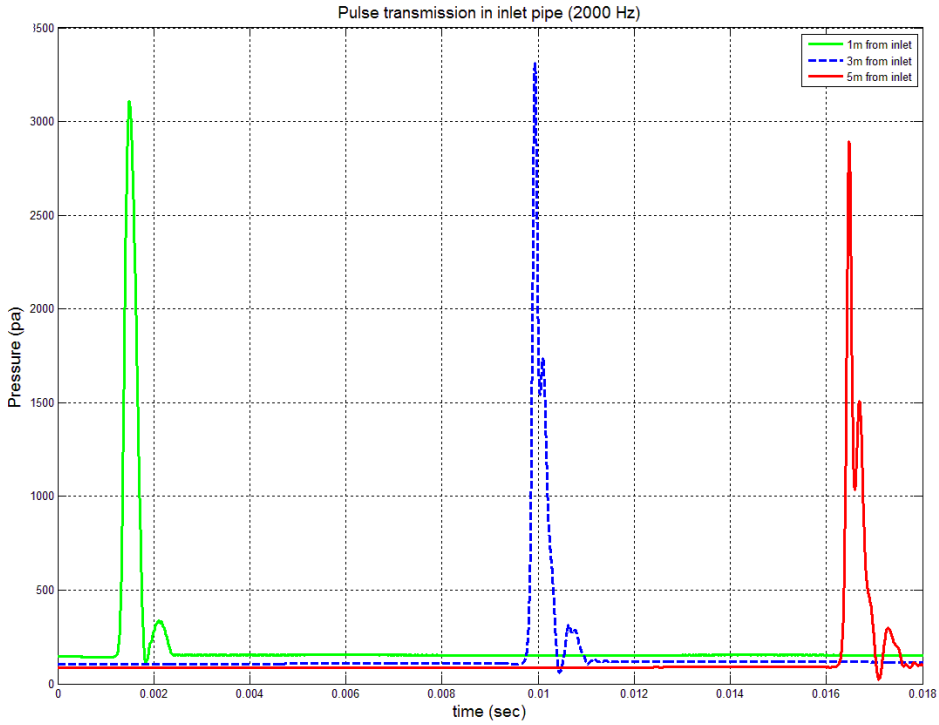

***Figure 8.23**: Stretching of pressure pulse during propagation in inlet pipe for (a) 3000Hz and (b) 2000Hz pure pulse.*

(a)

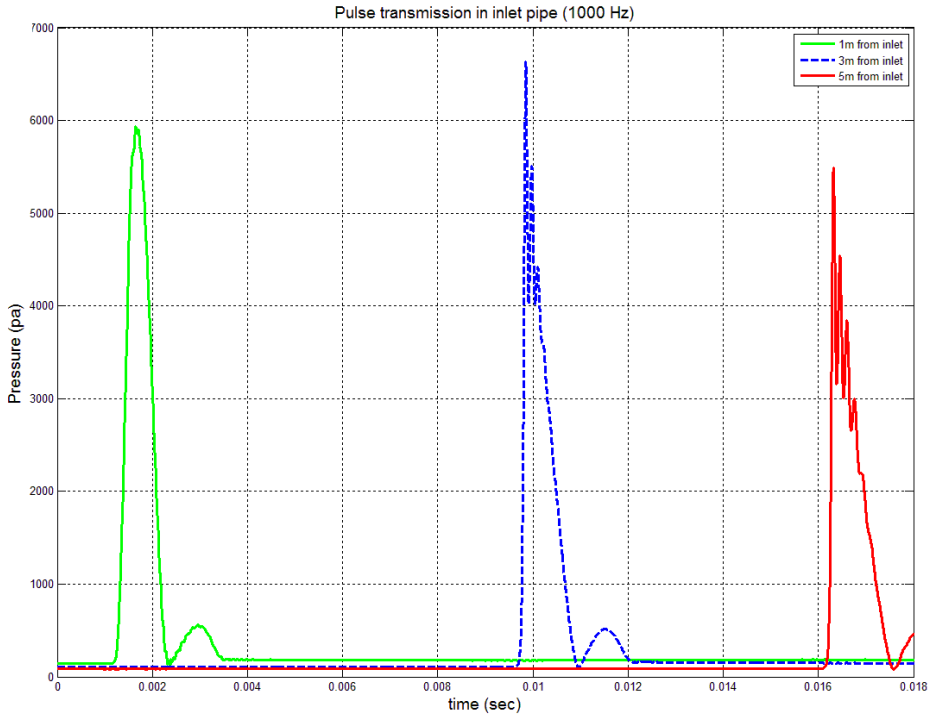

(b)

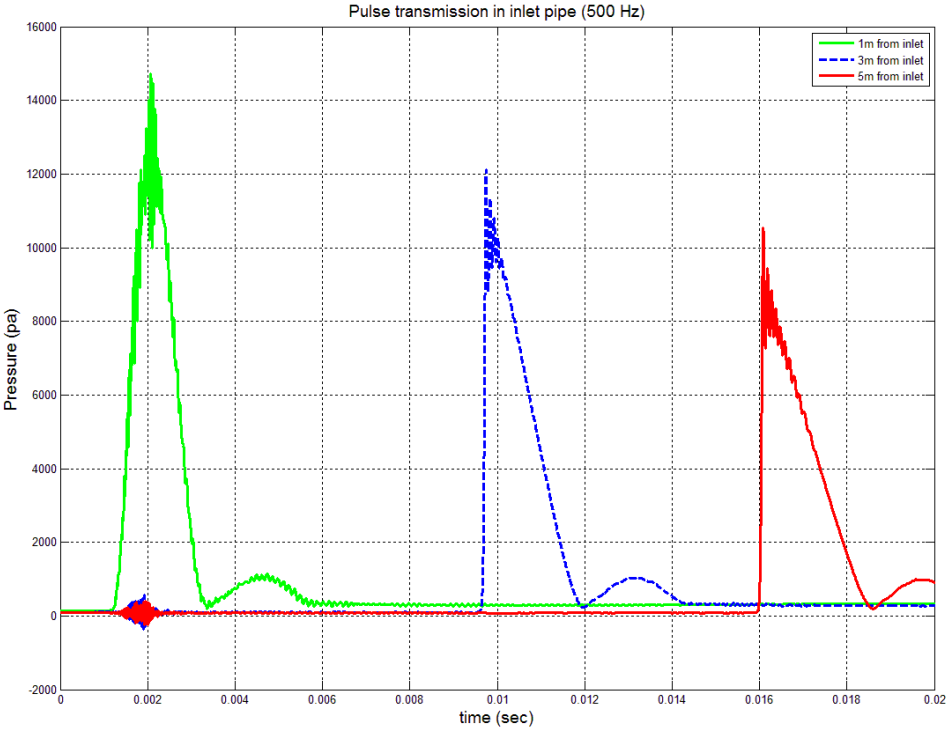

***Figure 8.24**: Stretching of pressure pulse during propagation in inlet pipe for (a) 1000Hz and (b) 500Hz pure pulse.*

As it is evident from the figure 8.25 (a), the attenuation inside the simple expansion muffler for pure sinusoidal sound propagation has higher attenuation at their natural sinusoidal frequency than at other frequencies. This observation can also be supplemented with the pulse propagation demonstrated in figure 8.24 for lower frequency ranges and in figure 8.23 for higher frequency range, where the pulse stretches and thereby attenuates at their frequencies. This phenomenon was not captured by the laminar compressible solver in section 4.4.1 and 4.4.2, where either there was no turbulence effect taken into account or the model of turbulence and numerical method itself had some limitations. The better capturing of various acoustic scales and acoustic attenuation in the present work is due to the fact that the current LES simulation of sound propagation in muffler captures turbulence scales and flow separation effects more accurately than the previous simulations done in chapter 4.

For a much higher frequency range of 3000Hz to 5000Hz, the transmission spectrum and transmission pulse plot is shown in figure 8.23. The transmission loss spectrum shows good agreement in the range of validated frequency of 0 to 3000Hz. It is important to note that the attenuation in the pulse at its own spectral frequency is much less affected in these higher frequency ranges, as demonstrated in the figure 8.23(a). It is due to the fact that at higher frequency, the length scale of turbulence does not have much larger interaction with the pulse and therefore the attenuation at its own spectral frequency is not much expected. The transmission pulse plot in figure 8.26 (b) shows reasonable increase in fluctuation with increasing input frequency in comparison to the transmission pulse plot in figure 8.25 (b). These increased high frequency fluctuations are very important to understand the various frequencies inside the expansion chamber muffler.

(a)

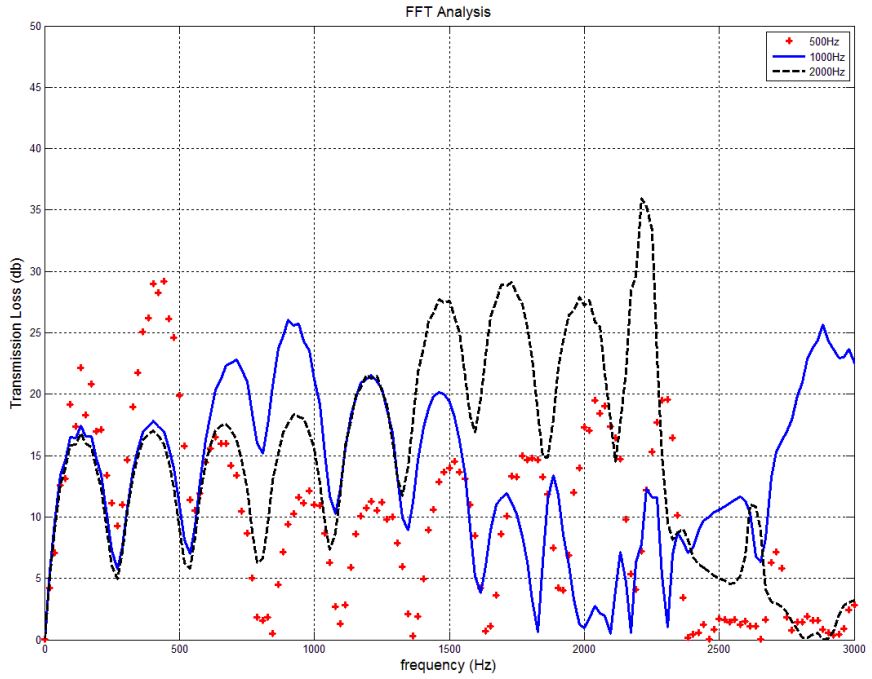

(b)

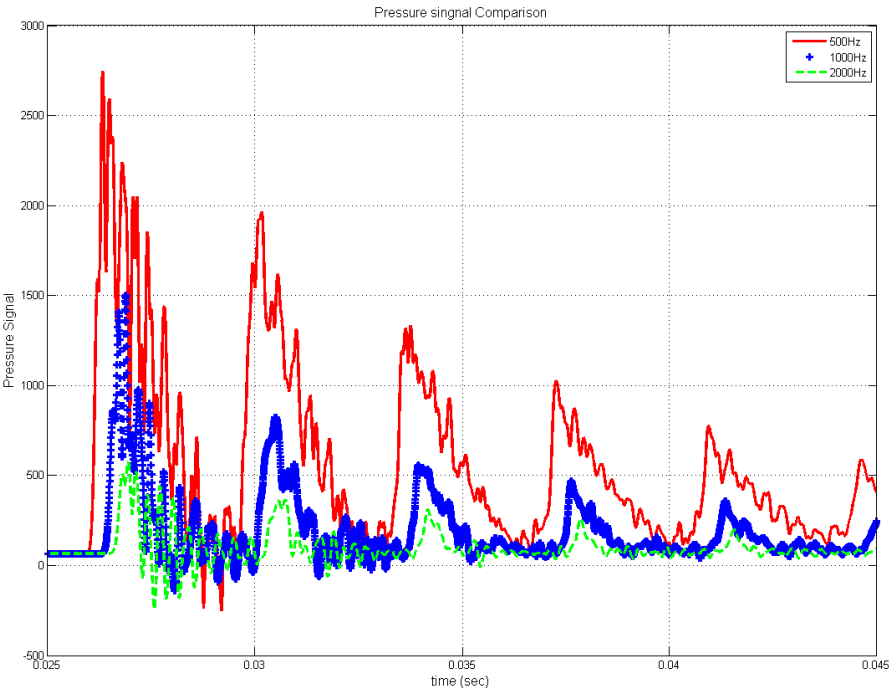

Figure 8.25: (a) *Comparison of transmission loss spectrum for various lower forced pulsation frequencies. (b) Comparison of transmission pulse for various lower forced pulsation frequencies. (Forced frequencies involved are 500Hz, 1000Hz and 2000Hz)*

(a)

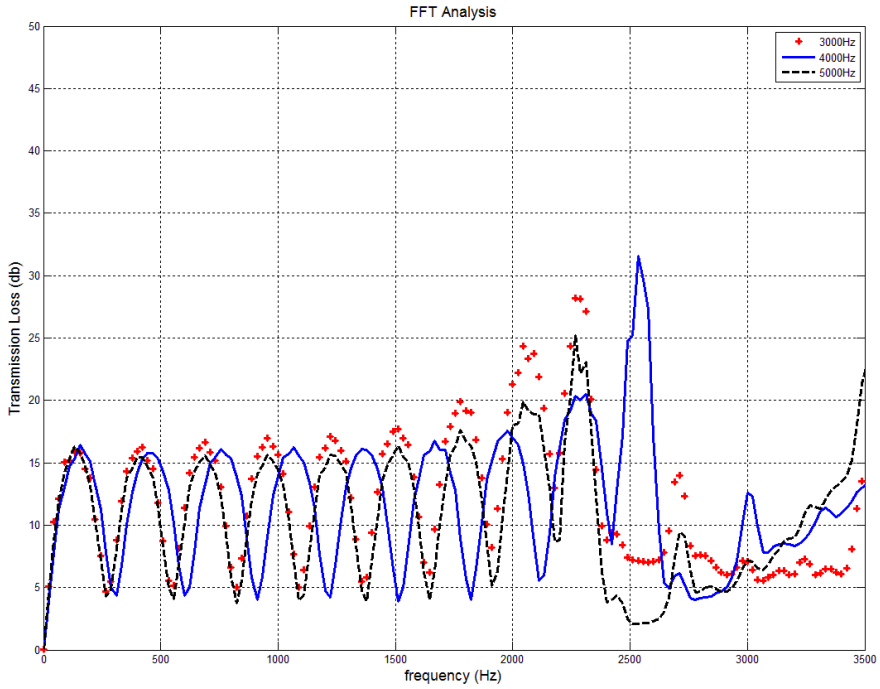

(b)

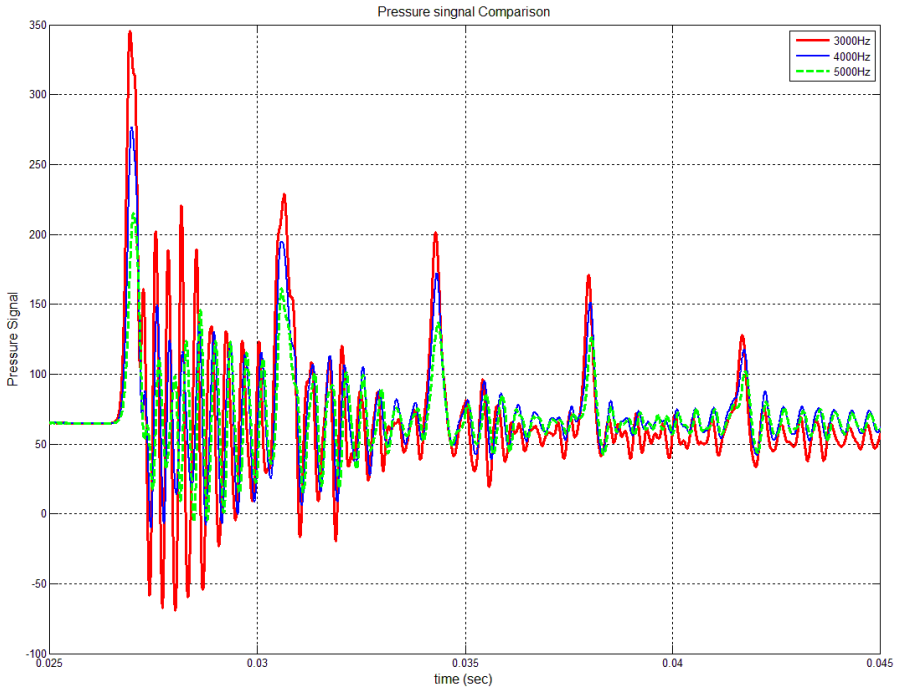

Figure 8.26: (a) *Comparison of transmission loss spectrum for various higher forced pulsation frequencies. (b) Comparison of transmission pulse for various higher forced pulsation frequencies (Forced frequencies involved are 3000Hz, 4000Hz and 5000Hz).*

Regarding the shift in Strouhal number range upon introduction of forced pulsation at inlet, it is perhaps the high frequency reflections (mostly near the sinusoidal frequency range, as shown in figure 8.26(b)) inside the expansion chamber from forced pulsation which causes the increase in vortex roll-up (decreases overall local average Mach number) and hence increases the Strouhal number for chamber resonance. It was found in figure 8.16 that the Strouhal number for chamber resonance increases considerably from 1.1 to 1.6, upon forced pulsation.

8.6 Closure

The chapter performs LES simulation of expansion muffler using mixed synthetic boundary condition for the inflow. A two-dimensional simulation is successfully conducted to understand the physics of the flow and predict the response of the simple expansion muffler upon forced pulsation at the inlet. Thereafter, a three-dimensional LES simulation is conducted to understand the flow acoustic inside the muffler. The analysis of flow acoustics inside muffler indicates that the chamber resonance occurs at Strouhal number 1.1, for a Mach number of 0.03. Forced pulsation of various frequencies are imposed at the inlet of the simple expansion muffler for the 3D LES simulation and it is found that the chamber resonance for the forced pulsation shifts to a higher Strouhal number of 1.6. The transmission loss spectrum for various forced pulsation of different frequencies show higher attenuation at the sinusoidal frequencies itself. The effect of turbulence and back-pressure on the pulse propagation is also highlighted in the context of flow-acoustic and forced-pulse interaction.

Chapter 9

Conclusions and Future work

9.1 Conclusions

This thesis has developed and validated a pressure based Navier-Stokes compressible solver for simulation of acoustic propagation of noise in turbulent flow through ducts and mufflers. Moreover, a mixed synthetic inflow boundary condition is also developed and validated for LES of channel flow. In the end, LES of a simple expansion muffler has been conducted to analyse the flow-acoustics and acoustic-pulse interactions inside the expansion muffler. This chapter presents an overview of different numerical and experimental results and conclusions. Following the conclusions, directions for future works are also itemised.

In Chapter 2, a new hybrid pressure-based Karki-PISO compressible solver was proposed and verifications were conducted for spatial and temporal accuracies. The proposed Karki-PISO solver has provided a low Mach number universal solver that can simulate the Navier-Stokes equations using a unique pressure-correction technique. This solver was further put to investigation in Chapter 4 to successfully analyse the behaviour of various geometrical and numerical aspects of simple expansion muffler design. The simulation of simple expansion muffler for forced pulsation at the inlet also provided an interesting similarity with the analytical and similar previous experimental results. In case of considerable mean flow, the simulation of a circular pipe captured the resonance frequency of the pipe in the transmission loss spectrum. It was found that the transmission loss spectrum provides an unrealistic linear increase in sound attenuation at higher frequency due to the simplifications and averaging in RANS techniques. For a more complicated

turbulent flow involving separation and reattachment, a simple expansion muffler was analysed for forced pulse propagation over a considerable mean flow profile at the inlet of the muffler. Although the transmitted pulse in the muffler captured all the high amplitude peaks, it was found that the transmission pulse did not capture very high frequency fluctuation, which was clearly averaged out by RANS simulation. The linear unrealistic increase in attenuation in transmission loss spectrum also pointed to RANS averaging. This was later confirmed by the LES simulation results obtained for a simple expansion muffler in Chapter 8.

In Chapter 5, a set of benchmark experimental results were obtained for a simple expansion muffler both with and without mean flow. The experimental results without mean flow showed a lower attenuation in the lower range of transmission loss spectrum, which was captured by the Karki-PISO compressible solver with acceptable shift in frequency plane. The experimental simulation with mean flow provided some interesting results which showed higher attenuation for certain mean velocities. The attenuation towards the higher frequency end of the transmission loss spectrum was reduced with increasing velocity inside the muffler from those certain values. This higher attenuation for a mixed random pulse forced at the inlet of the muffler was further confirmed with the LES results obtained in Chapter 8 from the simulation of forced pure pulse propagation in a simple expansion muffler, where there was higher attenuation in pulse propagation at their natural frequencies in the transmission loss spectrum.

A mixed synthetic inflow boundary condition was introduced in Chapter 6 with its evolution in the context of initial boundary generation for LES. This mixed synthetic boundary condition was further successfully adopted in simulating channel flow and pulse propagation in channel with mean flow in Chapter 7. It was found that the LES captures the large scales of mean flow better and provides accurate channel resonance inside the duct, compared with other resonance modes. In

Chapter 8, LES of a simple expansion muffler was performed to analyse the flow-acoustic present in the mean flow simulation of the muffler. Chamber resonance due to tonal noise and vortex shedding due to turbulence interactions and the other modes of these periodic structures were found for certain Strouhal number in flow. The effect of forced pulsation inside the expansion muffler was observed with regards to the shift in Strouhal numbers for these periodic structures with Strouhal number for chamber resonance shifting from 1.1 to 1.6. The interaction of flow-acoustic with the turbulence scales inside the muffler was observed with flow-visualisation, contours and isosurfaces to capture a greater insight into the physics of the interaction.

To summarise, a set of Navier-Stokes equations were solved for the acoustic propagation of pulse in a simple expansion muffler using a pressure based low Mach number flow solver. The LES simulation of pulse propagation provided an accurate set of solutions for noise propagation in a complex separating flow. It could be hoped that with recent improvements in computational resources, this pressure based Karki-PISO solver could fill the gap between the computational aeroacoustics solver and general CFD solvers.

9.2 Future Work

The following research could be considered to be future extensions of the current research work:

a) **Finer mesh**: Although LES of a simple expansion muffler has provided a good agreement from theory in our frequency-range of interest, it is known from the mesh independence study in Chapters 4 and 5 that the spatial discretization errors do exist for the higher frequency ranges. These higher frequency ranges can be further investigated by using finer mesh (less than 4mm mesh spacing) for simple expansion muffler geometry.

b) **Near-wall investigations**: The present research was focused on the bulk flow region and near-wall effects were largely overlooked. Future work will focus on the near-wall flow-acoustic interactions and also on the analysis of the various forced pulse propagation in the internal flow problems. In this regard, other applications (apart from the simple expansion muffler) of internal flow acoustic propagation and attenuation will be studied.

c) **Improvement in the mixed Synthetic inflow boundary**: Improvement in the mixed synthetic boundary should be presented so that near-wall functions can be avoided. The near-wall models are usually associated with the accuracies in the statistics in the wall region of the flow.

d) **Further Applications**: Other complex turbulent flow applications for acoustic simulation will be studied. A wall mounted Helmholtz resonators or other will be studied. The wall mounted resonators can facilitate an opportunity for the near-wall investigation of the flow-acoustic interaction in the device.

Bibliography

ADDAD, Y., LAURENCE, D., TALOTTE, C. and JACOB, M.C., 2003. Large eddy simulation of a forward–backward facing step for acoustic source identification. *International Journal of Heat and fluid flow,* **24**, pp. 562-571.

ALI, I., ESCOBAR, M., KALTENBACHER, M. and BECKER, S., 2008. Time domain computation of flow induced sound. *Computers & Fluids,* **37**, pp. 349-359.

ANTONIA, R.A. and KIM, J., 1992. Low Reynolds-number effects in a fully developed turbulent channel flow, , 14-18 December 1992.

ARENAS, J.P., GERGES, S.N.Y., VERGARA, E.F. and AGUAYO, J.L., 2004. On the techniques for measuring muffling devices with flow, 2004.

ASTLEY, R.J., 2009. Numerical methods for noise propagation in moving flows, with application to turbofan engines. *Acoustic Science & Technology,* **30**(4), pp. 227-239.

BACHERA, W., BAILLY, C. and LAFON, P., 1994. Stochastic approach to noise modeling for free turbulent flows. *AIAA Journal,* **32**(3), pp. 455-463.

BAILLY, C. and JUVE, D., 2000. Numerical Solution of Acoustic Propagation Problems Using Linearized Euler Equations. *AIAA Journal,* **38**(1), pp. 22-29.

BAILLY, C. and JUVE, D., 1999. A stochastic approach to compute subsonic noise using Linearized Euler's Equations. *AIAA Journal,* **37**, pp. 496-506.

BAILLY, C., LAFON, P. and CANDEL, S., 1996. Computation of noise generation and propagation for free and confined turbulent flows, , 6-8 May 1996.

BAILLY, C., LAFON, P. and CANDEL, S., 1995. A stochastic approach to compute noise generation and radiation of free turbulent flow, 1995.

BARBIERI, R. and BARBIERI, N., 2006. Finite element acoustic simulation based shape optimization of a muffler. *Applied Acoustics,* **67**, pp. 346-357.

BARDINA, J., FERZINGER, J.H. and REYNOLDS, W.C., 1980. Improved subgrid-scale models for large-eddy simulation, *AIAA 13th Fluid and Plasma Dynamics Conference*, 14-16 July 1980, pp. 10.

BARNARD, A.R., 2004. Measurement of Sound Transmission Loss Using a Modified Four Microphone Impedance Tube, , 12-14 July 2004.

BARTON, I.E., 1998. Comparision of SIMPLE and PISO-type algorithms for transient flows. *International journal for numerical methods in fluids,* **26**, pp. 459-483.

BAUER, M. and ZEIBIG, A., 2006. Towards the Applicability of the Modified von Kármán Spectrum to Predict Trailing Edge Noise. *New Results In Numerical And Experimental Fluid Mechanics V.* pp. 381-388.

BIJL, H. and WESSELING, P., 1998. A unified method for computing incompressible and compressible flows in boundary-fitted coordinates. *Journal of Computational Physics,* **141**, pp. 153-173.

BILLSON, M., ERIKSSON, L. and DAVIDSON, L., 2003. Jet noise prediction using stochastic turbulence modeling, *9th AIAA/CEAS Aeroacoustics Conference and Exhibit*, 12-14 May 2003.

BINDER, G., TARDU, S., BLACKWELDER, R.F. and KUENY, J.L., 1985. Large amplitude periodic oscillations in the wall region of a turbulent channel flow, , 7-9 August 1985, pp. 16.1-16.7.

BLAISDELL, G.A. and SPYROPOULOS, E.T., 1996. The effect of the formulation of nonlinear terms on aliasing errors in spectral methods. *Applied Numerical Mathematical,* **21**, pp. 207.

BLOM, C.P.A., VERHAAR, B.T., VAN DER HEIJDEN, J. C. and SOEMARWOTO, B.I., 2001. A linearized Euler method based prediction of turbulence induced noise using time-averaged flow properties, *39th AIAA Aerospace Sciences Meeting and Exhibit*, 1 July 2001.

BOGEY, C., BAILLY, C. and JUVE, D., 2002. Computation of flow noise using source terms in Linearised Euler's Equations. *AIAA Journal,* **40**(2), pp. 235-242.

BRAATEN, M.E. and SHYY, W., 1987. Study of pressure correction methods with multigrid for viscous flow calculations in nonorthogonal curvilinear coordinates. *Numerical Heat Transfer,* **11**, pp. 417-442.

BRADSHAW, P., FERRISS, D.H. and JOHNSON, R.F., 1964. Turbulence in the noise producing region of a circular jet. *Journal of Fluid Mechanics,* **19**(4), pp. 591-624.

BRANDT, A., 1977. Multi-Level adaptive solutions to boundary-value problems. *Mathematics of Computation,* **31**(138), pp. 333-390.

BREUER, M. and RODI, W., 2007. Large-eddy simulation of turbulent flow through a straight square duct and a 180$ deg bend. In: P. VOKE, R. KLEISER and J. CHOLLET, eds, *Direct and Large Eddy Simulation I.* pp. 273-285.

BRUN, C. and HABERKORN, M., 2008. Large Eddy Simulation of compressible channel flow: Argument in favor of universality of compressible turbulent wall bounded flows. *Theor. Comput. Fluid Dyn.,* **22**, pp. 189-212.

BYRNE, K.P., SKEEN, M. and KESSISSOGLOU, N.J., 2006. Measurement of the sound transmission loss of a small expansion chamber muffler to consider the effect of mean flow and wall compliance. *Proceedings of ACOUSTICS*, 20-22 November 2006, pp. 257-264.

CHOI, Y. and MERKLE, C.L., 1993. The application of preconditioning in viscous flows. *Journal of Computational Physics,* **105**, pp. 207-223.

CHORIN, A.J., 1968. Numerical solution of the Navier-Stokes equations. *Mathematics of Computation,* **22**, pp. 745-762.

CHORIN, A.J., 1967. A numerical method for solving incompressible viscous flow problems. *Journal of Computational Physics,* **2**, pp. 12-26.

CHOW, F.K. and MOIN, , 2003. A further study of numerical errors in large-eddy simulations. *Journal of Computational Physics,* **184**, pp. 366-380.

CHUNG, Y.M. and SUNG, H.J., 1997. Comparative study of inflow conditions for spatially evolving simulation. *AIAA Journal,* **35**(2), pp. 269-274.

COLONIUS, T. and LELE, S.K., 2004. Computational Aeroacoustics: progress on nonlinear problems of sound generation. *Progress in Aerospace Sciences,* **40**, pp. 345-416.

COMTE, P., HABERKORN, M., BOUCHET, G., PAGNEUX, V. and AUREGAN, Y., 2006. Large-Eddy Simulation of acoustic propagation in a turbulent channel flow. *Direct and Large-Eddy Simulation VI.* pp. 521-528.

CRANK, J. and NICOLSON, P., 1947. A practical method for numerical integration of solutions of partial differential equations of heat-conduction type, *Proceedings Cambridge Philos. Soc.*, vol 43 1947, pp. 50.

DAVIDSON, L., 2007a. Hybrid LES-RANS: Inlet boundary conditions for flows including recirculation, 2007a, pp. 689-694.

DAVIDSON, L., 2007b. Using isotropic synthetic fluctuations as inlet boundary conditions for unsteady simulations. *Advances and Applications in Fluid Mechanics,* **109**(1), pp. 1-35.

DAVIDSON, L. and BILLSON, M., 2006. Hybrid LES/RANS using synthesized turbulence for forcing at the interface. *International Journal of Heat and fluid flow,* **27**(6), pp. 1028-1042.

DAVIDSON, L. and BILLSON, M., 2004. Hybrid RANS-LES using synthetized turbulence for forcing at the interface, 2004.

DAVIDSON, L. and DAHLSTROM, S., 2007. Hybrid LES-RANS: An approach to make LES applicable at high Reynolds number. *International journal of computational fluid dynamics,* **19**, pp. 415-427.

DAVIDSON, P.A., 2004. *Turbulence, an introduction for scientist and engineers.* Oxford University Press.

DE VILLIERS, E., 2006. *The potential for large eddy simulation for the modelling of wall bounded flows*, Imperial College.

DEARDORFF, J.W., 1970. A numerical study of three-dimensional turbulent channel flow at large Reynolds number. *Journal of Fluid Mechanics,* **41**(2), pp. 453-480.

DESANTES, J.M., TORREGROSA, A.J. and BROATCH, A., 2001. Experiments on Flow Noise Generation in Simple Exhaust Geometries *Acta Acustica united with Acustica,* **87**(1), pp. 46-55.

DESPIRITO, J. and BINSEEL, M.S., 2008. *Modeling of acoustic pressure waves in Level-dependent Earplugs.* ART-TR-4607.

DI MARE, L., KLEIN, M., JONES, W.P. and JANICKA, J., 2006. Synthetic turbulence inflow conditions for large-eddy simulation. *Physics of Fluids,* **18**(2), pp. 25107.

DONG, Y. and LU, X., 2004. Large eddy simulation of a thermally stratified turbulent channel flow with temperature oscillation on the wall. *International Journal of Heat and Mass transfer,* **47**, pp. 2109-2122.

DUCROS, F., COMTE, P. and LESIEUR, M., 1996. Large-eddy simulation of transition to turbulence in a boundary layer developing spatially over a flat plate. *Journal of Computational Physics,* **326**, pp. 1-36.

EGGELS, J.G.M., UNGER, F., WEISS, M.H., WESTERWEEL, J., ADRIAN, R.J., FRIEDRICH, R. and NIEUWSTADT, F.T.M., 1994. Fully developed turbulent pipe flow: a comparison between direct numerical simulation and experiment. *Journal of Fluid Mechanics,* **268**, pp. 175-210.

EGGELS, J.G.M., WESTERWEEL, J., NIEUWSTADT, F.T.M. and ADRIAN, R.J., 1993. Direct numerical simulation of turbulent pipe flow, A comparison between simulation and experiment at low Re-number. *Advances in Turbulence IV.* Netherlands: Kluwer Academic Publishers, pp. 319-324.

ERLEBACHER, G., HUSSAINI, M.Y., SPEZIALE, C.G. and ZANG, T.A., 1992. Towards the large-eddy simulation of compressible turbulent flows. *Journal of Fluid Mechanics,* **238**, pp. 155-185.

EWERT, R., 2008. Broadband slat noise prediction based on CAA and stochastic sound sources from a fast random particle-mesh (RPM) method. *Computers and Fluids,* **37**, pp. 369-387.

EWERT, R., 2005. The Simulation Of Slat Noise Applying Stochastic Sound Sources Based On Solenoidal Digital Filters (SDF), , 18-20 July 2005.

EWERT, R. and EMUNDS, R., 2005. CAA Slat Noise Studies Applying Stochastic Sound Sources Based On Solenoidal Digital Filters, , 23 - 25 May 2005.

FATHALI, M., KLEIN, M., BROECKHOVEN, T., LACOR, C. and BAELMANS, M., 2009. Stochastic generation of velocity fluctuation for turbulent inflow and initial condition. *COMPUTATIONAL FLUID DYNAMICS 2006.* pp. 1-6.

FATHALI, M., KLEIN, M., BROECKHOVEN, T., LACOR, C. and BAELMANS, M., 2008. Generation of turbulent inflow and initial conditions based on multi-correlated random fields. *INTERNATIONAL JOURNAL FOR NUMERICAL METHODS IN FLUIDS,* **57**(1), pp. 93-117.

FATHALI, M., MEYERS, J., RUBIO, G., SMIRNOV, S. and BAELMANS, M., 2008. Sensitivity analysis of initial condition parameters on the transitional temporal turbulent mixing layer. *Journal of Turbulence,* **9**(12), pp. 1-28.

FREUND, J.B., LELE, S.K. and MOIN, P., 1996. Calculation of the radiated sound field using an open Kirchhoff surface. *AIAA Journal,* **35**(5), pp. 909-916.

FUREBY, C., 1996. On subgrid scale modeling in large eddy simulations of compressible fluid flow. *Physics of Fluids,* **8**(5), pp. 1301-1311.

FUREBY, C., GOSMAN, A.D., TABOR, G., WELLER, H.G., SANDHAM, N. and WOLFSHTEIN, M., 1997. Large eddy simulation of turbulent channel flows, 1997, pp. 28.

FUREBY, C., TABOR, G., WELLER, H.G. and GOSMAN, A.D., 1997. A comparative study of subgrid scale models in homogeneous isotropic turbulence. *Physics and Fluids,* **9**(5), pp. 1416-1429.

GEORGE, W.K. and DAVIDSON, L., 2004. Role of Initial Conditions in Establishing Asymptotic Flow Behavior. *AIAA Journal,* **42**(3), pp. 438-446.

GERMANO, M., PIOMELLI, U., MOIN, P. and CABOT, W.H., 1991. A dynamic subgrid-scale eddy viscosity model. *Physics of Fluids,* **3**(7), pp. 1760-1765.

GEURTS, B., VREMAN, B., KUERTEN, H. and THEOFILIS, , 1993. LES modelling error in free and wall bounded compressible shear layers. In: W. RODI and MARTELLI, eds, *Engineering turbulence modelling and experiments 2.* Elsevier Science Publishers, pp. 325.

GHANEM, R., 1999. The Nonlinear Gaussian Spectrum of Log-Normal Stochastic Processes and Variables. *Journ. Appl. Mech,* **66**(4), pp. 964-973.

GHOSAL, S., 1996. An analysis of numerical error in large eddy simulations of turbulence. *Journal of Computational Physics,* **125**, pp. 187-206.

GLENDENING, J.W. and TRACY, H., 2001. Influence of advection differencing error upon Large-Eddy Simulation accuracy. *Boundary-Layer Meteorology,* **98**(1), pp. 127-153.

GLOERFELT, X., BAILLY, C. and JUVE, D., 2003. Direct computation of the noise radiated by a subsonic cavity flow and application of integral methods. *Journal of Sound and Vibration,* **266**(1), pp. 119-146.

GLOERFELT, X., BAILLY, C. and JUVE, D., 2001. Computation of the noise radiated by a subsonic cavity using direct simulation and acoustic analogy, *7th AIAA/CEAS Aeroacoustics* 2001, pp. 1-12.

GOEDECKE, G.H., OSTASHEV, V.E., WILSON, D.K. and AUVERMANN, H.J., 2004. Quasi-Wavelet Model Of Von Kármán Spectrum Of Turbulent Velocity Fluctuations. *Boundary-Layer Meteorology,* **112**(1), pp. 33-56.

HAMILTON, J.M., KIM, J. and WALEFFE, F., 1995. Regeneration mechanisms of near-wall turbulence structures. *Journal of Fluid Mechanics,* **287**, pp. 317-348.

HARLOW, F.H. and AMSDEN, A.A., 1971. A numerical fluid dynamics calculation method for all flow speeds. *Journal of Computational Physics,* **8**, pp. 197-213.

HARLOW, F.H. and AMSDEN, A.A., 1968. Numerical calculation of almost incompressible flow. *Journal of Computational Physics,* **3**, pp. 80-93.

HARLOW, F.H. and WELCH, J.E., 1965. Numerical calculation of Time-Ddependent viscous incompressible flow of fluid with free surface. *The Physics of Fluids,* **8**(12), pp. 2182-2189.

HAWKEN, D.M., TAMADDON-JAHROMI, H.R., TOWNSEND, P. and WEBSTER, M.F., 1990. A Taylor-Galerkin-based algorithm for viscous incompressible flow. *International Journal for Numerical Methods in Fluids,* **10**, pp. 327-351.

HINZE, J.O., 1975. *Turbulence.* 2nd Edn. McGraw-Hill.

HWANG, C., LEE, D.J. and CHAE, K.S., 2007. Time accurate finite difference method for performance prediction of a silencer with mean flow and non-linear incident wave. *Journal of Mechanical Science and Technology,* **21**(1), pp. 1-11.

ISSA, R.I., 1985. Solution of the implicitly discretised fluid flow equations by Operator-splitting. *Journal of Computational Physics,* **62**, pp. 40-65.

ISSA, R.I., AHMADI-BEFRUI, B., BESHAY, K.R. and GOSMAN, A.D., 1991. Solution of the implicitly discretised reacting flow equations by operator-splitting. *Journal of Computational Physics,* **93**, pp. 388-410.

ISSA, R.I., GOSMAN, A.D. and WATKIN, A.P., 1986. The computation of compressible and incompressible recirculating flows by a non-iterative implicit scheme. *Journal of Computational Physics,* **62**, pp. 66-82.

JARRIN, N., BENHAMADOUCHE, S., LAURENCE, D. and PROSSER, R., 2006. A Synthetic-Eddy-Method for Generating Inflow Conditions for LES. *International Journal of Heat and fluid flow,* **27**, pp. 585-593.

JARRIN, N., PROSSER, R., URIBE, J., BENHAMADOUCHE, S. and LAURENCE, D., 2009. Reconstruction of Turbulent Fluctuations for Hybrid RANS-LES simulations using a synthetic Eddy Method. *International Journal of Heat and Fluid Flow,* **30**, pp. 435-442.

JASAK, H., WELLER, H.G. and GOSMAN, A.D., 1999. High resolution NVD differencing scheme for arbitrarily unstructured meshes. *International journal for numerical methods in fluids,* **31**, pp. 431-449.

JENNY, P. and MULLER, B., 1999. Convergence acceleration for computing steady-state compressible flow at low Mach numbers. *Computers & Fluids,* **28**, pp. 951-972.

JEONG, J., HUSSAIN, F., SCHOPPA, W. and KIM, J., 1997. Coherent structures near the wall in a turbulent channel flow. *Journal of Fluid Mechanics,* **332**, pp. 185-214.

JONES, W.P. and LAUNDER, B.E., 1972. The prediction of laminarization with a two-equation model of turbulence. *International Journal of Heat and Mass Transfer,* **15**(2), pp. 301-314.

KARKI, K.C., 1986. *A calculation procedure for viscous flows at all speeds in complex geometries*, University of Minnesota.

KARKI, K.C. and PATANKAR, S.V., 1989. Pressure based calculation procedure for viscous flows at all speeds in arbitarary configurations. *AIAA Journal,* **27**(9), pp. 1167-1174.

KARWEIT, M., BLANC-BENON, P., JUVE, D. and COMTE-BELLOT, G., 1991. Simulation of the propagation of an acoustic wave through a turbulent velocity field: A study of phase variance. *Journal of the Acoustical Society of America,* **89**(1), pp. 52-62.

KIM, J., MOIN, P. and MOSER, R., 1987. Turbulence statistics in fully developed channel flow at low Reynolds number. *Journal of Fluids Mechanics,* **177**, pp. 133-166.

KLEIN, M., SADIKI, A. and JANICKA, J., 2003. A digital filter based generation of inflow data for spatially developing direct numerical or large eddy simulations. *Journal of Computational Physics,* **186**(2), pp. 652-665.

KLEIN, R., 1995. Semi-Implicit extension of a Godunov-type scheme based on low Mach number asymptotics I: One-Dimensional flow. *Journal of Computational Physics,* **121**, pp. 213-237.

KNIGHT, D., ZHOU, G., OKONG, N. and SHUKLA, V., 1998. Compressible Large Eddy Simulation using unstructured grids. *Aerospace Sciences Meeting and Exhibit, 36th, Reno, NV,* .

KOLMOGOROV, A.N., 1991. The local structure of turbulence in incompressible viscous fluid for very large Reynolds numbers. *Proceeding of Royal Society of London (Reprint),* **434**, pp. 9-13.

KOLMOGOROV, A.N., 1942. The equations of turbulent motion in an incompressible fluid. *Izvestia Acad Sci USSR Physc,* **6**, pp. 56-58.

KORNEV, N. and HASSEL, E., 2007. Method of random spots for generation of synthetic inhomogeneous turbulent fields with prescribed autocorrelation functions. *Communications in Numerical Methods in Engineering,* **23**, pp. 35-43.

KORNEV, N., KROGER, H. and HASSEL, E., 2008. Synthesis of homogeneous anisotropic turbulent fields with prescribed second-order statistics by the random spots method. *Communications in Numerical Methods in Engineering,* **24**, pp. 875-877.

KORNEV, N., KROGER, H., TURNOW, J. and HASSEL, E., 2007. Synthesis of artificial turbulent fields with prescribed second-order statistics using the random-spot method, , 27 September 2007, pp. 1-3.

KRAICHNAN, R.H., 1969. Diffusion by a random velocity field. *Physics of Fluids,* **13**(1), pp. 22-31.

KURGANOV, A. and TADMOR, E., 2000. New high-resolution central schemes for nonlinear conservation laws and convection-diffusion equations. *Journal of Computational Physics,* **160**, pp. 241-282.

LAIZET, S. and LAMBALLAIS, E., 2009. High-order compact schemes for incompressible flows: A simple and efficient method with quasi-spectral accuracy. *Journal of Computational Physics,* **228**(16), pp. 5989-6015.

LAMBALLAIS, E., LESIEUR, M. and MÉTAIS, O., 1997. Probability distribution functions and coherent structures in a turbulent channel. *Physical Review E,* **56**(6), pp. 6761-6766.

LAX, P.D., 1954. Weak solutions of nonlinear hyperbolic equations and their numerical computation. *Communications on pure and applied,* **7**(1), pp. 159-193.

LE, A., COLEMAN, G.N. and KIM, J., 2000. Near-wall turbulence structures in three dimensional boundary layers. *Int. Journal of Heat and Fluid Flow,* **21**, pp. 480-488.

LE, H., MOIN, P. and KIM, J., 1997. Direct numerical simulation of turbulent flow over a backward-facing step. *Journal of Fluid Mechanics,* **330**, pp. 349-374.

LEE, S., LELE, S.K. and MOIN, P., 1992. Simulation of spatially evolving turbulence and the applicability of Taylor's hypothesis in compressible flow. *Physics of Fluids A,* **4**(7), pp. 1521-1530.

LENORMAND, E., SAGAUT, P. and PHUOC, L.T., 2000. Large eddy simulation of subsonic and supersonic channel flow at moderate Reynolds number. *International Journal for Numerical Methods in Fluids,* **32**, pp. 369-406.

LESIEUR, M., 1997. *Turbulence in Fluids.* 4th edition edn. Netherland: Springer.

LIGHTHILL, J., 1992. *Report on the final panel discussion on computational aeroacoustics.* 92-53.

LIU, H., LU, S. and ZENG, F., 2009. A Study on the Effects of Higher Order Mode Wave on Mufflers Performance. *Modern Applied Science,* **3**(1), pp. 170-175.

LUMMER, M., GROGGER, H.A. and DELFS, J.W., 2001. Using RANS mean flow fields in numerical aeroacoustics simulations (CAA), *RTO AVT Syposium on Ageing Mechanism and control*, 8-11 October 2001, pp. 1.

LUND, T.S., WU, X. and SQUIRES, K.D., 1998. Generation of Turbulent Inflow Data for Spatially-Developing Boundary Layer Simulations. *Journal of Computational Physics,* **140**, pp. 233-258.

MANNA, M. and VACCA, A., 2008. Spectral dynamic of pulsating turbulent pipe flow. *Computers & Fluids,* **37**, pp. 825-835.

MAO, Z.-. and HANRATTY, T.J., 1986. Studies of the wall shear stress in a turbulent pulsating pipe flow. *Journal of Fluid Mechanics,* **170**, pp. 545-564.

MENDONCA, F., READ, A., CARO, S., DEBATIN, K. and CARUELLE, B., 2005. Aeroacoustic simulation of double diaphragm orifices in an aircraft climate control system, , 23-25 May 2005, pp. 1-11.

MERKLE, C.L. and CHOI, Y., 1988. Computation of low-speed compressible flows with time-marching procedures. *International Journal for Numerical Methods in Engineering,* **25**, pp. 293-311.

MERKLE, C.L., VENKATESWARAN, S. and BUELOW, P.E.O., 1992. The relationship between pressure-based and density-based algorithms, , January 6-9 1992.

MESBAH, M., 2006. *Flow Noise Prediction Using the Stochastic Noise Generation and Radiation Approach*, Katholieke Universiteit Leuven.

MIDDELBERG, J.M., BARBER, T.J., LEONG, S.S., BYRNE, K.P. and LEONARDI, E., 2004. Computational Fluid Dynamics analysis of the acoustic performance of various simple expansion chamber mufflers, , 3-5 November 2004, pp. 123-128.

MIDDELBERG, J.M., BARBER, T., LEONG, S., LEONARDI, E. and BYRNE, K.P., 2003. Determining the acoustic performance of a simple reactive muffler using Computational Fluid Dynamics, , 7-9 April 2003.

MOHIUDDIN, A.K.M., RAHMAN, A. and GAZALI, Y.B., 2007. Experimental investigation and simulation of muffler performance, , 29-31 December 2007.

MOIN, P. and KIM, J., 1982. Numerical investigation of turbulent channel flow. *Journal of Fluid Mechanics,* **118**, pp. 341-377.

MOSER, R.D., KIM, J. and MANSOUR, N.N., 1999. Direct Numerical Simulation of turbulent channel flow up to Re = 590. *Physics of Fluids,* **11**(4), pp. 943-945.

MOUREAU, V., BERAT, C. and PITSCH, H., 2007. An efficient semi-implicit compressible solver for large-eddy simulations. **226**, pp. 1256-1270.

MUNJAL, M.L., 1997. Plane wave analysis of side inlet/outlet chamber mufflers with mean flow. *Applied Acoustics,* **52**(2), pp. 165-175.

MUNJAL, M.L., 1987. *Acoustics of Ducts and Mufflers.* New York: John Wiley and sons.

MUNZ, C.D., ROLLER, S., KLEIN, R. and GERATZ, K.J., 2003. The extension of incompressible flow solvers to the weakly compressible regime. *Computers & Fluids,* **32**, pp. 173-196.

NAGARAJAN, S., LELE, S.K. and FERZINGER, J.H., 2003. A robust high-order compact method for large eddy simulation. *Journal of Computational Physics,* **191**, pp. 392-419.

NESSYAHU, H. and TADMOR, E., 1990. Non-oscillatory central differencing for hyperbolic conservation laws. *Journal of Computational Physics,* **87**(2), pp. 408-463.

NIKITIN, N., NICOUD, F., WASISTHO, B., SQUIRES, K.D. and SPALART, P., 2000. An approach to wall modeling in large-eddy simulations. *Physics of Fluids,* **12**(7), pp. 1629.

OBIKANE, Y., 2009. Aeroacoustic Simulation in Automobile Muffler by Using the Exact Compressible Navier-Stokes Equation. *Computational Fluid Dynamics 2008,* **4**, pp. 93-98.

OPENFOAM, 2007. *OpenFOAM-The Open Source CFD Toolbox: Programmers Guide.*

OSTASHEV, V.E., BRÄHLER, B., MELLERT, V. and GOEDECKE, G.H., 1998. Coherence functions of plane and spherical waves in a turbulent medium with the von Karman spectrum of medium inhomogeneities. *J. Acoust. Soc. America,* **104**(2), pp. 727-737.

PANIGRAHI, S.N. and MUNJAL, M.L., 2007. A generalized scheme for analysis of multifarious commercially used mufflers. *Applied Acoustics,* **68**, pp. 660-681.

PANTANO, C., PULLIN, D.I., DIMOTAKIS, P.E. and MATHEOU, G., 2008. LES approach for high Reynolds number wall-bounded flows with application to turbulent channel flow. *Journal of Computational Physics,* **227**, pp. 9271-9291.

PATANKAR, S.V., 1980. *Numerical heat transfer and fluid flow.* New York: McGraw-Hill.

PATANKAR, S.V. and SPALDING, D.B., 1972. A calculation procedure for Heat, Mass and Momentum transfer in three-dimensional parabolic flows. *International Journal of Heat and Mass Transfer,* **15**, pp. 1787-1806.

PIOMELLI, U., 1993. High Reynolds number calculations using the dynamic subgrid-scale stress model. *Physics of Fluids A,* **5**, pp. 1484-1490.

PISCAGLIA, F., JASAK, H. and RUSCHE, H., 2010. Lib-ICE: a C++ object oriented library for ICE simulation- acoustics and aftertreatment, , 21-24 June 2010.

POLETTO, R., REVELL, A., CRAFT, T. and JARRIN, N., 2011. Divergence Free Synthetic Eddy Method for Embedded LES inflow Boundary Conditions, , 28-31 July 2011.

POPE, S., 2000. *Turbulent flows.* Cambridge: Cambridge University Press.

POTENTE , D., 2005. General Design principles for an automotive muffler, , 9-11 November 2005, pp. 153-158.

PRANDTL, L., 1925. Uber die ausgebildete Turbulenz. *ZAMM,* **5**, pp. 136-139.

PULLIAM, T.H. and STEGER, J.L., 1980. Implicit finite-difference simulations of three-dimensional compressible flow. *AIAA Journal,* **18**(2), pp. 159-167.

RAI, M.M. and MOIN, P., 1993. Direct numerical simulation of transition and turbulence in a spatially evolving boundary layer. *Journal of Computational Physics,* **109**, pp. 169-192.

RHIE, C.M., 1989. Pressure based Navier-Stokes solver using the multigrid method. *AIAA Journal,* **27**(8), pp. 1017-1018.

RHIE, C.M. and CHOW, W.L., 1983. Numerical study of the turbulent flow past an airfoil with trailing edge seperation. *AIAA Journal,* **21**(11), pp. 1525-1532.

RICHARDSON, L.F., 2007. *Weather Prediction by Numerical Process (1922).* second Ed. edn. New York: Cambridge University Press.

RIZZETTA, D.P., VISBAL, M.R. and BLAISDELL, G.A., 2003. A time-implicit high-order compact differencing and filtering scheme for large-eddy simulation. *International Journal for Numerical Methods in Fluids,* **42**, pp. 665-693.

ROCHE, J.M., VUILLOT, F., LEYLEKIAN, L., DELATTRE, G., PIOT, E. and SIMON, F., 2010. Numerical and Experimental Study of Resonant Liners Aeroacoustic Absorption under Grazing Flow. *16th AIAA/CEAS Aeroacoustics Conference,* (3767), pp. 1-18.

ROGALLO, R.S., 1981. *Numerical experiments in homogeneous turbulence.* Nasa TM-81315.

RONNEBERGER, D. and AHRENS, C.D., 1977. Wall shear stress caused by small amplitude perturbations of turbulent boundary-layer flow: an experimental investigation. *Journal of Fluid Mechanics,* **83**(3), pp. 433-464.

ROSSITER, J.E., 1966. *Wind tunnel experiments on the flow over rectangular cavities at subsonic and transonic speeds.* 3438. Her Majesty's stationary office: Aeronautical research council,.

ROSSOW, C.-., 2000. A flux-splitting scheme for compressible and incompressible flows. *Journal of Computational Physics,* **164**, pp. 104-122.

ROSSOW, C.-., 2003. A blended pressure/density based method for the computation of incompressible and compressible flows. *Journal of Computational Physics,* **185**, pp. 375-398.

ROUX, A., GICQUEL, L.Y.M., SOMMERER, Y. and POINSOT, T.J., 2008. Large eddy simulation of mean and oscillating flow in a side-dump ramjet combustor. *Combustion and Flame,* **152**, pp. 154-176.

ROUX, A., LARTIGUE, G., POINSOT, T.J., MEIER, U. and BERAT, C., 2005. Studies of mean and unsteady flow in a swirled combustor using experiments, acoustic analysis, and large eddy simulations. *Combustion and Flame,* **141**, pp. 40-54.

ROWLEY, C.W., 2002. *Modeling, Simulation, and Control of Cavity Flow Oscillations*, California Institute of Technology, Pasadena, California.

ROWLEY, C.W., COLONIUS, T. and BASU, A.J., 2002. On self-sustained oscillations in two-dimensional compressible flow over rectangular cavities. *Journal of Fluids Mechanics,* **455**, pp. 315-346.

RUBIO, G., ROECK, W.D., DESMET, W. and BAELMANS, M., 2006a. Large Eddy Simulation for computation of Aeroacoustic sources in 2D-Expansion chambers. VI edn. Dordrecht, Netherlands: Springer Science, pp. 555-564.

RUBIO, G., ROECK, W.D., MEYERS, J., BAELMANS, M. and DESMET, W., 2006b. Aeroacoustic noise source mechanisms in simple expansion chambers, , 8-10 may 2006b, pp. 1-9.

RUDMAN, M. and BLACKBURN, H.M., 1999. Large eddy simulation of turbulent pipe flow, , 6-8 December 1999, pp. 503-508.

SCHLUTER, J.U., PITSCH, H. and MOIN, P., 2004. Large-eddy simulation inflow conditions for coupling with Reynolds-averaged flow solvers. *AIAA Journal,* **42**(3), pp. 478-484.

SCHNEIDER, G.E. and KARIMIAN, S.M.H., 1994. Advances in control-volume-based finite-element methods for compressible flows. *Computational Mechanics,* **14**, pp. 431-446.

SCHOPPA, W. and HUSSAIN, F., 2000. Coherent Structure dynamics in near-wall turbulence. *Fluid Dynamics Research,* **26**, pp. 119-139.

SCHUMANN, U., 1975. Subgrid scale model for finite difference simulations of turbulent flows in plane channels and annuli. *Journal of Computational Physics,* **18**, pp. 376-404.

SCOTTI, A. and PIOMELLI, U., 2002. Turbulence Models in Pulsating Flows. *AIAA Journal,* **30**(3), pp. 537-544.

SCOTTI, A. and PIOMELLI, U., 2001. Numerical simulation of pulsating turbulent channel flow. *physics of fluids,* **13**(5), pp. 1367-1384.

SELAMET, A. and JI, Z.L., 1999. Acoustic attenuation performance of circular expansion chambers with extended inlet/outlet. *Journal of Sound and Vibration,* **223**(2), pp. 197-212.

SELAMET, A. and RADAVICH, P.M., 1997. The effect of length on the acoustic attenuation performance of concentric expansion chambers: An Analytical, Computational and Experimental investigation. *Journal of Sound and Vibration,* **201**(4), pp. 407-426.

SEROR, C., SAGAUT, P., BAILLY, C. and JUVE, D., 2001. On the radiated noise computed by large-eddy simulation. *Physics of Fluids,* **13**(2), pp. 476-487.

SEYBERT, A.F., SOENARKO, F.J., RIZZO, F.J. and SHIPPY, D.J., 1985. An advanced computational method for radiation and scattering of acoustic waves in three dimensions. *Journal of Acoustic Society of America,* **77**(2), pp. 362-368.

SHYY, W., CHEN, M.-. and SUN, C.-., 1992a. Pressure-Based Multigrid Algorithm for Flow at All Speeds. *AIAA Journal,* **30**, pp. 2660-2669.

SHYY, W., CHEN, M. and SUN, C., 1992b. A pressure-based FMG/FAS algorithm for flow at all speeds, , January 6-9 1992b.

SMAGORINSKY, J.S., 1963. General circulation experiments with the premitive equations. *Monthly,* **91**(3), pp. 99-164.

SMIRNOV, A., SHI, S. and CELIK, I., 2001. Random Flow Generation Technique for Large Eddy Simulations and Particle-Dynamics Modeling. *Journal of Fluids Engineering,* **13**(2), pp. 359-361.

SNELLEN, M., LIER, L.V., GOLLIARD, J. and VEDY, E., 2003. Prediction of the flow induced noise for practical applications using the SNGR method, , July 2003.

SPALART, P.R., 1988. Direct simulation of a turbulent boundary layer up to Re=1410. *Journal of Fluid Mechanics,* **187**, pp. 61-98.

SPALART, P.R. and WATMUFF, J.H., 1993. Experimental and numerical study of a turbulent boundary layer with pressure gradients
. *Journal of Fluid Mechanics,* **249**, pp. 337-371.

SUH, J., FRANKEL, S.H., MONGEAU, L. and PLESNIAK, M.W., 2006. Compressible large eddy simulation of wall-bounded turbulent flows using a semi-implicit numerical scheme for low Mach number aeroacoustics. *Journal of Computational Physics,* **215**, pp. 526-551.

SUWANDI, D., MIDDELBERG, J., BYRNE, K.P. and KESSISSOGLOU, N.J., 2005. Predicting the Acoustic performance of mufflers using Transmission Line theory, , 9-11 November 2005, pp. 181-187.

TABOR, G.R., BABA-AHMADI, M.H., DE VILLERS, E. and WELLER, H.G., 2004. Construction of inlet conditions for LES of turbulent channel flow, , 24-28 July 2004.

TAM, C.K.W., 2006. Recent advances in computational aeroacoustics. *Fluid Dynamics Research,* **38**, pp. 591-615.

TAM, C.K.W. and JU, H., 2009. A Computational and Experimental Study of Resonators in Three Dimensions, *15th AIAA/CEAS Aeroacoustics Conference*, 11-13 May 2009, pp. 3171.

TAM, C.K.W., JU, H., JONES, M.G., WATSON, W.R. and PARROTT, T.L., 2003. A Computational and Experimental Study of Slit Resonators, 2003.

TAM, C.K.W., KURBATSKII, K.A., AHUJA, K.K. and GAETA, J., 2001. A Numericaland Experimental Investigation of the dissipation mechanisms of resonant acoustic liners. *Journal of Sound and Vibration,* **245**(3), pp. 545-557.

TAM, C.K.W. and WEBB, J.C., 1993. Dispersion-Relation-Preserving finite difference schemes for computational acoustics. *Journal of Computational Physics,* **107**(2), pp. 262-281.

TARDU, S.F., BINDER, G. and BLACKWELDER, R.F., 1994. Turbulent channel flow with large-amplitude velocity oscillations. *Journal of Fluid Mechanics,* **267**, pp. 109-151.

TAYLOR, G.I., 1935. Statistical Theory of Turbulence, 1935, pp. 421.

THOMPSON, K.W., 1990. Time dependent boundary conditions for hyperbolic systems, II. *Journal of Computational Physics,* **89**(2), pp. 439-461.

THOMPSON, K.W., 1987. Time dependent boundary conditions for hyperbolic systems. *Journal of Computational Physics,* **68**(1), pp. 1-24.

TURKEL, E., 1987. Preconditioned methods for solving the incompressible and low speed compressible equations. *Journal of Computational Physics,* **72**(2), pp. 277-298.

URIBE, J.C., JARRIN, N., PROSSER, R. and LAURENCE, D., 2010. Development of a Two-velocities Hybrid RANS-LES Model and its Application to a Trailing Edge Flow. pp. 181-197.

VELOUDIS, I., YANG, Z., MCGUIRK, J., PAGE, G.J. and SPENCER, A., 2007. Novel Implementation and Assessment of a Digital Filter Based Approach for the Generation of LES Inlet Conditions. *Flow Turbulence Combustion,* **79**, pp. 1-24.

VON KARMAN, T., 1930. Mechanische ahnlichkeit und turbulenz. 1930, pp. 85-105.

VREMAN, B., 1995. *Direct and Large-eddy simulation of the compressible turbulent mixing layer*, University de Twente.

WALL, C., PIERCE, C.D. and MOIN, P., 2002. A semi-implicit method for resolution of acoustic waves in low Mach number flows. *Journal of Computational Physics,* **181**, pp. 545-563.

WEBSTER, M.F., KESHTIBAN, I.J. and BELBLIDIA, F., 2004. Computation of weakly-compressible highly-viscous liquid flows. *Engineering Computations,* **1**(7), pp. 777-804.

WHITMIRE, J. and SARKAR, S., 2000. Validation of acoustic-analogy predictions for sound radiated by turbulence. *Physics of Fluids,* **12**(2), pp. 381-391.

WILCOX, D.C., 2006. *Turbulence modeling for CFD.* 3rd Ed. edn. San Diego, California: DCW industries.

WILSON, C.E., 1994. *Noise Control: Measurement, Analysis, and Control of Sound and Vibration.* 2nd edn. Krieger Publishing Company.

XU, T., GE, C.J., ZOU, P., XU, T.S. and ZUO, W.J., 2009. Improved method for flow field based on SIMPLER and PISO. *Journal of Jilin University (E&T edition),* **39**(3), pp. 668-672.

XU, X., LEE, J.S. and PLETCHER, R.H., 2005. A compressible finite volume formulation for large eddy simulation of turbulent pipe flow at low Mach number in cartesian coordinates. *Journal of Computational Physics,* **203**, pp. 22-48.

YASUDA, T., WU, C., NAKAGAWA, N. and NAGAMURA, K., 2010. Predictions and experimental studies of the tail pipe noise of an automotive muffler using a one dimensional CFD model. *Applied Acoustics,* **71**, pp. 701-707.

YOSHIZAWA, , 1986. Statistical theory for compressible turbulent shear flows, with the application to subgrid modeling. *Physics and Fluids,* **29**(6), pp. 2152-2163.

ZIENKIEWICZ, O.C. and CODINA, R., 1995. A general algorithm for compressible and incompressible flow- Part I. The split, characteristic-Based Scheme. *International Journal for Numerical Methods in Fluids,* **20**, pp. 869-885.

Appendix

Navier-Stokes equations solved in this work for RANS and LES simulations are as follows:

RANS Equations:

$$\frac{\partial \bar{\rho}}{\partial t} + \frac{\partial \bar{\rho}\widehat{u_\iota}}{\partial x_i} = 0, \tag{10.1}$$

$$\frac{\partial \bar{\rho}\widehat{u_\iota}}{\partial t} + \frac{\partial \bar{\rho}\widehat{u_\iota}\widehat{u_j}}{\partial x_j} = -\frac{\partial P}{\partial x_j} + \frac{\partial \tau_{ij}}{\partial x_j} + \frac{\partial \bar{\sigma}_{ij}}{\partial x_j}, \tag{10.2}$$

$$\frac{\partial \bar{\rho}\hat{E}}{\partial t} + \frac{\partial \bar{\rho}\widehat{u_j}\hat{h}}{\partial x_j} = \frac{\partial}{\partial x_j}\left(\bar{\sigma}_{ij}\widehat{u_\iota} + \overline{\sigma_{\iota j}u_\iota^{'}}\right) - \frac{\partial}{\partial x_j}\left(\bar{q}_j + c_p\overline{\rho u^{'}T^{'}} + \bar{\sigma}_{ij}\widehat{u_\iota}\tau_{ij} + \overline{\rho u^{'}k}\right) \tag{10.3}$$

$$P = (\gamma - 1)\{\bar{\rho}\hat{E} - \frac{1}{2}\rho(\hat{u}^2 + \hat{v}^2 + \hat{w}^2) - \bar{\rho}k\} \tag{10.4}$$

Where $\widehat{\ }$ denotes density weighted Favre-averaged variable and $\bar{\ }$ denotes averaged variable. $\bar{\sigma}_{ij}$ is usually computed using Boussinesq assumption (Eq. 3.15) and

$$\hat{h} = \hat{E} + \frac{\bar{p}}{\bar{\rho}}$$

$$\bar{q}_j = -\frac{c_p\hat{\mu}}{Pr}\frac{\partial \hat{T}}{\partial x_j}$$

LES Equations:

$$\frac{\partial \bar{\rho}}{\partial t} + \frac{\partial \bar{\rho}\hat{u}_\iota}{\partial x_i} = 0, \tag{10.5}$$

$$\frac{\partial \bar{\rho}\hat{u}_\iota}{\partial t} + \frac{\partial \bar{\rho}\hat{u}_\iota\hat{u}_\jmath}{\partial x_j} = -\frac{\partial \bar{P}}{\partial x_j} + \frac{\partial(\hat{\tau}_{ij} + \tau_{ij,SGS})}{\partial x_j}, \tag{10.6}$$

$$\frac{\partial \bar{\rho}\hat{E}}{\partial t} + \frac{\partial \bar{\rho}\hat{u}_\jmath\hat{E}}{\partial x_j} = -\frac{\partial \bar{P}\hat{u}_\iota}{\partial x_j} + \frac{\partial \hat{u}_\iota}{\partial x_j}(\hat{\tau}_{ij} + \tau_{ij,SGS}) - \frac{\partial}{\partial x_j}\left(\hat{q}_j + q_{j,SGS}\right) \tag{10.7}$$

Where $\widehat{\ }$ denotes density Favre-filtered resolved variable and $\bar{\ }$ denotes filtered variable and

$$\tau_{ij,SGS} = 2\mu_t S_{ij}$$

$$q_{j,SGS} = -\left(\frac{\mu_t c_p}{Prt}\right)\frac{\partial \hat{T}}{\partial x_j}$$

Where μ_t is turbulent viscosity, S_{ij} is the resolved rate of strain and *Prt* is turbulent Prandtl number.